Efficiency Improvement Strategies and Control of Permanent Magnet Motor Drives

By
Parag Mahendra Kshirsagar

Dissertation submitted to the Faculty of Virginia Polytechnic Institute and State University
in partial fulfillment of the requirements for the degree of

Doctor of Philosophy
in
Electrical and Computer Engineering

Krishnan Ramu, Chair
Daniel. J. Stilwell, Co-Chair
Douglas. K. Lindner
Jaime De La Reelopez
Mahendra P Singh

Sept 22 2015
Blacksburg, Virginia

Keywords: Permanent Magnet Brushless DC motors, Permanent magnet synchronous motors, non-sinusoidal currents, reduced switching frequency, current control, programmed pulse width modulation, sensorless control

ABSTRACT

Efficiency Improvement Strategies and Control of Permanent Magnet Motor Drives

By
Parag Mahendra Kshirsagar
Prof. Krishnan Ramu, Chair
The Bradley Department of Electrical and Computer Engineering

Permanent magnet brushless dc (PMBDC) and synchronous machines (PMSM) drives are favored in variable speed applications for their high efficiency operation. Energy efficiency improvement in such motor drives is of interest in recent times because of rising cost of energy. Accordingly, two current control options for improving efficiency of these drives are taken for study and they are; (i) injecting sinusoidal and non-sinusoidal currents in PMBDC machines and (ii) lowering switching frequency of inverter driving the PMSM but without having significant low ordered sidebands of currents. Both these methods are applicable to existing types of permanent magnet motors and hence do not upset their existing optimized designs.

The first part of this research will focus on efficiency improvement in PMBDC machines with non-sinusoidal back electro-motive force (EMF) using various current excitation strategies. Accordingly, influence of sine, square and non-sinusoidal harmonic current on their performance is evaluated. To facilitate such a study, analytical expressions based on generalized back EMF for all the three excitation schemes have been derived to highlight their influence on torque ripple, motor harmonic losses and hence efficiency. An analytical approach on estimation of core losses under loaded operation has been elaborated to highlight the impact of stator current harmonics on efficiency of motor. Analytical as well as experimental results show that it is advantageous to use non-sinusoidal harmonic injection (NSHI) scheme in the speed range until the sum of inverter conduction losses and stator resistive losses exceeds core losses of the machine. When core losses become dominant, the algorithm is modified to sinusoidal current control thus maintaining higher efficiency operation. To achieve such an operation, a hybrid control scheme encompassing sinusoidal to NSHI field oriented sensorless controller has been implemented and the efficiency improvement is validated experimentally.

The second part of this research will consider efficiency improvement in PMSM drive system by reducing switching frequency of the inverter driving them. At reduced switching frequencies, programmed pulse width modulation methods that results in elimination or reduction of the low ordered sidebands of the currents are considered. To facilitate the efficiency evaluation, analytical loss models of the motor and the inverter are developed. Then loss comparison between five PMSM drive systems of various power ratings is made to quantify the efficiency improvement for fan type applications. Experimental efficiency measurements made on a PMSM drive system validates the analysis and approach considered in this research.

To implement the programmed pulse width modulation (PWM) on a state of the art microcontroller, a novel approach of carrier based pulse width modulator is proposed. To reduce cost of the system and improve reliability, operation of the PMSM drive without position sensor is essential. Accordingly, a rotor position sensorless controller algorithm considering reduced switching frequency operation is developed, analyzed and its laboratory implementation is presented. Simulation and experimental results validate both the design methodology and the expected performance attained by the proposed control strategy.

In conclusion, improving efficiency at reduced or no cost of investment is critical to pay itself in shorter period of time. Accordingly, the proposed current control options elaborated this research provides an opportunity for further efficiency improvement in present permanent magnet motor drives favored in wide range of applications.

ACKNOWLEDGEMENTS

This dissertation is a culmination of seven years of part time work while being employed full time at the United Technologies Research Center (UTRC). While pursuing this research, I have been supported by many inspiring people around the globe. I would like to take this opportunity to sincerely express how grateful I am to them.

At first I would like to express deep and sincere gratitude to my advisor Prof. Krishnan Ramu for accepting me as his student and guiding me not only for the research in this dissertation but also in life. I also thank him for his patience considering my long distance and part time nature of the work. His ingenious ideas and adherence to high quality work helped me in successfully finishing this dissertation.

Special thanks to my committee members Prof. Daniel J. Stilwell, Prof. Douglas K. Lindner, Prof. Jamie De La Reelopez, and Prof. Mahendra P. Singh, for reviewing this dissertation. Their feedback and comments were valuable in shaping this dissertation.

During the course of this work I was lucky to be have been influenced by many creative minds. I would like to thank them all considering their deep technical expertise in the subject matter. Amongst the alumni from Virginia Polytechnic Institute and State University, I would like to thank my colleague and dear friend Dr. Nimal Lobo for his persistent support throughout this work. I would also like to thank Dr. Gerald Francis, Dr. Alessandro Lidozzi, Dr. Jihoon Jang, David Lugo for their discussions and guidance on motor control digital hardware development. I sincerely express my gratitude to Prof Dushan Boroyevich, Prof. Rolando Burgos and Prof. Fred Wang who supported me while I was a research student at the Center for Power Electronics Systems (CPES).

From UTRC, I would like to thank my mentor Dr. Vladimir Blasko, and my great friends Dr. Shashank Krishnamurthy, Dr. Jagadeesh Tangudu, Dr. Luis Arnedo, Dr. Xin Wu, Dr. Suman Dwari, Dr. Dong Jiang, Dr. Jerry Piech, and Dr. Vivek Venugopal for their valuable discussions on advanced research topics on modeling, analysis, design and testing in the area of motors and drives. I would also like to thank Dr. Isaac Cohen, Dr. Brian McCabe, Dr. Zaffir Chaudhry and Dr. David Parekh for giving me time flexibility for completion of this dissertation. I’m grateful to the UTRC lab technicians William Rioux and Cliff Lamb who have been of tremendous help for the experimental setup used in this work. From Yaskawa Electric America, I would like to thank my mentor Dr. Mahesh Swamy for sharing his wealth of experience and motivating me in pursuing the research topic considered here. I would also like to thank my father, Mahendra Kshirsagar for his support and all the technical discussion in the area of power electronics.

I would like to thank my loving and patient wife Dr. Beata Wawrzyniak for all the sacrifices she made and her relentless support to complete this work. I cannot express in words how grateful I am to her. I would also like to thank my daughter Ania Kshirsagar and my sister Priya Kshirsagar who cheered me during the writing phase of this dissertation. Above all, I would like to thank my mother Shamala Kshirsagar for all the sacrifices she made in supporting my work. To her I owe the most.

I would like to express my gratitude to all my extended family members and friends around the world whose support and encouragement have been very valuable for me towards completion of the degree.

Finally I would like to thank God for giving me the strength and showing me the path in this journey.

Parag Kshirsagar.
October 14th 2015
Connecticut, USA

TABLE OF CONTENTS

LIST OF FIGURES

LIST OF TABLES

Chapter 1 Introduction

1.1. Abstract

Energy efficiency improvement in variable speed motor drives is of widespread interest because of the rising cost of energy and also efforts on reducing the carbon foot print for environmental protection. The permanent magnet motor drives are especially favored in variable speed applications due to their high efficiency of operation. This chapter will mainly provide the motivation and approaches for further improving efficiency in these motor drive system without modifying the state of the art drive hardware or redesign of the motors. Significant contributions of this research on the total system loss reduction by control of the stator current excitation waveforms in permanent magnet brushless DC motor (PMBDCM) and permanent magnet synchronous motor (PMSM) drives are highlighted.

1.2. Motivations and objectives

Electric motor drives are amongst the largest consumers of electricity in US and account for approximately 60% of the total energy consumption [1]. In 2014 itself, the residential and commercial building sector, which required high volume of these electric motors driven systems for space cooling and heating, consumed approximately one-third (20 quad BTU) of the total energy delivered in US [2]**.** The heating and cooling applications typically require vapor compressors, chillers, venting fans, pumps, blowers and heater fans. They are mainly driven by variable speed drives (VSD). Widespread adoption of variable speed systems is primarily attributed to as much as 30 percent annual energy savings over fixed speed systems [3]. One of the important goals of researchers in this area has been to further improve efficiency of VSD's due to the rising cost of energy.

Table 1-1. Annual Cost Savings and Efficiency Improvement.

Power (kW)	**Current Efficiency (%)**	**Annual Cost of Energy ($M)**	**% Efficiency improvement**	**Annual Cost Savings ($M)**
1	80.0	52	1.0	0.52
5	88.0	237	1.0	2.10
10	91.0	462	1.0	6.30

In order to understand the relationship between annual cost of savings on energy consumption and efficiency improvement, consider an installation where there are 10000 variable speed drive units in the power range of 1kW, 5 kW and 10 kW and are operating for 3500 hours annually at $0.12 per kW-hr utility rate. Then the impact of one percent efficiency improvement in each unit on the annual cost of savings is listed in Table 1-1.

From the above table, it is evident that a small increment in efficiency can result in significant cost reduction per year for the given number of installed variable speed drive systems. The savings are higher at higher power ratings and also in applications which require large number of these units. The predominant losses in variable speed drive systems are in the motors and the inverters driving them. Hence the system efficiency improvement strategies are centered on the reduction of losses in the motor or inverter or both.

For the space cooling and heating applications, the commercial variable speed drives are offered with either a three-phase induction or a permanent magnet motor both of which are driven by an inverter [4]. Emerging technologies such as synchronous reluctance and switched reluctance motor drives are possible candidates in future. Since permanent magnet motor drives yield highest peak efficiency at present [5], they are considered in the analysis henceforth. It is known that the payback due to their higher efficiency compensates for the additional upfront cost during the lifetime of the motor drive system. Then techniques that can further improve their efficiency without modifying the inverter and without disrupting the optimized motor design are highly desirable to pay itself in shorter period of time. Accordingly, this research will focus on various control strategies for improving the efficiency of the permanent magnet motor drive system considering the space cooling and heating applications. These applications require low dynamic performance, do not need to be operated at very low speeds (below 0.1 p.u.), and the effect of torque ripple due to PWM harmonics on the mechanical components such as impellers, vanes, and crank shaft is not a critical requirement. Given the constraint of using the existing hardware, the only option for improving the efficiency is then to modify the stator current excitation waveforms of the motor using the inverter.

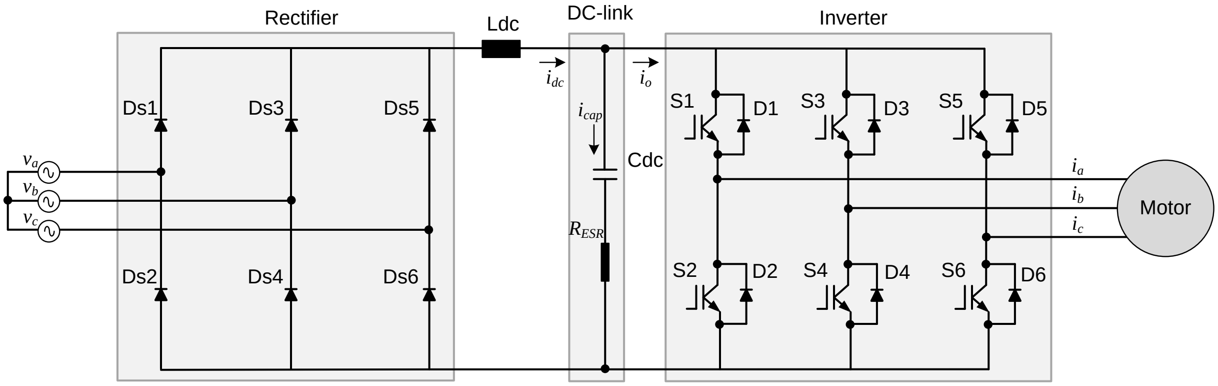

Figure 1.1Typical configuration of a variable speed motor drive

.

Figure 1.1shows the state of the art PMSM drive system configuration. It comprises of an inverter driving a load which in this study is a permanent magnet synchronous motor. A diode rectifier circuit provides DC voltage to the inverter by rectifying the AC line voltage from a single or three phase source. For three phase systems the input source voltage is usually 240 V or 480 V. For given voltage and power ratings, insulated gate bipolar transistors (IGBTs) are the commonly used inverter semiconductor devices. For power level below 100 kW, the switching frequency of the inverter is typically in the range of 5-12 kHz [4]. For power level above 100 kW, the switching frequency range is reduced to 2-4 kHz, so as to minimize the inverter losses. The inverter can synthesize sinusoidal, non-sinusoidal or square wave currents depending on the motor type and the application under consideration and the performance desired.

The commercially available permanent magnet motors can be classified into two types based on their back electromotive force (EMF) waveforms: (a) non-sinusoidal or permanent magnet brushless DC (PMBDC) motors and (b) sinusoidal or permanent magnet synchronous (PMSM) motors. For a three phase system, both types of motors can be driven by the same inverter. The PMBDCM and PMSM drive systems efficiency can be improved by optimizing the losses in the machine or inverter or both. The motor's predominant losses are its resistive and core losses. The resistive losses are proportional to the magnitude of the square of the current and the resistance of the machine phases. The core losses are a function of the machine electrical frequency and the flux density magnitude. Then the remaining dominant losses are in the inverter in the form of its conduction and switching losses. The former loss is proportional to the magnitude of the current in the case of the IGBT while the latter loss is a function of the current and switching frequency of the inverter. Therefore in order to improve the efficiency of the PMBDCM and PMSM drives, two novel current control options are proposed and taken for study. They are:

a. by *injecting sinusoidal and non-sinusoidal* currents in PMBDC machines over the variable speed operation and

b. by *reducing the switching frequency of inverter* driving the PMSM but without having significant low ordered sidebands of the currents.

The proposed methods for efficiency improvement of PMBDCM and PMSM have yet to appear in the present literature and hence considered for research. The motivation and objectives for selection of the proposed control strategies in these motors will be discussed in two parts in the following sections. The first part will focus on improving the efficiency of PMBDCM considering square, sinusoidal and non-sinusoidal current waveforms. Influence of these current waveforms on the stator resistive and core losses in motors with different back EMF waveforms and the corresponding proposed control strategy is discussed in the same section. The second part will focus on reducing the switching frequency of the inverter driving a PMSM. The programmed pulse width modulation method that results in elimination or reduction of the low ordered sidebands of the currents is considered. The

PMSM drive system efficiency improvement analysis validating the proposed concept is also discussed. To achieve the desired efficiency improvement a novel implementation method of the programmed pulse width modulator on the state of the art digital signal processor platform is highlighted. To eliminate the need for rotor position sensor considering reduced cost and higher reliability operation of PMSM, a novel rotor position sensorless algorithm for speed closed loop is presented. Finally the scope of work in this dissertation is outlined and the contributions are highlighted.

1.3. Part I: Current excitation strategies for improving efficiency in PMBDCM drives

This section will initially introduce PMBDCM with various back EMF waveforms and their excitation strategies. Then influence of square, sinusoidal and non-sinusoidal current waveforms on the stator resistive and core losses will be illustrated to highlight the effect of harmonics on PMBDCM performance. The detailed analysis of the same is provided in chapter 3.

Most of the previous work on current excitation strategies for PMBDCM has been focused on minimization their torque ripple and stator resistive loss [6-14]. The following points highlight the topics that need to be further explored:

1. PMBDC machines have back-EMF voltage waveforms that can vary anywhere from trapezoidal to sinusoidal. To cover wide range in practice, a generalized analysis that can show the influence of higher harmonics in back-EMF and stator current excitation waveform on the torque ripple and motor harmonic losses is essential.
2. The present literature does not discuss the influence of non-sinusoidal currents on core losses of PMBDCM. Although injection of harmonics in the stator flux minimizes the torque ripple and stator resistive losses, they increase the stator core losses. Low cost and low horsepower machines can have core losses as high as stator resistive losses [1]. These losses are higher at higher speeds of operation and increases in proportion to square of the harmonic frequency. Core loss evaluation for various back EMF machines excited by non-sinusoidal currents has yet to appear.

Before dwelling on the efficiency improvement of PMBDCMs, it is essential to understand their back EMF waveforms and is discussed in the following sections.

1.3.1 Back EMF waveforms in PMBDCM

PMBDCMs have trapezoidal back electromotive force (EMF) waveforms. Their rotors are assembled with ceramic, samarium cobalt or neodymium ferrite boron magnets. The magnets may be interior to the rotor or on the surface. The stators may have concentrated, fractional slot or distributed windings. The combination of the stator and rotor geometry, type of stator winding and the magnet orientation determines the shape of the voltage seen at the terminals of the machine in generating mode of operation. This voltage, also referred as back EMF, is either sinusoidal or non-sinusoidal (trapezoidal) in shape. There exist multiple combinations of the stator and rotor geometries which when coupled with the type of winding and magnet orientation results in various non-sinusoidal back EMF waveforms.

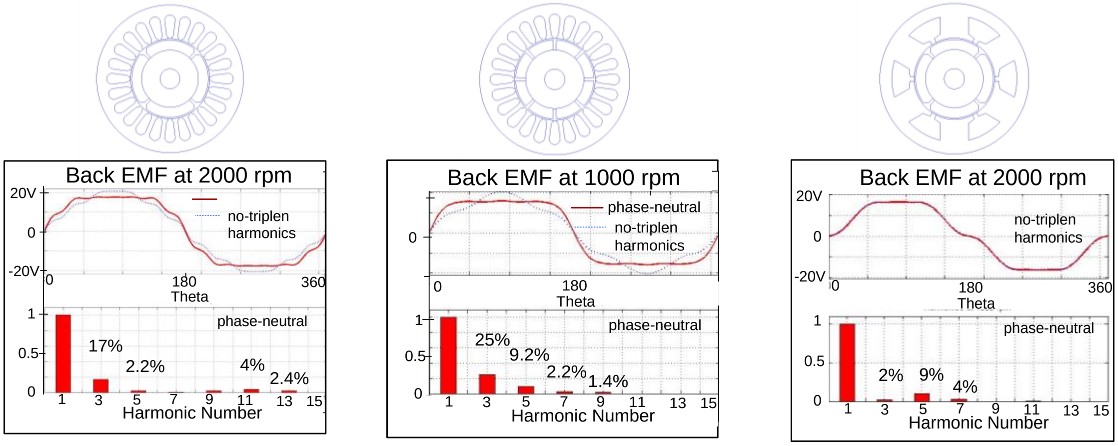

(a) (b) (c)

Figure 1.2. Back EMF of various surface mount permanent magnet machines (a) 4 pole 24 slot machine (b) 8 pole 24 slots (c) 4 pole 6 slots

Figure 1.2 (a-c) shows phase voltage waveforms for a three phase 4 pole-24 slots, 8 poles-24 slots and 4 poles-6 slot machines respectively. From the harmonic spectrum, it is seen that the amplitude of non-triplen harmonics in figure 1.2 (a) is lower than that in figure 1.2 (b) and (c). It can be deduced that the resulting line-line voltage waveform of the 4 pole-24 slot machine is more sinusoidal than that of the 8 poles-24 slots and 4 poles-6 slot machines.

Depending on the nature of the back EMF waveform, the current control strategy must be modified to reduce the losses in the machine and the inverter. Typically the neutral of the three-phase PMBDCM is floating. Therefore the inverter driving it cannot generate third harmonic component of the current. As a result, the triplen harmonics in the motor back EMF do not contribute towards torque production. Therefore only the non-triplen harmonics (5^{th}, 7^{th}, 11^{th},etc.) are considered for analysis.

1.3.2 Stator current excitation strategies in PMBDCM

Given the back EMF voltage waveforms, there are three stator current excitation methods applicable for PMBDCMs and they are: (a) square wave (b) sine wave and (c) non-sinusoidal harmonic-injected currents. Illustration of the same for a trapezoidal back EMF waveform is shown in Figure 1.3.

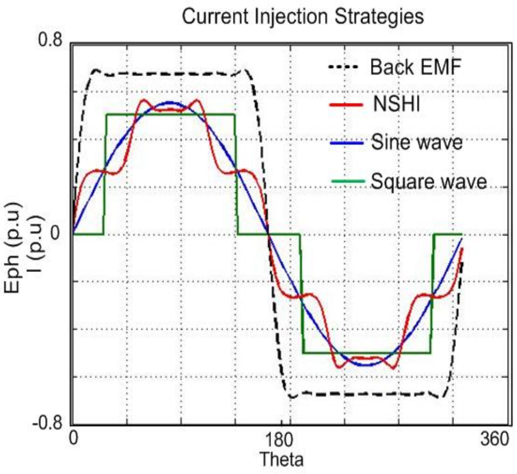

Figure 1.3Trapezoidal back E.M.F. and corresponding current injection strategies: Non-Sinusoidal Harmonic Injection (NSHI), sine, and square.

- The square wave (or rectangular) currents are essentially generated by controlling a DC current with given amplitude for 120 degrees in a phase winding of the machine. The polarity of the phase current is same as that of the back EMF waveform. The commutation event of the phase current is controlled by the Hall- effect rotor position feedback sensors such that the three phase currents are aligned with their corresponding phase back EMF waveform [3],[4].
- The sine wave currents in PMBDCM can be generated by a high bandwidth current controller which tracks a sinusoidal reference current to generate the desired torque in the machine. The phase angle is controlled so that the currents are in phase with their corresponding back EMF waveforms. There are alternative methods to synthesize a sine wave current in PMBDCM and are detailed in chapter 3.
- The non-sinusoidal currents are synthesized by superimposing the sinusoidal currents with high ordered harmonics which are essentially derived from the measured or the estimated back EMF voltage [6]. The flux harmonics due to the stator currents interact with the rotor induced flux linkage harmonics resulting in either aiding or cancelling the resultant harmonic fields in the air-gap. This feature can be used to increase the average torque or minimize the torque ripple in the machine. Since the current harmonics are used to improve the motor performance, this excitation scheme is referred to as non-sinusoidal harmonic-injection (NSHI) strategy.

Comparison of the aforementioned current excitation schemes for improving the machine performance will be discussed using analytical formulation in the following section.

1.3.3 Hybrid excitation strategy for higher efficiency operation of PMBDCMs

In order to improve the efficiency of PMBDCM, it is essential to analyze the motor performance considering the three current excitation methods. Accordingly, detailed analysis of the motor losses due to the various excitation waveforms is developed in chapter 3. It is shown that although NSHI method results in lower stator resistive losses, it increases the core losses in the motor. The analysis is generalized to cover a broad range of motors in practice. It is shown that for higher efficiency operation in variable speed drives system, a hybrid approach that combines the sine and NSHI excitation is desirable and hence proposed in this research.

Fig 1.6 shows the conceptual operation of the hybrid current excitation scheme for PMBDCM with higher amplitude of harmonics in their back EMF waveform. In the proposed method, NSHI scheme is applied at lower speeds as the stator resistive losses dominate the total losses of the motor. At higher speeds, the control is changed to sinusoidal current injection as the core losses dominate the total losses in the motor. From the analytical and experimental results it is shown that a hybrid approach serves the purpose of higher efficiency operation under the variable speed operating range.

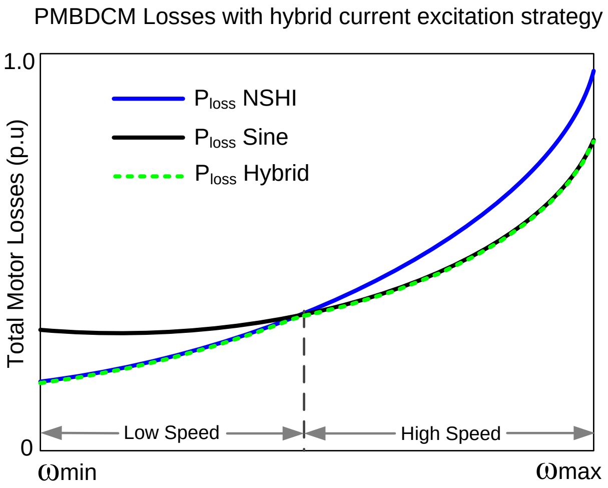

Figure 1.4 Proposed hybrid current injection strategy for variable speed drive operation

From the above discussion, this first part of the research will address following objectives:

1. A simplified methodology to analyze performance of non-sinusoidal machines with various back EMF waveforms. Derivation of analytical expressions for the three-stator excitation schemes as a function of generalized back EMFs to study effect of higher harmonics in the back EMF on torque ripple, stator resistive losses, and inverter losses.
2. Analytical calculation of core losses in the machine due to sinusoidal and non-sinusoidal excitation schemes and its validation using two dimensional finite element simulations.
3. Steady state evaluation of efficiency by loss comparison between sine, square and NSHI schemes on various PMBDCM at low as well as higher speeds of operation.

4. Development and model based verification of a control scheme that will improve efficiency in PMBDCMs using the proposed hybrid approach.
5. Experimental validation of the proposed hybrid control scheme and efficiency evaluation of various stator excitation strategies.
6. Development of a speed sensorless controller to eliminate the rotor position sensor for lower cost and more reliable operation.

These objectives will be addressed in chapter 3 of this dissertation.

1.4. Part II - Efficiency improvement strategies of PMSM drives considering reduced switching frequency operation.

Unlike PMBDCMs, the permanent magnet synchronous machines (PMSMs) have sinusoidal back EMF waveforms hence requiring sinusoidal current excitation. The currents in PMSM are synthesized by an inverter which generates high frequency sinusoidally modulated voltage pulses. These voltage pulses are filtered by the motor impedance to generate sinusoidal currents at the fundamental frequency along with higher ordered sidebands. They cause the resistive and core losses in the motor and conduction and switching losses in the inverter.

The PMSM drive system efficiency can be improved by optimizing the losses in the machine or inverter or both. The motor resistive losses are proportional to the magnitude of the square of the current and the resistance of the machine phases. The core losses are a function of the frequency and flux density. Therefore, given the current magnitude and stator frequency, the machine losses can be considered constant. Then the remaining dominant losses are in the inverter in the form of its conduction and switching losses. The former loss is proportional to the magnitude of the current while the latter is a function of the current and switching frequency of the inverter. Given the current in the inverter, then the losses that can be minimized are dependent on the switching frequency. Therefore, the approach considered in this research is that given an optimally designed permanent magnet machine and its control algorithm, the only option to improve the system efficiency is by reducing the inverter switching losses by minimizing the switching frequency.

At reduced switching frequencies, the small impedance offered by PMSM to the inverter voltage transients causes higher current waveform distortion and higher losses in the motor. To reduce this distortion, programmed pulse width modulators (PWM) are preferred over conventional carrier based modulators and therefore considered in this study.

Analytical loss modeling of the motor and the inverter is central to the efficiency evaluation at low switching frequencies. Accordingly, for the motor, the stator resistive and core losses are derived analytically and validated using simulations. Similarly, for the inverter, the conduction and switching losses are derived considering programmed PWM and validated using circuit based simulations.

Then using the analytical method, a loss comparison of five PMSM drive systems of various power ratings is made to quantify the efficiency improvement. It is shown that the efficiency of the PMSM drive system can be improved by switching frequency reduction and applying programmed PWM techniques. Such an approach has not been reported in the existing literature and hence considered in this research.

The following sections will discuss the motivation, analysis and implementation methods required to improve the efficiency of PMSM drive system considering reduced switching frequency operation.

1.4.1. PMSM inverter output power at reduced switching frequencies

To understand the influence of low switching frequency operation on PMSM drive performance, it is essential to evaluate the relationship between switching frequency and output power of the inverter with the constraint on lower motor harmonic losses. The objective is to maximize the output power by reducing the switching frequency and minimize the motor harmonic losses at the same time. The output power of the inverter is given by.

$$P_{inv} = \sqrt{3}V_{rms}I_{rms}\cos(\emptyset) \tag{1.1}$$

where V_{rms} and I_{rms} are the root mean square of the line-line voltage and phase currents, respectively, and $cos(\emptyset)$ is the power factor. The semiconductor switching loss of the inverter is given by [15]

$$P_{sw} = \frac{f_{sw}E_{sw}I_{pk}}{\pi}\frac{V_{dc}}{V_{ce}} = \sqrt{2}\frac{f_{sw}E_{sw}I_{rms}}{\pi}\frac{V_{dc}}{V_{ce}} \tag{1.2}$$

where f_{sw}, is switching frequency of inverter,E_{sw} is the total switching energy (Joules) dissipated due to the peak currentI_{pk} flowing through the device. V_{dc}, is the DC bus voltage of the inverter andV_{ce} is the operating voltage of device. From (1.2), it is seen the switching losses are proportional to the motor phase rms current. Hence, if the switching losses are reduced by reducing the switching frequency, the magnitude of the root mean square of the current and resulting output power will increase proportionally. It can be illustrated by considering a three phase inverter with insulated gate bipolar transistor (IGBT) devices.

Figure 1.5 shows relationship between output power and switching frequency of two IGBTs with voltage rating of 1200V and current rating of 30A and 50A respectively. The three phase motor drive is analyzed with 650 V_{dc}, 480V output voltage, fundamental frequency of 60Hz and power factor of 0.95

and with the assumption of adequate cooling for semiconductor devices in order to maintain the device junction temperature within allowable limits. . Two important observations are made from this graph:

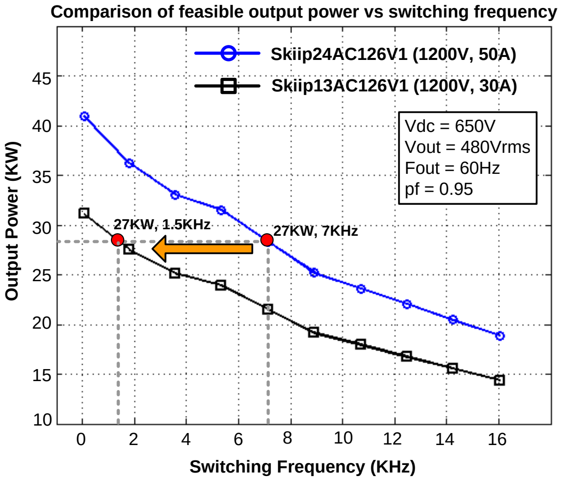

Figure 1.5 Simulation results: Influence of switching frequency on output power of the inverter.

(i) The power handling capacity of the device increases as the switching frequency is reduced. For example, in case of a 50A device, the output power increases by 50 percent when the switching frequency is reduced from 9 kHz to 1.5 kHz. Depending on the device rating and the power level, reduction of switching frequency can result in 20%-80% higher power of the inverter. The increase is higher in semiconductor devices of higher power ratings (>100 kVA) [22].

(ii) While the power rating of the inverter increases, an opportunity for selection of device with smaller power rating is feasible. For example, a 30A device operating at 1.5 kHz can deliver the same output power (27 kW) as the 50A device operating at 7 kHz. Such a feature is highly desirable in low cost drive applications where smaller rating devices can be used to deliver the same output power.

The present research on variable speed motor drives is trending towards high switching frequency operation (greater than10 kHz) due the advent of faster devices enabled by advanced materials such as silicon carbide and gallium nitride. These devices are still considered as an emerging technology with known limitation of high volume manufacturing, reliability and cost [16], [17]. Such devices are more expensive than the current state of art IGBTs. The motor drives incorporating such advanced semiconductor devices typically require an output filter to minimize the volts-sec applied to the motor terminals at high switching frequencies [18]. Therefore only state of the art IGBT devices are pursued in this research.

While reduction of switching frequency reduces the losses in the inverter, it increases the stator resistive and core losses proportionally. Hence a comprehensive analysis of the total losses in the machine and inverter is required to quantify the total efficiency improvement using the apt PWM modulator. To facilitate the study, analytical stator resistive and core loss prediction techniques for low switching frequency operation are derived in this research. The losses are evaluated considering various pulse width modulating (PWM) methods as discussed in following section.

1.4.2. Influence of PWM strategy on losses in PMSM

For reduced switching frequency operation, it is critical to select the right pulse width modulators to reduce the current harmonic distortion in the motor and drive. Various pulse width modulation strategies that have been reported in the literature are:

(a) Asynchronous and synchronized carrier based modulation [19]
(b) Programmed pulse width modulation (PWM)
  i. Selective harmonic elimination [20],[21]
  ii. Synchronous optimal modulation [22]

The asynchronous carrier based modulators (also known as sub-oscillation modulation methods) are typically applied, when the ratio of the switching frequency to fundamental frequency N is high (above 15) while for the smaller ratios, the programmed PWM methods are common [19]. Operation of PMSM with various PWM methods for improving the system efficiency requires a careful analysis of the motor harmonic losses. The motor harmonic losses are proportional to the mean square magnitude of the harmonic current. The root mean square amplitude of the motor harmonic current I_σ is defined as

$$I_\sigma = \frac{1}{\omega_1 L_s}\,\sigma, \qquad \sigma = \sqrt{\frac{1}{2}\sum_{n=3,\cdots}^{\infty}\left(\frac{V_n}{n}\right)^2} \tag{1.3}$$

where ω_1 is the fundamental frequency and L_s is the motor inductance, V_n is the harmonic amplitude of the inverter voltage. To estimate the harmonic distortion factor σ, the amplitude of the harmonic voltages (V_n) is calculated using fast Fourier transform of the output switching voltage waveform. Then the square of harmonic distortion σ^2 also known as loss factor is calculated to gauge the harmonic losses in the motor [19]. The magnitude of the loss factor σ^2 varies with different modulation strategies. It also varies as a function of the modulation index M. In order to reduce the magnitude of loss factor it is not uncommon to have a PWM that utilizes different switching to fundamental frequency ratios N [19].The value of N is reduced for higher modulation indices mainly to reduce the switching losses. The corresponding analysis for various modulators is presented in chapter 4.

Figure 1.2 highlights one of the analysis results showing the relationship between the loss factor and modulation index for different PWM methods. The PWMs being compared are: (a) synchronous optimal PWM with the number of switching pulses varied from $N = 15$ up to $N = 5$, (b) discontinuous PWM (DPWM) with $N = 7$, (c) synchronous SVM with $N = 9$, (d) sine PWM with $N = 7$, and (e) selective harmonic elimination (SHE) PWM with $N = 7$. It is seen that synchronous optimal modulator with $N = 15$ through 5 has lower loss factor than all other modulators. It is achieved by combining different pulse numbers to reduce the loss factor. The PWM pulse patterns are computed offline considering steady state operation only. The lowest switching frequency achieved for the case presented is 246 Hz with a fundamental frequency of 22.3 Hz.

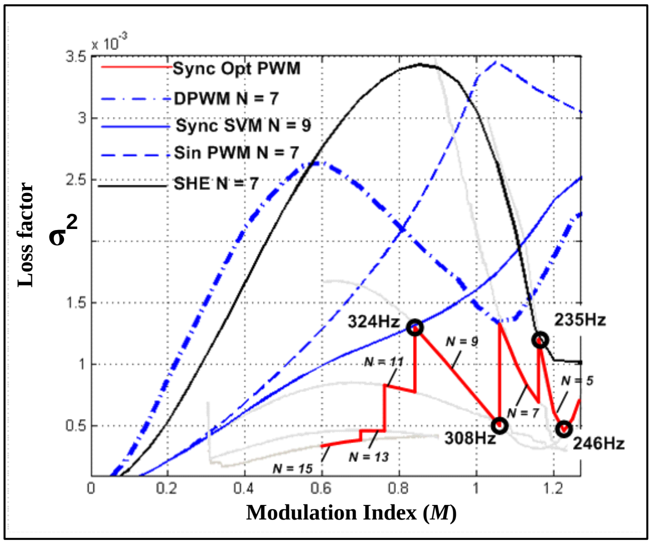

Figure 1.6Simulation results: distortion comparison between various PWM modulation strategies.

Analysis of reduced switching frequency operation of PMSM considering different modulators has not been reported in present literature. Hence, to cover a wide range of applications in practice, the total loss analysis is made on five different PMSM motor drive systems of various power ratings. They are listed in Table 1.2. The choice of the motor drive systems and their parameters are based on the data available from literature and industrial applications. The analysis required estimating the motor stator resistive and core losses and the inverter semiconductor resistive and switching losses. To calculate the core losses, an analytical loss estimation procedure was developed and validated using finite element modeling method. The analytical method for estimating the semiconductor device losses was validated using detailed circuit simulations.

Summary of the total system efficiency improvement of the PMSM drives listed in Table 1.2 is presented in figure 1.7. The results show that the total system efficiency improvement considering reduced switching frequency operation is higher (more than 1 percent) in PMSM drives of higher power and voltage ratings. Detailed analysis for the same considering PWM methods, motor inductance, phase resistance, lamination steel and semiconductor devices is also presented in chapter 4.

Table 1-2.Various surface mount permanent magnet motors and their drives evaluated for efficiency improvement at reduced switching frequencies.

Cases	**1**	**2**	**3**	**4**	**5**
Machine Geometry (not to scale)	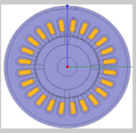	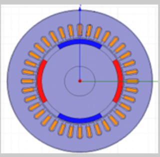	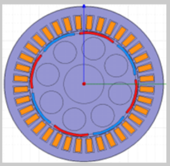	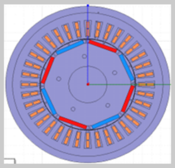	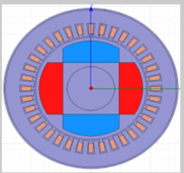
Power (kW)	**0.2**	**2.2 kW**	**8.5 kW**	**22 kW**	**125 kW**
Motor AC Voltage (V)	27	230	305	512	460
Speed (rpm)	2000	3000	3000	822	27000
Stator resistance (ohm)	0.25	0.35	0.22	0.25	0.023
Stator inductance (mH)	0.75	4.6	4.7	7.5	0.1
Max Electrical Frequency (Hz)	66.67	100	133.33	54.8	900
Torque (Nm)	1	18	42	250	48
Magnet Type	Ceramic 8D	NdFeB	NdFeB	NdFeB	NdFeB
Lamination Steel Type	M-800	M-800	M800	M-19	M-19
IGBT and Diode Rating	100V, 17A	600V, 20A	1200V, 30A	1200V, 55A	1200V, 450A
DC voltage (V)	48	310	640	800	750

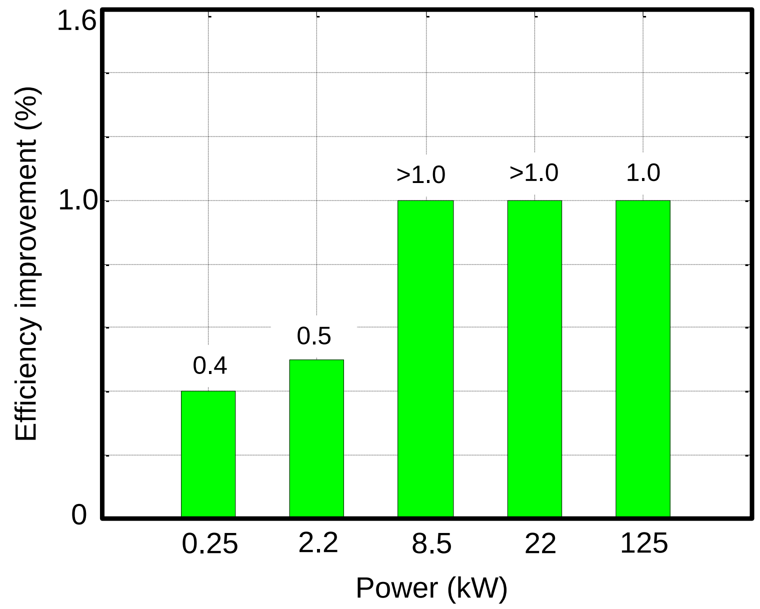

Figure 1.7 Total system (inverter and motor) efficiency improvement considering reduced switching frequency operation of PMSM for various power levels.

Given the advantages of the proposed approach, the following section will discuss the PWM implementation strategy and the control of PMSM at reduced switching frequencies.

1.4.3. Implementation of programmed PWM for reduced switching frequency operation of PMSM

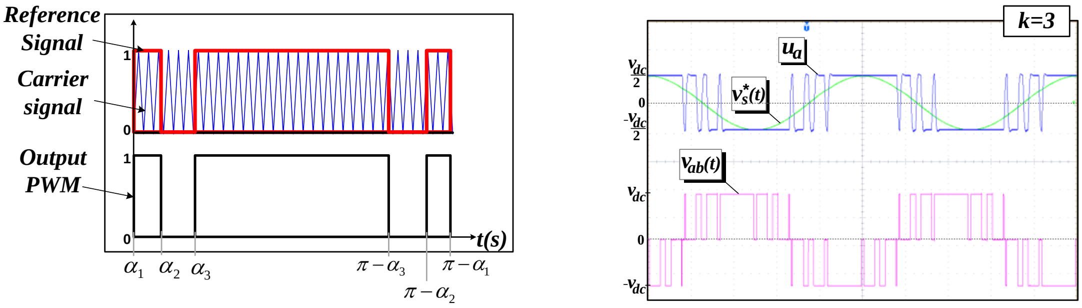

(a) (b)

Figure 1.8. (a) Carrier based programmed PWM implementation approach , (b) Experimental results: programmed PWM with modulation index M=0.9 showing phase A voltage u_a^*, reference fundamental voltage $v_s(t)^*$ and line-line votage $v_{ab}(t)$ for commutation angles k = 3 or N = 7

A novel method for implementation of programmed PWM given state of the art microcontroller platform has also been developed and verified in chapter 5. In this method, the switching pulses with low values of N are considered as a train of discontinuous PWM signals and are compared with a high frequency carrier signal. The resulting output is the reference programmed PWM signal. Concept of the carrier based programmed PWM implementation is shown in Fig 1.8 (a). The corresponding output PWM waveform of the inverter phase voltage $v_s(t)^*$ and line-line voltage $v_{ab}(t)$for N = 7 is shown in Fig 1.8 (b).

The proposed method is unique due its simple implementation with the inexpensive state of the art microcontrollers. It overcomes the disadvantages of the timer period and microprocessor processor clock frequency requirements to synthesize the lowest switching frequency. The implementation method also allows ease of transition from asynchronous to synchronous to programmed PWM methods. The limitations of the method are discussed in chapter 5.

1.4.4. Current control of PMSM at low switching frequency

Current control affects in general not the system efficiency but only the damping and possible instability. Accordingly, for stable motor performance, simple current controller implementation is essential. The existing literature [23], [24] focuses on complex variable current and model predictive control of induction motor drives operating low switching frequency. These methods require detailed model of the inverter and motor to pre-calculate the voltage vector that has to be applied to the motor terminals. Hence a good plant parameter estimation technique is mandatory for their implementation.

An alternative simple approach of controlling the current is with feedback oversampling. Such an approach in combination with programmed PWM for PMSM drives has not been discussed in literature and hence proposed, analyzed and experimentally verified in chapter 5. In the proposed method, increasing the sampling rate of the feedback currents reduces the sampling delays. Also if the new reference voltages are computed after every sampling instant and the most updated value is applied at the next switching cycle, the controller bandwidth can be significantly improved.

A space phasor variable modeling is used to analyze and design the current controller for PMSM operating at low ratio of switching frequency to fundamental frequency. The space phasor variable modeling method reduces the system model size and allows more intuitive insight into the relationships between the motor state variable (*current or flux linkages*) and the cross coupling between the orthogonal windings [25]. Figure 1.9(a) shows the root locus of the characteristic equation of the current controller at various sampling frequencies with fundamental frequency of 200 Hz using the space phasor variable modeling approach. It is seen that when the sampling frequency f_s is increased from 2.5 kHz to 10 kHz, the pole p_3 moves toward left half of complex plane while the complex poles, $p_1$andp_2 move further left thus validating the improved stability of the system. Detailed derivation and analysis of the same is discussed in chapter 5.

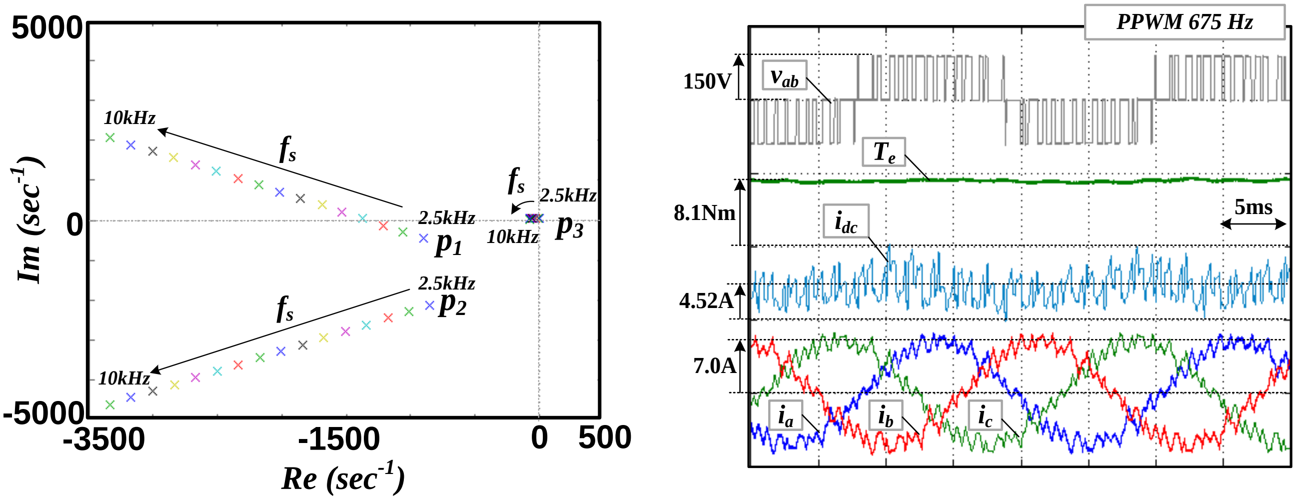

(a) (b)

Figure 1.9. (a) Root locus of the current controller characteristic equation considering oversampling approach, and (b) Current closed loop steady state operation of PMSM with programmed PWM and $N = 15$.

Experimental result of the steady state operation of PMSM with closed loop current control and programmed PWM ($N = 15$) operation of the drive is shown in figure 1.9 (b). The results validate the stable steady state operation of PMSM in torque mode using the proposed current control method. Transient response of current controller and its analysis are discussed in chapter 5. The fan or pump type application considered in this research do not require high dynamic response making the proposed approach easily applicable.

Given the current controller design, the speed control algorithm must be developed for stable operation of PMSM. Due to cost sensitivity and reliability constraints, rotor positon sensorless control is desirable. Methods for rotor position sensorless control of PMSM at reduced switching frequency and using programmed PWM methods has yet to appear. The following section will highlight the same.

1.4.5. Rotor position sensorless control of PMSM at reduced switching frequencies

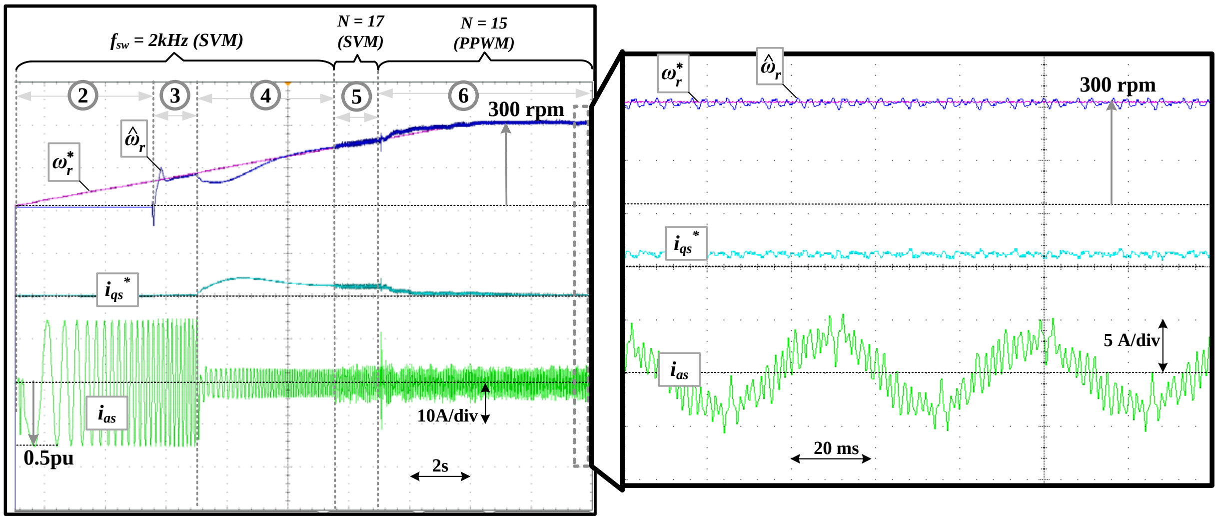

Figure 1.10.Experimental results: Starting operation of PMSM with various operating regions and transitioning to programmed PWM modulation and zoomed view.

To control the speed of PMSM a unique sensorless vector control at low switching frequencies for climate control system application is proposed. A novel combination of rotor position sensorless algorithm with programmed PWM for PMSM is developed and its laboratory implementation is verified. Stability analysis of the proposed control method incorporating a back EMF observer and tracking controller for low switching frequency operation is provided in chapter 6. A guideline for selection of the controller gains is also provided in the same chapter.

Figure 1.10 shows the ramp up operation of the PMSM from zero to reference speed. It is attained by controlling the operation through various regions to achieve the steady state with low switching frequency operation. The switching frequency during steady state is only 300Hz. The experimental results validate both the design methodology and the expected performance attained by the proposed control strategy. The zoomed view shows the tracking of the reference and the estimated speeds, reference q- axis current and the steady state motor phase current. The proposed algorithm demonstrates that both high system efficiency and low cost sensorless operation of PMSM drive is feasible.

1.5. Summary and Conclusions

This chapter provided the motivation and approaches for further improving efficiency in these motor drive system without modifying the state of the art drive hardware or redesign of the motors. Significant contributions of this research on the total system loss reduction by control of the stator current excitation waveforms in permanent magnet brushless DC motor (PMBDCM) and permanent magnet synchronous motor (PMSM) drives were highlighted.

Given the two different types of machines, two novel current control options for improving the efficiency of the motor drive system and were proposed for PMBDCMs and PMSMs. Both methods show total system efficiency improvement without resorting to hardware redesign.

1.6. Potential impact on the research community and industry

Energy efficiency improvement in variable speed motor drives is of widespread interest because of the rising cost of energy and also efforts on reducing the carbon foot print for environmental protection. The permanent magnet motor drives are especially favored currently in variable speed applications due to their high efficiency operation. This research shows techniques for further improving efficiency in these motor drive systems without modifying the state of the art drive hardware or redesign of the motors.

Even an 1 percent increment in efficiency can result in significant cost reduction per year for the given number of installed variable speed drive systems. The savings are higher at higher power ratings and also in application which has large number of installed units. Since a typical variable speed drive already has the necessary components installed, the proposed methods are essentially a software upgrade. The analysis and insight into the combined operation of inverter and permanent magnet motor in this research will enable engineers to design the motor drive system for higher efficiency or lower cost depending on the application requirement.

Relevant publications associated with the presented research:

1. P. Kshirsagar and R. Krishnan, “High Efficiency Excitation Strategy for Variable Speed Non-Sinusoidal Back-EMF PMSM Machines,” *IEEE Transactions on Industry Applications Joint Special Issue - Nov/Dec 2012*
2. P. Kshirsagar and R. Krishnan, “Sensorless Control of Permanent Magnet Motors Operating at Low Switching Frequency for Climate Control Systems,” *IEEE Sensorless Electric Drives Conference, Sept 2012*

3. P. Kshirsagar and R. Krishnan, “Efficiency improvement evaluation of non-sinusoidal back-EMF PMSM machines using field oriented current harmonic injection strategy,” in *Energy Conversion Congress and Exposition (ECCE), 2010 IEEE*, 2010, pp. 471 –478.
4. P. Kshirsagar and R. Krishnan, “Efficiency Improvement in PMSM Drives through Switching Frequency Reduction: Part I- Modeling and Analysis,” in *Applied Power Electronics Conference (APEC), 2016 IEEE, submitted*.
5. P. Kshirsagar and R. Krishnan, “Efficiency Improvement in PMSM Drives through Switching Frequency Reduction: Part II- Implementation and Experimental Validation,” in *Applied Power Electronics Conference (APEC), 2016 IEEE, submitted*.
6. Kshirsagar, P., Burgos, R.P., Lidozzi, A., Jihoon Jang, Wang, F., Boroyevich, D., and Seung-Ki Sul,“Implementation and Sensorless Vector-Control Design and Tuning Strategy for SMPM Machines in Fan-Type Applications,”*IEEE Transactions on Industry Applications Joint Special Issue - Nov/Dec 2012*

References

[1] R. Krishnan, *Electric Motor and Drives- Modeling Analysis and Control*, Prentice Hall Inc., 2001.

[2] [Online] http://www.eia.gov/forecasts/aeo/er/

[3] [Online] http://www1.eere.energy.gov/manufacturing/tech_deployment/pdfs/variable_speed_pumping.pdf

[4] M. Swamy, and T. Kume, "Present State and A Futuristic Vision Of Motor Drive Technology", Yaskawa, [Online]. http://www.yaskawa.com/site/dmdrive.nsf/7904b73e29cb909686256f5c00609d86/86256ec30069e4328625749f004d51cd/$FILE/WP.AFD.03.pdf

[5] M. Melfi, S. Evon, and R. McElveen, "Induction versus permanent magnet motors," *IEEE Ind. Appl. Mag.*, vol. 15, no. 6, pp. 28 –35, Dec. 2009.

[6] F. Piriou, A. Razek. R. Perret, H. Le-Huy, 'Toque Characteristics of Brushless DC Motors with Imposed Current Waveforms", *IEEE IAS 1986*, pp, 176-181.

[7] D. Hanselman, "Minimum Torque Ripple, Maximum Efficiency Excitation of Brushless Permanent Magnet Motors", *IEEE Trans. Ind. Electron*., vol. 41, no. 3, 1994, pp. 292-300.

[8] P.L. Chapman, S.D. Sudhoff, C.A. Whitcomb, "Optimal Current Control Strategies for Surface-Mounted Permanent-Magnet Synchronous Machine Drives", *IEEE Trans. Energy Convers.*, vol. 14, no. 4, Dec 1999.

[9] J.Y. Hung, Z. Ding, "Minimization of Toque Ripple in Permanent- Magnet Motors: A Closed Form Solution", *IEEE IECON*, 1992, pp. 459-463.

[10] R. Leidhold, G. Garcia, "PMAC motor control strategy, based on the instantaneous active and reactive power, for ripple-torque and copper-losses minimization", *IEEE IECON*, 2000. vol.2, pp-1401-1405.

[11] N. Bianchi, S. Cervaro, L. Malesani, "Current Shapes For Minimizing Torque Ripple In SPM Motors", *Proc. ICEM* , 2000 pp. 1237-1241.

[12] T. Kim, H-W Lee, M. Ehsani, "High Performance Brushless Permanent Magnet Motor/Generator Drives in Electric and Hybrid Electric Vehicles", *IEEE PESC Annu. Mtg.*, Oct 2006, pp. 1 – 5.

[13] D.Grenier, R. Mende, and J.P. Louis, "Comparison of several control strategies for DC Brushless Drives", *IEEE IECON*, 1994. vol.1, pp-26-31

[14] A. Oliveira, J. Monteiro, M. Aguiar, D. Gonzaga, "Extended DQ transformation for vectorial control applications of Non-Sinusoidal Permanent Magnet Synchronous Machines", *IEEE Power Electron. Spec. Conf*, 2005, pp 1807-1812.

[15] F. Casanellas, "Losses in PWM Inverters Using IGBTs," *IEE Proc. Elec. Pow. Appl.*, vol. 141, no. 5, pp. 235-239, Sep. 1994.

[16] B. Ozpineci, L.M. Tolbert, S.K. Islam, M. Chintavali, "Comparison of Wide Bandgap semiconductors for power applications", [Online]http://power.eecs.utk.edu/pubs/epe2003_wide_bandgap.pdf

[17] P. Roussel, "SiC Power Devices – if we only had a switch…,"Vol. 2, Issue 5, Semiconductor Today – Compounds and Advanced Silicon, June 2007.

[18] J.M. Erdman, R.J. Kerkman, D.W. Schlegel, and G.L. Skibinski, "Effect of PWM inverters on AC motor bearing currents and shaft voltages," *IEEE Trans. Ind. Appl.*, vol. 32, no. 2, pp. 250 –259, Apr. 1996.

[19] J. Holtz, "Pulsewidth Modulation for Electronic Power Conversion." *Proc. IEEE 82*, no. 8 (August 1994): 1194 – 1214.

[20] P.N. Enjeti, P.D. Ziogas, and J.F. Lindsay, "Programmed PWM Techniques to Eliminate Harmonics - A Critical Evaluation." *IEEE Industry Applications Society Annu. Mtg., 1988, Conference Record of the 1988*, vol.1, pp. 418 – 430, 1988.

[21] B.D. Bedford, R.G. Hoft, *Principles of Inverter Circuits*, J Wiley, New York , 1964.

[22] G.S. Buja, and G.B. Indri, "Optimal Pulsewidth Modulation for Feeding AC Motors." *IEEE Trans. Ind. Appl.*, vol. IA-13, no. 1 (January 1977): 38 –44.

[23] J. Holtz and S. Stadtfeld, ''A predictive controller for the stator current vector of AC machines fed from a switched voltage source,'' in Proc. Int. Power Electronics Conf. (IPEC), Tokyo, 1983, pp. 1665–1675.

[24] T. Geyer and G. Papafotiou, ''Model predictive control in power electronics: A hybrid systems approach,'' in Proc. 4th IEEE Conf. Decision and Control and European Control Conf., Seville, Spain, 2005, pp. 5606–5611.

[25] J. Holtz, "The Representation of AC Machine Dynamics by Complex Signal Flow Graphs", *IEEE Trans on Ind Electron*. Vol. 42. No. 3, June 1995

Chapter 2 Literature Review

2.1. Abstract

This chapter will review the efficiency improvement strategies of permanent magnet motor drives considering various stator current excitation waveforms and reduced switching frequency operation of the inverter driving them. For improving the PMBDC efficiency over wide operating speed range with torque ripple minimization, various modeling approaches and corresponding control strategies are reviewed. For improving the efficiency of PMSM drive system considering reduced switching frequency operation, various pulse width modulation methods and their impact on motor performance are assessed. To perform the efficiency evaluation, analytical loss estimation methods in sinusoidal and non- sinusoidal permanent magnet motors drives are examined. Also, approaches to control the currents in PMSM at reduced switching frequency to achieve stable dynamic performance are studied. Finally, rotor position sensorless control strategies to eliminate rotor position feedback sensor are also reviewed.

2.2. Outline

The literature reviewed in this chapter is organized as follows:

Section 2.3 contains the review of various stator excitation methods in the form of square, sine and non-sinusoidal current waveforms in PMBDC machines. Analytical methods to estimate the influence of stator current harmonics on stator resistive and core losses of PMBDCMs and PMSMs are reviewed in section 2.4. The semiconductor loss evaluation methods are discussed in section 2.5.

Review of models for PMBDCMs and PMSMs are given in Section 2.6. The modeling methods are not only for system simulation but also for the formulation of the controller.

Section 2.7 contains a review of efficiency improvement strategies in PMSMs considering reduced switching frequency operation of the inverter. The reduced switching frequency operation of PMSM requires choice of pulse width modulators with low harmonic distortion. Hence, various PWM methods and the corresponding control strategies for PMSM drive system are also reviewed in the same section.

To control the current in the machine, a review of various current control methods is presented in Section 2.8. The review of feedback sampling methods considering reduced switching frequency operation will be made in the same section.

Position sensorless control of permanent magnet motors is essential for high reliability and low cost operation. Accordingly, various sensorless control strategies are reviewed in section 2.9.

2.3. Stator current excitation waveforms of PMBDC motors

There are three stator current excitation waveforms of permanent magnet brushless DC motors PMBDCM reported in the literature and they are: (a) square wave, (b) sine wave and (c) sine-harmonic currents. Overview of these current waveforms from the perspective of PMBDC efficiency improvement is given in the following sections.

2.3.1. Square wave excitation:

The PMBDCM can provide up to 15 percent higher torque than sinusoidal motors for the same stator resistive losses [1]. These motors are mainly excited by square wave current waveforms. The square wave currents in three phase AC motors have been studied since the advent of thyristor based inverters [2]. The inverter is commutated such that the semiconductor devices are on for 120 degrees or 180 degrees during a fundamental cycle which results in square or rectangular current waveforms [3]. The magnitude of the square wave currents are synthesized by hysteresis or PWM control while the phase currents are commuted using rotor position hall effect sensors [4]. Analysis of the square or rectangular current waveforms on permanent magnet brushless DC motors has been reported in [5-7]. In [6], the performance limitation of PMBDC motor operating at low and high motor speeds considering square wave currents was shown. The main issues arising from such current waveforms are the harmonic torque ripple and the associated motor harmonic losses. For fan type of loads, torque ripple may not be of a major concern, however for higher efficiency operation, the motor harmonic losses are not desirable.

2.3.2. Sine wave excitation:

The sinusoidal current waveform excitation is predominantly applied in case of permanent magnet motors with sinusoidal back EMF waveforms [8]. In [9] and [10], it is shown that, for the same average torque, sinusoidal motors offer higher efficiency than brushless DC motors. The influence of sine and square wave excitation on efficiency of concentrated winding PMBDC motors has been investigated in [11] with main focus on flux weakening operating regimes. It is shown that square wave currents can generate twice the core losses as sinusoidal currents.

In [12], the total system efficiency of PMBDC and PMSM motors was compared considering sinusoidal and square wave excitation. It was concluded that sinusoidal currents in PMBDC motor drives resulted in lower system efficiency than square wave currents. However in the study, the switching devices in PMBDC inverter were clamped to DC link for certain time interval of the fundamental cycle while in case of the PMSM inverter they were not. Consequently, the PMBDC inverter operated at lower switching frequency than PMSM inverter. Therefore the total efficiency of PMBDC drive system was better. If the PMSM inverter was operated considering discontinuous PWM as discussed in [41], the conclusions could have be different. Hence this aspect needs further evaluation.

The sinusoidal current waveforms generate higher torque ripple than square wave currents in trapezoidal back EMF machines [1] and [13]. This is because the fundamental component of the current interacts with the fifth and seventh harmonic component of the back EMF to generate sixth harmonic pulsating torque ripple. The analysis can be extended to higher ordered harmonics and is discussed in [6]. Therefore, the sinusoidal current excitation in PMBDC machines may yield better efficiency but may not be suitable for applications requiring lower torque ripple.

2.3.3. Non-sinusoidal excitation:

Non-sinusoidal excitation is designed based on the back EMF harmonics in PMBDCM to meet certain objective functions such as: (a) higher average torque, (b) lower torque ripple or (c) higher motor efficiency [14-23]. In [14-18] an algorithm based on back EMF harmonics and in the form of look-up table was developed to inject non-sinusoidal currents in PMBDCM to minimize torque ripple and stator resistive losses thus claiming maximum efficiency in the given speed range. With a similar objective, references [19-23] obtained various solutions for currents that would improve efficiency in the machine. These references compared the efficiency improvement with respect to square wave excitation strategy.

The references [14-23] mainly focused on minimizing the torque ripple and simultaneously achieving higher motor efficiency through stator resistive loss reduction. In references [15-23], sinusoidal current waveforms for reducing stator resistive losses were not discussed. Also, a collective approach for PMBDCMs considering different back EMF waveforms and evaluating applicability of sinusoidal vs. non-sinusoidal currents for efficiency improvement has not been considered. Most importantly, the above references did not incorporate the influence of non-sinusoidal currents on the motor’s core losses. It is known that machines with higher harmonics in back EMF tend to have higher core losses [1]. In case of variable speed applications it is desirable to maintain higher efficiency over the entire operating speed-torque envelope. Hence the influence of non-sinusoidal currents on stator resistive as well as core losses of the machine must be addressed.

2.4. Stator resistive, core and inverter loss estimation methods

The estimation of predominant motor losses in the form of stator resistive and core losses is critical for efficiency evaluation. The following sections will review the loss estimation methods in the literature.

In the following sections, special attention will be given to research focusing on the influence of stator current harmonics on resistive and core losses.

2.4.1. Estimation of stator resistive losses:

There are two types of stator resistive losses depending on the frequency of the current flowing through the conductor and they are: (a) DC resistive losses, and (b) AC resistive losses [1, 24].

The DC stator resistive losses are proportional to product of resistance of the phase winding and the square of amplitude of the phase current. In case of non-sinusoidal current waveforms, it is critical to achieve a good estimation of the amplitude of the current harmonics for accurate estimation of its root mean square value. The DC stator resistive losses are also dependent on the type of conductor, its cross sectional area and the operating temperature.

The AC resistive losses are mainly the skin and proximity effect losses [25-27]. The skin effect losses are due to smaller skin depth of the conductor available at higher operating frequencies. In such cases, the current concentration occurs around the surface of the conductor rather than in the core. This reduces the effective cross sectional area of the conductor causing higher resistive losses. The proximity losses are due to the induced eddy fields between two adjacent conductors which produce currents in a direction opposite to the flow of the existing current. Proximity losses are dependent on the arrangement of the conductors in a given slot of the machine. The skin effect and proximity losses become relevant at higher fundamental operating frequencies [27].

In [28], influence of PWM on increase in skin and proximity losses in the conductors of a PMSM motor for traction application was experimentally demonstrated. It was shown that for the chosen design, the AC losses were as high as 30 percent of the total DC resistive losses. Motors in traction type applications typically have more turns in the stator windings to meet the requirement of high torque at zero speed. Consequently, depending on the design, their copper losses in the form of DC and AC losses tend to be higher. In case of fan or pump type of applications, the load torque is almost negligible at zero speed, therefore such type of motors do not need as many turns in the stator windings as in case of traction type applications and hence the influence of AC losses is smaller.

Since the focus of this work is predominantly on low speed machines (<300 Hz electrical frequency), review of the AC resistive losses will not be pursued further.

In a typical machine, the end winding inductance is much smaller than the main inductance. Hence the impedance to the harmonic currents is lower in the end windings than that in the core. Consequently, the stator resistive losses in the end winding tend to be higher than those in the stator core. To minimize the losses in the end windings, concentrated winding motors are considered advantageous than distributed winding machines.

2.4.2. Estimation of core losses in PMBDCM and PMSMs:

The core losses are associated with the magnetic steel used in the motors. The nature of core losses in the form of eddy currents and hysteresis losses was first evaluated and explained by Steinmetz in 1920 [29]. The procedure for estimating core losses for permanent magnet synchronous machine under no load condition was developed in [30]. It was shown that the core losses are a function of machine geometry, material properties and the electrical speed. Given the machine dimensions, preliminary estimation of flux densities in stator tooth and yoke was used to predict core losses under no load condition [31]. The models used for the accurate estimation of flux densities in the stator tooth and yoke rely on finite-element simulations to obtain the correction factors necessary for tuning the flux density estimation results. Calculation of the correction factor requires significant computation effort through finite element simulations. In [33], an improved core loss model of PMSM was provided without resorting to the correction factors. The loss modeling took into account the excess of core losses which are not accounted for in [30-32].In [34], a core loss model considering stator skewing effect was also considered.

The analytical approaches explained in [30-34] predicts the no load core losses by estimating rate of change of flux densities in stator tooth and yoke under no load operation of the machine. The influence of load on core losses and its prediction has been explained in [35]. It is known that the square wave rotor flux density has the highest amplitude of higher order harmonics resulting in highest stator core losses while sine wave flux density results in the lowest core losses [1]. The same is true for current harmonics in the stator for respective square wave and sinusoidal currents. In [11], it is shown that for square wave current injection the eddy current losses are much higher than that of sinusoidal excitation. Although the core loss increase due to square wave current in comparison to sine wave current was demonstrated in [11], the influence of non-sinusoidal harmonic injection current was not evaluated.

The influence of switching frequency on core losses was evaluated in [37-41]. To understand the core losses due to switching frequency harmonics in permanent magnet motor, it is essential to understand the eddy and hysteresis loss components in the steel laminations [36]. Accordingly, research on evaluating the core losses at various switching frequencies using experimental results was discussed in [37-39].

In [38] and [39], the core loss as a function of the switching frequency was measured by varying the switching frequency from 1 kHz up to 16 kHz as an AC signal. It should be noted that this signal is not similar to the switching ripple riding over the sine wave fundamental signal. The main conclusion from the measurements was that the core losses do not increase significantly above 5 kHz as the impedance offered by the coil to the applied voltage is higher. However below 2 kHz, since the impedance is lower, the current harmonic amplitude is higher and hence the resulting losses are higher (up to 10 percent). The results show a general trend of how the losses may increase or decrease as a function of switching frequency. However the analysis cannot be used as is for PMSM efficiency evaluation because: (a) the core losses in PMSM due to the fundamental frequency are dominant, and (b) the switching frequency ripple amplitude in the current is dependent on the motor power factor and the PWM method applied. It is known that asynchronous carrier based PWM methods yield higher total harmonic distortion than synchronous PWM methods [41]. Hence the evaluation of core losses in PMSM considering reduced switching frequency operation requires further study.

Influence of various slot harmonics and stator current harmonics on various core loss components including magnet eddy losses were discussed in [42]. The analysis assumed asynchronous PWM with switching to fundamental frequency ratio of 16. With such a low switching to fundamental ratio, the amplitude of the sidebands near the switching frequency is higher [41]. Consequently, the losses associated are also higher. In [41], it is shown that the harmonic losses can be reduced significantly by using synchronous carrier based PWM methods. Hence, the core losses with synchronous PWM methods that yield lower harmonic content needs further evaluation.

2.5. Estimation of semiconductor losses

The predominant losses in semiconductor devices are the conduction and switching losses. The conduction loss is proportional to the magnitude of the square of the current while the switching loss is a function of the current and switching frequency of the inverter. Analytical estimation of inverter losses have been widely reported in [43-48]. However, in these methods, the crucial assumption is that the semiconductor device current is sinusoidal and its amplitude remains constant during the switching period. Such an assumption cannot be used for non-sinusoidal current waveforms that occur at very low switching frequencies as the current amplitude may vary significantly between the switching intervals. Also the assumption that the peak switching current waveform remains constant during the switching interval may not be applicable at low switching frequencies. For accurate estimation of the total device losses, circuit simulations are generally applied. Analytical methods for estimating inverter losses at reduced switching frequencies have been mainly studied for slow switching devices such as thyristors and transistors. This research will apply similar methods to estimate the Insulated Gate Bipolar Transistor (IGBT) losses.

The above sections reviewed the predominant loss estimation methods in permanent magnet motor drive system. The next section will focus on literature addressing modeling and controlling of PMBDCM and PMSM drives.

2.6. Modeling and control of PMSM and PMBDCM motors

Three phase permanent magnet motor drives are multi input multi output and can be represented as multi-variable systems. It is essential to model them in a way to have a better insight into the system variables and their interactions leading to a better and intuitive way of performing: (a) steady state analysis, (b) controller design, and (c) stability analysis. Accordingly, various models have been reported in the literature. The following sections will review modeling and control of non-sinusoidal (PMBDCM) and sinusoidal (PMSM) drive systems.

2.6.1. A. Modeling and control in synchronous reference frame (dq-model)

The modeling of synchronous machine considering synchronous reference frame was first proposed in [49]. In this method, the three phase motor windings phase spatially separated by 120 degrees are transformed into two phase windings (direct and quadrature d-q axes) that are orthogonal to each other. The direct and indirect field oriented control of induction machine based on synchronous reference frame modeling was developed in [50] and [51] respectively. For synchronous reference frame modeling and control, it is assumed that the motor back EMF is sinusoidal and that the other higher ordered harmonics can be ignored as they do not contribute toward torque production. The modeling and control technique is be applied to permanent magnet synchronous machines and the same is discussed in [52].

2.6.2. Modeling and control with phase variables

A simple way to model and control trapezoidal back EMF machines (PMBDCM) is by representing the current and voltages in them as three phase variables (*abc-phases*). Such machines are usually controlled by rectangular wave currents, which are aligned with the back EMFs resulting in constant torque production. Since the current commutation occur at every 60° (electrical degrees), the machine can be modeled using line-line voltage equations. The phase variable modeling is the most common approach for control and analysis of PMBDC machines [53].The rectangular currents generate torque ripple because the commutation requires a finite time to rise due to the motor inductance and the back EMF. The trapezoidal motors can also be controlled using sinusoidal or sine-harmonic currents. Models for the same are discussed in following sections.

2.6.3. Modeling and control in multiple d-q reference frame:

Due to the trapezoidal motor back EMF of PMBDCMs, they are modeled based on the number of harmonics in the back EMF. Then a co-ordinate transformation is applied on the measured variables (current in this case) at each harmonic frequency thereby resulting in multiple reference frames [54]. It results in large and complex controller structure and computationally intensive controller algorithms [55]. Nevertheless, it captures the non-sinusoidal behavior of the machine. It should be highlighted that the reference currents generated with d-q modeling approach are no longer square wave as they are sinusoidal currents with super-imposed harmonics.

2.6.4. Modeling and control in synchronous reference frame with superimposed harmonics:

In [56], [57], a permanent magnet machine model based on complex state variables was introduced. It is based on fundamental model of the machine superimposed with flux linkage harmonics in the rotor reference frame. The addition of harmonics on the corresponding d and q axes represents the deviation of the machine from its sinusoidal behavior. The primary objective of this modeling method is to achieve torque ripple minimization in position control problem in servo application. The model is based on a stored lookup data of the non-sinusoidal back EMF. In order to track the reference currents, high bandwidth current regulators are required.

2.6.5. Modeling and control considering stationary reference frame

The stationary reference frame enables control of machine by transforming variables from three-phase system to a two-phase system. The stationary reference frame models have been used to develop closed loop observers for estimating torque and speed for sensorless control in [58]. The stationary reference frame transformation provides the control algorithm an option to transition between sinusoidal to non-sinusoidal current control. It also enables the implementation of torque ripple and stator resistive loss minimization control. However using the stationary reference frame transformation, the current regulators have to track sinusoidal or non-sinusoidal currents. The current tracking performance deteriorates due to phase delay with increase in operating (fundamental) frequency. With higher ordered harmonics, the phase delay effect is dominant. Hence alternative modeling methods are resorted to.

2.6.6. Modeling and control with pseudo d-q transformation

In [59] a unique pseudo d-q modeling approach was illustrated with the objective of forcing the d-axis current to zero by applying a pseudo three-phase to two-phase co-ordinate transformation. A new rotor position dependent phase variable is added to the original rotor position angle. By applying such a co-ordinate transformation, the three phase non-sinusoidal variables can be converted to two-phase variables such that the magnitude of d-axis variable is zero. The q-axis variable has an average dc component superimposed with rotor position dependent ac component. The amplitude of this ac component depends on the amplitude of the harmonics in the back EMF. Current controllers designed with pseudo d-q transformation have the same limitation as in stationary reference frame due to the system phase delay and regulation of the ac component.

2.6.7. Modeling with extended d-q transformation

The objective of the extended d-q coordinate transform is to achieve time invariant (DC) variables from the non-sinusoidal currents or back EMF by appropriately rotating the reference frame and normalizing the current vector magnitude with respect to rotor position. This transformation was proposed in [60]. In contrast to the conventional reference frame approach this coordinate transformation requires two more variables in addition to the rotor position. The current regulator controller bandwidth limitation in [59] is resolved in [60] because the controllers have to track only the dc variables instead of ac and dc variables as discussed in previous section. In [61], it was shown that for the same current controller bandwidth, such transformation enables better tracking performance than pseudo d-q transformation method.

2.6.8. Complex variable space phasor modeling

Classical *dq* modeling approach requires analysis of PMSM with two stator time constants and the cross coupling between the d and q axes due to rotor speed. Using the space phasor modeling approach, it is easy to visualize PMSM as a DC machine [62]. In separately excited DC machines, keeping the field current constant and varying the armature current, the electromagnetic torque can be controlled directly. Similarly, in case of PMSM, for a constant permanent magnet field, the torque is directly proportional to stator current phasor. Consequently, the stator can be modeled as single time constant instead of two when compared with the classical *dq* modeling approach. The space phasor approach reduces the model size and allows more intuitive insight into the relationships between the motor state variable (*current or flux linkages*) and the cross coupling between the orthogonal windings. The two cross coupling terms are reduced to one complex term. From the above model of PMSM, it is seen that for fixed permanent magnet field λ_m, by varying the stator voltage, the stator current can be controlled.

The electromagnetic torque is the product of three variables: (i) stator current phasor, (ii) rotor flux linkages also known as rotor field, and (iii) sine of the angle between the current phasor and the rotor field and this angle also known as torque angle. Thus the torque can be controlled by controlling the stator current phasor magnitude and the torque angle when the rotor field is constant. The modeling approach uses this simple formulation to represent the machine dynamics. The complex variable form of representation also leads to simpler analytical solution of dynamical transients of the machine as there is only one differential equation to solve [62].

This section covered various modeling methods for control of PMBDCM and PMSM drive systems. The next part will focus on literature related to the reduced switching frequency operation of PMSM drives.

2.7. Reduced switching frequency operation of PMSM drives

At reduced switching frequencies, the small impedance offered by PMSM to the inverter voltage transients can cause higher current waveform distortion and higher losses in the motor and inverter. To reduce this distortion, programmed pulse width modulators (PWM) are preferred over conventional carrier based modulators and therefore considered in this study. Analytical loss modeling of the motor and the inverter is central to the efficiency evaluation at low switching frequencies. Accordingly, the following section will review the current literature on reduced switching frequency operation of PMSM drive system.

2.7.1. Operation of PMSM drives at reduced switching frequency

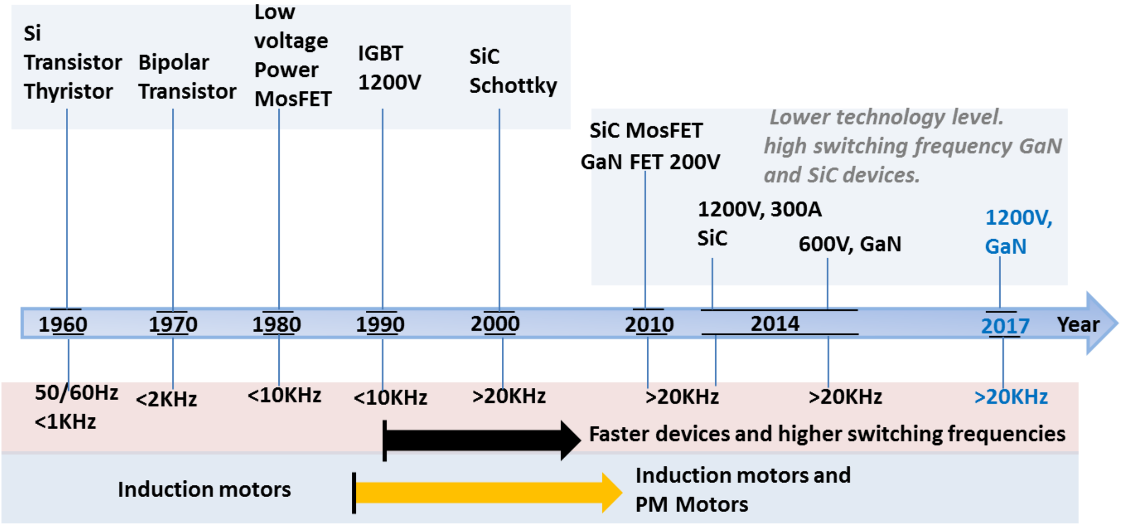

Figure 2.1 Timeline of device technology and switching frequency in last five decades and corresponding motor technology.

State of the art three phase variable speed motor drives have switching frequencies in the range of 2 kHz to 20 kHz depending on their power level. High switching frequencies (above 10 kHz) are used in applications where precise position control or low acoustic noise is desired. For applications where such requirements are not stringent, the switching frequency can be significantly reduced. The operation of motor drives with low switching frequency was a highly researched topic in the 1960's and the 70's because of use of slow devices such as thyristors and bipolar transistors [63-65] dominated the field of variable speed drives at that time. In order to minimize the motor harmonic losses at low switching frequencies, programmed pulse width modulation (PWM) methods were resorted to [64]. The optimized PWM methods were mainly developed for reduction of losses in the stator as well as in the rotor of the induction machines [66]. After the advent of faster switching devices such as MOSFETs and IGBTs, programmed PWM methods are currently limited to medium voltage high power drives [67] and mainly for induction machines.

Recently, wide band-gap devices that can switch faster than IGBTs have been developed [68]. They are based on Silicon Carbide and Gallium Nitride technology and are most commonly reported in high temperature and high power density applications. They are promoted for their higher efficiency operation due to their lower switching losses at high switching frequencies. These devices are still emerging and are extensively researched for low cost high volume manufacturing [69]. The corresponding timeline is shown in Figure 2.1.For lower cost alternatives, IGBTs are still the mainstream devices and are focus of this research.

Research on reduced switching frequency control of permanent magnet motors remains yet to be explored in depth. In comparison to induction machines, PMSMs have significant advantages in power density, and motor and drive system efficiencies. Power density is enhanced in the PMSM due to PM-field excitation which reduces the ampere-turn requirement on the stator side and additionally having no windings on the rotor side resulting in elimination of resistive losses on it. The permanent magnets contribute to a reduction of stator and elimination of rotor resistive losses as well as harmonic core losses [70-72]. In [73], it was shown that in induction machines operating at reduced switching frequencies and asynchronous PWM (800Hz), the rotor harmonic losses were up to 50 percent of the total machine losses. Since PMSMs do not have rotor windings, the corresponding total harmonic losses are lower allowing further reduction of switching frequency. In [74], the advantage of higher q-axis inductance in interior permanent magnet motors for reduced switching frequency operation was mentioned however was not pursued for further research.

The lower harmonic losses imply lower de-rating of the PMSM at reduced switching frequencies than in the case of the induction machines. These aspects of combined PMSM and inverter sizing in light of reduced switching operation have not been discussed in the current literature prior to this research is to be noted.

2.7.2. Loss Analysis of PMSM drive system at reduced switching frequencies

Literature on detailed loss evaluation of PMSM drive system with complementing PWM strategies at reduced switching frequencies is very limited. In [75], losses in a 1.5 kW PMSM drive system were evaluated to optimize the system efficiency considering motor inductance as a variable. The total system losses were calculated by varying the switching frequency from 16 kHz to 450 Hz using asynchronous carrier based PWM. The research also considered a six-step modulation method to analyze the total system losses at the fundamental frequency. The motor stator resistive losses were calculated using conventional method [1], while the core losses were calculated using finite element simulations. The analysis showed that, at certain value of motor inductance, six-step mode of operation resulted in lower system level losses than asynchronous carrier based PWM above 5 kHz. The choice of the inductance with this method allows lower de-rating of the drive.

In [76], total system losses in a 3kW interior permanent magnet synchronous motor (IPMSM) drive operating at various switching frequencies were analyzed. This study had similar approach to the one in [75] except that instead of varying the motor inductance to reduce harmonic current amplitude, a three-level voltage source inverter was considered. The switching frequency of the inverter was varied from 10 kHz to 5 kHz using asynchronous carrier based PWM. A single-pulse modulation method was also considered to analyze the losses at the fundamental frequency. Based on the analytical calculations of the system losses, it was shown that, single-pulse mode of operation was more efficient than carrier based PWM at 5 kHz when the operating speed was higher.

Based on the above review, analysis on benefits of reduced switching frequency incorporating various PWM methods for permanent magnet motors driven by two-level inverters and its experimental validation and needs more investigation.

2.7.3. Modulation strategies considering reduced switching frequency operation

There is significant amount of literature discussing the various switching strategies and the resulting modulation methods for a three phase inverter [77]-[121].In the following sections, various pulse width modulation methods will be reviewed considering reduced switching frequency operation of the inverter. The classification of the modulation methods based on fixed or variable switching frequency operation is shown in Figure 2.2. From the review, it is seen that at very low switching frequencies, programmed pulse width modulation methods have advantages over fixed switching frequency based methods. For reduced switching frequency operation, it is critical to select the right pulse width modulators to reduce the current harmonic distortion in the motor and drive. The hysteresis and random PWM are generally applied at higher switching frequencies [77].

For reduced switching frequency operation, just the synchronization between carrier and the fundamental frequency can reduce the amplitude of low ordered current sidebands by up to 70 percent [41]. Synchronization implies that the ratio of carrier frequency ‘f_s’ and the fundamental frequency ‘f_1’has only *real (N)* integral values. Furthermore, the zero crossing of the carrier and the modulating signals are also synchronized. Any phase shift between them may result in higher current distortion for lower values of *N*. Such an approach is applicable to all of the fixed switching frequency modulators. In case of variable frequency modulators, low integral value of N is typically applied to model predictive and programmed PWM methods. The following sections will review in further detail each of the modulation methods.

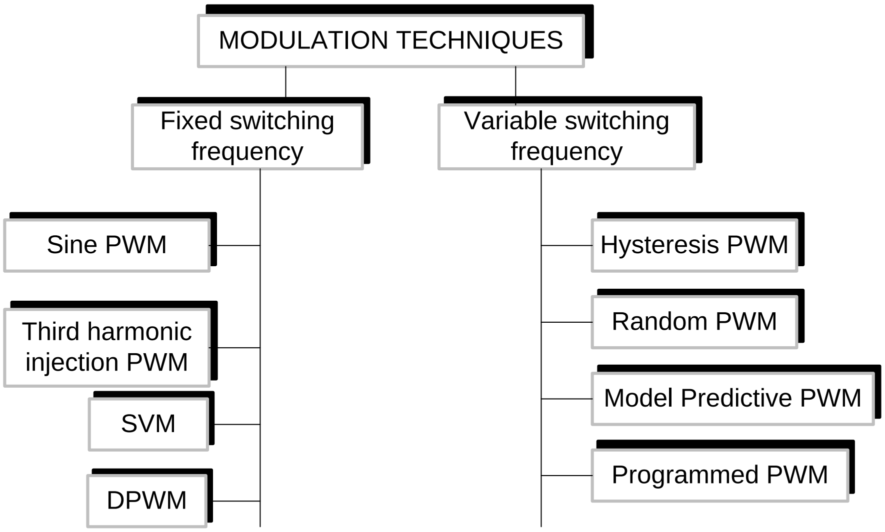

Figure 2.2 Classification of PWM techniques for two level converters

2.7.3.1. Sine PWM

The sine PWM is the simplest modulator where in a sine waveform is compared with a high frequency triangle waveform (an up-down counter) to generate the binary output switching pulses. When the phase of the sine wave is same as that of the triangle, the corresponding method is known as synchronous carrier based modulation [78]. Various aspects related to sampling of sine PWM methods catered for microprocessor based inverter is discussed in [79].

2.7.3.2. Third Harmonic injection PWM

When third harmonic voltage also known as zero sequence is added to the fundamental voltage waveform, the inverter output voltage gain and current harmonic distortion can be improved [80-82]. If the amplitude of the zero sequence voltage is 1/6th of the fundamental voltage, then the gain of the inverter is increased by 15 percent [80]. In [82], it is also shown that if the amplitude of the zero sequence voltage is1/4th of fundamental voltage, the resulting current harmonic distortion is lowest amongst the known continuous pulse width modulation methods.

2.7.3.3. Space vector modulation (SVM) and discontinuous PWM

A three phase two level six-switch inverter has eight switching states. The six states that produce an output voltage vector are known as active states while the remaining two states that produce zero output voltage are known as zero states. Distribution of the zero states around the active states in one switching period results in various PWM strategies. When the two zero states are symmetrically distributed around active states, it results in center aligned space vector modulation (SVM) and was first reported in [83-84] for a rectifier and brushless servo application. Since then, variants of this method were developed with different objectives [85-90]. When only one of the zero states is used to reduce the number of switching transitions, it results in discontinuous pulse width modulation (DPWM) [91-94]. The modulation strategies that yield minimum loss are essentially combination of various DC bus clamping methods which are a function of the load power factor [95].

2.7.3.4. Model Predictive Control

Model predictive control (MPC) is performed in discrete time, where during each sample time interval, the output voltage reference is estimated for each valid switching state using a model of the plant [96-97]. All the estimated values are calculated by a cost function and eventually the switching state that minimizes the cost function is applied at the next interval [98]. Reducing the switching frequency with lower harmonic distortion is one such cost function [97].

2.7.3.5. Selective harmonic elimination PWM

Selective harmonic elimination is one of the first programmed pulse width modulation strategies developed. It is designed to eliminate higher ordered harmonics and in effect minimize the motor harmonic losses [99-114]. Depending on the number of pulses used and the polarity of the PWM waveform, various solutions for the commutation control angles are developed in [100-102]. The carrier based techniques to realize the selective harmonic elimination PWM has been proposed in [113], however they are not easily adaptable to current state of art motion control digital signal processor platforms due to need of triangle waveform super imposed with higher ordered harmonics. Hence further work is required to adopt the programmed selective harmonic elimination PWM methods on the state of art motion control dedicated microcontrollers.

2.7.3.6. Synchronous Optimal PWM

When thyristors based motor drives were prominent, the low switching speed of devices instigated the evolution of programmed modulation techniques [115-117]. In this technique the switching angles are pre-calculated based on an optimizing function; which is minimization of all harmonics to reduce the motor harmonic losses. Then lookup tables are used for implementation of this scheme especially for open loop Voltz per Hertz control of induction motor drives. The number of switching pulses is reduced as the fundamental frequency increases based on predefined patterns. The patterns are programmed up to the highest modulation index of $4/\pi$.

In [118], it is shown that synchronous optimal PWM has higher voltage gain then model predictive control and within the voltage limits, they have similar harmonic distortion. At higher modulation indices, synchronous optimal PWM has superior performance in comparison to model predictive control.

2.7.4. Implementation of PWM algorithms at low switching frequencies

When the switching frequency of the inverter is reduced, its switching losses are reduced in proportion thereby resulting in higher output power rating of the inverter [115]. At low switching frequencies, the inverter is controlled using programmed PWM because it offers lower current harmonic distortion than carrier based PWM [66]. However carrier based PWM is easier to implement on digital hardware than programmed PWM [79], [82], [119-121]. To implement carrier based PWM, a sinusoidal reference signal is compared with a high frequency triangle (or carrier) signal. The high frequency carrier signal is generated using an up-down counter which is readily available in microcontrollers for motor control. The programmed PWM, on the other hand, is implemented by storing offline calculated commutation angles in lookup tables and then recalled for PWM generation using dedicated digital logic circuit [63],[64],[67]. Therefore the microcontrollers that have digital hardware catered for carrier based PWM cannot be easily modified for programmed PWM generation [82]. Due to the complexity of implementation and hardware requirements, programmed PWM is less favored in low voltage drives [82], [64].

To simplify the implementation, a regular-sampled method for generating programmed PWM was proposed in [121]. The implementation is made using two sinusoidal phase shifted signals to generate rising and falling edge pulses. Such an approach requires four counters to synthesize the switching waveform. If a single counter approach is used then the computation time of the PWM algorithm increases [121]. Since the state of art microcontrollers do not have so many timers dedicated for PWM generation, the approach becomes tedious. In [122], an alternative method to generate the programmed PWM using principles of carrier based PWM was proposed. The approach focused on comparing a sine wave voltage reference with a modified triangle to generate the programmed PWM pulses using an analog comparator circuit. The digital implementation of the same was not discussed. Although the feasibility of the method was shown, it is difficult to implement the same on state of art digital signal processor because of limitation on maximum allowable counter period and the processor clock frequency.

Based on the above review it is seen that implementation of programmed PWM on commercially available microcontrollers is complex and difficult. A simple implementation similar to that of a carrier based PWM on a state of art digital signal processor has yet to appear and will be highly valued in practice.

2.8. Current regulation control at low switching frequency

Various current control methods have been reported in the literature [122-129] and the most commonly used are:

(i) Hysteresis control[123],

(ii) Proportional Integral (PI) current control [123],

(iii) PI current control with feedback oversampling [125]

(iv) Complex variable current control [126], [128],

(v) Dead-beat current control [127] and

(vi) Model predictive current control [129,130]

While all of the aforementioned methods show good performance at higher switching frequencies, only a few have acceptable performance at low switching frequencies.

Hysteresis current controller is not suitable at low switching frequency operation because the resulting output switching pulses are asynchronous with the rotor angle and not optimized for lower current ripple causing high current harmonic distortion.

The PI current controller is more widely used control scheme for PMSM and has acceptable performance for systems with low dynamic requirements. For systems requiring fast dynamic response at low switching frequency, feedback oversampling, complex variable current, dead-beat and model predictive current controllers are advantageous

The dead-beat and model predictive current controllers can be sensitive to parameter variations and un-modeled time delays in the system. At low switching frequencies, the cross coupling between the inverter orthogonal winding d and q axes due to and inverter sampling delay becomes significant and must be compensated [128]. The inverter delay compensation is achieved through complex variable current regulators resulting in improved dynamic performance even at low switching frequencies [128].

Current control affects in general not the system efficiency but only the damping and possible instability. Accordingly, for stable motor performance, simple current controller implementation is essential. The existing literature [129, 130] focuses on complex variable current control and model predictive control of induction motor drives operating low switching frequency.

2.8.1. Motor dynamic operation at reduced switching frequency

Dynamic response of permanent magnet motors is superior to induction machines due to its lighter rotor and its higher capacity for peak torques. This is true only if the exact rotor position is available and the inverter control can achieve accurate current alignment of stator currents with the motor back-EMFs [131]. In case of sensorless position control, accurate estimation of rotor position during transient operation can be challenging. In such cases, stability of the system can be determined through open-loop operation of the machine. It is known that induction machine inherently has more stable open loop response than PMSM [132-134] which can be operated on open loop only for a short duration of time with oscillatory speeds and chaotic torque generation. Hence it can be inferred that during low switching frequency operation, when the inverter control bandwidth is low, induction machines can have more stable operation while the capacity for the stable operation of PMSM is extremely limited both in its torque and speed responses as well as reduced torque capabilities. Since the present literature only covers low switching frequency operation of induction motors, while the challenges for applying the same or similar techniques for PMSM are yet to be resolved, the control of induction machines at low switching frequency is not discussed any further in this section.

The two important aspects that must be considered in the low switching frequency control of PMSM drives are: (a) current regulation and (b) rotor position control. Both these aspects are critical to avoid pull-out of PMSM under transient load conditions during low switching frequency operation. Current regulation at low switching frequency has been demonstrated on induction machines using complex variable current regulators [128]. Complex variable current regulation of PMSM with low carrier to fundamental ratio (lower switching pulses) and carrier based PWM has been shown in [135] only for high speed traction application. PMSM current control methods using programmed PWM has not been discussed in any of the published literature so far.

2.8.2. PMSM efficiency evaluation at reduced switching frequency

Previous work on low switching operation of motor drives has been focused on induction machines [136, 137]. In [136], the total system efficiency optimization of induction motor drive using programmed PWM was shown. The strategy for computation of commutation angles based on total system losses was evaluated. It was also shown that commutation angles calculated using simple inductive loads gave near optimal performance in minimizing total system losses.

In [115-117], the efficiency improvement in a three-level inverter for medium voltage induction motor drive was demonstrated by applying synchronous optimal programmed PWM. It was experimentally shown that the motor phase current harmonic distortion with optimal PWM at switching frequency of 250 Hz was similar to that of a space vector PWM at 1 kHz. The reduction in switching frequency doubled the power rating of the inverter. The research mainly focused on reducing the switching losses of the inverter while harmonic losses analysis of the motor was not discussed.

In [138], total system losses incurred in the inverter as well induction motor due to reduced switching frequency was experimentally evaluated. Programmed PWM was implemented to reduce the current harmonic distortion at low switching frequency. For efficiency evaluation, the induction motor losses were measured using a calorimeter. Based on single measurement point, it was concluded that programmed PWM at low switching frequency (650 Hz) resulted in lower system losses than space vector modulation at high switching frequency (20 kHz). It was also shown that programmed PWM had lower harmonic losses in the motor than six step square wave modulation. Although a total system efficiency improvement was claimed, it is to be noted that the benefits diminished when the operation at low switching frequency (650Hz) was compared to the one at 10 kHz. This is because the reduction of losses of the inverter was offset by the increase in the motor harmonic losses. Since the induction motor has higher harmonic losses in stator as well as rotor, the benefits of reducing switching frequency is lower in comparison to PMSM [73].

In [76], total system loss analysis of a 3kW interior permanent magnet synchronous motor (IPMSM) drive operating at various switching frequencies was made. For lower current distortion operation, a three level inverter was considered. Operation of a carrier based PWM with switching frequency of 5 kHz was compared with a six-step mode of operation. Based on experimental measurements, it was shown that at higher operating speeds, six-step operation was more efficient than carrier based PWM at 5 kHz. It should be noted that three-level inverter requires twice the number of switching devices and capacitors in comparison to two-level converter. While the conclusions favored operation at low switching frequency using three-level six-step commutation, the research did not explore the advantages of programmed PWM in a two-level inverter when the switching frequency is reduced below 5 kHz.

Based on the above discussions, it is seen that given a two-level inverter, experimental evaluation of PMSM drive system efficiency at low switching frequency has not been studied in depth. Also application of programmed PWM for improving PMSM drive system efficiency has not been reported. Experimental validation of reduced switching frequency incorporating various PWM methods for permanent magnet motors driven by two-level inverters and its demonstrated benefits are yet to appear in research.

2.9. Rotor position sensorless control of PMBDC and PMSMs

Permanent magnet motor drive systems are cost and energy efficiency sensitive. They require rotor position information for their stable operation and most of the high performance drives use expensive resolvers and position encoders resulting in high cost. The position sensors are also an additional source of reliability concern, in applications operating under harsh environmental conditions, thus making them unsuitable. Cost sensitivity and other described features and functions require position sensorless operation. That being the case, the applications considered in this research do not need high dynamic response or require low speed operation or demand operation with low torque ripple. Therefore, the sensorless control techniques reviewed in this literature mainly focuses on estimating the rotor position from the motor back electromotive force.

2.9.1 Sensorless control with two-phase commutation of PMBDCM

PMBDCMs are controlled by injecting square wave currents to generate the average torque. This is achieved by switching the devices at every 60 degrees. The switching events are determined by detecting the back EMF zero crossing using a Hall Effect sensor [6], [71], [139-141]. The sensors even with their low resolution meet the requirements for control of the motor and prove to be a cost effective solution compared to an absolute encoder in case of PMSM.

In [142-144], various techniques to eliminate the Hall-effect sensors are discussed. These control strategies focus on emulating the Hall Effect signals, which is the zero crossing of the back EMF. A pseudo neutral is created by a resistive network connected in star across the motor terminals. The voltage between this pseudo neutral and the dc link midpoint has similar behavior as third harmonic voltage in back EMF. Since the current commutation occurs at the maximum and minimum peak of this third harmonic voltage, a commutation sequence can be generated accordingly [142]. Resistive back EMF sensing has limitation at very low speed, as the motor back EMF amplitude is small to detect. Yet in applications such as home appliances, fans and pumps, continuous operation at such low speed is not required and hence this approach remains popular within industry. The machines are started in open loop and then eventually operated in speed-closed loop using resistive back EMF detection method (self-commutation). This technique requires additional voltage signal detection circuit along with isolation.

2.9.2 Sensorless Control Strategies based on back EMF observers

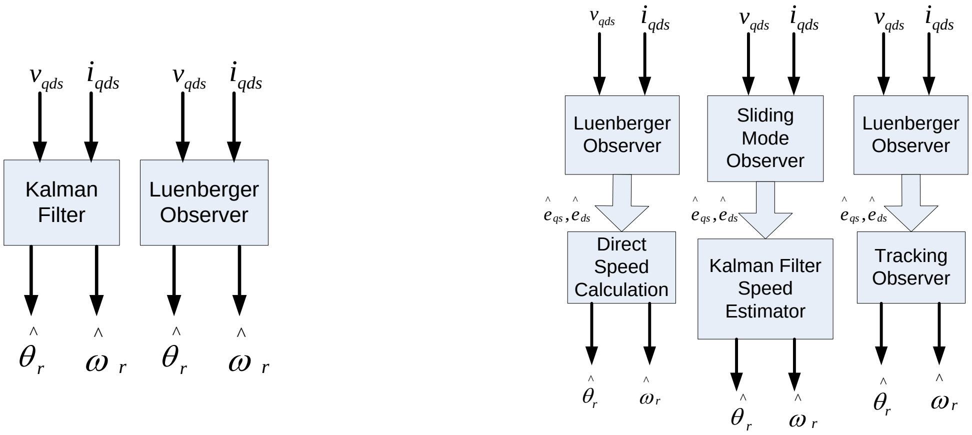

(a) (b)

Figure 2.3 Observers for estimation of speed and rotor position using (a) direct estimation and (b) two-stage estimation techniques

When the rotor speed is above 0.05 p.u. [145], the back electromotive force (EMF) voltage based techniques for the rotor position and speed estimation resorted to [145-155]. The various methods given in Figure 2.3 for estimating the back EMF voltage are: (a) voltage integration [146], state observer including mechanical system [147], (b) nonlinear observer [148], (c) extended Kalman Filter [149], (d) state observer in stationary reference frame [150], and (e) state observer in synchronous reference frame [151-152]. These estimation schemes generally show good performance in high-speed region. The following sections will review these methods. It should be noted that these methods require high switching and sampling frequencies.

2.9.2.1. Voltage Integration Method

This method is based on the stator flux linkage which is obtained by integrating the motor terminal voltage minus the voltage drop across the stator resistance [146]. In order to obtain the flux vector, two line-to-line voltages are measured and then integrated after the resistance voltage drop is excluded. Once the flux vector is obtained, rotor position is estimated by using inverse tangent function and some mathematical calculation. The method is simple to implement, but performance is dependent on the accuracy of voltage measurement, which is generally poor due to switching harmonics. Voltage reference can be used in place of the measured voltage. As the method is inherently open-loop type, inverter nonlinearities can degrade the sensorless performance.

2.8.2.2. State Observer Including Mechanical System:

This method uses the d- and q-axis currents, rotor speed, and rotor position as the state variables. Because the currents and rotor speed are simultaneously used as state variables, the system becomes a nonlinear. Furthermore, the mechanical system comprising of moment of inertia, coefficients of viscous and coulomb friction as parameters is included. The system is considered as a linear observer under certain assumptions. Parameter sensitivity evaluation is essential for good rotor position and speed estimation [147], [148].

2.8.2.4. Extended Kalman Filter:

Extended Kalman Filter provides the optimal estimation for a nonlinear system when the system model and measurements have some errors and noise superimposed on them. Appropriate selection of error covariance matrices is essential for good performance. Tuning procedure guideline and selection of error covariance matrices is not as trivial as in case of linear state observers [149].

2.8.2.5. State Observer in Stationary Reference Frame:

State observer in stationary reference frame can estimate the rotor position by using an inverse tangent function. Rotor speed can be calculated by using the estimated back EMF voltages. Because the state variables are ac quantities even in the steady state, bandwidth of state observer should be large enough to prevent the phase delay [150].

2.8.2.6. State Observer in Rotor Reference Frame

State observer in rotor reference frame can estimate the state variables without any phase delay as these variables are dc quantities in steady state. This method requires additional rotor position and speed estimation scheme [151-152]. For the state observer in rotor reference frame, the d- and q-axis back EMF voltages are chosen as state variables. In order to estimate the rotor position and speed, a tracking observer is used in [154]. The advantage of this dual approach is the greater flexibility attained to tune the estimator and PMSM speed control system.

In this research, the state observer in rotor reference frame will be used for control of trapezoidal as well as sinusoidal back EMF machines.

Conclusions

This chapter reviewed the state of the art of the efficiency improvement strategies of permanent magnet motor drives considering various stator current excitation waveforms and reduced switching frequency operation of the inverter driving them. The following points highlight the areas that need further research and analysis to push the motor drive system efficiency envelope further with respect to the current state of the art systems.

1. In case of PMBDC motors, improving the efficiency by reducing not only the stator resistive losses but also the core losses using various stator current excitations has not been reported and needs further study. Influence of current excitation strategies on performance of PMBDCMs with various back EMF waveforms needs further evaluation.
2. The topic on efficiency improvement of PMSM drive system considering reduced switching frequency operation has yet to appear in the literature and hence needs comprehensive analysis along with the controller development. The analytical inverter and PMSM loss models considering reduced switching frequency operation and programmed PWM have not been reported and therefore requires detailed evaluation.
3. For the control of PMBDCM and PMSM motors, current control strategies and their performance require further analysis. In case of PMBDCM, the stator current control strategies with control of desired harmonics for low and high speed operation need further evaluation. In case of PMSM operating at reduced switching frequencies, simple current control methods taking into account the large sampling delays need to be further analyzed for stable operation of the motor.
4. A simple implementation of carrier based programmed PWM on state of art motion control digital signal processor platform is highly desired for ease of adoption into the existing systems. Sampling methods complementing the PWM methods also needs to be addressed.
5. Since the rotor position sensorless control strategies are highly desired due to cost and reliability requirements, applications of such methods to the aforementioned problems needs to be further pursued. Accordingly, rotor position sensorless control strategy considering harmonics in the back EMF and motor currents need further evaluation. Also sensorless control strategy considering reduced switching frequency operation for PMSM has yet to appear.

The following chapters will delve further into the aforementioned topics and address them with detailed analysis and experimental results.

References

[1] R. Krishnan, *Permanent Magnet Synchronous and Brushless DC Motor Drives*, CRC Press, 2010.

[2] B.D. Bedford, R.G. Hoft, *Principles of Inverter Circuits*, J Wiley, New York , 1964.

[3] T. Lipo and F. Turnbull, "Analysis and comparison of two types of square-wave inverter drives," *IEEE Trans.Ind. Appl.*, vol. IA-11, Mar./Apr. 1975, pp. 137-147.

[4] T. Nehl, F. Fouad, and N. Demerdash, "Digital simulation of power conditioner-machine interaction for electronically commutated dc permanent magnet machine," *IEEE Trans. Magn*., vol. MAG-17, pp.3284-3286, Nov. 1981

[5] PillayP. , and R. Krishnan, “Modeling, simulation, and analysis of permanent-magnet motor drives. II. The brushless DC motor drive,” *IEEE Trans. Ind. Appl*., vol. 25, no. 2, pp. 274 –279, Mar/Apr. 1989.

[6] PillayP. , and R. Krishnan, “Application characteristics of permanent magnet synchronous and brushless DC motors for servo drives,” *IEEE Trans. Ind. Appl*., vol. 27, no. 5, pp. 986 –996, Oct. 1991.

[7] T. M. Jahns, “Torque production in permanent-magnet synchronous motor drives with rectangular current excitation,” *IEEE Trans. Ind. Appl*., vol. 20, no. 4, pp. 803-813, July/Aug. 1984.

[8] T.M. Jahns, and W.L. Soong, “Pulsating torque minimization techniques for permanent magnet AC motor drives-a review”, IEEE Trans. Ind. Electron., Apr 1996, Vol 43-2, pp 321-330.

[9] Y. F. Shi, Z.Q. Zhu, and D. Howe, ”Torque-speed characteristics of interior-magnet machine in brushless AC and DC modes, with particular reference to their flux-weakening performance,” Proc. Int. Power Electronics and Motion Control Conf., IPEMC 2006, 13-16 August, 2006, Shanghai, China.

[10] J.R. Hendershot Jr., TJE Miller, Design of Brushless Permanent Magnet Machines, Motor Design Books LLC, 2010.

[11] Z.Q. Zhu, J.X. Shen, D. Howe, ”Flux-weakening characteristics of trapezoidal back-emf machines in brushless DC and AC modes,” *Proc.Int. Power Electronics and Motion*

[12] M. Miyamasu, K. Akatsu, “Efficiency comparison between Brushless dc motor and Brushless AC motor considering driving method and machine design”, IECON Nov. 2011, pp 1830 – 1835

[13] J. Holtz , L. Springob, “Identification and Compensation of Torque Ripple in High-Precision Permanent Magnet Motor Drives”, IEEE Trans. Ind. Electron, Vol. 43, No. 2, 1996, pp. 309-320.

[14] F. Piriou, A. Razec. R. Perret, H. Le-Huy, 'Toque Characteristics of Brushless DC Motors with Imposed Current Waveforms”, *IEEE* IAS 1986, pp, 176-181.

[15] J.Y. Hung, Z. Ding, "Minimization of Toque Ripple in Permanent- Magnet Motors: A Closed Form Solution”, *IEEE IECON*, 1992, pp. 459-463

[16] D. Hanselman, “Minimum Torque Ripple, Maximum Efficiency Excitation of Brushless Permanent Magnet Motors”, *IEEE Trans. Ind. Electron*, Vol. 41, No. 3, 1994, pp. 292-300.

[17] *P.L.* Chapman, S.D. Sudhoff, C.A. Whitcomb, “Optimal Current Control Strategies for Surface-Mounted Permanent-Magnet Synchronous Machine Drives”, *IEEE Trans. Energy Convers*, Vol. 14, No. 4, Dec 1999.

[18] R.Leidhold, G. Garcia, “PMAC motor control strategy, based on the instantaneous active and reactive power, for ripple-torque and copper-losses minimization”, *IEEE IECON*, 2000. vol.2, pp-1401-1405.

[19] N. Bianchi, S. Cervaro, L. Malesani, “Current Shapes For Minimizing Torque Ripple In SPM Motors”, *Proc. ICEM* , 2000 pp. 1237-1241.

[20] T. Kim, H-W Lee, M. Ehsani, “High Performance Brushless Permanent Magnet Motor/Generator Drives in Electric and Hybrid Electric Vehicles”, *IEEE PESCAnnu. Meeting*, Oct 2006, pp. 1 – 5.

[21] D Grenier,. R Mende,. J.P Louis, ,“Comparison of several control strategies for DC Brushless Drives”, *IEEE IECON*, 1994. vol.1, pp-26-31

[22] A. Lidozzi, L. Solero, F. Crescimbini, R. Burgos “Sensorless Speed Vector Control of a Trapezoidal back-EMF PMSM Machine using Pseudo- Park Transformation for Fan Motor Drives”, *IEEE Power Electron. Spec. Conf*, 2008, pp-2167-2171.

[23] A. Oliveira, J. Monteiro, M. Aguiar, D. Gonzaga, “Extended DQ transformation for vectorial control applications of Non-Sinusoidal Permanent Magnet Synchronous Machines”, *IEEE Power Electron. Spec. Conf*,2005, pp 1807-1812.

[24] J. Pyrhönen, T. Jokinen, V. Hrabcová, Design of rotating electrical machines, John Wiley&Sons, Ltd., 2008

[25] X. Tang, C.R. Sullivan, “Stranded wire with uninsulated strands as a low-cost alternative to litz wire”, Proc. 2003 IEEE Power Electronics Specialists Conference, Vol. 2, pp. 289-295, June 2003

[26] S. Singh, C. Ifrim, L. Luca, B. Wawrzyniak, “Copper Losses and Temperature Distribution in the Slots of a Liquid Filled, High Speed Permanent Magnet Motor”, *IGTE Symposium* Sept-2012.

[27] P.B. Reddy, T.M. Jahns, T.P. Bohn, “Modeling and analysis of proximity losses in high-speed surface permanent , magnet machines with concentrated windings” in Energy Conversion Congress and Exposition, Atlanta, GA, 2009, pp. 996-1003

[28] S. Iwasaki, R.P. Deodhar, Y. Liu, A. Pride, Z.Q. Zhu, J.J. Bremner, “Influence of PWM on the proximity loss in permanent-magnet brushless AC machines”, IEEE Trans. on Ind. Appl., Vol. 45, No. 4, pp. 1359-1367, July/August 2009

[29] C. P. Steinmetz, “On the law of hysteresis”, AIEE Transactions, vol. 9,pp. 3–64, 1892, Reprinted under the title ”A Steinmemtz contribution to the ac power revolution”, introduction by J. E. Brittain, in Proceedings of the IEEE 72(2) 1984, pp. 196-221.

[30] G.R. Slemon and X. Liu, “Core losses in permanent magnet motors,” *IEEE Trans. Magnetics*, vol. 26, no. 5, pp. 1653-1655, Sept.1990.

[31] C. Mi, G.R. Slemon, and R. Bonert, “Modeling of iron losses of permanent-magnet synchronous motors,” Industry Applications, IEEE Transactions on, vol. 39, no. 3, pp. 734–742, Jun. 2003.

[32] K.J. Tseng, S.B. Wee, “Analysis of Flux Distribution and Core Losses in Interior Permanent Magnet Motor”, *IEEE Tran. Energy Convers*., vol. 14, no. 4, Dec 1999, pp. 969-975.

[33] W. Roshen, “Iron loss model for permanent magnet synchronous motors,” IEEE Trans. on Magn., vol. 43, no. 52, August 2007.

[34] F. Deng, “An improved iron loss estimation for permanent magnet brushless machines,” *IEEE Trans. Energy Convers.*, vol. 14, no. 4, pp. 1391–1395, Dec. 1999.

[35] R. Rabinovici, T.J.E. Miller, “Eddy-current losses of surface-mounted permanent magnet motors”, *IEE Proc. Electr. Power Appl.*, Vol 144, No 1, Jan 1997, pp. 61-64.

[36] G. R. Slemon, “Electric Machine Drives”, Addison-Wesley series in electrical engineering., 1992

[37] Z. Gmyrek, A. Boglietti, and A. Cavagnino, “Estimation of Iron Losses in Induction Motors: Calculation Method, Results, and Analysis,” *IEEE Trans. Ind. Electron.*, vol. 57, no. 1, pp. 161 –171, Jan. 2010.

[38] A. Boglietti, P. Ferraris, M. Lazzari, and M. Pastorelli, “Influence of the inverter characteristics on the iron losses in PWM inverter-fed induction motors,” *IEEE Trans. Ind. Appl.*, vol. 32, no. 5, pp. 1190 –1194, Oct. 1996.

[39] T.L. Mthombeni and P. Pillay, “Lamination core losses in motors with nonsinusoidal excitation with particular reference to PWM and SRM excitation waveforms,” *IEEE Trans. Energy Convers.*, vol. 20, no. 4, pp. 836–843, Dec. 2005.

[40] L.T. Mthombeni, and P. Pillay, “Core losses in motor laminations exposed to high-frequency or nonsinusoidal excitation,” *IEEE Trans. Ind. Appl.*, vol. 40, no. 5, pp. 1325–1332, Oct. 2004.

[41] J. Holtz, “Pulsewidth Modulation for Electronic Power Conversion.” *Proc. IEEE 82*, no. 8 (August 1994): 1194 – 1214.

[42] K. Yamazaki and A. Abe, “Loss Investigation of Interior Permanent-Magnet Motors Considering Carrier Harmonics and Magnet Eddy Currents,” *IEEE Trans. Ind. Appl.*, vol. 45, no. 2, pp. 659 –665, Apr. 2009.

[43] P. Dahono, Y. Sato, T. Kataoka, “Analysis of Conduction Losses in Inverters,” *IEE Proc. Elec. Pow. Appl*., vol. 142, no. 4, pp. 225-232, July 1995.

[44] L. Mestha, and P. Evans, “Analysis of On-State Losses in PWM Converters,” *IEE Proceed. Part B*, vol. 136, no. 4, pp. 189-195, 1989.

[45] F. Casanellas, “Losses in PWM Inverters Using IGBTs,” *IEE Proc. Elec. Pow. Appl*., vol. 141, no. 5, pp. 235-239, Sep. 1994.

[46] L. Mestha, and P. Evans, “Optimization of Losses on PWM Converters,” *Conf. Proc. PE-VSD.*, pp. 394-397, 1988.

[47] F. Blaabjerg, U. Jaeger, S. Munk-Nielsen, and J. Pedersen, “Power Losses in PWM-VSI Inverter using NPT or PT IGBT Devices,” *IEEE Trans. Power Electron*., vol. 10, no. 3, pp. 358-367, May 1995.

[48] J. Kolar, H. Ertl, and F. Zach, “Influence of the Modulation Method on the Conduction and Switching Losses of a PWM Converter System,” *IEEE Trans. Ind. Appl*., vol. 27, no. 6, pp. 1063-1075, Nov./Dec. 1991.

[49] R. H. Park, "Two-Reaction Theory of Synchronous Machines," *AIEE Transactions*, Vol. 48, pp. 716-730, July 1929

[50] Hasse K “On the dynamic behavior of induction machines driven by variable frequency and voltage sources” , ETZ Arch. Bd. 89,. H. 4, 1968, pp. 77-81.

[51] Blaschke, F. "The Principle of Field Orientation as Applied to the New TransvectorClosed Loop Control for Rotating Machines", Siemens Rev., , Vol. 39, No. 5, pp. 217-220, *1972*

[52] P. Pillay and R. Krishnan, “Modeling, analysis and simulation of a high performance, vector controlled, permanent magnet s*ynchronous motor drive,” in Proc. IEEE IAS Ann. Mtg., 1987.*

[53] F. Rodriguez, and A. Emadi, “A Novel Digital Control Technique for Brushless DC Motor Drives: Steady State and Dynamics,” *32nd IEEE Annual Conference on Industrial Electronics, IECON 2006*, pp. 1545 –1550, 2006.

[54] P.L. Chapman, S.D. Sudhoff, and C.A. Whitcomb, “Multiple Reference Frame Analysis of Non-sinusoidal Brushless DC Drives.” *IEEE Trans. Energy Convers.*, vol. 14, no. 3 (September 1999): 440 –446.

[55] Lei Hao, H.A. Toliyat, "BLDC Motor Full-speed Operation Using Hybrid Sliding Mode Observer." *18th Annual IEEE Applied Power Electronics Conference and Exposition, APEC '03,* 2003, vol. 1, pp. 286 –293, 2003.

[56] J. Holtz, and L. Springob, "Identification and Compensation of Torque Ripple in High-precision Permanent Magnet Motor Drives." *IEEE Trans. Ind. Electron.*, vol. 43, no. 2 (April 1996): 309–320.

[57] L. Springob, and J. Holtz. "High-bandwidth Current Control for Torque-ripple Compensation in PM Synchronous Machines." *IEEE Trans. Ind. Electron.*, vol. 45, no. 5 (October 1998): 713–721.

[58] C. De Angelo, G. Bossio, J. Solsona, G.O. Garcia, and M.I. Valla, "Mechanical Sensorless Speed Control of Permanent-magnet AC Motors Driving an Unknown Load." *IEEE Trans. Ind. Electron.*, vol. 53, no. 2 (April 2006): 406 – 414.

[59] D. Grenier, R. Mende, and J.P. Louis, "Comparison of several control strategies for DC Brushless Drives", *IEEE IECON*, 1994. vol.1, pp-26-31

[60] A. Oliveira, J. Monteiro, M. Aguiar, D. Gonzaga, "Extended DQ transformation for vectorial control applications of Non-Sinusoidal Permanent Magnet Synchronous Machines", *IEEE Power Electron. Spec. Conf*, 2005, pp 1807-1812.

[61] P. Kshirsagar, and R. Krishnan, "Efficiency Improvement Evaluation of Non-sinusoidal back-EMF PMSM Machines Using Field Oriented Current Harmonic Injection Strategy." *IEEE Energy Conversion Congress and Exposition (ECCE),* 2010, pp. 471 –478, 2010.

[62] J. Holtz, "The Representation of AC Machine Dynamics by Complex Signal Flow Graphs", *IEEE Trans onInd Electron*. Vol. 42. No. 3, June 1995

[63] P.H. Nayak, and R.G. Hoft, "Optimizing the PWM Waveform of a Thyristor Inverter." *IEEE Trans. Ind. Appl.*, no. 5 (October 1975), pp. 526–530.

[64] P.N. Enjeti, P.D. Ziogas, and J.F. Lindsay, "Programmed PWM Techniques to Eliminate Harmonics - A Critical Evaluation." *IEEE Industry Applications Society Annu. Mtg., 1988, Conference Record of the 1988*, vol.1, pp. 418 – 430, 1988.

[65] B.D. Bedford, R.G. Hoft, *Principles of Inverter Circuits*, J Wiley, New York , 1964.

[66] G.S. Buja, and G.B. Indri, "Optimal Pulsewidth Modulation for Feeding AC Motors." *IEEE Trans. Ind. Appl.*, vol. IA-13, no. 1 (January 1977): 38 –44.

[67] J. Holtz, and B. Beyer,"OptimalPulsewidth Modulation for AC Servos and Low-cost Industrial Drives." *IEEE Trans. Ind. Appl.*, vol. 30, no. 4 (August 1994): 1039 –1047.

[68] B. Ozpineci, L.M. Tolbert, S.K. Islam, M. Chintavali, "Comparison of Wide Bandgap semiconductors for power applications", [Online]http://power.eecs.utk.edu/pubs/epe2003_wide_bandgap.pdf

[69] P. Roussel, "SiC Power Devices – if we only had a switch…,"Vol. 2, Issue 5, Semiconductor Today – Compounds and Advanced Silicon, June 2007.

[70] G.R. Slemon and X. Liu, "Core losses in permanent magnet motors," *IEEE Trans. Magnetics*, vol. 26, no. 5, pp. 1653-1655, Sept.1990.

[71] M. Melfi, S. Evon, and R. McElveen, "Induction versus permanent magnet motors," *IEEE Ind. Appl. Mag.*, vol. 15, no. 6, pp. 28 –35, Dec. 2009.

[72] R. Krishnan, *Permanent Magnet Synchronous and Brushless DC Motor Drives*, CRC Press, 2010.

[73] E. Dlala and A. Arkkio, "A General Model for Investigating the Effects of the Frequency Converter on the Magnetic Iron Losses of a Squirrel-Cage Induction Motor," *Magnetics, IEEE Transactions on*, vol. 45, no. 9, pp. 3303 – 3315, Sep. 2009.

[74] T. Jahns, G. Kliman, and T. Neumann, "Interior PM Synchronous Motors for Adjustable Speed Drives", IEEE Trans. on Ind. Appl., vol. IA-22, July/Aug 1986, pp. 738-747.

[75] J. Itoh, T. Ogura, "Evaluation of Total Loss for an Inverter and Motor by Applying Modulation Strategies", *EPE-PEMC* 2010, S12-21 – S12-28

[76] D. Sato, J. Itoh "Total Loss Comparison of Inverter Circuit Topologies with Interior Permanent Magnet Synchronous Motor Drive System", *ECCE* 2013, pp 57-543.

[77] S. C. Peak and A. B. Plunkett, "Transistorized PWM inverter induction motor drive system," in Proc. IEEE IAS Annul. Meeting, 1982, pp. 892-898.

[78] A. Schonung and H. Stemmler, "Static Frequency Changers with Subharmonic Control in Conjunction with Reversible Variable Speed AC Drives", Brown Boveri Rev., 1964, pp. 555-557.

[79] .R. Bowes, and A. Midoun, "New PWM switching strategy for microprocessor controlled inverter drives," *IEE Proceedings Electric Power Applications*, B, vol. 133, no. 4, pp. 237–254, 2008.

[80] J. A. Houldsworth and D. A. Grant, "The use of harmonic distortion to increase the output voltage of a three-phase PWM inverter," IEEE Trans.Ind. Appl., vol. IA-20, no. 5, pp. 1224–1228, Sep. 1984.

[81] D. Holmes, “The Significance of Zero Space Vector Placement for Carrier-Based PWM Schemes,” *IEEE Trans. Ind. Appl.*, vol. 32, no. 5, pp. 1122-1129, Sep./Oct. 1996.

[82] S.R. Bowes, and D. Holliday, “Optimal regular-sampled PWM inverter control techniques,” *IEEE Trans. Ind. Electron.*, vol. 54, no. 3, pp. 1547–1559, 2007.

[83] A. Busse and J. Holtz, ‘‘Multiloop control of a unity power factor fast-switching AC to DC converter,’’ in Conf. Rec. IEEE Power Electronics Specialists Conf. (PESC’82), 1982, pp. 171–179.

[84] G. Pfaff, A. Weschta, and A. Wick, ‘‘Design and experimental results of a brushless AC servo drive,’’ Conf. Rec. IEEE/IAS Annu. Meeting, 1982, pp. 692–697.

[85] J. Holtz, and B. Beyer,“OptimalPulsewidth Modulation for AC Servos and Low-cost Industrial Drives.” *IEEE Trans. Ind. Appl.*, vol. 30, no. 4 (August 1994): 1039 –1047.

[86] G. Narayanan, and V. Ranganathan, “Synchronized PWM Strategies Based on Space Vector Approach. Part I: Principles of Waveform Generation,” *IEE Proc. Elec. Pow. Appl.*, vol. 146, no. 3, pp. 267-275, May 1999.

[87] G. Narayanan, and V. Ranganathan, “Synchronized PWM Strategies Based on Space Vector Approach. Part II: Performance Assessment and Application to V-f Drives,” *IEE Proc. Elec. Pow. Appl.*, vol. 146, no. 3, pp. 276-281, May 1999.

[88] G. Narayanan, and V. Ranganathan, “Two Novel Synchronized Bus-Clamping PWM Strategies Based on Space Vector Approach for High Power Drives,” *IEEE Trans. Power Electron.*, vol. 17, no. 1, pp. 84-93, Jan. 2002.

[89] H. Krishnamurthy, G. Narayanan, R. Ayyanar, and V. Ranganathan, “Design of Space-Vector-Based Hybrid PWM Techniques for Reduced Current Ripple,” *Conf. Proceed. IEEE APEC’03*, vol. 1, pp. 583-588, 2003.

[90] G. Narayanan, and V. Ranganathan, “Extension of Operation of Space Vector PWM Strategies with Low Switching Frequencies using Different Overmodulation Algorithms,” *IEEE Trans. Power. Electron.*, vol. 17, no. 5, pp. 788-798, Sep. 2002.

[91] V. Blasko, “Analysis of a Hybrid PWM Based on Modified Space-Vector and Triangle-Comparison Methods,” *IEEE Trans. Ind. Appl.*, vol. 33, no. 3, pp. 756-764, May/June 1997.

[92] A. Hava, R. Kerkman, and T. Lipo, “A High-Performance Generalized Discontinuous PWM Algorithm,” *IEEE Trans. Ind. Appl.*, vol. 34, no. 5, pp. 1059-1071, Sep./Oct. 1998.

[93] J. Ojo, “The generalized discontinuous PWM scheme for three-phase voltage source inverters”, *Ind Electron IEEE Trans on*. Vol. 51. No. 6, Dec 2004, pp-1280-1289

[94] D. Chung, and S. Sul, “Minimum-Loss Strategy for Three-Phase PWM Rectifier,” *IEEE Trans. Ind. Electron.*, vol. 46, no. 3, pp. 517-526, June 1999.

[95] D. Zhao, V. S. S. P. K. Hari, G. Narayanan, R. Ayyanar, “Space-Vector-Based Hybrid Pulsewidth Modulation Techniques for Reduced Harmonic Distortion and Switching Loss”, IEEE Trans on Power Electro., Vol. 25, No. 3, Mar 2010, pp – 760-774

[96] J. Holtz and S. Stadtfeld, ‘‘A predictive controller for the stator current vector of AC machines fed from a switched voltage source,’’ in Proc. Int. Power Electronics Conf. (IPEC), Tokyo, 1983, pp. 1665–1675.

[97] T. Geyer and G. Papafotiou, ‘‘Model predictive control in power electronics: A hybrid systems approach,’’ in Proc. 4th IEEE Conf. Decision and Control and European Control Conf., Seville, Spain, 2005, pp. 5606–5611.

[98] Vazquez, S., Leon, J.I. ; Franquelo, L.G. ; Rodriguez, J. ; Young, H.A. ; Marquez, A. ; Zanchetta, P., “Model Predictive Control: A Review of Its Applications in Power Electronics”, *IEEE, Industrial Electronics Magazine* Vol:8, Issue:1, Mar 2014, pp 16-31.

[99] F.G. Turnbull, “Selected harmonic reduction in static dc-ac inverters,” *IEEE Trans. Commun. Technol.*, vol. CE-83, pp. 374–378, Jul. 1964

[100] B. Mokrytzki, “Pulse Width Modulated Inverters for AC Motor Drives.” *IEEE Trans. Ind. and Gen. Appl.*, Transactions On IGA-3, no. 6 (November 1967): 493 –503.

[101] H.S. Patel, and R.G. Hoft, “Generalized Techniques of Harmonic Elimination and Voltage Control in Thyristor Inverters: Part I–Harmonic Elimination.” *IEEE Trans. Ind. Appl.*, IA 9, no. 3 (May 1973), pp. 310 –317.

[102] H.S. Patel, and R.G. Hoft, “Generalized Techniques of Harmonic Elimination and Voltage Control in Thyristor Inverters: Part II — Voltage Control Techniques.” *IEEE Trans. Ind. Appl.*, IA-10, no. 5 (September 1974), pp. 666 – 673.

[103] P.N. Enjeti, P.D. Ziogas, and J.F. Lindsay, “Programmed PWM Techniques to Eliminate Harmonics - A Critical Evaluation.” *IEEE Industry Applications Society Annu. Mtg., 1988, Conference Record of the 1988*, vol.1, pp. 418 – 430, 1988.

[104] T. Kato, “Sequential Homotopy-based Computation of Multiple Solutions for Selected Harmonic Elimination in PWM Inverters.” *IEEE Trans. Circuits Syst. I, Fundam. Theory Appl.*, 46, no. 5 (2002), pp.586–593.

[105] F.C. Zach, and H. Ertl, “Efficiency Optimal Control for AC Drives with PWM Inverters.” *IEEE Trans. Ind. Appl.*, IA-21, no. 4 (July 1985), pp. 987 –1000.

[106] V.G. Agelidis, A. Balouktsis, and I. Balouktsis, “On Applying a Minimization Technique to the Harmonic Elimination PWM Control: The Bipolar Waveform.” *IEEE Power Electron. Lett.*, 2, no. 2 (2004), pp. 41–44.

[107] M.G. HosseiniAghdam, S.H. Fathi, and G.B. Gharehpetian, “Comparison of OMTHD and OHSW Harmonic Optimization Techniques in Multi-Level Inverter with Non-Equal DC Sources.” *International Journal of Electrical and Electronics Engineering*, vol. 4, no. 2 (2009), pp. 72–79.

[108] A.K. Al-Othman, N.A. Ahmed, A.M. Al-Kandari, and H. K. Ebraheem, “Selective Harmonic Elimination of PWM AC/AC Voltage Controller Using Hybrid RGA-PS Approach.” *International Journal of Electrical, Computer and Systems Engineering*, vol. 1, no. 4 (2007).

[109] D.A. Deib, and H.W. Hill Jr., “A Flexible Method of Minimizing Harmonic Distortion in Force-commutated Converters.” *Applied Power Electronics Conference and Exposition, 1992. APEC’92. Conference Proceedings 1992, Seventh Annual*, pp. 844–851, 2002.

[110] D.A. Deib, and H.W. Hill Jr., “The Advantages of Harmonic-distortion Minimization over Traditional Harmonic-elimination Techniques.” *Power Electronics Specialists Conference, 1993. PESC’93 Record., 24th Annual IEEE*, pp. 1048–1054, 2002.

[111] Z. Du, L.M. Tolbert, and J. N. Chiasson, “Active Harmonic Elimination for Multilevel Converters.” *IEEE Trans. Power Electron.*, vol 21, no. 2 (2006), pp. 459–469.

[112] J. Sun, S. Beineke, and H. Grotstollen, “Optimal PWM Based on Real-time Solution of Harmonic Elimination Equations.” *IEEE Trans. Power Electron.*, vol. 11, no. 4 (2002), pp. 612–621.

[113] J.R. Wells, B.M. Nee, P.L. Chapman, and P.T. Krein, “Selective Harmonic Control: A General Problem Formulation and Selected Solutions.” *IEEE Trans. Power Electron.*, vol. 20, no. 6 (2005), pp. 1337–1345.

[114] S.R. Bowes and A. Midoun, “Suboptimal switching strategies for microprocessor-controlled PWM inverter drives,” *IEE Proc. Electric Power Applications*, B, vol. 132, no. 3, pp. 133–148, 2008.

[115] J. Holtz and X. Qi, “Optimal Control of Medium-Voltage Drives—An overview,” *IEEE Trans. Ind. Electron.*, vol. 60, no. 22, pp. 5472–5481, Dec 2013.

[116] N. Oikonomou, J. Holtz, “Closed-Loop Control of Medium-Voltage Drives Operated With Synchronous Optimal Pulsewidth Modulation,” *IEEE Trans. Ind. Appl.*, vol. 44, no. 1, pp. 115–123, Jan-Feb 2008.

[117] J. Holtz and N. Oikonomou, “Fast dynamic control of medium voltage drives operating at very low switching frequency—An overview,” *IEEE Trans. Ind. Electron.*, vol. 55, no. 3, pp. 1005–1013, 2008.

[118] J. Holtz, “Power Electronics – A Continuing Challenge”, *IEEE Mag onInd Electron*. Vol. 42. No. 3, pp 6-15, June 2011

[119] J. Sun, and H. Grotstollen, “Optimized Space Vector Modulation and Regular Sampled PWM: A Reexamination,” Conf. Proc. IEEE IAS’96, vol. 2, pp. 956-963, 1996.

[120] S. Bowes, and Y. Lai, “The Relationship Between Space-Vector Modulation and Regular-Sampled PWM,” IEEE Trans. on Ind. Elec., vol. 44, no. 5, pp. 670-679, Oct. 1997.

[121] S.R. Bowes, and A. Midoun, “Microprocessor implementation of new optimal PWM switching strategies,” IEE Proceedings Electric Power Applications, B, vol. 135, no. 5, pp. 269–280, 2002.

[122] J.R. Wells, B.M. Nee, P.L. Chapman, and P.T. Krein, “Selective Harmonic Control: A General Problem Formulation and Selected Solutions.” *IEEE Trans. Power Electron.*, vol. 20, no. 6 (2005), pp. 1337–1345.

[123] M. P. Kazmierkowski and L. Malesani, Current Control Techniques for Three-Phase Voltage-Source PWM Converters: A Survey“, *IEEE Transactions on Industrial Electronics*, Vol. 45,No. 5, Oct. 1998, pp. 691-703.

[124] T. Ohmae, T. Matsuda, K. Kamiyama, and M. Tachikawa, “A Microprocessor-Controlled High-Accuracy Wide-Range Speed Regulator for Motor Drives,” *IEEE Trans. Ind. Electron.*, vol. IE-29, no. 3, pp. 207 –211, Aug. 1982.

[125] Bocker, J, Buchholz, O. “Can oversampling improve the dynamics of PWM controls?”, (ICIT), IEEE International Conference on Industrial Technology, pp 1818 – 1824, Feb. 2013,

[126] F. Briz, M.W. Degner, and R.D. Lorenz, “Analysis and Design of Current Regulators Using Complex Vectors,” *IEEE Trans. Ind. Appl.*, vol. 36, no. 3 (June 2000), pp. 817 –825.

[127] L.Springob, and J. Holtz. “High-bandwidth Current Control for Torque-ripple Compensation in PM Synchronous Machines.” *IEEE Trans. Ind. Electron.*, vol. 45, no. 5 (October 1998): 713–721.

[128] J. Holtz, J. Quan, G. Schmittt, J. Pontt, J. Rodriguez, P. Newman, and H. Miranda, “Design of Fast and Robust Current Regulators for High Power Drives Based on Complex State Variables.” *Industry Applications Conference, 2003. Conf. Rec 38th IAS Annu. Mtg.*, vol.3, pp. 1997 – 2004, 2003

[129] J. Holtz and S. Stadtfeld, ‘‘A predictive controller for the stator current vector of AC machines fed from a switched voltage source,’’ in Proc. Int. Power Electronics Conf. (IPEC), Tokyo, 1983, pp. 1665–1675.

[130] T. Geyer and G. Papafotiou, ‘‘Model predictive control in power electronics: A hybrid systems approach,’’ in Proc. 4th IEEE Conf. Decision and Control and European Control Conf., Seville, Spain, 2005, pp. 5606–5611.

[131] R. Krishnan, *Permanent Magnet Synchronous and Brushless DC Motor Drives*, CRC Press, 2010.

[132] T. Sebastian, G. R. Slemon, "Operating Limits of Inverter-Driven Permanent Magnet Motor Drives", *IEEE Trans. Ind. Appl.*, Vol. Ia-23, No. 2, March/April 1987.

[133] R. Krishnan, *Electric Motor and Drives- Modeling Analysis and Control*, Prentice Hall Inc., 2001.

[134] R. S. Colby and D. W. Novotny, "Efficient operation of surface mounted PM synchronous motors," IEEE Trans. Ind. Appt., vol. IA-23, no. 6, pp. 1048-1054, Nov./Dec. 1987.

[135] J-S Yim,S K Sul, B H Bae, N R. Patel, S Hiti, "Modified Current Control Schemes for High-Performance Permanent-Magnet AC Drives With Low Sampling to Operating Frequency Ratio", *IEEE Trans. Ind. Appl.*, vol. 45, no. 2 pp.763 –771, Apr 2009.

[136] F.C. Zach, and H. Ertl, "Efficiency Optimal Control for AC Drives with PWM Inverters." *IEEE Trans. Ind. Appl.*, IA-21, no. 4 (July 1985), pp. 987 –1000.

[137] D. Murphy and F.G. Turnbull, *Power Electronic Control of AC Motors*, Pergamon Press, Oxford, 1988

[138] C.Y.Leong, N-A. Parker-Allotey, R.A. McMahon, "Loss Comparison between an SPWM and Harmonic Elimination Excited Small, (<1kW) Induction Motor Drive using Pspice Simulation and Calorimetry" *IEEE IAS Conf, 2008*, pp 1-6.

[139] R. Carlson, M. Lajoie-Mazenc, and J. Fagundes, "Analysis of torque ripple due to phase commutation in brushless DC machines," *IEEE Trans. Ind. Appl*., vol. 28, no. 3, pp. 632-638, 1992.

[140] C. Berendsen, G. Champenois, and A. Bolopion, "Commutation strategies for brushless DC motors: Influence on instant torque," IEEE Trans. on Power Electron.. vol. 8, no. 2 , pp. 231-236, Apr. 1993.

[141] D. Jouve and D. Bui, "Torque ripple compensation in DSP based brushless servo drive," *Proc. PCIM, Intelligent Motion*, 1993, pp. 28-37.

[142] J.C. Moreira, "Indirect Sensing for Rotor Flux Position of Permanent Magnet AC Motors Operating over a Wide Speed Range," *IEEE Trans. Ind. Appl.*, vol. 32, no. 6 (December 1996), pp. 1394 –1401.

[143] Su Gui-Jia, and J.W. McKeever. "Low-cost Sensorless Control of Brushless DC Motors with Improved Speed Range." *IEEE Trans. Power Electron.*, vol. 19, no. 2 (March 2004), pp. 296 – 302.

[144] J.X. Shen, Z.Q. Zhu, and D. Howe. "Sensorless Flux-weakening Control of Permanent-magnet Brushless Machines Using Third Harmonic Back EMF." *IEEE Trans. Ind. Appl*., vol. 40, no. 6 (December 2004), pp.1629 – 1636.

[145] J. Holtz, "Sensorless drives with PM synchronous machines" *ECCE Tutorial* Sept 2009

[146] R. Wu and G.R. Slemon, "A Permanent Magnet Motor Drive without a Shaft Sensor," *IEEE Trans. Ind. Appl*., vol. 27, no. 5, pp. 1005-1011, 1991.

[147] R.B. Sepe and J.H. Lang, "Real-Time Observer-Based (Adaptive) Control of a PMSM without Mechanical Sensors," *IEEE Trans. Ind. Appl*., vol. 28, no. 6, pp. 1345-1352, 1992.

[148] K.R. Shouse and D.G. Taylor, "Sensorless Velocity Control of Permanent-Magnet Synchronous Motors," *IEEE Trans. Control Syst. Technol.*, vol. 6, no. 3, pp. 313-324, 1998.

[149] S. Bolognani, R. Oboe, and M. Zigliotto, "Sensorless Full-Digital PMSM Drive with EKF Estimation of Speed and Rotor Position," *IEEE Trans. Ind. Electron.*, vol. 46, no. 1, pp. 184-191, 1999

[150] J.–S. Kim and S.–K. Sul, "High Performance PMSM Drives Without Rotational Position Sensors using Reduced Order Observer," *Conf. Rec. IEEE 30th IAS Annu. Mtg*., vol. 1, pp. 75-82, 1995.

[151] J.–S. Kim and S.–K. Sul, "New Approach for High-Performance PMSM Drives without Rotational Position Sensors," *IEEE Trans. Power Electron*., vol. 12, no. 5, pp. 904-911, 1997.

[152] Y.–C. Son, B.–H. Bae, and S.–K. Sul, "Sensorless Operation of Permanent Magnet Motor using Direct Voltage Sensing Circuit," *Conf. Rec. IEEE 37th IAS Ann. Mtg.*, vol. 3, pp. 1674-1678, 2002.

[153] R.D. Lorenz and K.W. Van Patten, "High-Resolution Velocity Estimation for All-Digital, AC Servo Drives," *IEEE Trans. Ind. Appl.*, vol. 27, no. 4, pp. 701-705, 1991.

[154] P. Kshirsagar, R.P. Burgos, A. Lidozzi, Jihoon Jang, F. Wang, D. Boroyevich, and Seung-Ki Sul, "Implementation and Sensorless Vector-Control Design and Tuning Strategy for SMPM Machines in Fan-Type Applications." *IEEE Industry Appln, Power Electron. Joint Special Issue, Nov-Dec 2012*

Chapter 3 High Efficiency Current Excitation Strategy for Variable Speed Non-Sinusoidal Back EMF Machines

3.1. Abstract

Opportunities for energy efficiency improvements in motor drives remain a forefront topic of interest in recent times due to their extensive use and applications. The approach considered in this work is to evaluate various stator current excitation strategies and their impact on efficiency of permanent magnet brushless dc (PMBDC) machines. Such machines have non-sinusoidal back EMF and the influence of sine, square and non-sinusoidal harmonic current on their efficiencies is investigated. To facilitate such a study, analytical expressions for generalized back EMF of all the three excitation schemes have been derived to highlight their influence on torque ripple and motor harmonic losses thus leading to efficiency evaluation. An analytical approach on estimation of iron losses under loaded operation has been elaborated to highlight the impact of stator current harmonics on efficiency of the motor. Analytical as well as experimental results show that it is advantageous to use non-sinusoidal harmonic injection (NSHI) scheme in the speed range until the sum of drive conduction and stator resistive losses exceeds iron losses of the machine. When iron losses become dominant, the algorithm is modified to sinusoidal current control thus maintaining higher efficiency operation. To realize the hybrid current injection strategy, a field oriented rotor position sensorless control has been implemented.

3.2. Introduction

There are three stator current excitation waveforms of permanent magnet brushless DC motors PMBDCM reported in the literature and they are: (a) square wave, (b) sine wave, and (c) mix of sine-harmonic currents. The mix of sine-harmonic current excitation is referred as non-sinusoidal harmonic injection (NSHI) method in this work. An overview of the present work on these current waveforms from the perspective of PMBDC efficiency improvement is provided.

3.2.1. Square or rectangular wave current excitation

The PMBDCM can provide up to 15 percent higher torque than sinusoidal motors for the same stator resistive losses [1]. These motors are mainly excited by square wave current waveforms. The square wave currents in three phase AC motors have been studied since the advent of thyristor based inverters [2]. The inverter is commutated such that the semiconductor devices are on for 120 degrees or 180 degrees during a fundamental cycle which results in rectangular current waveforms, usually referred to as square wave currents in literature [3]. The magnitude of the square wave currents are synthesized by hysteresis or PWM control while their time durations are controlled using rotor position hall effect sensors [4]. Analysis of the square current waveforms on permanent magnet brushless DC motors has been reported in [5-7]. In [6], the performance limitation of PMBDC motor operating at low and high motor speeds considering square wave currents was shown. The main issues arising from such current waveforms are the harmonic torque ripple and the associated motor harmonic losses. For fan type of loads, torque ripple may not be of a major concern, however for higher efficiency operation, the motor harmonic losses are not desirable.

The sinusoidal current waveform excitation is predominantly applied in case of permanent magnet motors with sinusoidal back EMF waveforms [8]. In [9] and [10], it is shown that, for the same average torque, sinusoidal motors offer higher efficiency than brushless DC motors. The influence of sine and square wave excitation on efficiency of concentrated winding PMBDC motors has been investigated in [11] with main focus on flux weakening operating regimes. It is shown that square wave currents can generate twice the core losses as sinusoidal currents.

In [12], the total system efficiency of PMBDC and PMSM motors was compared considering sinusoidal and square wave excitation. It was concluded that sinusoidal currents in PMBDC motor drives resulted in lower system efficiency than square wave currents. However in the study, the switching devices in PMBDC inverter were clamped to DC link for certain time interval of the fundamental cycle while in case of the PMSM inverter they were not. Consequently, the PMBDC inverter operated at lower switching frequency than PMSM inverter. Therefore the total efficiency of PMBDC drive system was better. If the PMSM inverter was operated considering discontinuous PWM as discussed in [32], the conclusions could have be different. Hence this aspect needs further evaluation.

3.2.2. Sinusoidal current excitation

The sinusoidal current waveforms generate higher torque ripple than square wave currents in trapezoidal back EMF machines [1] and [13]. This is because the fundamental component of the current interacts with the fifth and seventh harmonic component of the back EMF to generate sixth harmonic pulsating torque ripple. The analysis can be extended to higher ordered harmonics and is discussed in [6]. Therefore, the sinusoidal current excitation in PMBDC machines may yield better efficiency but may not be suitable for applications requiring lower torque ripple.

3.2.3. Non-sinusoidal current excitation

Non-sinusoidal excitation is designed based on the back EMF harmonics in PMBDCM to meet certain objective functions such as: (a) higher average torque, (b) lower torque ripple or (c) higher motor efficiency [14-23]. In [14-18] an algorithm based on back EMF harmonics and in the form of look-up table was developed to inject non-sinusoidal currents in PMBDCM to minimize torque ripple and stator resistive losses thus claiming maximum efficiency in the given speed range. With a similar objective, references[19-23] obtained various solutions for currents that would improve efficiency in the machine. These references compared the efficiency improvement with respect to square wave excitation strategy.

The references [14-23] mainly focused on minimizing the torque ripple and simultaneously achieving higher motor efficiency through stator resistive loss reduction. In references [15-23], sinusoidal current waveforms for reducing stator resistive losses were not discussed. Also, a collective approach for PMBDCMs considering different back EMF waveforms and evaluating applicability of sinusoidal vs. non-sinusoidal currents for efficiency improvement has not been considered. Most importantly, the above references did not incorporate the influence of non-sinusoidal currents on the motor’s core losses. It is known that machines with higher harmonics in back EMF tend to have higher core losses [1]. In the case of variable speed applications it is desirable to maintain higher efficiency over the entire operating speed-torque envelope. Hence the influence of non-sinusoidal currents on both stator resistive as well as core losses of the machine must be addressed.

Based on the above discussion, following points highlight the topics that need to be further explored:

1. PMBDC machines have back-EMF voltage waveforms that can vary anywhere from trapezoidal to sinusoidal. To cover wide range in practice, a generalized analysis that can show the influence of higher harmonics in back-EMF and stator current excitation waveform on the torque ripple and motor harmonic losses is essential.
2. The present literature does not discuss the influence of non-sinusoidal currents on core losses of PMBDCM. Although injection of harmonics in the stator flux minimizes the torque ripple and stator resistive losses, they increase the stator core losses. Low cost and low horsepower machines can have core losses as high as stator resistive losses [1]. These losses are higher at higher speeds of operation and increase in proportion to square of the harmonic frequency. Core loss evaluation for various back EMF machines excited by non-sinusoidal currents has yet to appear.

Accordingly, the research is organized as follows:

Section 3.3 contains the analytical expressions for the three stator excitation schemes as a function of generalized back EMF characteristics to demonstrate that non-sinusoidal current injection scheme has the lowest torque ripple, higher power conversion ratio and lowest stator resistive losses and inverter conduction losses.

Section 3.4 gives a comprehensive analytical approach to estimate qualitative and quantitative core losses in the motor under loaded condition for various stator current excitation schemes showing that sinusoidal current injection yields lowest core losses.

Section 3.5 has the closed form solution for non-sinusoidal currents and corresponding controller implementation yields better tracking performance over conventional approaches.

Section 3.6 deals with efficiency and loss comparisons of sine, square and sine-harmonic current control made on two BLDC machines at various speeds validates the trade-off highlighted using analytical loss estimation methods. The proposed hybrid approach of sine with harmonics injection for higher efficiency operation in entire speed range for variable speed drives applications is also included here.

3.3. Generalization of back EMF in non-sinusoidal machines

For deriving the generalized back EMF certain assumptions on the stator flux density are made relative to the motion of the rotor. They are:

a) As the magnet rotates the flux density in a stator tooth at the leading edge of the magnet rise linearly from zero to a maximum and then remain essentially constant.

b) At the lagging edge of the magnet, the tooth flux drops from maximum to zero in the same pattern. The rise or fall time of the tooth flux density is assumed to be the time interval for the magnet edge to traverse one tooth width. The same assumption is then extended to back EMF waveform which is essentially proportional to the voltage induced due to the rate of change of flux in the stator tooth.

Irrespective of the type of winding (distributed, concentric, fractional or alternate teeth wound) and type of rotor (surface mount or interior type), the back EMF of brushless DC machine is typically non-sinusoidal. Generalized phase to neutral back EMF expression for three phase non-sinusoidal PM machine is described by (3.1) [1] and is shown in Figure 3.1 (a).

$$E_{an} = \frac{4}{\pi} E_m \begin{Bmatrix} a_1 sin(\theta_r) + a_3 sin(3\theta_r) + a_5 sin(5\theta_r) + a_7 sin(7\theta_r) \\ + a_9 sin(9\theta_r) + a_{11} sin(11\theta_r) + a_{13} sin(13\theta_r) + \dots \end{Bmatrix}$$

$$a_1 = \frac{sin(F)}{F}, a_3 = \frac{sin(3F)}{3^2 F}, a_5 = \frac{sin(5F)}{5^2 F} \dots \tag{3.1}$$

$$E_m = \omega_r \lambda_m, F = \omega_r t_p$$

where, 'F' is variable that determines the slope of the trapezoidal back EMF waveform to reach its peak value E_m in time t_p for phase A, ω_r is the electrical velocity with electrical angle θ_r, and λ_m is the peak flux linkage. Similar expressions for phases *B* and *C* can be obtained by displacing 120° and 240° from phase *A* back EMF, respectively. The variable *'F'* captures the time taken by the tooth flux density to change from zero to its peak value which is proportional to the ratio of width of the stator tooth to rotor velocity.

Consider a floating neutral in a star connected machine where triplen harmonics have no effect. Accordingly, phase induced EMF without triplen harmonics can be written as:

$$E_{ao} = \frac{4}{\pi} E_m \begin{Bmatrix} a_1 sin(\theta_r) + a_5 sin(5\theta_r) + a_7 sin(7\theta_r) \\ + a_{11} sin(11\theta_r) + a_{13} sin(13\theta_r) + \cdots \end{Bmatrix} \tag{3.2}$$

and it is shown in Figure 3.1(b).

Back EMF described in (3.2) has fundamental and odd non-triplen harmonics derived from (3.1). The corresponding 5^{th}, 7^{th} and 11^{th} harmonic amplitude variation as a function of 'F' are shown in Figure 3.1(c). In general, machines tend to be more sinusoidal for larger values of 'F' and more trapezoidal for smaller values of. 'F'.

One of the objective and significant contributions of this research is to analytically show the influence of stator current waveforms on these generalized back EMF waveforms with respect to torque ripple, inverter peak currents and motor harmonic losses as a function of 'F'. Such an analysis enables prudent selection of motor and drive combination.

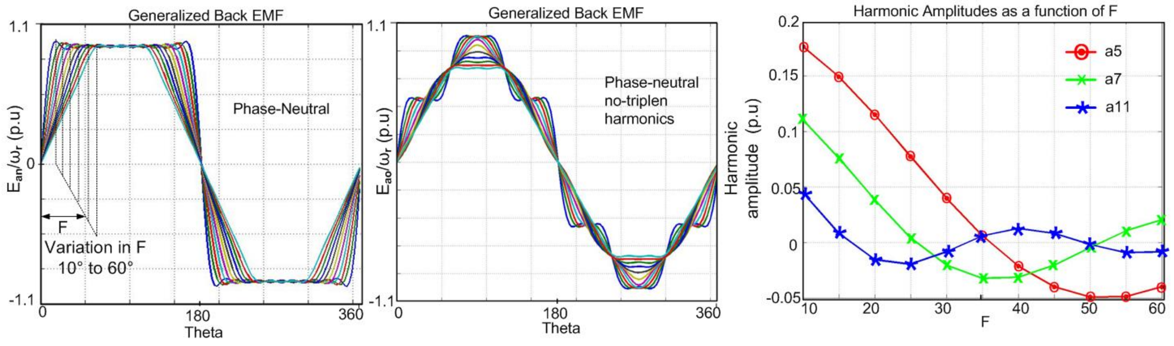

(a) (b) (c)

Figure 3.1 (a) Generalized back EMF variation as a function of F, (b) back EMF with non triplen harmonics, and (c) 5th, 7th and 11th amplitude variation as function of F

3.3.1. RMS Currents

The electromagnetic torque derived from power balance equation of the machine and is given as [1],

$$T_e = \frac{P}{2\omega_r}\left[E_{ao}i_a + E_{bo}i_b + E_{co}i_c\right], \tag{3.3}$$

where P is number of poles and i_a, i_b, i_c are the phase currents for phases A, B and C, respectively. Generalized phase A current that can be injected in the stator can be expressed as

$$i_a(\theta_r+\varphi) = i_m\left(\sum_{k=0}^{\infty} b_p\, sin\big(p(\theta_r+\varphi)\big) + \sum_{k=0}^{\infty} b_q\, sin\big(q(\theta_r+\varphi)\big)\right) \tag{3.4}$$

$$p = 6k+1, q = 6k-1, \qquad k = 0,1,2\ldots, p>0, q>0$$

where i_m is the peak amplitude of phase current, φ is the angle between the injected current and the back EMF, and b_p and b_q are the magnitude of the current harmonics that can be injected by a three phase inverter.

Table3-1. Expressions for Square, Sine and Non-Sinusoidal excitations

Square Wave	***Sine Wave***	***Non-Sinusoidal***
Peak current		
$i_{m\_sq} = \pi^2 F \frac{T_e}{\frac{3}{2}.\frac{P}{2}.16.\lambda_m.a_1.\cos(\varphi)}$	$i_{m\_s} = \pi F \frac{T_e}{\frac{3}{2}.\frac{P}{2}.4.\lambda_m.a_1.\cos(\varphi)}$	$i_{m\_ns} = \pi F \frac{T_e}{\frac{3}{2}.\frac{P}{2}.4.\lambda_m.(a_1^2+a_5^2+a_7^2+\cdots).\cos(\varphi)}$
RMS current		
$i_{rms_{sq}} = \sqrt{\frac{2}{3}}\, i_{m_{sq}}$	$i_{rms_{sin}} = \frac{i_{m_{sin}}}{\sqrt{2}}$	$i_{rms_{ns}} = \frac{i_{m_{ns}}}{\sqrt{2}}\sqrt{(a_1^2+a_5^2+a_7^2+a_{11}^2+\cdots)}$
Instantaneous current		
$i(t) = i_{m\_sq}\left(\sum_{k=0}^{\infty} b_p\, sin\big(p(\theta_r+\varphi)\big) + \sum_{k=0}^{\infty} b_q\, sin\big(q(\theta_r+\varphi)\big)\right)$ $p = 6k+1, q = 6k-1,$ $k = 0,1,2\ldots, p>0, q>0$	$i(t) = i_{m\_s}\cdot a_1 sin(\theta+\varphi)$	$i(t) = i_{m\_sq}\left(\sum_{k=0}^{\infty} a_q\, sin\big(p(\theta_r+\varphi)\big) + \sum_{k=0}^{\infty} a_p\, sin\big(q(\theta_r+\varphi)\big)\right)$ $p = 6k+1, q = 6k-1, k = 0,1,2\ldots, p>0, q>0$

Since the neutral of the machine is floating, these currents cannot interact with the back EMF triplen time harmonics in the machine. For same average torque, it is now possible to express the peak amplitude of the three excitation currents as a function of 'F'. Then using (3.3), and (3.4), the peak, rms, and instantaneous currents are derived and given in Table3-1.

For sine wave currents, it is the fundamental components of back EMF and current that primarily contributes to torque production. For non-sinusoidal current injection scheme, in order to minimize torque ripple the generalized solution is obtained such that $b_1 = a_1$, $b_q = a_p$ and $b_p = a_q$. It is one of the multiple solutions as per the procedure in [14]. A closed form solution for the same is elaborated in section 3.5. The time series solution for non-sinusoidal instantaneous phase A current is shown in Table3-1. Similar expression for currents in phases *B* and *C* can be obtained by displacing the time series solution by 120° and 240° from phase A, respectively. To synthesize the same average torque, NSHI strategy has lowest rms current requirement amongst all the three schemes as the odd non-triplen harmonics also contribute towards torque production. Coefficients for the instantaneous square wave currents in Table3-1are listed in Appendix. It should be noted that although the analysis does not account for influence of armature reaction on the air-gap flux density, the results obtained should still be relevant for preliminary calculations. The analysis presented henceforth is derived from the expressions in Table3-1.

3.3.2. Torque Ripple

The torque ripple cannot be ignored when addressing vibration and acoustic noise issues in compressor and fan type variable speed applications. It should be clarified that only the torque ripple originating from harmonics in the back EMF is considered in this analysis, while the ripple due to slot harmonics which is intrinsic to the machine geometry is not considered.

Figure 3.2(a) shows the average electromagnetic torque produced in PMBDCMs as a function of 'F'. For the case shown in the figure, the desired electromagnetic torque is 1 Nm, in a four pole machine with peak flux linkage λ_m of 0.0495 Vpk/rad/s. The torque is generated by using the instantaneous currents obtained from Table3-1and substituting them in (3.3). The torque ripple can be expressed as

$$T_{e\_ripple} = \frac{T_{e\_max} - T_{e\_min}}{T_{e\_avg}} \tag{3.5}$$

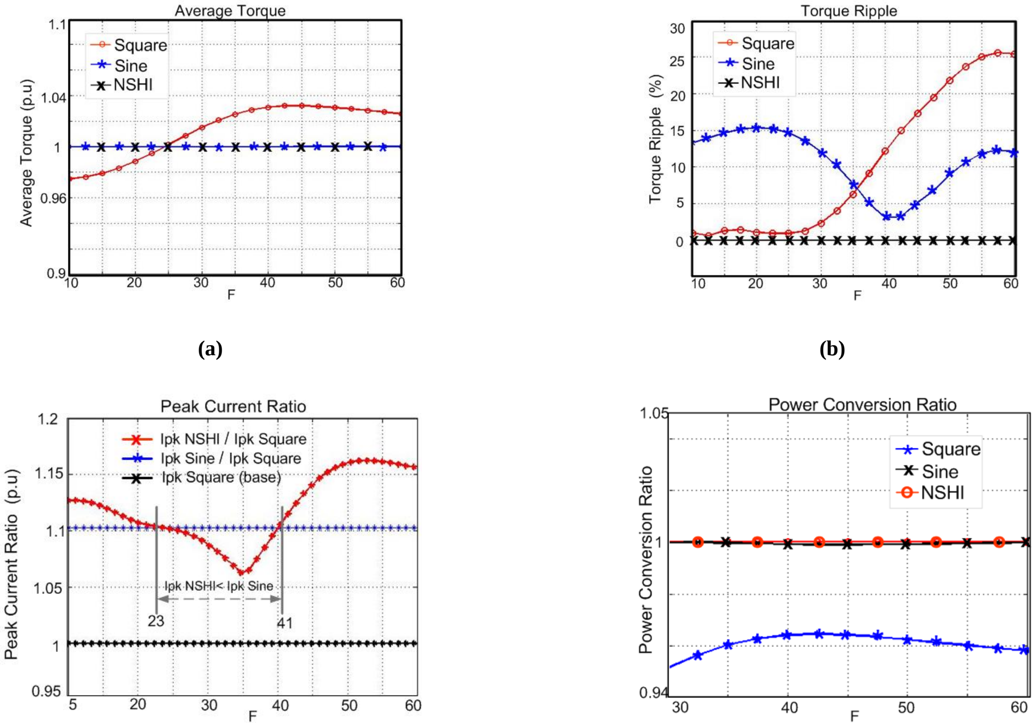

(a) **(b)**

(c) **(d)**

Figure 3.2 Performance comparison of the three injection schemes as a function of variation in F: (a) Average torque, (b) Torque ripple, (c) stator resistive loss ratio, and (d) electro-mechanical power conversion ratio

where, T_{e_max} and T_{e_min} are the maximum and minimum amplitudes of the instantaneous torque with the desired average torque T_{e_avg}. Accordingly, Figure 3.2 (b) shows that for square wave current injection, and 'F' less than 35°, the torque ripple is less than 5%. It increases up to 25% when the back EMF becomes more sinusoidal for larger values of 'F'. In case of square wave currents, the commutation torque ripple due to finite rise time of the currents is neglected. In case of sinusoidal currents, the torque ripple is less than 5% only for the values of 'F' between 35° and 45° where the back EMF is more sinusoidal. Non-sinusoidal excitation (NSHI), on the other hand, maintains the torque ripple below 5% for all the values of 'F' thus proving its superiority over sine and square injection schemes from a torque ripple suppression perspective. It is inferred that injecting appropriate harmonics in the stator effectively generates a magneto-motive force through the three phase windings that reduces the high frequency air-gap flux density variation thereby reducing the torque ripple.

3.3.3. Peak Currents

The semiconductor device rating is dependent on the instantaneous peak and rms currents applied to the motor. These currents also determine the saturation in the stator. Ratios of the instantaneous peak currents of the three current injection schemes are shown in Figure 3.2 (c). It is shown that for ‘F’ between 23° and 41°, NSHI scheme has lower peak current than sinusoidal current injection scheme. Although square wave currents have lowest peak currents for all values of ‘F’, their rms current is highest amongst the three schemes. The higher rms current in square wave currents can be understood by evaluating electromechanical power conversion ratio of the machine due to the three excitation schemes and is explained in following subsection.

3.3.4. Electro-mechanical Power Conversion Ratio

The ratio of active and apparent electromechanical power is defined as electromechanical power conversion ratio. The real and reactive electromechanical power for an arbitrary excitation is given as [18],

$$\begin{bmatrix} P_L \\ Q_L \end{bmatrix} = \begin{bmatrix} i_{qs}^s & i_{ds}^s \\ -i_{ds}^s & i_{qs}^s \end{bmatrix} \begin{bmatrix} e_{qs}^s \\ e_{ds}^s \end{bmatrix} \tag{3.6}$$

where, $i_{dqs}^s$and e_{dqs}^s are the machine currents and back EMF voltages in two-phase stationary reference frame while P_L and Q_L are the active and reactive electromechanical power, respectively. Then the power conversion ratio *pr* of the machine can be defined as:

$$pr = \frac{P_L}{\sqrt{P_L^2 + Q_L^2}} \tag{3.7}$$

For maximum utilization of the machine, *pr* should be unity implying that the reactive power Q_L must me zero. Figure 3.2 (d) shows the power conversion ratio of the machine due to the three stator excitation schemes. Square wave has lowest conversion ratio (0.95) in comparison with sine and NSHI schemes which operate at unity. The square wave current waveform has higher odd non-triplen harmonics that may result in higher torque in BLDC motors. However due to its low power conversion ratio, it requires higher rms currents for the same average torque production in comparison to sine and NSHI schemes. Higher rms current implies higher stator resistive losses in the motor and conduction losses in the semiconductor devices. Influence of excitation scheme on motor harmonic losses is elaborated in the next section.

3.3.5. Stator resistive losses

To improve the efficiency of motor, it is critical to evaluate the various losses created by stator currents in the drive system. In this aspect, the losses in the machine are stator resistive and core losses depending on power level and operating speed while in the inverter they are mainly conduction and switching losses. This section will highlight analytical calculation of motor harmonic losses based on the expressions in Table3-1.

The stator resistive loss analysis does not account for the space harmonics due to windings and influence of armature reaction on stator currents, the qualitative performance results derived should still be applicable for initial designs. Comparison of stator resistive losses between square ($P_{cu\text{-}square}$), sine ($P_{cu\text{-}sine}$) and NSHI ($P_{cu\text{-}NSHI}$) schemes can be obtained by taking ratio of the square of rms currents required for the same average electromagnetic torque.

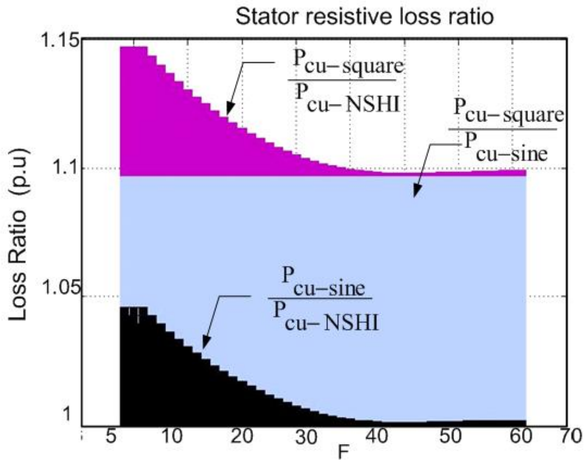

Figure 3.3. Stator resistive loss ratioof the three current excitation schemes as a function of *F*

The stator resistive loss ratio is obtained by taking ratio of the square of rms currents from Table3-1. Figure 3.3 shows the ratio of stator resistive losses for all the three injection schemes. Both sine and non-sinusoidal excitation have at least 9% lower loss than square wave excitation. It is shown that when the value of '*F*' is less than 30°, the non-sinusoidal harmonic injection scheme has even lower resistive losses than the sinusoidal injection scheme. This is primarily due to the lower rms current requirements for the same average torque. From the same result, it is inferred that the inverter conduction losses will also be reduced in proportion to the reduction in stator resistive losses. Thus minimizing torque ripple also minimizes motor resistive losses if NSHI scheme is used. It should be noted that the torque ripple is minimized by introducing higher order current harmonics into the stator core. Thus understanding the influence of such a scheme on core losses is vital from an efficiency perspective.

3.4. Influence of excitation on stator core losses

The core losses are a function of electrical speed and assuming a fan's motor speed can vary from 10% to 100% of the rated speed, it is important to have a qualitative view of the core losses. The core losses are a function of the frequency and flux density. From harmonic current input perspective, square wave rotor flux density has the highest amplitude of higher order harmonics resulting in the highest stator core losses while sine wave flux density results in the lowest core losses [1]. Same is true for current harmonics in the stator for respective square wave and sinusoidal currents. In [24], it is shown that for square wave currents, the eddy current losses are much higher than that of sinusoidal excitation.

The primary objective of the analytical method in this research is to obtain a relative estimate of increase in eddy current losses, especially tooth eddy current losses under unsaturated condition. The tooth eddy-current loss is assumed to be concentrated in those teeth which are near the edges of the surface- mounted magnets and, thus, is independent of the angular width of magnets [27]. Also the effects of saturation, cross-saturation and hysteresis in various part of the motor are not considered in analytical calculations. Finite element based solutions are used for capturing these effects. Influence of stator time harmonics on magnet eddy losses is ignored.

3.4.1. Qualitative assessment of core losses considering generalized back EMF expression of PMBDCM

The objective of this method is to illustrate qualitative variation in eddy current losses due to different current waveforms by using generalized back EMF expressions. The hysteresis losses are ignored in this analysis, however they will be considered in the analytical prediction method when the machine dimensions are available. To simplify the analysis, the core losses are assumed to be dominant in stator. Correspondingly, the eddy current loss due to the changing flux density in stator tooth is given as [25].

$$P_{et} = \frac{k_e}{2\pi}\int_0^{2\pi}\left(\frac{dB_t(t)}{dt}\right)^2 dt = \frac{k_e}{A_T 2\pi}\int_0^{2\pi}\left(\frac{d\emptyset_t(t)}{dt}\right)^2 \tag{3.8}$$

where, P_{et} is the eddy current core loss in stator tooth of the area A_T. $B_t(t)$is the instantaneous tooth flux density while $\emptyset_t(t)$ is the instantaneous tooth flux and k_e is the eddy current loss coefficient.

To evaluate the change in eddy current loss due various stator excitation methods, it is imperative to find the variation in rate of change of flux density or the tooth flux in the stator core. Hence considering the machine operating under load, the effective tooth flux $\emptyset_t(t)$ can be expressed as superposition of the rotor flux $\emptyset_{tr}(t)$ reflected in the stator and the flux due to the stator currents $\emptyset_{ts}(t)$ for a given phase as

$$\emptyset_t(t) = \emptyset_{ts}(t) + \emptyset_{tr}(t) \tag{3.9}$$

The rate of change of flux in the stator tooth is considered equivalent to the EMF induced in a single turn search coil [26]. Hence, the superposition can be now expressed as,

$$\frac{d\phi_t(t)}{dt} = \frac{d\phi_{ts}(t)}{dt} + \frac{d\phi_{tr}(t)}{dt} \tag{3.10}$$

Considering no load operation with $\emptyset_{ts}(t) = 0$, the rate of change of flux in stator tooth due to rotor flux $\emptyset_{tr}(t)$ is also referred as no load back EMF in the tooth [28], [29]. The benefit of using the search coil approach is that the analysis can take into account the generalized back EMF expression in (3.1). In this illustration, the back EMF is considered as trapezoidal.

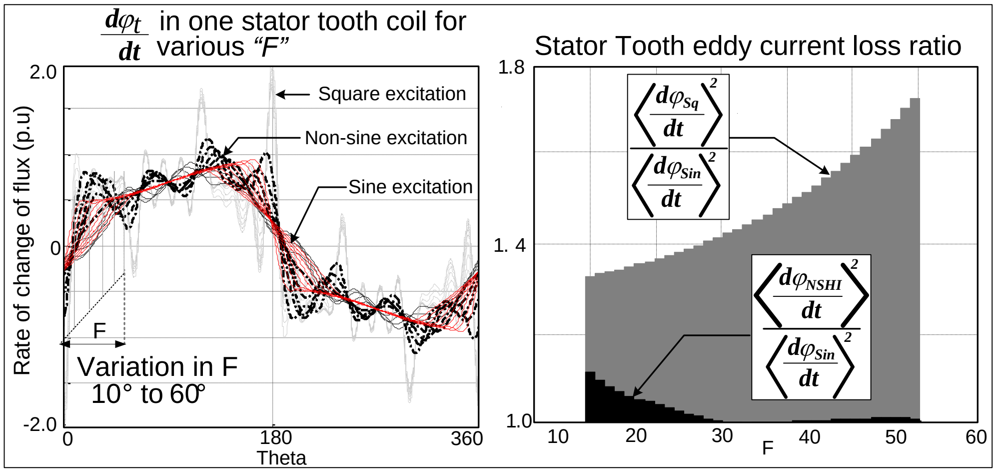

(a) (b)

Figure 3.4. Tooth eddy current loss variation as a function of '*F*'. (a) time series waveforms of rate of change of tooth flux under loaded operation, (b) average ratio of square of rate of change of tooth flux due to non-sinusoidal and sinusoidal current injection.

Considering PMBDCM operation under load, the tooth flux $\emptyset_{ts}(t)$ is calculated from the three phase stator currents according to the procedure in [28]. The resultant tooth flux obtained from (3.10) due to square, sinusoidal and NSHI current scheme is referred as ϕ_{Sq},ϕ_{Sin} and ϕ_{NSHI} respectively.

Figure 3.4(a) shows the resultant rate of change of flux in the stator tooth coil with square, sinusoidal and NSHI current excitation and under the assumption of unsaturated iron core. The distortion in the rate of change of flux from its original trapezoidal shape is due to the superposition of orthogonal components $\emptyset_{ts}(t)$ and $\emptyset_{tr}(t)$ resulting in armature reaction. In evaluating this illustration, the effective stator flux in the tooth due to rotor, $\emptyset_{tr}(t)$, is 1 p.u while the flux due to stator excitation, $\emptyset_{ts}(t)$, is 0.2 p.u. It is noted that square wave excitation has significant harmonics in the resultant rate of change on tooth flux waveform in comparison to non-sinusoidal and sine wave excitation. Since the sinusoidal currents yield the lowest core losses amongst the three current waveforms, they are considered as a baseline for this comparison. The mean square ratio of rate of change of tooth flux due to square, non-sinusoidal and sinusoidal currents is calculated from (3.10) and plotted in Figure 3.4 (b). Following observations are made from the figure:

(i) The tooth eddy current loss ratio due to square wave over sinusoidal currents is significantly higher than that of NSHI over sinusoidal current.

(ii) For less trapezoidal machines (as in case of F = 55°), the square wave currents results in 75 percent more losses than sinusoidal currents while NSHI currents results in only 2 percent higher losses than sinusoidal currents.

(iii) For more trapezoidal machines (as in case of F = 15°), the square wave currents results in 35 percent more losses than sinusoidal currents while NSHI currents yields 10 percent higher losses than sinusoidal currents. Thus the eddy current losses in stator core cannot be ignored for NSHI current excitation.

The above analysis can be similarly extended to the eddy current loss in stator yoke. Using the generalized back EMF expression, the qualitative analysis described in this subsection shows that for the same average torque, presence of harmonics in the stator current increases the stator core losses. The increase in core losses is dependent on the type of machine under consideration. In case of lack of data on the machine geometry, the elaborated qualitative analysis is applicable. In order to better estimate the increase in core losses due to various excitation schemes, it is essential to calculate them analytically using dimensional data of the machine. Such a method is described in the following section.

3.4.2. Analytical estimation of core loss using dimensional data of PMBDCM

Given the machine dimensions, preliminary estimation of flux densities in the stator tooth and yoke can be used to predict core losses under no load condition [1]. The core losses are then calculated with following assumptions and they are [27]: (i) unsaturated operation of the machine, (ii) the flux densities are assumed to be trapezoidal, (iii) only normal component of tooth and yoke flux density is considered while the tangential components of the flux density in tooth and yoke are ignored, (iv) leakage fluxes in the tooth, slots, pole face, and magnets are ignored. The analytical approach explained in [27] predicts core losses by estimating rate of change of flux densities in stator tooth and yoke under no load operation of the machine. The methodology presented in this section is developed based on the approach provided in [27] and extended for PMBDCMs operating under loaded condition by predicting the flux densities using the principle of superposition.

To estimate the core losses an outer rotor machine as shown in Figure 3.5 (a) is considered. The dimensions of the machine are provided in the Appendix Table A.2. The electrical parameters of the machine (II) are given in Table 3.3. Corresponding trapezoidal stator tooth and yoke flux densities are shown in Figure 3.5 (b) and (c), respectively. They can be constructed approximately based on machine geometry and is explained in [27]. Analogous to the back EMF expression in (3.1), the generalized expression for no load flux density in the air-gap, stator tooth and yoke is given as,

$$B_{gty}(t) = \frac{4}{\pi} B_{gty-pk} \sum_{k=0}^{\infty} a_n \sin(n\omega_r t)$$

$$a_n = \frac{sin\left(nF_{gty}\right)}{n^2 F_{gty}} \tag{3.11}$$

$$n = 2k+1, \quad k = 0,1,2 \ldots$$

$$F_{gty} = \omega_r t_{gty}$$

where, $B_{gty}(t)$ and B_{gty-pk} represents the instantaneous and peak flux densities in the air-gap, stator tooth and yoke respectively while t_{gty} is the corresponding time required for rate of rise of flux density from zero to its peak amplitude. ω_r is the electrical angular velocity of the rotor and a_n is the amplitude of n$^{\text{th}}$ harmonic of the trapezoidal flux density. The peak flux density can be calculated from residual flux density as per the description in [1]. For accurate reconstruction of the flux density waveforms, the peak flux density may be obtained from FEA method [27]. Based on the machine geometry, the time required for rate of rise of flux density in stator tooth, as shown in Figure 3.5 (b), is given as [26],

$$t_t = \frac{T_s}{2} \frac{1}{3N_{s/P}} \tag{3.12}$$

where, $t_t$is the time taken by the stator flux density to reach its peak value B_{tpk}, T_s is electrical time period and $N_{s/P}$ is the number of slots per pole per phase. The time t_y required by the yoke flux density to reach its peak value B_{ypk} is given as [26],

$$t_y = \frac{W_m}{2r\omega_m} \tag{3.13}$$

where $W_m$is width of the magnet, r is outer radius of stator and ω_m is mechanical angular velocity. The corresponding yoke flux density is shown in Figure 3.5 (c).

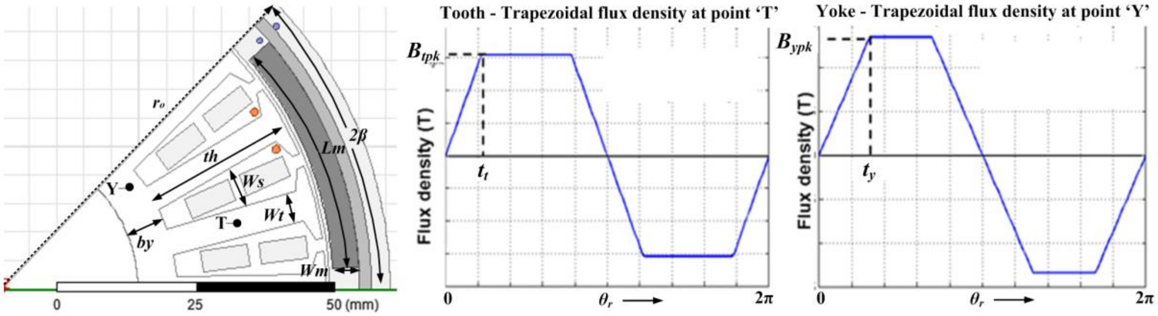

(a) (b) (c)

Figure 3.5(a) Outer rotor machine with: (b) Flux density in stator tooth at point T, and (c) yoke flux density at point Y

In order to assess the influence of load, it is essential to evaluate the resultant flux densities due to various excitation schemes. Accordingly, the resultant air-gap flux density $B_{gs}(t)$ is given by the superposition of the stator flux density $B_s(t)$ due to stator excitation and the no-load air-gap flux density $B_g(t)$ at a spatial position where angle $\theta_r = 0$. During constant torque operation of PMBDCM, the stator and no-load air-gap flux densities are orthogonal to each other. Then the resultant flux density is expressed as

$$B_{gs}(t) = B_g(t) + B_s(t) \tag{3.14}$$

In the above expression, the no load air-gap flux density $B_g(t)$ is calculated from (3.11) while the procedure for estimation of stator flux density $B_s(t)$ due to NSHI excitation scheme for given average torque is elaborated as follows.

The stator flux density at arbitrary spatial position is dependent on air-gap length 'g' and permeability of free space 'μ_o' given by the following relationship [1]:

$$B_s(\theta, t) = \frac{\mu_o F_s(\theta, t)}{g} \tag{3.15}$$

where θ is the arbitrary position of the rotor, $F_s(\theta, t)$ is the total magneto-motive force (MMF) in the stator. It is given as

$$F_s(\theta, t) = F_a(\theta, t) + F_b(\theta, t) + F_c(\theta, t) \tag{3.16}$$

where, $F_a(\theta, t)$,$F_b(\theta, t)$, and $F_c(\theta, t)$ are the three-phase MMFs generated by the instantaneous three-phase currents $I_a(t)$, $I_b(t)$, and $I_c(t)$ in spatially distributed three-phase windings $N_a(\theta)$, $N_b(\theta)$, and $N_c(\theta)$, respectively. The stator phase MMFs are calculated as [1],

$$\begin{aligned} F_a(\theta, t) &= \tfrac{1}{P} I_a(t) N_a(\theta), \\ F_b(\theta, t) &= \tfrac{1}{P} I_b(t) N_b(\theta), \\ F_c(\theta, t) &= \tfrac{1}{P} I_c(t) N_c(\theta) \end{aligned} \tag{3.17}$$

where P is the number of poles. The NSHI currents having only the fundamental, 5th and 7th harmonic components are given as,

$$\begin{aligned} I_a(t) &= I_m[a_1 sin(\omega_r t) + a_7 sin(5\omega_r t) + a_5 sin(7\omega_r t)] \\ I_b(t) &= I_m\left[a_1 sin\left(\omega_r t - \frac{2\pi}{3}\right) + a_7 sin\left(5\left(\omega_r t - \frac{2\pi}{3}\right)\right) + a_5 sin\left(7\left(\omega_r t - \frac{2\pi}{3}\right)\right)\right] \\ I_c(t) &= I_m\left[a_1 sin\left(\omega_r t + \frac{2\pi}{3}\right) + a_7 sin\left(5\left(\omega_r t + \frac{2\pi}{3}\right)\right) + a_5 sin\left(7\left(\omega_r t + \frac{2\pi}{3}\right)\right)\right] \end{aligned} \tag{3.18}$$

where, $a_1 = 1$, $a_7 = 0.092$, and $a_5 = 0.022$. and are obtained from the back EMF of machine in Figure 3.6 (b). Note the coefficients of the 5th and 7th harmonic components to reduce the torque ripple.

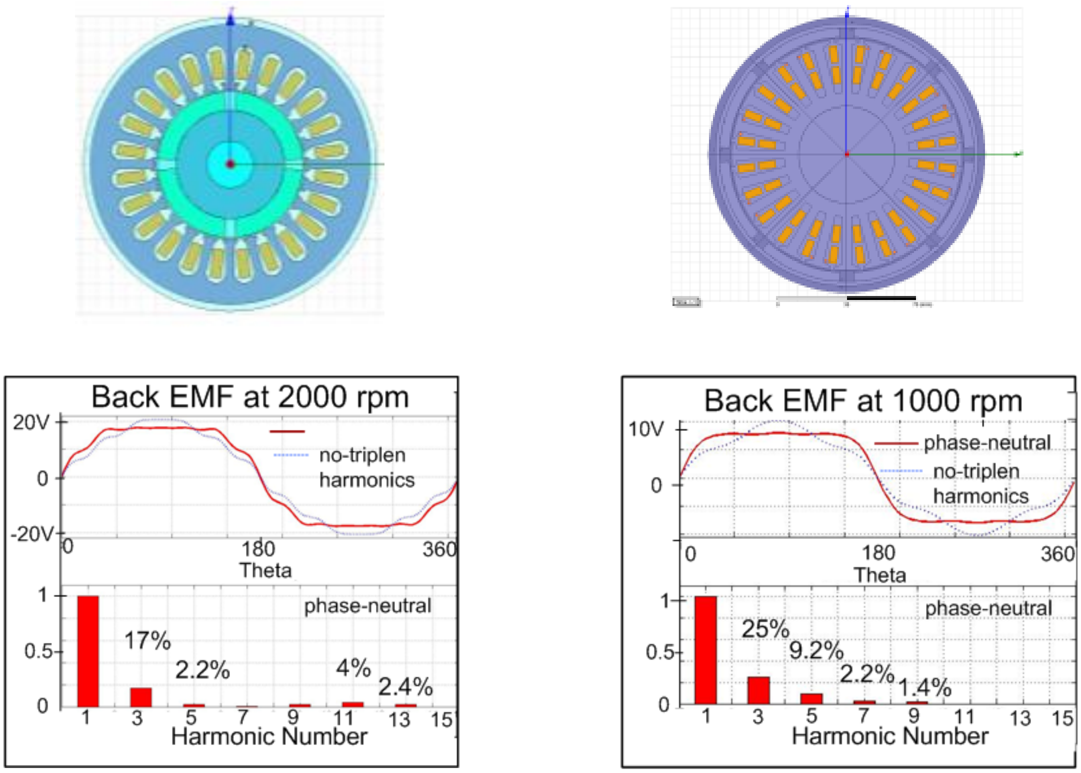

(a) (b)

Figure 3.6. Measured terminal phase voltage (Back EMF): (a) Machine I - inner rotor, (b) Machine II - outer rotor

The higher ordered harmonics may be included for improved accuracy in calculation of losses. Although the winding functions comprise of space harmonics, only fundamental component will be considered for simplicity. The winding functions are given as,

$$\begin{aligned} N_a(\theta) &= N_{ph}sin(\theta_r) \\ N_b(\theta) &= N_{ph}sin\left(\theta_r - \frac{2\pi}{3}\right) \\ N_c(\theta) &= N_{ph}sin\left(\theta_r + \frac{2\pi}{3}\right) \end{aligned} \qquad (3.19)$$

where N_{ph} is the effective number of turns per phase. Evaluating equations (3.16) through (3.19), the total MMF due to stator excitation is given as,

$$F_s(\theta,t) = \frac{3I_mN_{ph}}{2P}[a_1cos(\omega_r t - \theta_r) - a_7cos(5\omega_r t + \theta_r) + a_5cos(7\omega_r t - \theta_r)] \qquad (3.20)$$

Substituting (3.20) in(3.15) and assuming spatial position with angle $\theta_r = 0$, the effective stator flux density due to stator is given as,

$$B_s(t) = \frac{\mu_o}{g}\frac{3I_mN_{ph}}{2P}[a_1cos(\omega_r t) - a_7cos(5\omega_r t) + a_5cos(7\omega_r t)] \qquad (3.21)$$

Once the effective stator flux density is known, the resultant air-gap flux density $B_{gs}(t)$ can be estimated using (3.14). Then the stator tooth and yoke flux densities, $B_t(t)$ and $B_y(t)$ respectively, are estimated using the following relationships [1],

$$B_t(t) = \frac{W_t + W_s}{W_t} B_{gs}(t)\,, \qquad B_y(t) = \frac{W_m}{2b_y} B_{gs}(t) \tag{3.22}$$

where W_t, W_s are tooth width and slot width respectively, W_m is magnet thickness and b_y is the yoke height. Although the procedure described above is elaborated for NSHI scheme, it can be easily modified for sinusoidal excitation by zeroing the coefficients a_5 and a_7.

Figure 3.7 (a-d) shows the absolute magnitude of the resultant flux densities in the stator tooth and yoke due to sinusoidal and NSHI excitation schemes. These resultant flux densities are plotted at points ‘T’ and ‘Y’, respectively, and shown in Figure 3.5 (a). The FEA analysis of the machine is performed at 2000 rpm with a constant load torque of 0.2 Nm. The comparison between the analytical and FEA results shows the effectiveness of the procedure in reconstruction of the resultant flux densities. It should be mentioned that the accuracy of the method is dependent on the accuracy of estimation of no-load flux density in stator tooth and yoke.

The core losses predominantly comprise of eddy and hysteresis current losses which are calculated from the resultant flux densities obtained from (3.22). The total eddy current losses in the stator teeth and yoke are given by,

$$P_{et} = k_e \rho_i V_t \sum_{k=1}^{\infty} (k\omega_r B_{ktm})^2\,,\ P_{ey} = k_e \rho_i V_y \sum_{k=1}^{\infty} \left(k\omega_r B_{kym}\right)^2 \tag{3.23}$$

where V_t and V_y is the total volume of stator teeth and yoke,respectively, ρ_i is the mass density of steel with eddy loss coefficient k_e, while B_{ktm} and $B_{kym}$are the kth harmonic amplitudes of the teeth and yoke flux densities, respectively. These flux densities are calculated by Fourier decomposition of the time series waveform obtained in (3.22).

The hysteresis losses in stator teeth and yoke, respectively, are given as,

$$P_{ht} = k_h \rho_i V_t \sum_{k=1}^{\infty} k\omega_r (B_{ktm})^n,\ P_{hy} = k_h \rho_i V_y \sum_{k=1}^{\infty} k\omega_r \left(B_{kym}\right)^n \tag{3.24}$$

where k_h is the hysteresis loss coefficient and *n* is the Steinmetz coefficient. The extraneous losses are not considered in this study.

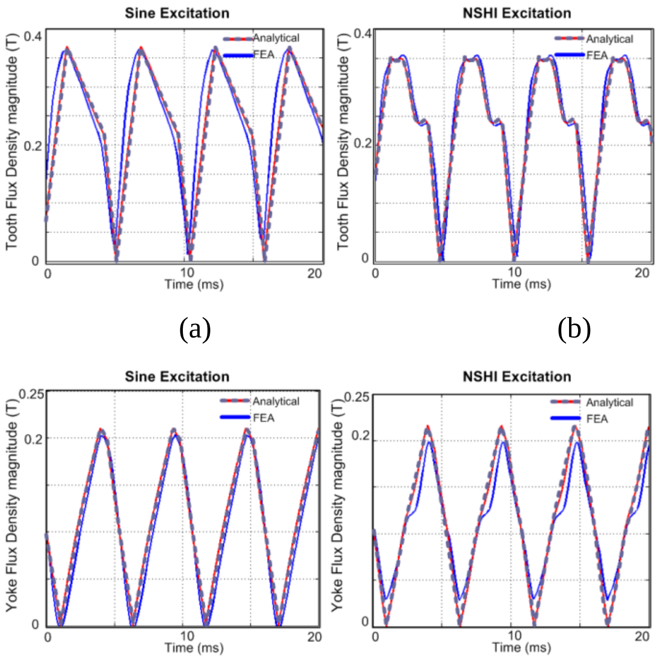

(a) (b)

(c) (d)

Figure 3.7. FEA result: Absolute magnitude of the resultant flux densities in the stator tooth and yoke considering sinusoidal current excitation: (a) and (c),and NSHI excitation: (b) and (d), respectively.

The eddy and hysteresis loss coefficients k_e and $k_{h,}$ respectively, vary with every operating frequency and amplitude of flux density in a given steel lamination. These coefficients are obtained using finite element simulations. Then the total core losses P_{iron} are given as

$$P_{iron} = P_{et} + P_{ey} + P_{ht} + P_{hy} \tag{3.25}$$

Using the parameters listed in Table A.1 given in Appendix, and substituting them in (3.22) through (3.25), the total core losses using analytical method for sinusoidal and NSHI scheme are listed in Table 3-2. It is seen that the core losses due to NSHI is 6% higher than sinusoidal currents. The comparison between the analytical and finite element analysis result shows that the procedure illustrated has an error within 15%. Hence the analytical results can provide adequate insight into the core losses of the machine. In case of very high speed PMBDC machines, the analytical procedure described above must be modified to take into account the rotor losses. High speed PMBDCMs are beyond the scope of this work and hence estimation of rotor losses is not pursued further.

Table 3-2.Total Core Losses in Machine II

Excitation	**Analytical**	**FEA**	**% Error**
Sine	13.8 W	12 W	15.4
NSHI	14.628 W	13 W	14

From the above results, it is seen that NSHI currents results in higher core losses than sinusoidal currents for the chosen PMBDCM. Evaluation of the same using finite element simulations for two different types PMBDCMs is discussed in the next section.

3.4.2.1. Core loss analysis in PMBDCM for various current excitations using Finite Element Simulation

Core losses in PMBDCM for sinusoidal and non-sinusoidal current excitation are evaluated by simulating two machines (I and II) whose dimensions are given in Table A.1 and Table A.2 in the appendix. The PMBDCMs considered in this study have two different back EMF waveforms. The harmonic spectra of these machines are normalized to the fundamental amplitude and shown in Figure 3.6 (a) and (b). It is seen that the back EMF of machine I has less than 5 percent of the 5^{th}, 7^{th}, 11^{th} and 13^{th} harmonic components in comparison to the fundamental. Hence this PMBDCM is similar to a sinusoidal back-EMF machine (with ‘*F*’ > 30°). Machine II on the other hand has 9.2 percent of the 5^{th} harmonic amplitude with respect to the fundamental component and thereby analogous to a trapezoidal back-EMF machine (‘*F*’ < 30°).

The parameters of the two machines are listed in Table 3-3. Both machines have ceramic-8D magnets and M-56 grade steel. Machine I and II are operated with constant load torque of 1 Nm and 0.2 Nm, respectively, and variable speed operation. The three stator current injection strategies are studied to quantify the core losses in the machine. Then detailed comparison between sinusoidal and NSHI current scheme using the FEA simulations is made to assess the increase in core losses due to the later.

Table 3-3. Machine parameters

Symbol	***Machine I (F>30)***	***Machine II(F<30)***
r_s	0.35 ohm	0.17 ohm
L_s	600 uH	150 uH
λ_m	0.0495 Vp/rad/s	0.0115 Vp/rad/s
Poles	4	8
Speed	2000 rpm	2000 rpm
Torque	1 Nm	0.2 Nm
Power	200W	50W
Vdc	48V	18V

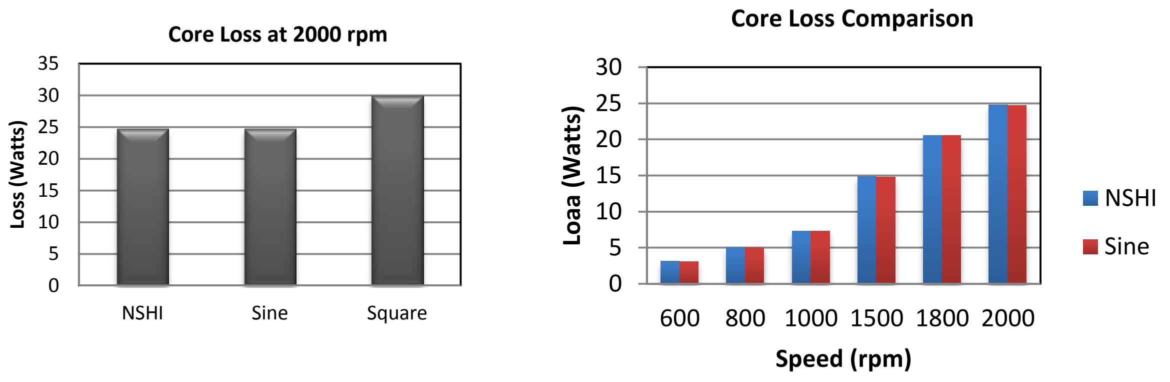

(a)

(b)

Figure 3.8. Simulation results for machine I: (a) Core loss comparison of sine, square and NSHI scheme at 2000 rpm, and (b) Core loss comparison of sine, and NSHI scheme at various speed of operation

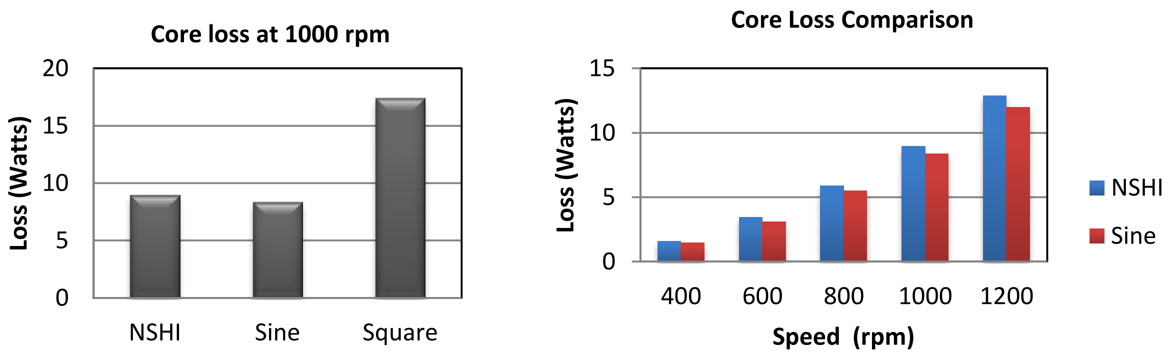

(a)

(b)

Figure 3.9. Simulation results for machine II: (a) Core loss comparison of sine, square and NSHI scheme at 1000 rpm, (b) Core loss comparison of sine, and NSHI scheme at various speed of operation

Figure 3.8 (a) shows the core loss comparison results for machine I. It is seen that for the same output power and operating speed of 2000 rpm, the square wave current results in highest core losses amongst the three excitation schemes. Figure 3.8 (b) shows that the core loss due to NSHI and sine excitation scheme is similar. Due to more sinusoidal back EMF, the injected harmonic currents are also small resulting in similar core losses.

Figure 3.9 (a) shows the core loss comparison results for machine II. It is seen that for the same output power and operating speed of 1000 rpm, the square wave current results in highest core losses amongst the three excitation schemes. Figure 3.9 (b) shows that the core loss due to NSHI method is higher than the sinusoidal excitation. Machine II has higher amplitude of the 5th harmonic in its back EMF. Hence higher amplitude of the 7th harmonic of current must be injected [14].The higher amplitude of the 5th and 7th harmonic current together increases the total core losses in the stator. The core losses increase by 6 percent for the maximum speed and load condition. In case of lower grade lamination steel, which is generally used to reduce cost of the motor, the core losses can be even higher (above 10%).

From the results in section 3.3 and 3.4 it is seen that although the stator resistive loss for NSHI is lowest amongst all schemes, it is the core loss at higher frequencies that deteriorates the performance of the NSHI scheme. Thus there exists a tradeoff between stator core losses, resistive losses and torque ripple minimization techniques for harmonic current injection strategy. Although presence of harmonics in the stator flux is useful to smooth the air-gap flux and minimize torque ripple, they do increase the stator core losses. From the above analysis, for higher efficiency operation, it is imperative to use a combination of both sinusoidal and non-sinusoidal current injection - a hybrid approach. This approach should be evaluated especially for more trapezoidal PMBDCMs ('F' < 30°). The influence of sine, square and NSHI scheme on core losses will be demonstrated using experimental results in section 3.6. From a control perspective, it is critical to model the machine in closed form so as to minimize the Fourier series calculation in the controller's implementation. The following section explains the derivation of such a model.

3.5. Control strategies for Non-Sinusoidal Machines

3.5.1. Closed form solution for non-sinusoidal currents

The closed form solution provides better insight into the cancellation of back EMF and current harmonics thereby resulting in theoretical ripple free electromagnetic torque. Fourier series of non-sinusoidal back EMFs in (3.1) and the corresponding non-sinusoidal instantaneous currents listed in Table3-1 can also be expressed in closed form and presented in Table 3-4.

Table 3-4. Closed form expression for back EMF and currents

Back EMF	***Non-Sinusoidal Currents***
$e_a = \varepsilon E_m \cos(\theta_r + \mu)$ $e_b = \varepsilon E_m \cos\left(\theta_r + \mu - \frac{2\pi}{3}\right)$ $e_c = \varepsilon E_m \cos\left(\theta_r + \mu + \frac{2\pi}{3}\right)$	$i_a = \frac{1}{\varepsilon} I_m \cos(\theta_r + \mu)$ $i_b = \frac{1}{\varepsilon} I_m \cos\left(\theta_r + \mu - \frac{2\pi}{3}\right)$ $i_c = \frac{1}{\varepsilon} I_m \cos\left(\theta_r + \mu + \frac{2\pi}{3}\right)$

where, e_a, e_b, e_c are the phase back EMF voltages for phases A, B, and C respectively, while μ and ε are function of rotor position θ_r, with an average value of zero and unity, respectively, taken over an electrical cycle and given as,

$$\varepsilon = \sqrt{\frac{3}{2}}\frac{\omega_r\lambda_m}{\sqrt{E_{ao}^2 + E_{bo}^2 + E_{co}^2}}$$

$$\mu = \tan^{-1}\left(\frac{-E_{ao}}{\frac{1}{\sqrt{3}}(E_{co} - E_{bo})}\right) - \theta_r \tag{3.26}$$

The instantaneous output power of the machine is,

$$P_{out} = [e_a i_a + e_b i_b + e_c i_c] \tag{3.27}$$

Substituting expressions in Table 3-4 in (3.29), the output power is given as,

$$P_{out} = \varepsilon E_m \frac{1}{\varepsilon} I_m \left[\cos^2(\theta_r + \mu) + \cos^2\left(\theta_r + \mu - \frac{2\pi}{3}\right) + \cos^2\left(\theta_r + \mu + \frac{2\pi}{3}\right)\right] \tag{3.28}$$

which on simplification yields,

$$P_{out} = \frac{3}{2} E_m I_m \tag{3.29}$$

Equation (3.29) can be expressed in terms of torque, peak flux linkage and peak current as,

$$T_e = \frac{3}{2}\frac{P}{2}\lambda_m I_m \tag{3.30}$$

Since all the variables in (3.30) are constant in time, this expression analytically proves that the solution obtained for non-sinusoidal currents generates ripple free torque. The result in (3.30) is specific to the compensation of flux linkage in the air gap due to time series harmonics and does not take into account effects of space harmonics.

Formulation of the currents in Table 3-4 is central to controller implementation in *abc*, two phase stationary, or rotor synchronous reference frames. Since *abc* and two phase stationary reference frame implementations have known limitations of current controller bandwidths, the implementation in rotor reference frame will be considered henceforth. For rotor synchronous reference frame transformation in presence of harmonics in back EMF and current, a non-sinusoidal co-ordinate transformation was proposed in [23].

The following section explains the development of the transformation and corresponding mathematical model for controller implementation.

3.5.2. Non-sinusoidal coordinate transformation

The objective of the coordinate transform is to achieve time invariant (DC) variables from the non-sinusoidal currents by appropriately rotating the reference frame and normalizing the current vector magnitude with respect to rotor position, developed in [23] and it is explained using Figure 3.10. In contrast to the conventional reference frame approach this coordinate transformation requires two more variables in addition to the rotor position as shown in Figure 3.10:

(i) perturbation in amplitude 'κ', where $\kappa = \frac{1}{\varepsilon}$, and

(ii) perturbation in position/phase 'μ'.

Thus κ, μ, and θ_r form the variables for the co-ordinate transformation. With reference to Figure 3.10, the time invariant transformation is achieved by the following steps:

1. The non-sinusoidal currents are transformed to two phase stationary reference frame so that the two current vectors are orthogonal to each other.
2. Then the reference frame is rotated with respect to the rotor position and its displacement (θ_r + μ) as given in (3.26) resulting in the current i_{dp}^r along d-axis is zero while the current i_{qp}^r along q-axis varies in magnitude.

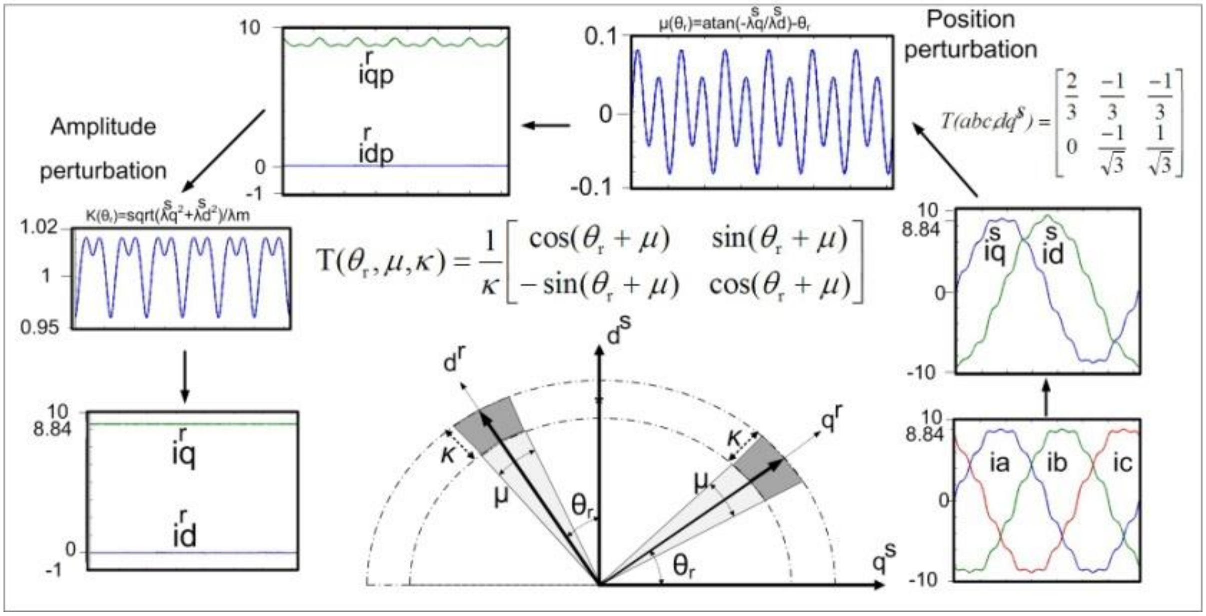

Figure 3.10. Non-sinusoidal coordinate transformation on abc currents

3. The gain of the transformation ‘κ’ is the inverse of ‘ε’ which is computed from (3.26).
4. Applying the transformation T(θ_r,μ,κ) given in Figure 3.10, the current variables are transformed into DC variables with the q-axis current having magnitude i_q^r while the d-axis current is zero.

5. Since the currents injected are functions of the back EMF this reference frame transformation requires online-computation of the variables ‘κ’ and ‘μ’.

The PMBDCM model in *abc* reference frame is given as,

$$\vec{v}_{abcs} = r\vec{\imath}_{abcs} + L\frac{d}{dt}\vec{\imath}_{abcs} + \omega_r\vec{\lambda}_{abcs} \tag{3.31}$$

where $\vec{v}_{abcs}$ is the per phase applied stator phase voltages vector, $\vec{\imath}_{abcs}$ is the generated stator phase currents vector,$\vec{\lambda}_{abcs}$ is the phase flux linkages vector in the machine, L is the inductance matrix of the machine, ω_r is the electrical angular velocity of the rotor. Defining the machine parameters where r_s is the per phase stator resistance, L_s is the per phase stator self-inductance, and λ_m is the peak of flux linkage of a phase and applying the transformation explained in steps 1-4, the corresponding rotor reference frame the PMBDCM model is given as [23],

$$\begin{bmatrix} v_{ds}^r \\ v_{qs}^r \end{bmatrix} = \begin{bmatrix} r_s + \omega_r L_s \frac{1}{\kappa}\frac{d\kappa}{d\theta_r} & \omega_r L_s\left(1 + \frac{d\mu}{d\theta_r}\right) \\ -\omega_r L_s\left(1 + \frac{d\mu}{d\theta_r}\right) & r_s + \omega_r L_s \frac{1}{\kappa}\frac{d\kappa}{d\theta_r} \end{bmatrix} \begin{bmatrix} i_{ds}^r \\ i_{qs}^r \end{bmatrix} + \begin{bmatrix} L_s & 0 \\ 0 & L_s \end{bmatrix} \frac{d}{dt} \begin{bmatrix} i_{ds}^r \\ i_{qs}^r \end{bmatrix} + \omega_r\lambda_m \begin{bmatrix} 0 \\ \frac{1}{\kappa^2} \end{bmatrix} \tag{3.32}$$

In the model given by (3.32), when k=1 and μ=0, the model takes the form of conventional sinusoidal permanent magnet motor. It is this property of the model that enables the hybrid control and transition from sinusoidal to non-sinusoidal current injection modes. This work demonstrates the application of such a model for efficiency improvement of non-sinusoidal machines applied in variable speed applications. Following section explains the sensorless field oriented vector control scheme using the developed model.

3.5.3. Non-sinusoidal field oriented control

As deduced from section 3.4, a hybrid current injection strategy can be applied to improve the efficiency of the variable speed motor. The hybrid approach is implemented by using variables ‘μ’ and ‘κ’ which can be limited to zero and unity, respectively, thus facilitating the transition from NSHI scheme to conventional sinusoidal field oriented control scheme. Figure 3.11 shows the hybrid current injection strategy corresponding to the motor loss behavior for variable speed operation. For a given load and speed, NSHI scheme is applied until the stator resistive losses ‘P_{cu}’ dominate the total losses of the motor after which the control can be switched to sinusoidal current injection if the core losses ‘P_{fe}’ dominate the total losses in the motor. As explained in section 3.4, this approach should be considered especially for more trapezoidal machines (F < 30°). From the analytical derivation and corresponding FEA based results in section 3.4, the hybrid approach serves the purpose of highest efficiency considering variable speed operation and simultaneous reduction of torque ripple at lower speed of operation. The efficiency improvement between low speed and high speed regions will be evaluated using experimental results in section 3.6.

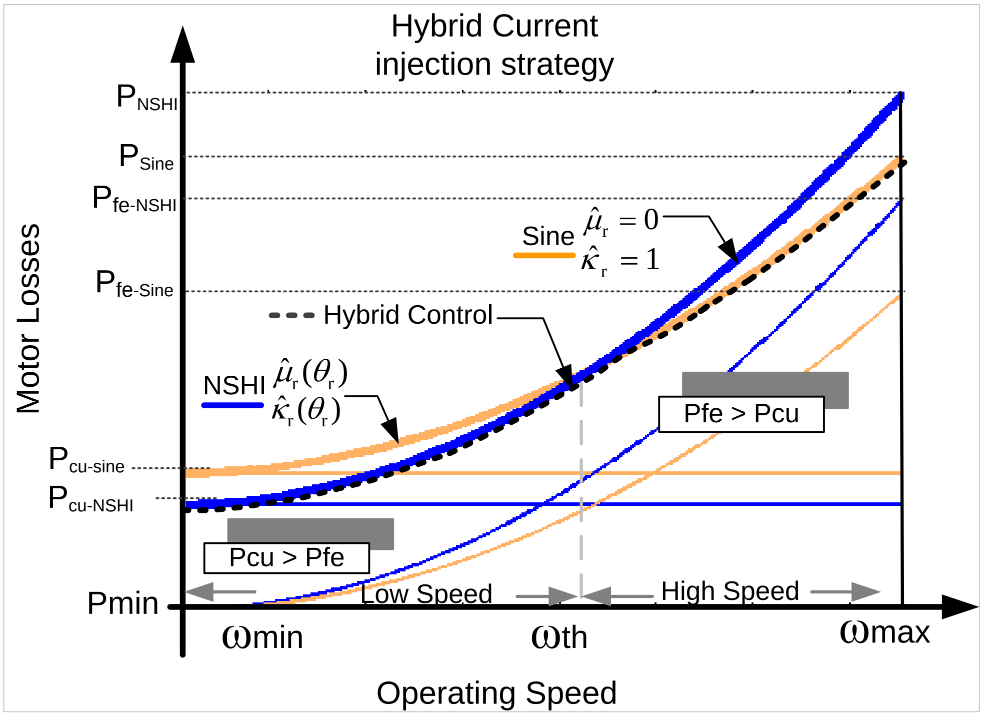

Figure 3.11. Hybrid current injection strategy for variable speed drive operation

3.5.4. *Current control and rotor position sensorless vector control of PMBDCM*

Based on the machine model developed in (3.32), a sensorless vector control strategy shown in Figure 3.12 is developed to demonstrate the performance of sinusoidal and non-sinusoidal stator field excitation on efficiency of the motor. To achieve good sensorless control performance, it is essential to have a good current controller implementation using variables ‘κ’ and ‘μ’ and ‘θ’. The current controller G_c and the plant model G_p considering the phase resistor and inductance are given, respectively, as,

$$G_c = \frac{K_r(1+s\tau_r)}{s\tau_r}, G_p = \frac{K_p}{(1+s\tau_p)(1+s\tau_d)} \tag{3.33}$$

where K_p is converter PWM gain, τ_p is first order stator time constant, τ_d is net inverter and microprocessor delay, τ_r is current controller's time constant and K_r is corresponding controller gain. The open loop transfer function is given as,

$$G_cG_p = \frac{K_pK_r(1+s\tau_r)}{s\tau_r(1+s\tau_p)(1+s\tau_d)} \tag{3.34}$$

Applying pole zero cancellation by setting $\tau_r = \tau_p$, and comparing the characteristic equation with a second order system with damping ratio of 0.707, the proportional integral regulator parameters are given as,

$$K_r = \frac{\tau_p}{2K_p\tau_d}\ , \tau_r = \tau_p \tag{3.35}$$

The decoupling terms for the current controller are calculated based on the motor model and are given as,

$$\begin{bmatrix} v^r_{d\_ff} \\ v^r_{q\_ff} \end{bmatrix} = \begin{bmatrix} \omega_r L_s \dfrac{1}{\kappa}\dfrac{d\kappa}{d\theta_r} & \omega_r L_s\left(1+\dfrac{d\mu}{d\theta_r}\right) \\ -\omega_r L_s\left(1+\dfrac{d\mu}{d\theta_r}\right) & \omega_r L_s \dfrac{1}{\kappa}\dfrac{d\kappa}{d\theta_r} \end{bmatrix} \begin{bmatrix} i^r_{ds} \\ i^r_{qs} \end{bmatrix} + \omega_r\lambda_m \begin{bmatrix} 0 \\ \dfrac{1}{\kappa^2} \end{bmatrix} \tag{3.36}$$

The decoupling terms reduce the requirement on the current regulator controller bandwidth because they compensate for the disturbances due to non-sinusoidal variables. Thus the current controller tracks the DC variables only.

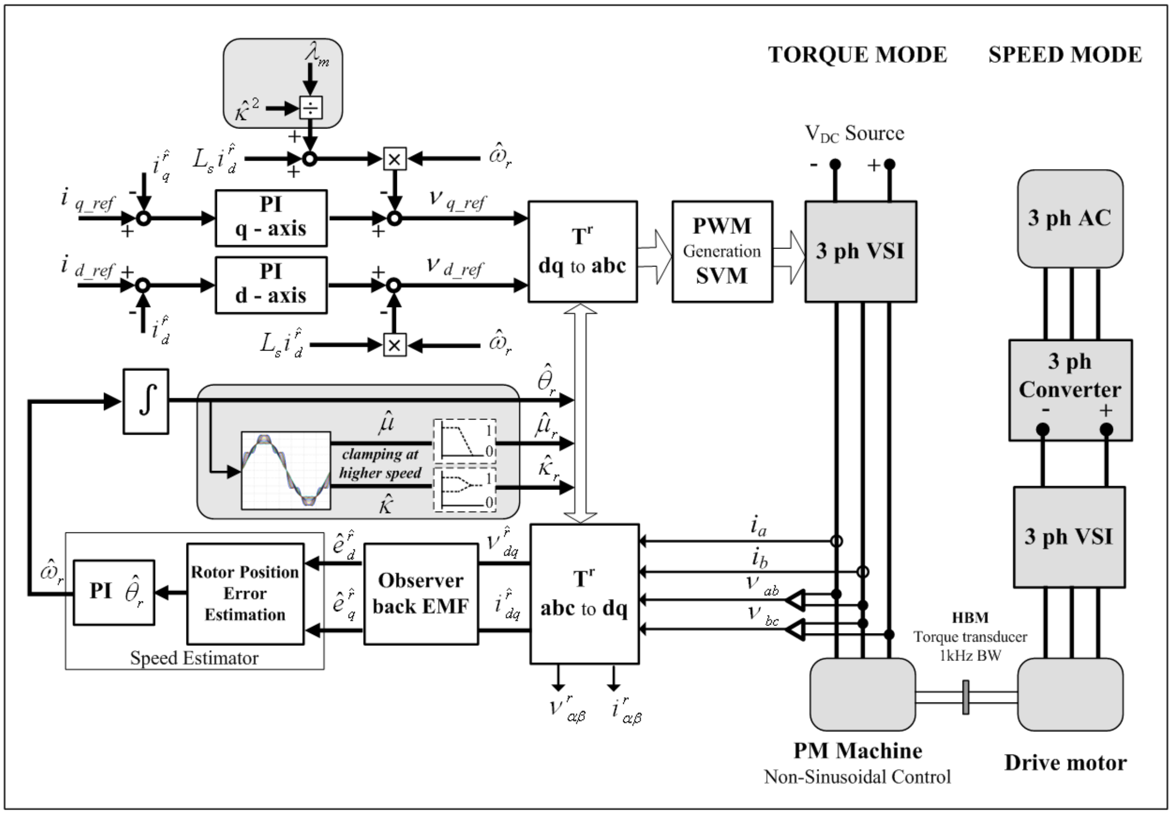

Figure 3.12. Hybrid sinusoidal to non-sinusoidal harmonic current injection strategy using variables ‘κ’ and ‘μ’ and ‘θ’

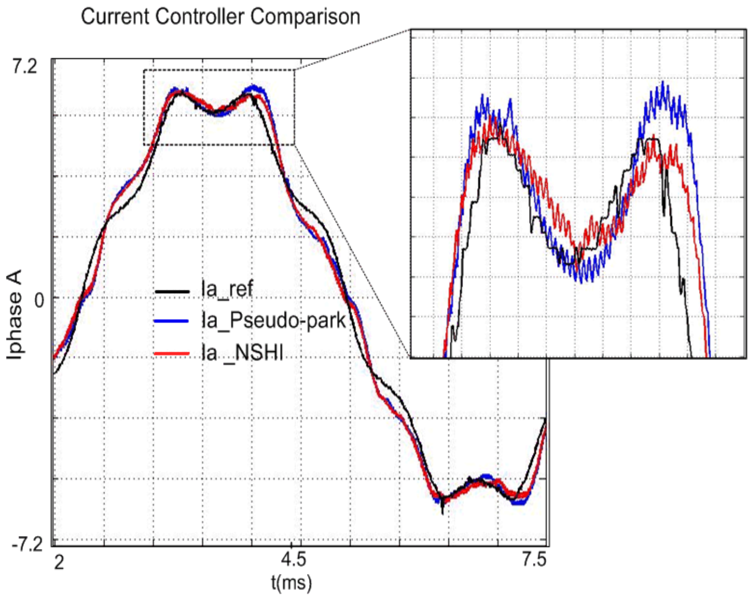

Figure 3.13. Experimental results: current controller comparison NSHI vs. pseudo Park [22] at 700 rpm.

Figure 3.13 shows the comparison of the current controller for a PMBDCM operating at 700 rpm using pseudo-Park transformation method given in [22] and the NSHI method in this research. In case of the pseudo-Park transformation method, the q- axis reference current has AC signal super-imposed on the DC signal. Consequently, in order to track the AC waveform, the current controller bandwidth required is very high. On the other hand, in case of the NSHI excitation using the co-ordinate transformation discussed above, the q-axis current does not have any AC signal. Hence from the enlarged figure it is seen that for the same current controller bandwidth, NSHI has better tracking performance than the pseudo Park transform method. For the non-sinusoidal co-ordinate transformation, the variables ‘μ’ and ‘κ’, are estimated from the motor back EMF during the commissioning phase. Such a procedure is developed in [22] using an online harmonic estimation using an adaptive filtering technique.

For rotor position sensorless control, a full-order Luenberger observer and a tracking controller given in [30] is used. The observer is designed for the fundamental component of the back EMF. Due to the low bandwidth of the tracking controller (< 5 Hz) [30], the higher ordered back EMF harmonic components are attenuated. Hence, the estimated rotor position is devoid of the back EMF harmonic components.

A discontinuous pulse width modulation (DPWM) scheme is applied to maximize DC bus utilization and to reduce inverter switching loss. The following section will show the experimental results and efficiency measurement results of the three current excitation methods.

3.6. Experimental results

Two machines, I and II, with parameters listed in Table 3.3 are considered. The experimental setup is shown in Figure 3.14. It comprises of a HBM-MP-60 torque and speed transducer, Yokogawa WT-1600 power analyzer with motor module and Danfysik current transducer.

Figure 3.15 (i) and (ii) shows the simulation and experimental results of the non-sinusoidal (NSHI) current excitation of machine I operating at 700 rpm. The corresponding waveforms are the three phase currents in *abc* reference frame I_{abc}, stationary reference frame $I_{\alpha\beta}$, tracking of the phase A current I_a with respect to the reference current $I_a^*$and the current vector trajectory in stationary reference frame. The closeness between the simulation and experimental results validates the modeling methodology and the current controller implementation.

In order to assess the motor efficiency performance due to the three excitation schemes, it is essential to evaluate their steady state operation. Accordingly, NSHI excitation method in Figure 3.12 is compared with sine wave and square wave currents.

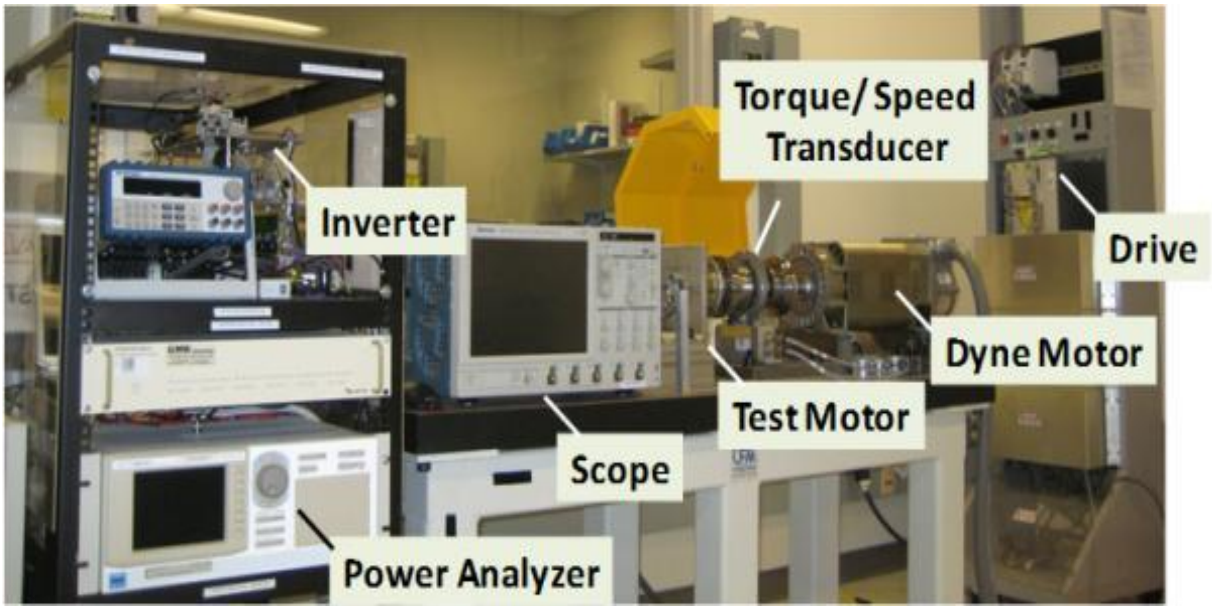

Figure 3.14Experimental test setup for evaluating motor efficiency using various harmonic injection schemes

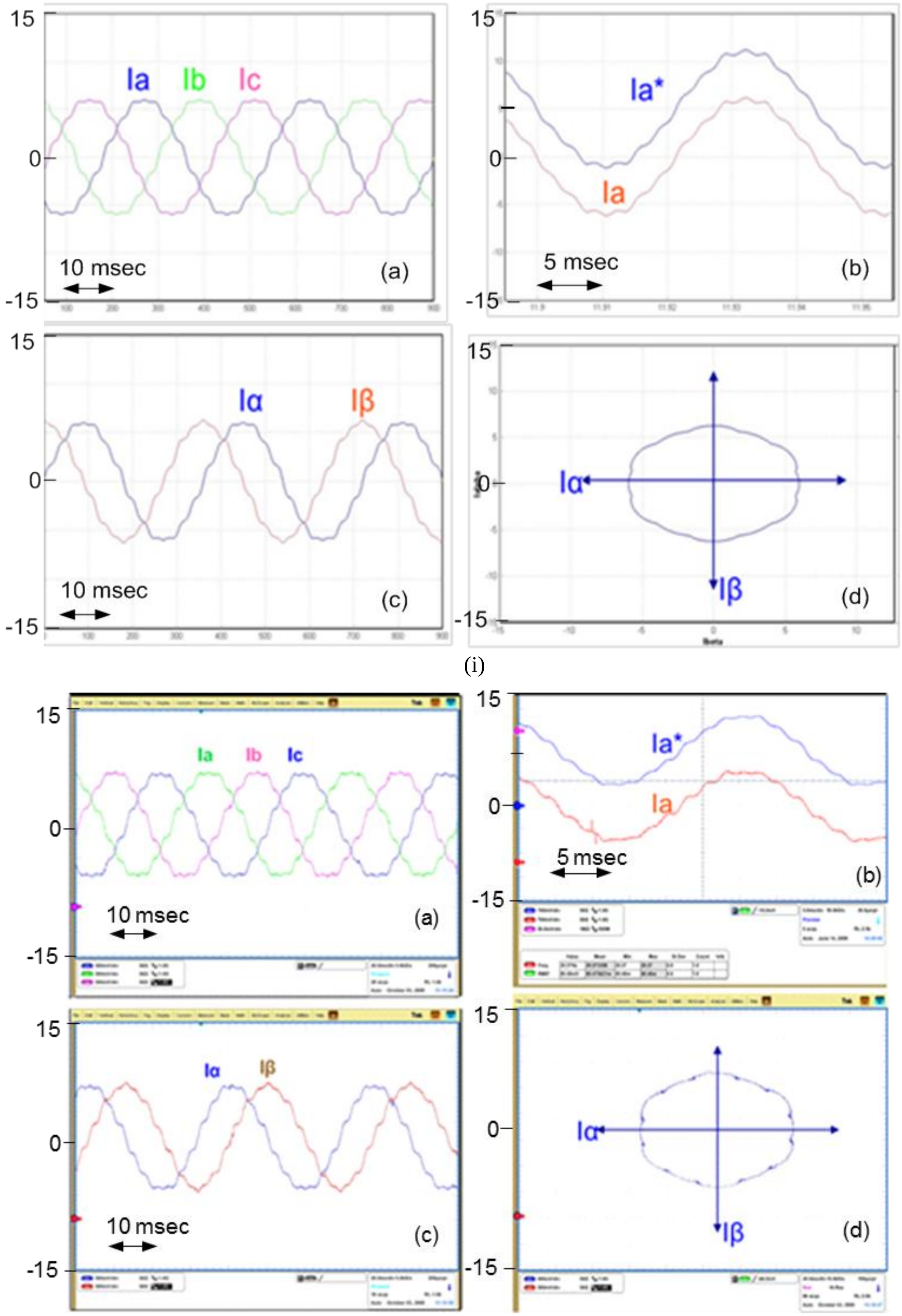

(i)

(ii)

Figure 3.15. Stator excitations for machine I at 700 rpm: (i) simulation result (ii) experimental result

Figures 3.16(a-c) show the steady state performance of all the excitation schemes for machine I. The reference speed is set to 700 rpm while the load torque is 1 N.m.

Figures 3.17 (a-c) show the steady state waveforms of the three excitation schemes considering machine II. The reference speed is 300 rpm and the load torque is 0.2 N.m.

For both cases, the variables shown are: (i) load torque, (ii) duty cycle, (iii) measured current, and (iv) estimated rotor position.

A continuous PWM was used for square wave current and is labeled as 'Duty-a' in Figure 3.16(a). Discontinuous PWM is used for sinusoidal and NSHI excitation and shown in Figures 3.16(b) and (c), respectively. The duty cycles are bounded between 1 and -1.The current regulator in case of machine I, cannot not be regulated beyond 1800 rpm using square wave excitation because the duty cycles using carrier based PWM are saturated. However, discontinuous PWM, due to their 15 percent higher voltage gain over continuous PWM method, allows a 10% higher speed operation for sine and NSHI excitation methods. As explained in section 3, square wave current injection requires higher rms current and which in turn requires higher voltage to generate the same average torque as compared to other schemes. The same behavior is noted in machine II.

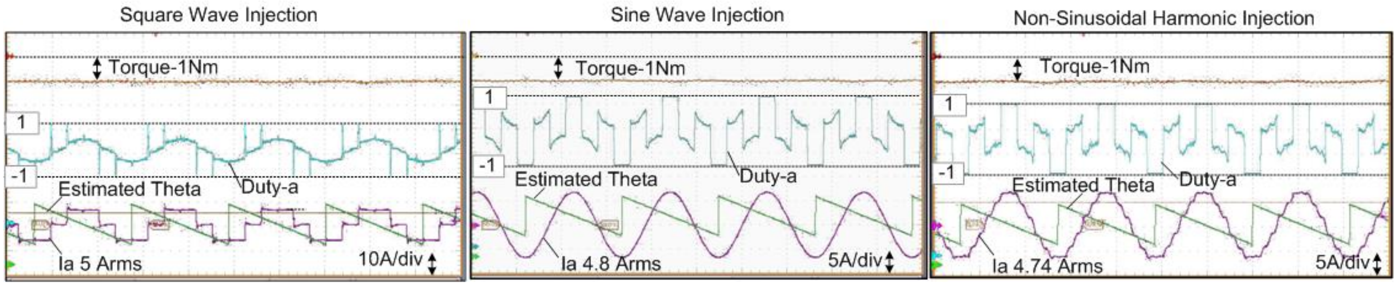

(a) (b) (c)

Figure 3.16.Experimental results: Stator excitations for machine I at 700 rpm (a) Square Wave Injection (b) Sine Wave Injection, (c) Non-Sinusoidal Harmonic Injection

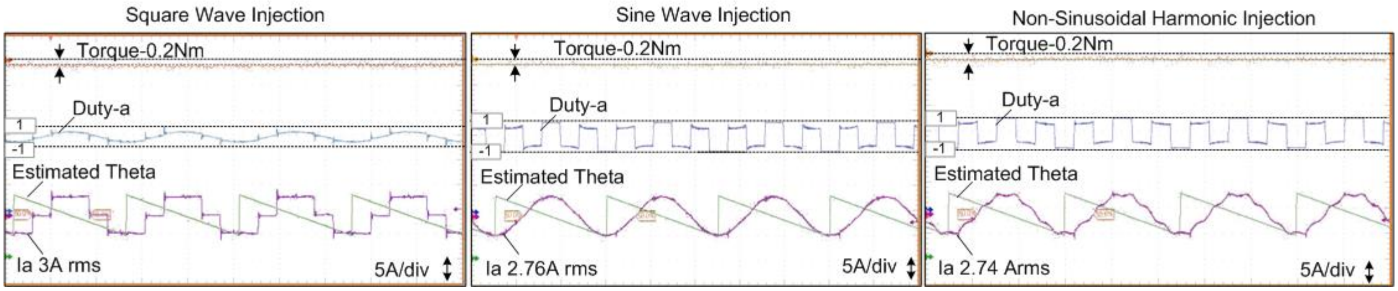

(a) (b) (c)

Figure 3.17.Experimental resultsof machine II at 300 rpm for: (a) Square Wave Injection (b) Sine Wave Injection, and (c) Non-Sinusoidal Harmonic Injection

To understand stator resistive and core losses, the machines under test are set in torque mode of operation while the drive motor is set in speed mode. Then using the drive motor, the speed is varied from 300 rpm to 2000 rpm for machine I and from 200 rpm to 1300 rpm for machine II. Using current control, stator currents are aligned with the back-EMF to achieve an average torque of 1N-m and 0.2 N-m for machine I and II, respectively. For each operating point, the active power, efficiency and rms currents are recorded from the power analyzer.

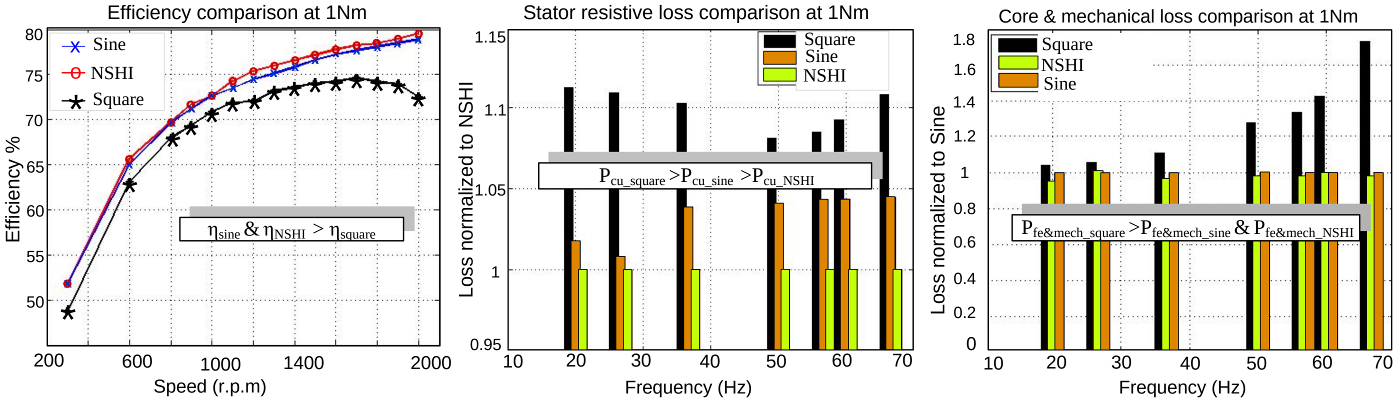

(a) (b) (c)

Figure 3.18.Experimental results: Performance of machine I (a) Efficiency comparison (b) stator resistive loss normalized to NSHI losses (c) Core and mechanical loss normalized to sine injection loss

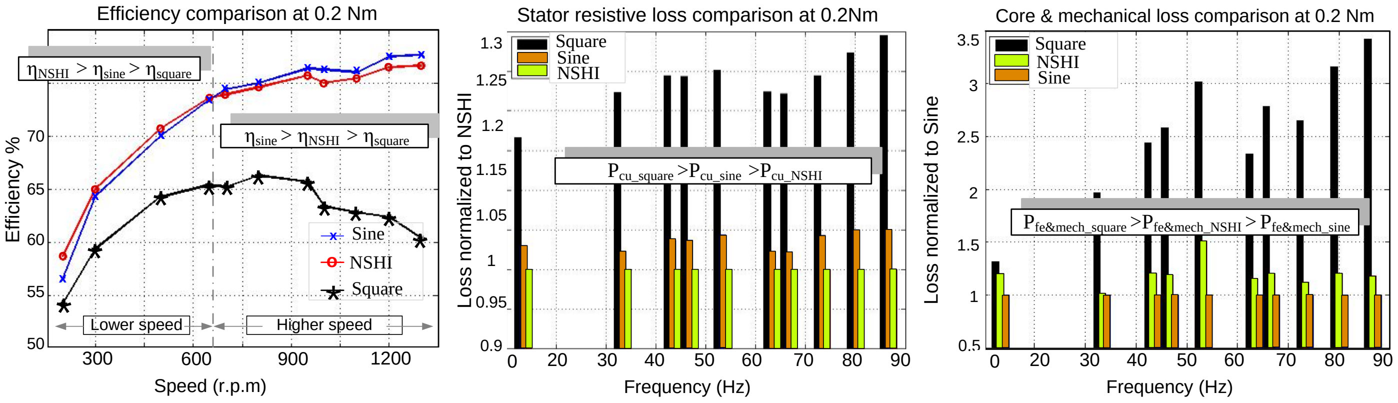

(a) (b) (c)

Figure 3.19.Experimental results for machine II: (a) Efficiency comparison, (b) stator resistive loss normalized to NSHI losses, and (c) Core and mechanical loss normalized to sine injection loss

Figure 3.18 (a) shows the three efficiency curves for machine I due to the three current excitation schemes. Since the machine I have low percentage of harmonics in its back EMF, sinusoidal and NSHI current injection schemes yield comparable efficiencies. However, both the schemes demonstrate higher efficiency over square wave excitation.

Figure 3.19 (a) shows the efficiency difference between the three current control schemes for machine II. It should be noted that this machine has higher back EMF harmonics. From Figure 3.19 (a), NSHI scheme has better efficiency amongst the three schemes below 700 rpm while sine current injection scheme has the highest efficiency amongst them beyond 700 rpm. The different efficiencies at low and higher speed of operation due to the NSHI and sinusoidal schemes respectively validate the case for hybrid current control proposed in section 3.5. To evaluate the differences in efficiencies it is essential to measure stator resistive and core loss ratio of the machine.

The stator resistive losses for the three phase system are calculated as

$$P_{cu} = r_s(I_{Arms}^2 + I_{Brms}^2 + I_{Crms}^2) \tag{3.37}$$

Then the stator resistive loss ratio for three excitation schemes is obtained from the measured stator rms currents and the measured stator resistance. Since NSHI scheme has the lowest stator resistive loss, it is used as the baseline. As explained in section 3.3, sinusoidal and NSHI schemes yield at least 10% lower losses than square wave injection scheme. The same is validated experimentally in Figure 3.18 (b) and Figure 3.19 (b) for machine I and II, respectively, at various speed of operation. It is also seen that sinusoidal current injection scheme has higher stator resistive losses than NSHI scheme.

The relationship between the core loss P_{fe}, mechanical loss P_m, stator resistive loss, shaft power and the input active power P_{in} is given as

$$P_{fe} + P_m = P_{in} - P_{out} - P_{cu} \tag{3.38}$$

where the shaft output power P_{out} is calculated as the product of the measured torque and the measured shaft angular speed. Since core and mechanical losses were not separated, combined losses given by (3.38) were used to study the influence of harmonics on the machine. The mechanical losses are assumed to be the same for the three excitation schemes and constant for a given speed of operation. It is understood that for a fixed speed and load torque, the difference in efficiencies of the machine for various stator excitations is mainly due to electrical and magnetic losses and not the frictional and windage losses. Accordingly, the combined core and mechanical loss ratio for the three excitation schemes was obtained using (3.38). Since, sinusoidal excitation scheme has the lowest core losses; it is used as the baseline.

Figure 3.18 (c) depicts that sinusoidal and NSHI schemes have similar losses which are much lower than square wave current injection scheme. The similarity of losses in sine and NSHI schemes is due to lower back EMF harmonics in machine I. Figure 3.19 (c) shows the combined loss comparison between the three current injection schemes as per (3.38). It is observed that, square wave current yields the highest losses. Also, NSHI scheme results in higher combined losses when compared with sinusoidal current injection scheme. The increase is attributed to higher back EMF harmonics in machine II that results in higher current harmonics as derived in Table 3.1. Although stator resistive losses for NSHI scheme is still the lowest amongst all, it is implied that the core losses deteriorate the performance of the NSHI scheme at higher speeds. Subsequently, the algorithm needs to be switched to sinusoidal current injection in order to retain higher efficiency operation as shown in Figure 3.11.

Such a method is referred to as a hybrid scheme that combines the strategy for injecting sinusoidal or NSHI currents based on operating point of the machine.

The experimental results, especially Figure 3.19 (a), validate the trade-off highlighted using analytical loss estimation methods. The increase in losses is in agreement with the prediction in section 3.4. Requirement of a hybrid approach must be evaluated based on the type of machine and its material properties by applying the analytical loss analysis provided in section 3.4.

3.7. Summary and Conclusions

The analysis and results presented in this chapter provide a valuable insight into multiple aspects in applying non sinusoidal back EMF PMBDCM for variable speed drive application. Performance and efficiency of the motor is evaluated analytically under various stator excitation schemes. Accordingly following are the significant contributions of this work.

1. The generalized expressions as a function of back EMF characteristics are derived to evaluate the motor performance. Using these expressions, the torque ripple, stator resistive losses, iron losses, and power conversion ratio of the square, sinusoidal and non-sinusoidal currents are evaluated and presented for motors having different back EMF waveforms.
2. An analytical approach to estimate qualitative and quantitative core losses in the motor under loaded condition for various stator excitation schemes show that sinusoidal current injection yields lowest core losses.
3. Efficiency and loss comparisons of sine, square and NSHI current control made on two PMBDCMs at various speeds validates the trade-off highlighted using analytical loss estimation methods. In this aspect, it is advantageous to use NSHI scheme in the speed range until the sum of drive conduction and stator resistive losses exceeds core losses of the machine. When core losses become dominant, the algorithm is modified to sinusoidal current control thus maintaining higher efficiency operation.
4. Closed form solution for non-sinusoidal currents and corresponding controller implementation yields better tracking performance over conventional approaches.
5. The proposed hybrid approach enables higher efficiency operation in entire speed range for variable speed drives applications.

APPENDIX

Coefficients for the instantaneous square wave currents in Table I

$$b_1 = 1, b_5 = 0.2, b_7 = 0.143, b_{11} = 0.091,$$
$$b_{13} = 0.077, b_{17} = 0.058, b_{19} = 0.053, b_{23} = 0.044$$

Table A.1. Machine II geometry and coefficients

Name	Value	Name	Value
Inner radius of stator (mm)	31.33	Stator length (mm)	25.4
Outer radius of stator (mm)	59.68	Tooth width (mm)	5.303
Thickness of magnets (mm)	4.8	Yoke depth (mm)	6.5
Tooth flux density (T)	0.293	Tooth height (mm)	24.80
Yoke Flux density (T)	0.204	Magnet Coverage (mm)	42.6
Tooth Volume (m^3)	8.02e-5	Slot width (mm)	7.15
Yoke Volume (m^3)	2.92e-5	Airgap length (mm)	1.27
Number of turns	32	Magnet Arc 2β (deg)	38.2
Number of Slots	24	Permeability coefficient	4πe-7
Eddy Loss coefficient (W/Kg)	4.05e-4	Steinmetz coefficient	2
Mass Density of Steel (Kg/m^3)	7650	Hysteresis Loss coefficient (W/Kg)	0.0105

Table A.2. Machine I with geometry and coefficients

Name	Value	Name	Value
Inner radius of stator (mm)	58.5	Stator length (mm)	76.3
Outer radius of stator (mm)	95	Tooth width (mm)	5.303
Thickness of magnets (mm)	4.8	Yoke depth (mm)	19.3
Tooth flux density (T)	1.6	Tooth height (mm)	17.2
Yoke Flux density (T)	1.2	Magnet Coverage (mm)	56.9
Tooth Volume (m^3)	2.94e-4	Slot width (mm)	7.6
Yoke Volume (m^3)	7.86e-4	Airgap length (mm)	2
Number of turns	24	Magnet Arc 2β (deg)	120
Number of Slots	36	Permeability coefficient	4πe-7
Mass Density of Steel (Kg/m^3)	7650	Steinmetz coefficient	2

REFERENCES

[1] R. Krishnan, *Permanent Magnet Synchronous and Brushless DC Motor Drives*, CRC Press, 2010.

[2] B.D. Bedford, R.G. Hoft, *Principles of Inverter Circuits*, J Wiley, New York , 1964.

[3] T. Lipo and F. Turnbull, "Analysis and comparison of two types of square-wave inverter drives," *IEEE Trans.Ind. Appl*., vol. IA-11, Mar./Apr. 1975, pp. 137-147.

[4] T. Nehl, F. Fouad, and N. Demerdash, "Digital simulation of power conditioner-machine interaction for electronically commutated dc permanent magnet machine," *IEEE Trans. Magn*., vol. MAG-17, pp.3284-3286, Nov. 1981

[5] PillayP. , and R. Krishnan, "Modeling, simulation, and analysis of permanent-magnet motor drives. II. The brushless DC motor drive," *IEEE Trans. Ind. Appl*., vol. 25, no. 2, pp. 274 –279, Mar/Apr. 1989.

[6] PillayP. , and R. Krishnan, "Application characteristics of permanent magnet synchronous and brushless DC motors for servo drives," *IEEE Trans. Ind. Appl*., vol. 27, no. 5, pp. 986 –996, Oct. 1991.

[7] T. M. Jahns, "Torque production in permanent-magnet synchronous motor drives with rectangular current excitation," *IEEE Trans. Ind. Appl*., vol. 20, no. 4, pp. 803-813, July/Aug. 1984.

[8] T.M. Jahns, and W.L. Soong, "Pulsating torque minimization techniques for permanent magnet AC motor drives-a review", IEEE Trans. Ind. Electron., Apr 1996, Vol 43-2, pp 321-330.

[9] Y. F. Shi, Z.Q. Zhu, and D. Howe, "Torque-speed characteristics of interior-magnet machine in brushless AC and DC modes, with particular reference to their flux-weakening performance," Proc. Int. Power Electronics and Motion Control Conf., IPEMC 2006, 13-16 August, 2006, Shanghai, China.

[10] J.R. Hendershot Jr., TJE Miller, Design of Brushless Permanent Magnet Machines, Motor Design Books LLC, 2010.

[11] Z.Q. Zhu, J.X. Shen, D. Howe, "Flux-weakening characteristics of trapezoidal back-emf machines in brushless DC and AC modes," *Proc.Int. Power Electronics and Motion*

[12] M. Miyamasu, K. Akatsu, "Efficiency comparison between Brushless dc motor and Brushless AC motor considering driving method and machine design", IECON Nov. 2011, pp 1830 – 1835

[13] J. Holtz , L. Springob, "Identification and Compensation of Torque Ripple in High-Precision Permanent Magnet Motor Drives", IEEE Trans. Ind. Electron, Vol. 43, No. 2, 1996, pp. 309-320.

[14] F. Piriou, A. Razec. R. Perret, H. Le-Huy, 'Toque Characteristics of Brushless DC Motors with Imposed Current Waveforms", *IEEE* IAS 1986, pp, 176-181.

[15] J.Y. Hung, Z. Ding, "Minimization of Toque Ripple in Permanent- Magnet Motors: A Closed Form Solution", *IEEE IECON*, 1992, pp. 459-463

[16] D. Hanselman, "Minimum Torque Ripple, Maximum Efficiency Excitation of Brushless Permanent Magnet Motors", *IEEE Trans. Ind. Electron*, Vol. 41, No. 3, 1994, pp. 292-300.

[17] *P.L.* Chapman, S.D. Sudhoff, C.A. Whitcomb, "Optimal Current Control Strategies for Surface-Mounted Permanent-Magnet Synchronous Machine Drives", *IEEE Trans. Energy Convers*, Vol. 14, No. 4, Dec 1999.

[18] R.Leidhold, G. Garcia, "PMAC motor control strategy, based on the instantaneous active and reactive power, for ripple-torque and copper-losses minimization", *IEEE IECON*, 2000. vol.2, pp-1401-1405.

[19] N. Bianchi, S. Cervaro, L. Malesani, "Current Shapes For Minimizing Torque Ripple In SPM Motors", *Proc. ICEM* , 2000 pp. 1237-1241.

[20] T. Kim, H-W Lee, M. Ehsani, "High Performance Brushless Permanent Magnet Motor/Generator Drives in Electric and Hybrid Electric Vehicles", *IEEE PESCAnnu. Meeting*, Oct 2006, pp. 1 – 5.

[21] D Grenier,. R Mende,. J.P Louis, ,"Comparison of several control strategies for DC Brushless Drives", *IEEE IECON*, 1994. vol.1, pp-26-31

[22] A. Lidozzi, L. Solero, F. Crescimbini, R. Burgos "Sensorless Speed Vector Control of a Trapezoidal back-EMF PMSM Machine using Pseudo- Park Transformation for Fan Motor Drives", *IEEE Power Electron. Spec. Conf*, 2008, pp-2167-2171.

[23] A. Oliveira, J. Monteiro, M. Aguiar, D. Gonzaga, "Extended DQ transformation for vectorial control applications of Non-Sinusoidal Permanent Magnet Synchronous Machines", *IEEE Power Electron. Spec. Conf*,2005, pp 1807-1812.

[24] Z.Q. Zhu, K. Ng, and D. Howe, "Analytical prediction of stator flux density waveforms and iron losses in brushless DC machines, accounting for load condition," vol. 2, pp. 814–817.

[25] G.R. Slemon and X. Liu, "Core losses in permanent magnet motors," *IEEE Trans. Magnetics*, vol. 26, no. 5, pp. 1653-1655, Sept.1990.

[26] K.J. Tseng, S.B. Wee, "Analysis of Flux Distribution and Core Losses in Interior Permanent Magnet Motor", *IEEE Tran. Energy Convers*., vol. 14, no. 4, Dec 1999, pp. 969-975.

[27] C. Mi, G.R. Slemon, and R. Bonert, "Modeling of iron losses of permanent-magnet synchronous motors," Industry Applications, IEEE Transactions on, vol. 39, no. 3, pp. 734–742, Jun. 2003.

[28] R. Rabinovici, T.J.E. Miller, “Eddy-current losses of surface-mounted permanent magnet motors”, *IEE Proc. Electr. Power Appl.*, Vol 144, No 1, Jan 1997, pp. 61-64.

[29] J.R. Hendershot Jr., TJE Miller, *Design of Brushless Permanent Magnet Machines*, Motor Design Books LLC, 2010.

[30] P. Kshirsagar, R.P Burgos, J. Jang, A.Lidozzi, , F. Wang, D. Boroyevich, S. K. Sul, “Implementation and Sensorless Vector-Control Design and Tuning Strategy for SMPM Machines in Fan-Type Applications”, *IEEE Transactions on Power Electronics and Industry Applications Joint Special Issue Nov-2012*.

[31] P. Kshirsagar, R Krishnan, “Efficiency Improvement Evaluation of Non-Sinusoidal Back-EMF PMSM Machines Using Field Oriented Current Harmonic Injection Strategy”, *IEEE Energy Conversion Congress Exposition (ECCE) Annu. Meeting*, 2010, pp- 471– 478.

[32] J. Holtz, “Pulsewidth Modulation for Electronic Power Conversion.” *Proc. IEEE 82*, no. 8 (August 1994): 1194 – 1214.

Chapter 4 Analysis of Efficiency Improvement in PMSM Drives through Switching Frequency Reduction

4.1. Abstract

In previous chapter, methods for improving efficiency of permanent magnet brushless DC motor (PMBDCM), using various stator excitation strategies were shown. This chapter will focus on improving the efficiency in permanent magnet synchronous motor (PMSM) drive system.

The PMSM drive system efficiency can be improved by optimizing the losses in the machine or inverter or both. The motor's predominant losses are its resistive and iron losses. Then the remaining dominant losses are in the inverter in the form of its conduction and switching losses. Considering the IGBT devices in thee inverter, its conduction loss is proportional to the magnitude of the current while the switching loss is a function of the current and switching frequency of the inverter. For a given the current in the inverter, then the losses that can be minimized are dependent on the switching frequency. Therefore, the approach considered in this research is that given an optimally designed permanent magnet machine and its control algorithm, the only option to improve the system efficiency is by reducing the inverter switching losses by minimizing the switching frequency.

At reduced switching frequencies, the small impedance offered by the phase windings of PMSM to the inverter voltage waveform causes distortion of current waveform which increases the losses in the motor. To reduce this distortion, programmed pulse width modulators (PWM) are preferred over conventional carrier based modulators and therefore considered in this study. Analytical loss modeling of the motor and the inverter is central to the efficiency evaluation at low switching frequencies. Accordingly, for the motor, the stator resistive and iron losses are derived and validated using finite element simulations. For the inverter, the conduction and switching losses are derived considering programmed PWM and validated using circuit based simulations. Using the analytical models, loss comparison between five PMSM drive systems of various power ratings is made to quantify the efficiency improvement. It is shown that the efficiency of the PMSM drive system can be improved by reducing the switching frequency of the inverter and applying programmed PWM techniques. Such an approach has not been reported in the existing literature and hence considered in this research.

4.2. Introduction

Most of the previous work on low switching operation of motor drives has been focused on induction machines. Application of the same for PMSM must be carefully evaluated as the two machines have different operational and control characteristics. The following sections highlight the differences between the relevant prior work and topics that have not been addressed on analysis of efficiency improvement in PMSM drives through switching frequency reduction.

4.2.1. Operation of PMSM drives at reduced switching frequency

State of the art three phase variable speed motor drives have switching frequencies in the range of 2 kHz to 20 kHz depending on their power level. High switching frequencies (above 10 kHz) are used in applications where precise position control or low acoustic noise is desired. For applications where such requirements are not stringent, the switching frequency can be significantly reduced. The operation of motor drives with low switching frequency was a highly researched topic in the 1960's and the 70's because of use of slow devices such as thyristors and bipolar transistors [1 3]. In order to minimize the motor harmonic losses at low switching frequencies, programmed pulse width modulation (PWM) methods were resorted to [4]. The optimized PWM methods were mainly developed for reduction of losses in the stator as well as in the rotor of the induction machines[4]. After the advent of faster switching devices such as MOSFETs and IGBTs, programmed PWM methods are currently limited to medium voltage high power drives [5] and mainly for induction machines. Research on reduced switching frequency control of permanent magnet motors remains yet to be explored in depth.

In comparison to induction machines, PMSMs have significant advantages in power density, and motor and drive system efficiencies. Power density is enhanced in the PMSM due to PM-field excitation which reduces the ampere-turn requirement on the stator side and additionally having no windings on the rotor side resulting in elimination of resistive losses on it. The permanent magnets contribute to a reduction of stator and elimination of rotor resistive losses as well as harmonic iron losses [6-8]. In [9], it was shown that in induction machines operating at reduced switching frequencies and asynchronous PWM (800Hz), the rotor harmonic losses were up to 50 percent of the total machine losses. Since PMSM do not have rotor windings, the corresponding total harmonic losses are lower allowing further reduction of switching frequency. In [10], the advantage of higher q-axis inductance in interior permanent magnet motors for reduced switching frequency operation was mentioned but was not pursued for further research.

The lower harmonic loss implies lower de-rating of the PMSM at reduced switching frequencies than in the case of the induction machines. These aspects of combined PMSM and inverter sizing in light of reduced switching operation have not been discussed in the current literature prior to this research is to be noted.

4.2.2. Loss Analysis of PMSM drive system at reduced switching frequencies

Literature on detailed loss evaluation of PMSM drive system with complementing PWM strategies at reduced switching frequencies is very limited. In [11], losses in a 1.5kW PMSM drive system were evaluated to optimize the system efficiency considering motor inductance as a variable. The total system losses were calculated by varying the switching frequency from 16 kHz to 450 Hz using asynchronous carrier based PWM. The research also considered a six-step modulation method to analyze the total system losses at the fundamental frequency. The motor stator resistive losses were calculated using conventional method while the iron losses were calculated using finite element simulations. The analysis showed that, at certain value of motor inductance, six-step mode of operation resulted in lower system level losses than asynchronous carrier based PWM above 5 kHz. The choice of the inductance with this method allows lower de-rating of the drive. Although low switching frequency operation of PMSM drive was evaluated, following important aspects related to its operation and detailed analysis of the losses remain to be addressed in [11]:

- The research primarily focused on high inductance machines to improve drive de-rating. Higher inductance essentially increases the copper and iron volume and also the cost of the system. Tradeoff between the motor and drive cost was not discussed.
- The modulation strategies for reducing the current harmonic distortion at low switching frequencies (below 1 kHz) were not explored. In [12], it is shown that programmed PWM offers lower current harmonic distortion than carrier based and six-step modulators. Thus it is essential to evaluate the losses in PMSM drive system considering programmed modulation methods as well.
- The semiconductor losses were calculated analytically using the instantaneous, root mean square and average amplitude of the reference current. The reference current is usually devoid of any harmonic content whereas at low switching frequencies, the actual current has significant harmonics. The sinusoidal approximation of the actual current by considering the reference current results in considerable errors in the estimation of conduction as well as switching losses. Therefore, accurate methods for estimating the instantaneous, root mean square and average amplitudes of the actual current are essential during modeling the semiconductor device losses at low switching frequencies.
- The approach of estimating the core losses in the motor considered only eddy current losses using finite element analysis simulations. The loss analysis did not account for the hysteresis losses. At reduced switching frequencies, both losses must be considered. Hence a simplified

analytical approach that incorporates the predominant components of core losses to understand the influence of low switching frequency on PMSM harmonic losses is necessary.

- The total system loss analysis was performed on a single 1.5 kW low voltage PMSM motor drive system. The study did not address the advantages or disadvantages of reducing the switching frequency for large power PMSM drives with semiconductor devices of larger voltage ratings. Thus a comparative loss analysis of PMSM drive systems operating at various power levels is required to cope with the wide range in practice.

In [13], total system losses in a 3kW interior permanent magnet synchronous motor (IPMSM) drive operating at various switching frequencies were analyzed. This study has similar approach to the one in [11] except that instead of varying the motor inductance to reduce harmonic current amplitude, a three-level voltage source inverter was considered. The switching frequency of the inverter was varied from 10 kHz to 5 kHz using asynchronous carrier based PWM. A single-pulse modulation method was also considered to analyze the losses at the fundamental frequency. Based on the analytical calculations of the system losses, it was shown that, single-pulse mode of operation was more efficient than carrier based PWM at 5 kHz when the motor operating speed was higher. However, the analysis in [13] lacked insight into the following points:

- The analysis did not consider synchronous modulators or programmed pulse width modulators. It is known from [12] that these modulators have superior harmonic performance at high modulation indices and low switching frequencies.
- Influence of semiconductor device voltage rating on system efficiency improvement cannot be easily gauged as the two and three level converters have different operating voltages and devices as well.
- For optimizing the switching frequency, it is essential to have analytical methods for estimating the core losses. The core loss estimation method is in [13] is dependent on finite element simulation making the system loss evaluation very time consuming.

Based on the above review, analysis on benefits of reduced switching frequency incorporating various PWM methods for permanent magnet motors driven by two-level inverters and its experimental validation require further investigation.

Accordingly, the proposed research work is:

1. ***Programmed PWM methods and its application to PMSM drives at reduced switching frequencies:***

   At reduced switching frequencies, it is essential to investigate pulse width modulators of the inverters driving the PMSM to reduce the total system losses. Accordingly, asynchronous and synchronous carrier based and programmed pulse width modulators are discussed in sections

4.3.The influence of motor inductance on current harmonic distortion for various PWM schemes is also detailed in the same section.

2. ***Analytical estimation of PMSM's stator resistive and core losses at reduced switching frequencies:***

   Analytical procedure for estimating PMSM's stator resistive and core losses at reduced switching frequency is presented in section 4.4. A comprehensive analysis of motor harmonic losses for various switching frequencies considering various motor lamination materials is provided in the same section.

3. ***Analytical estimation of inverter losses at reduced switching frequencies:***

   Analytical procedure for estimating the semiconductor losses is elaborated in section 4.5.The method is based on accurate estimation of the instantaneous, root mean square and average current through the switching device given the programmed PWM methods.

4. ***Comparative loss analysis of PMSM drive systems at reduced switching frequencies:***

   Using the analytical loss models of the motor and inverter, total system losses of five PMSM drive systems which are rated from 250W up to 100 kW are analyzed at reduced switching frequencies in section 4.6. The loss analysis validates that the total system efficiency can be improved at reduced switching frequencies.

4.3. Modulation strategies for reduced switching frequency operation

For reduced switching frequency operation, it is critical to select the right pulse width modulators to reduce the current harmonic distortion in the motor and inverter. Various pulse width modulation strategies that have been reported in the literature and they are:

(a) Asynchronous and synchronized carrier based modulation [12]
(b) Programmed pulse width modulation (PWM)
    i. Selective harmonic elimination [1-3]
    ii. Synchronous optimal modulation [4]

Considering variable speed operation of PMSM drive system, the switching frequency is gradually reduced as the motor attains its rated speed. During standstill and low speed of operation, the ratio of switching frequency to fundamental frequency is high (N> 15). In such cases, the asynchronous carrier based modulators (also known as sub-oscillation modulation) are used [12]. When this ratio is below 15, then synchronous or programmed PWM methods are applied [12].

Accordingly, the following sections present a brief summary of the asynchronous and synchronous carrier based modulators.

4.3.1. Asynchronous carrier based modulators

The three-phase instantaneous fundamental voltages $V_{abc}(t)$desired across the motor terminals are given as,

$$\begin{aligned} V_a(t) &= V_m \cos(\omega_r t + \varphi) \\ V_b(t) &= V_m \cos\left(\omega_r t - \frac{2\pi}{3} + \varphi\right) \\ V_c(t) &= V_m \cos\left(\omega_r t + \frac{2\pi}{3} + \varphi\right) \end{aligned} \tag{4.1}$$

where V_m is the peak amplitude of the applied voltage, ω_r is the rotor velocity and φ is the phase angle between the current and voltage vector. Since the neutral of the motor is not connected to the mid-point of the DC link capacitors of the inverter, a third harmonic zero sequence voltage $V_{no}(t)$ can be added to the fundamental voltages in (4.1) and the new reference phase voltages are given as [14],

$$\begin{aligned} V_a(t)^* &= V_a(t) + V_{no}(t) \\ V_b(t)^* &= V_c(t) + V_{no}(t) \\ V_c(t)^* &= V_c(t) + V_{no}(t) \end{aligned} \tag{4.2}$$

There are various types of the zero sequence voltages that can be added to the fundamental voltage. Depending on the nature and amplitude of the zero sequence voltage, infinite combination of modulation methods can exist. If the zero sequence voltage waveform is of continuous type (say, *sinusoidal*), then the modulation methods are known as continuous PWM (CPWM), whereas if it is of discontinuous type, the methods are known as discontinuous PWM (DPWM) [14-16].

4.3.1.1. *Continuous pulse width modulators (PWM)*

For continuous PWM, the zero sequence voltages given in (4.3) are the most commonly reported type [14-19]. If the amplitude of the zero sequence voltage is 1/6th of the fundamental voltage V_m, then the gain of the inverter is increased by 15 percent [14]. In [17], it is also shown that if the amplitude of the zero sequence voltage is 1/4th of fundamental voltage, the current harmonic distortion is lowest amongst the known CPWMs.

$$\begin{aligned} V_{no}(t) &= -\frac{V_m}{6}\cos(3\omega_r t) \\ V_{no}(t) &= -\frac{V_m}{4}\cos(3\omega_r t) \end{aligned} \tag{4.3}$$

4.3.1.2. *Space Vector Modulator (SVM) and Discontinuous PWM modulators (DPWM)*

Space vector modulation (SVM) and discontinuous PWM (DPWM) have been extensively studied in [12-16]. A three phase six-switch inverter has eight switching states. Of these eight states, six states produce a resultant output voltage vector. These six states are known as active states. The remaining two states do not produce any output voltage and therefore are known as zero states. The distribution of the zero states around the active states in one switching period results in various PWM strategies. When the two zero states are symmetrically distributed around active states, it results in center aligned space vector modulation (SVM) [14]. When only one of the zero states is used to reduce the number of switching transitions, it results in discontinuous pulse width modulation (DPWM). Since the zero states directly modulate the zero sequence voltage of the inverter, they can be expressed in closed form expression. Accordingly, a generalized zero sequence voltage equation for generating space vector as well as discontinuous PWM modulators is given as, [18]

$$V_{no}(t) = \frac{1}{2}V_{dc}\cdot[1-2\alpha(t)] + [\alpha(t)-1]\cdot V_{\max}(t) - \alpha(t)\cdot V_{min}(t) \tag{4.4}$$

where V_{dc} is the DC bus voltage, $and\, V_{max}(t)$ and $V_{min}(t)$ are the maximum and minimum instantaneous voltages, resepectively, and given as,

$$V_{max}(t) = \max[V_a(t), V_b(t), V_c(t)],\, V_{min}(t) = \min[V_a(t), V_b(t), V_c(t)] \tag{4.5}$$

and $\alpha(t)$ determines the selection of continuous or discontinuous zero sequence voltage waveform given as,

$$\alpha(t) = 0.5 \text{ or } \alpha(t) = 1 - 0.5 \cdot (1 + sgn[sin(3\omega_r t + \delta)]), \tag{4.6}$$

In (4.4), if $\alpha(t) = 0.5$, then the resulting reference voltage waveform is equivalent to space vector modulation, whereas if $\alpha(t) = 1 - 0.5 \cdot (1 + sgn[sin(3\omega_r t + \delta)])$, then the resulting voltage waveforms are of discontinuous PWM type. The variable δ in (4.6) is determined by the power factor of the load. It is varied to minimize the total inverter losses and is given as [19],

$$\delta = \tan^{-1}\left(\frac{{v_{dsr}}^*}{{v_{qsr}}^*}\right) - \tan^{-1}\left(\frac{{i_{dsr}}^*}{{i_{qsr}}^*}\right) \tag{4.7}$$

where ${v_{dsr}}^*$ and ${v_{qsr}}^*$ are the reference voltages while ${i_{dsr}}^*$ and ${i_{qsr}}^*$ are the reference currents in rotor reference frame. Using (4.1)-(4.7) asynchronous carrier based space vector and discontinuous modulators can be synthesized. In discontinuous PWM, the phase voltage is clamped to DC bus for 120 degrees which implies that the inverter phase leg is not switching for one third of the fundamental cycle. This approach significantly reduces the switching losses in the inverter.

The above modulation methods are typically considered when the system requires higher switching frequency operation. When the switching frequency is reduced such that the ratio of the switching frequency to fundamental frequency is below 15 [12], synchronous carrier based modulators are resorted to.

4.3.2. Synchronized carrier based modulation

For reduced switching frequency operation, just the synchronization between carrier and the fundamental frequency can reduce the amplitude of low ordered current sidebands by up to 70 percent [12]. Synchronization implies that the ratio of carrier frequency f_s and the fundamental frequency f_1 has only N integral values given as,

$$N = \frac{f_s}{f_1} \tag{4.8}$$

Furthermore, the zero crossing of the carrier and the modulating signals are also synchronized. Any phase shift between them may result in higher current distortion for lower values of N. It is to be noted that N also represents the number of switching pulses in one fundamental cycle.

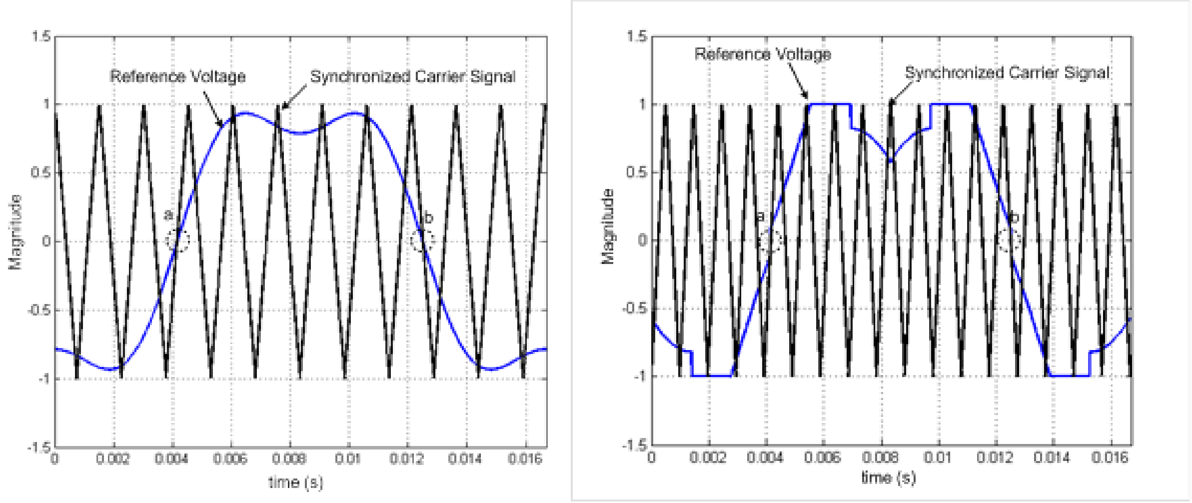

(a) (b)

Figure 4.1Synchronized carrier based modulator at M = 1.05: (a) with 25percent third harmonic injection and *N = 11*, (b) Discontinuous PWM with synchronized carrier signaland *N = 17*.

Figure 4.1 (a) shows the waveform of synchronized carrier based modulator with 25% third harmonic voltage added to the fundamental voltage and at a modulation index *M = 1.05*. The reference signal is compared with a synchronized carrier signal. The synchronization points are labeled as ‘a’ and ‘b’. The ratio of the switching frequency to the fundamental frequency is *11*.It should be noted that there are 11 cycles of carrier signal for one cycle of the reference voltage.

Figure 4.1 (b) shows the synchronized carrier based modulator with discontinuous PWM at the modulation index *M = 1.05* for N with a value of 17. The corresponding synchronization points are labeled as ‘a’ and ‘b’. In case of discontinuous PWM, the switching device is clamped to fully on state or off state for 120 degrees of the fundamental cycle. The corresponding reference voltage waveform shows its clamping at positive and negative peaks of the carrier signal. Since the switching losses are reduced due to the discontinuous PWM, the carrier frequency can be increased by 50 percent.

It is essential to evaluate the harmonic distortion in the motor current due to various carrier based modulators. Such a comparative evaluation is discussed in following section.

4.3.3. Current harmonic distortion of carrier based modulators

Operation of PMSM at lower switching frequencies requires detailed analysis of various PWM methods and their influence on the current harmonic distortion. The definition of current harmonic distortion will be briefly reviewed and will be applied to various PWM strategies for their comparative evaluation.

The stator resistance, in general, is smaller than the reactance and hence, by ignoring the stator resistance the stator harmonic phase current is given as,

$$I_n = \frac{V_n}{n\omega_1 L_s}\ , n = 2,3,4,\dots \tag{4.9}$$

where V_n and I_n are the harmonic amplitudes of the voltage and current, respectively, $\omega_1$is the fundamental frequency and L_s is the phase winding inductance. The stator harmonic resistive loss is proportional to the square of the rms value of the harmonic currents which is calculated in the following as,

$$I_\sigma = \sqrt{\frac{1}{2}\sum_{n=3,\cdots}^{\infty}\left(\frac{V_n}{n\omega_1 L_s}\right)^2} \tag{4.10}$$

Assuming the inductance remains constant over a wide frequency range, then for a given fundamental frequency, the expression of current harmonic distortion factor σ is given as [4],

$$\sigma = \sqrt{\frac{1}{2}\sum_{n=3,\cdots}^{\infty}\left(\frac{V_n}{n}\right)^2} \tag{4.11}$$

The expression in (4.11) represents the distortion due to the PWM modulator and the resultant voltage harmonics. Substituting (4.11) in (4.10), the rms harmonic current is given as,

$$I_\sigma = \frac{\sigma}{\omega_1 L_s} = \frac{\sigma}{Z} \tag{4.12}$$

where Z is the impedance of stator phase winding of the PMSM. The harmonic current I_σ can be minimized by using two approaches:(a) reducing distortion factor σ by reducing the voltage harmonics contributed by considered PWM schemes, and, (b) increasing the inductance and hence impedance of the machine. Both the methods must be evaluated at low switching frequencies to gauge their benefits. In [11] only the latter method was explored for a 1.5 kW PMSM.

To estimate the harmonic distortion factor σ, the amplitude of the harmonic voltages (V_n) is calculated using fast Fourier transform of the output switching voltage waveform. Then the square of harmonic distortion σ^2, also known as loss factor, is calculated to gauge the harmonic losses in the motor [12].

Figure 4.2 shows the relationship between the loss factor σ^2 and the modulation index ($M = 2V_m/V_{dc}$) for various PWM strategies and different values of *N*. Following observations are deduced from the chart:

1. The loss factor σ^2 reduces when the number of switching pulses *N* increases. It implies that the harmonic distortion is lower at higher switching frequencies. In the results shown, synchronized SVM with *N = 15* has the lowest value of σ^2.

2. For *N=7*and modulation index above 0.8, discontinuous PWM (DPWM) has lower distortion than sinusoidal PWM.
3. For *N =7* and modulation index above 0.95, DPWM has lower distortion than synchronous SVM with *N* = 9. The results show that for the same value of *N*, it is advantageous to consider a hybrid PWM technique that utilizes synchronous SVM up to modulation index of 0.95 and then transitions to DPWM for *M* above 0.95.

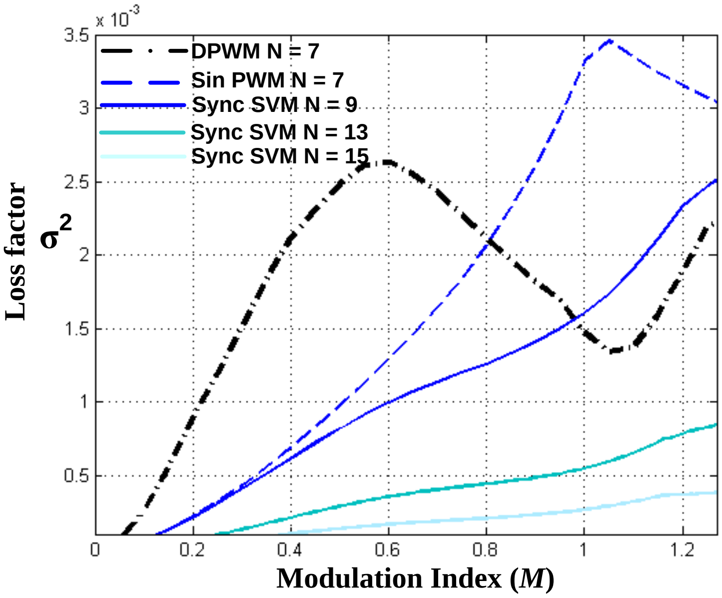

Figure 4.2. σ^2 versus modulation index for different carrier based modulators

4.3.3.1. Influence of motor inductance on rms harmonic current

The amplitude of the harmonic current can be reduced by increasing the inductance of the machine. The inductance of a three phase permanent magnet motor is given by [8],

$$L_s = \left(\frac{3}{2}\right)^2 \frac{\pi}{4} \mu_0 \frac{Lr}{l_g} \left(\frac{T_{ph}}{P_p}\right)^2 \tag{4.13}$$

where L is the length of machine, r is the outer radius of machine, $l_g$is the length of air-gap, T_{ph} are the number of turns per phase, and P_p are the number of pole pairs. From the (4.13), it is seen that the inductance is proportional to the square of the number of turns. Typically the machine is designed to operate at rated torque given by [8],

$$T_e = k(T_{ph} I_m),$$

$$k = \frac{3}{2}(DL)(B_m \sin\beta)\left(\frac{4}{\pi}k_w\right)\sin\delta \tag{4.14}$$

where D is the outer diameter of the machine stator, $B_m$is the peak flux density of magnet, β is the magnet arc length, $k_w$is the winding factor, $I_m$is the peak stator current, and δ is the control angle between the stator flux and rotor flux. The electromagnetic torque is directly proportional to the number of turns of the machine. It should be noted that with higher number of turns, the peak excitation current required for same torque will be lower due to the relationship in (4.14). However increasing the number of turns increases the volume of the machine and also its stator resistance. Also the motor dynamic performance is affected. For applications that do not need high dynamic performance, reducing switching frequency of inverter and increasing the motor inductance becomes a viable approach. Design of PMSM considering increased number of turns to increase the motor inductance is beyond the scope of this analysis. However, PMSMs with various inductances and PWM methods are analyzed qualitatively to understand the benefits of such an approach.

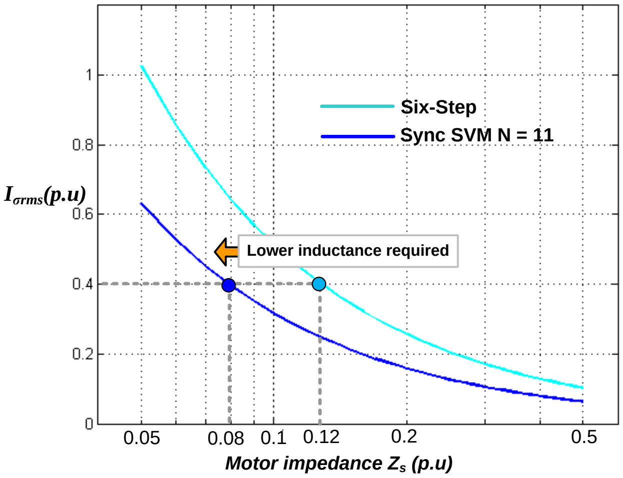

Figure 4.3. Comparison between six-step and synchronized SVM at N=11 considering per unit impedance and harmonic current amplitude (p.u)

The motor phase impedance is the product of the stator frequency and its phase inductance. Thus for a fixed stator frequency, the impedance is directly proportional to the motor inductance. Influence of motor impedance on rms harmonic current is shown in Fig 4.3. The impedance of the machine is varied from 5 percent to 50 percent of the base value. The synchronous SVM with $N = 11$ is compared with six-step quasi-square wave modulation at modulation index of 1.2. The synchronous inductance 'L_s' is plotted on a logarithmic scale due to the inverse relationship with the harmonic current amplitude as given in (4.5). It is seen that for high inductance values (above 0.5 p.u), the six-step and synchronous modulators will yield very low harmonic current amplitude. However for the case when the synchronous inductance is 5 percent, the six-step modulation method has 40 percent higher harmonic current than the synchronous SVM at $N=11$. It is also noted that in comparison to synchronous SVM, the six-step modulation requires at least 50% higher inductance to achieve the same harmonic current amplitude of 0.6 p.u.

Thus sizing of the machine is greatly affected with the choice of impedance and the harmonic currents in the machine. In [11], it was shown that for a PMSM with synchronous inductance of 0.26 p.u, the total system losses in six-step mode of operation were similar to those for the system operating at 5 kHz using carrier based modulators. However larger inductance implies larger voltage drop across the windings resulting in (a) higher phase resistance, (b) lower power factor of the motor [20], (c) lower operating speed, (d) higher DC link voltage requirement, and (e) higher VA rating of the system.

The other approach for reducing the current harmonic distortion is by modifying the PWM and it does not require redesign of the machine. The analysis in [11] or [13] does not consider the influence of programmed PWM for further reduction of the current harmonic distortion, and hence the following sections will elaborate on it.

4.3.4. Programmed PWM for selective harmonic elimination

A six-step square wave modulation contains 33.33% third harmonic, 20%fifth harmonic and 14.2% seventh harmonic components. When the fundamental component of the output voltage is reduced by varying the pulse width, harmonic components increase. It is essential to eliminate certain harmonics so as to achieve better current waveform quality. This section will explain the procedure to synthesize the voltage waveforms where some harmonics are selectively eliminated [3].

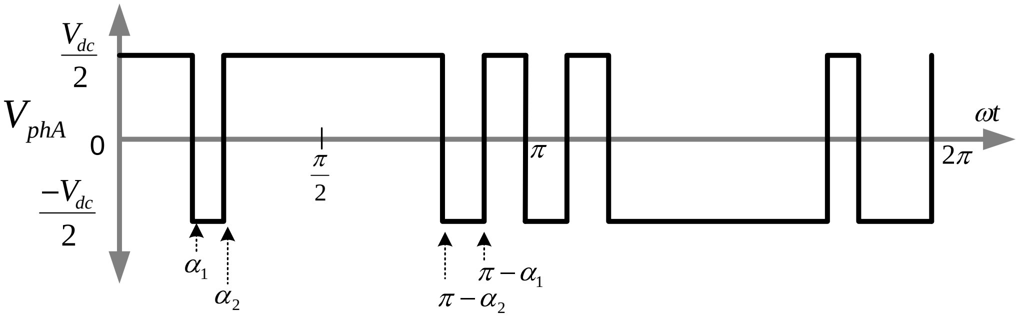

Figure 4.4. Phase voltage waveform of an inverter using selective harmonic elimination PWM (SHE PWM).

Figure 4.4 shows the waveform of an inverter phase voltage that is applied to the motor. The voltage has quarter wave symmetry and is commutated at angles $\alpha_1$and α_2.Certain harmonics caused by the PWM waveform can be reduced or eliminated by selecting the right commutation angles $\alpha_1$and α_2. Derivation of these angles to eliminate certain harmonics is elaborated as follows.

The inverter phase voltage, in terms of the generalized commutation angles, is expressed as,

$$V_{phA}\Big|_n = \frac{4}{\pi}\frac{V_{dc}}{2}\left(\frac{1 - 2\cos(n\alpha_1) + 2\cos(n\alpha_2)}{n}\right) \tag{4.15}$$

Where n is the harmonic component number, $V_{dc}$is the DC link voltage and $V_{phA}$is the phase voltage of nth harmonic. If the numerator of (4.15) is equated to zero for a given harmonic order, then that harmonic would be eliminated from the waveform. Since third and fifth harmonics have the largest content, then these two harmonic orders are taken into consideration. The corresponding voltage amplitudes are given as,

$$\begin{aligned} V_{phA}\Big|_3 &= \frac{4}{\pi}\frac{V_{dc}}{2}\left(\frac{1 - 2\cos(3\alpha_1) + 2\cos(3\alpha_2)}{3}\right) \\ V_{phA}\Big|_5 &= \frac{4}{\pi}\frac{V_{dc}}{2}\left(\frac{1 - 2\cos(5\alpha_1) + 2\cos(5\alpha_2)}{5}\right) \end{aligned} \tag{4.16}$$

In order to eliminate the third and fifth harmonic in the voltage waveform, the voltages in (4.16) are equated to zero as,

$$V_{phA}\Big|_3 = V_{phA}\Big|_5 = 0 \tag{4.17}$$

which gives,

$$\begin{aligned} 1 - 2\cos(3\alpha_1) + 2\cos(3\alpha_2) = 0 \\ 1 - 2\cos(5\alpha_1) + 2\cos(5\alpha_2) = 0 \end{aligned} \tag{4.18}$$

Considering quarter wave symmetry of the phase voltage shown in Figure 4.4, the constraint on the commutation angles is given as,

$$0 < \alpha_1 < \alpha_2 < \frac{\pi}{2} \tag{4.19}$$

Solving (4.18), the approximate values of commutation angles α_1 and α_2 are obtained as,

$$\begin{aligned} \alpha_1 &= 0.4122 \text{ rad} \\ \alpha_2 &= 0.5812 \text{ rad} \end{aligned} \tag{4.20}$$

Thus by controlling the two commutation angles, the 3rd and 5th harmonic voltages can be eliminated. This analytical technique is simple for reduced number of commutation pulses. However when the number of commutation pulses is more than two, numerical techniques must be applied to find solution for the commutation angles.

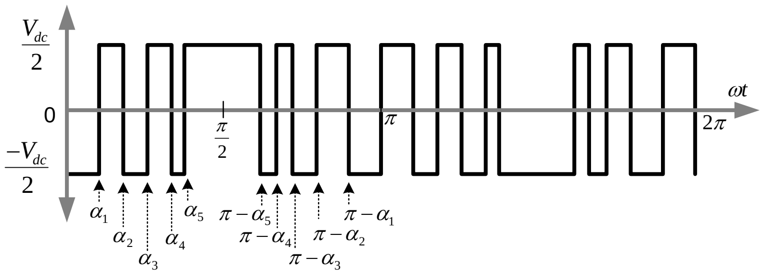

(a)

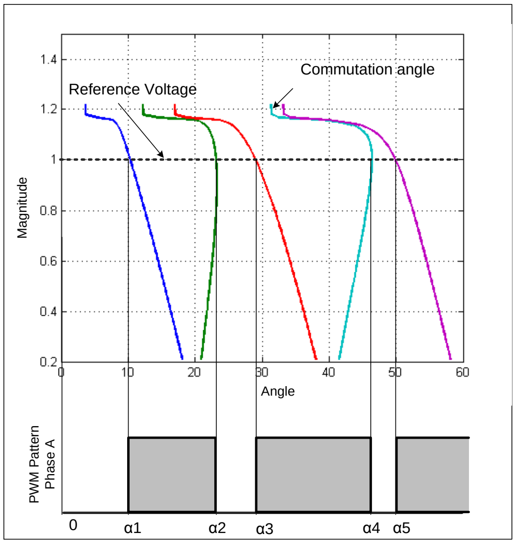

(b)

Figure 4.5. Selective harmonic elimination scheme with 11 pulses. (a) Phase voltage realization (b) Modulation index compared with commutation angle in quarter cycle resulting in corresponding PWM pattern.

Figure 4.5 (a) shows the phase voltage waveform of a three-phase inverter with five commutation angles. The output voltage can be synthesized such that the certain lower ordered frequency sidebands can be eliminated by choosing the right commutation angles ($\alpha_1 - \alpha_5$). In this illustration, the 5th, 7th, 11th and 13th harmonics can be eliminated. In general if the fundamental voltage is synthesized by using k commutation angles then the first odd non-triplen harmonics that can be eliminated are given by P-1 [4]. The number of switching pulses in a cycle are given by $N = 2k+1$ and the corresponding switching frequency is given as $f_{sw} = (2k+1) * f_1$.

The commutation angles are computed offline as a function of modulation index M assuming a steady state operation using a solver (*'Matlab- fminsearch'*). A good estimation of initial condition is critical for calculation of the commutation angles. Then the angles are stored in look-up tables for real time implementation.

Figure 4.5(b) shows the relationship between the numerically calculated five commutation angles $\alpha_1(t) - \alpha_5(t)$as a function of modulation index M. The commutation angles vary linearly with respect to the modulation index M up to 1.05 beyond which, they vary nonlinearly. The dotted line represents the modulation index. The intersection between the reference voltage line and the commutation angles determines the rising or falling edge of the inverter voltage pulse. When k is odd, then the intersection of reference voltage with every odd commutation angle results in a rising pulse while that with an even angle results in a falling pulse. The logic is reversed when the angle is greater than 180 degrees. In Figure 4.5(b), the five commutation angles results in a switching frequency f_{sw} = $(2*5+1)*f_{1.}$

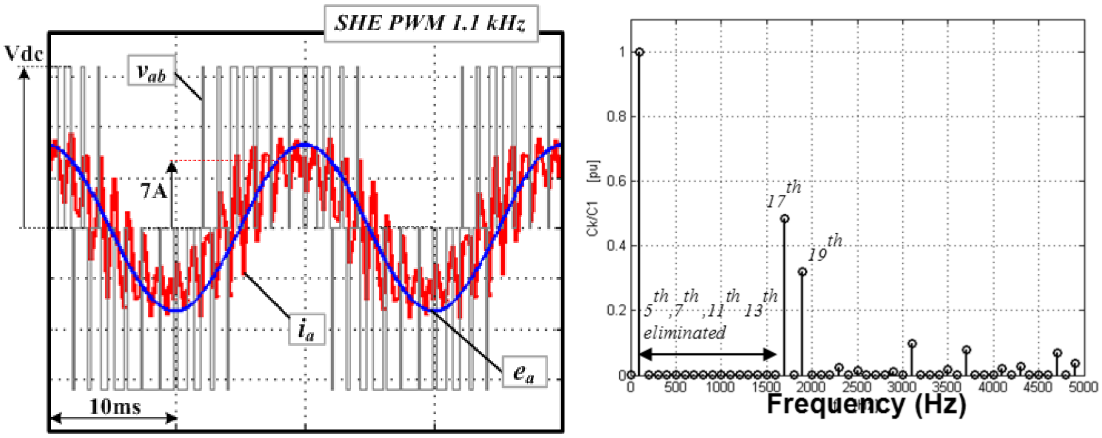

(a) (b)

Figure 4.6.(a) Steady state operation of 2 kW PMSM with SHE PWM with 5 commutation angles. v_{ab}-motor line-line voltage (scaled by 10), i_a- phase current, E_a- motor back EMF voltage (scaled by 10) (b) Harmonic spectrum of the current waveform

Figure 4.6(a) shows simulation of steady state operation of a 2 kW four pole PMSM using selective harmonic elimination method. In the simulation, the inverter is operating at 150V dc with modulation index of 0.9 and electrical frequency of 100 Hz. The inductance of the motor is 1.3 mH. The magnitude and phase of the line-line voltage is adjusted such that the motor current is in phase with the back EMF voltage. The current ripple is due the low ratio of switching frequency to fundamental frequency and higher harmonic voltages due to SHE PWM. Considering five commutation angles results in a switching frequency $f_{sw} = (2*5+1)*100 = 1.1$ kHz. Figure 4.6 (b) shows the motor harmonic current spectrum where the 5th, 7th, 11th and 13th harmonics are eliminated. It is noted that the subsequent 17th and 19th harmonics have significantly higher amplitude in comparison to remaining harmonic components. The high amplitude of the non-eliminated harmonics is a feature of SHE PWM and the distortion of the current is especially higher at lower values of the modulation indices [4]. Therefore the loss factor due to SHE PWM must be evaluated as a function of modulation index to cover the entire operating region of the motor.

Accordingly, Figure 4.7 shows the relationship between the loss factor and the modulation index for various PWM strategies. In the analysis, SHE PWM is compared with sine PWM, synchronous carrier based SVM and DPWM for different values of N. Following points can be inferred from the figure:

1. In comparison to sine PWM ($N=7$), synchronous SVM ($N = 9$) and DPWM ($N = 7$), the SHE PWM has lowest distortion for modulation indices above 1.15.
2. Synchronous SVM and DPWM have lower distortion than SHE PWM between modulation index of 0.6 and 1.15.
3. It is advantageous to use SHE PWM only for higher modulation indices ($M>1.1$).

The above result varies for larger number of switching pulses and must be reevaluated. However, the carrier based synchronous PWM methods generally yield low distortion at lower modulation indices in comparison to SHE PWM.

Figure 4.8 shows simulation results of a 2 kW four pole PMSM operating with asynchronous SVM and SHE PWM and N =11. The modulation index of the inverter is 1.1 while the electrical frequency of the motor is 73 Hz. For comparison of the two modulation methods, the variables under consideration are: (a) stator terminal line-line voltage, (b) motor phase current that is aligned with corresponding motor back EMF voltage (scaled by 0.5), and (c) current phasor trajectory. From the figure, it is seen that SHE PWM has lower current distortion than asynchronous SVM. It must also be noted that SHE PWM has better line-line voltage distribution than asynchronous SVM over the fundamental period. The comparison of the motor current phasor trajectory shows that SHE PWM has circular orbit in comparison to asynchronous SVM. The lower harmonic distortion considering SHE PWM implies lower losses in the motor.

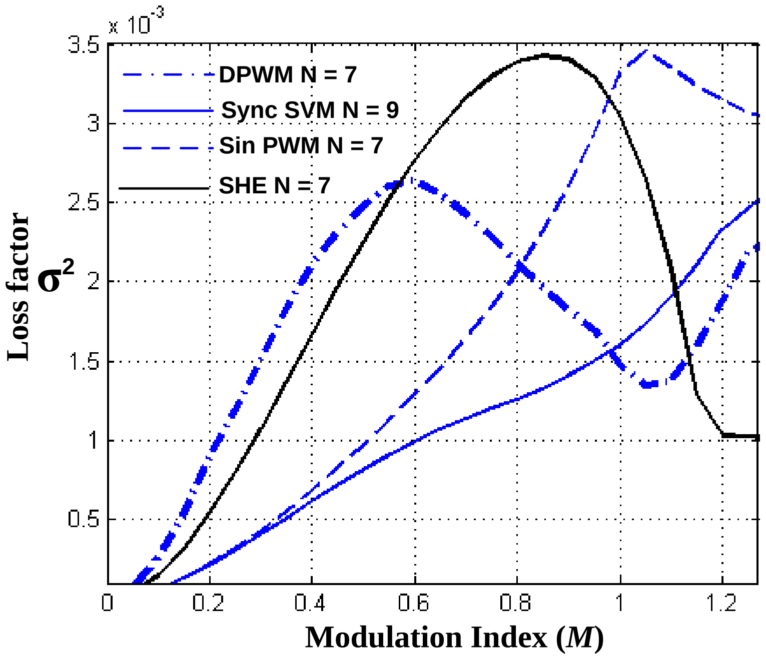

Figure 4.7.σ^2 vs. modulation index for different carrier based and SHE modulators

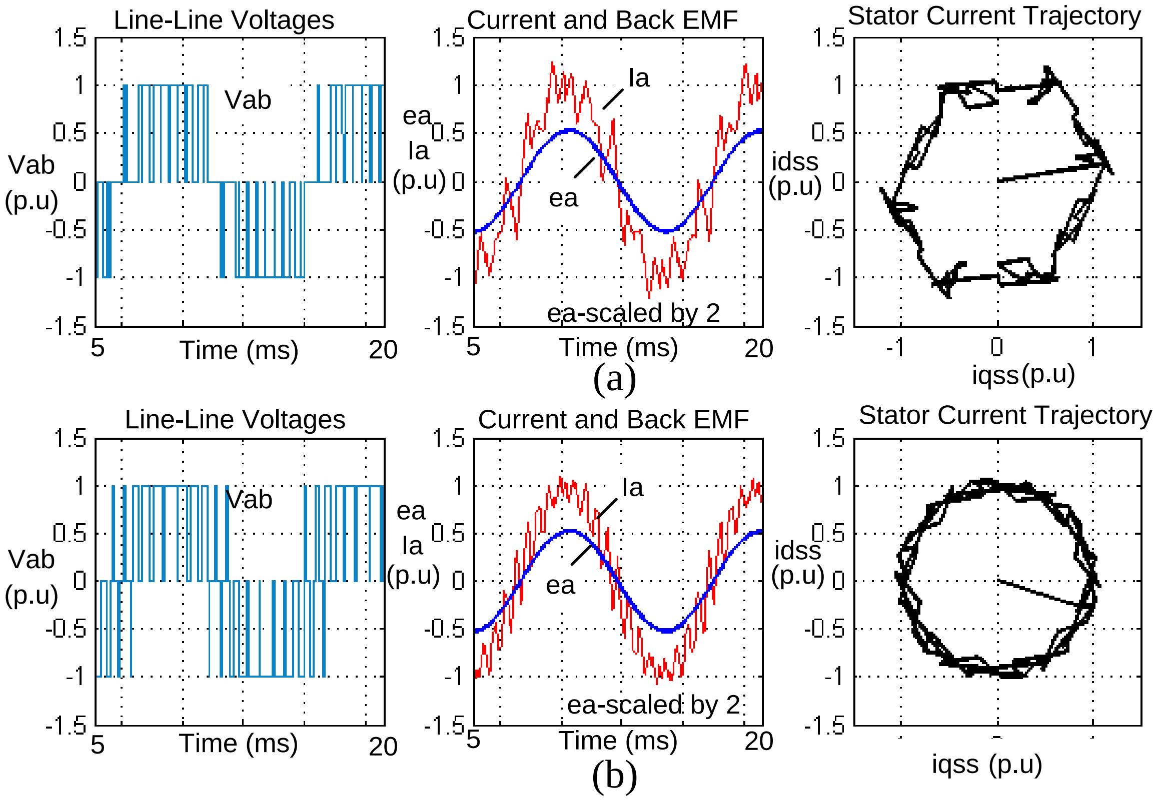

(a)

(b)

Figure 4.8. Simulation results: comparison between (a) classical SVPWM with N = 11 and (b) SHE PWM with N = 11 at 73Hz and M = 1.1 using the following variables: line-line voltage, phase A current and back EMF and stator current trajectory.

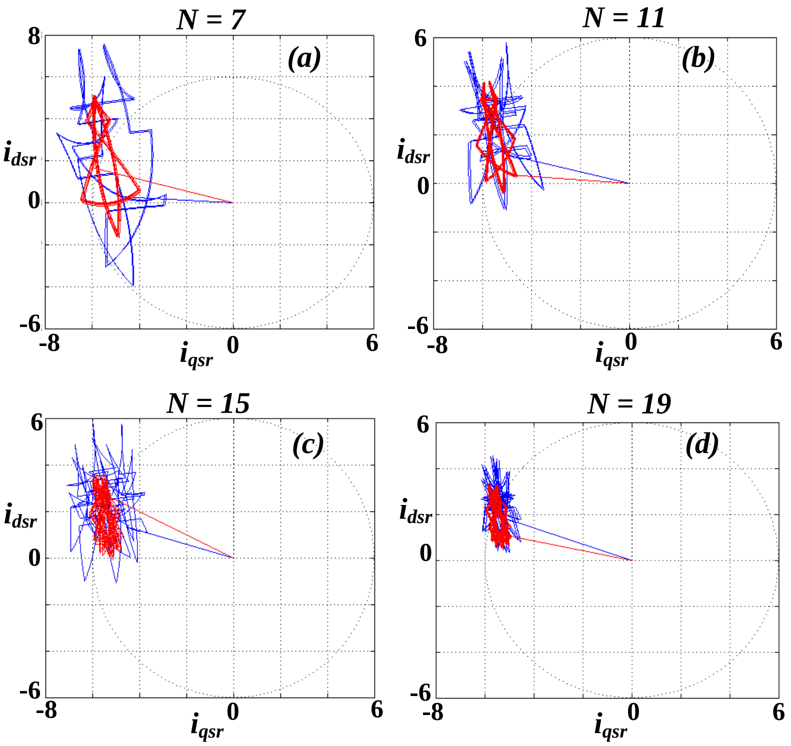

Figure 4.9. Stator current trajectory in rotor reference frame for: (a) $N = 7$, (b) $N = 11$, (c) $N = 15$ (d) $N = 19$ pulses for one fundamental cycle.

Figure 4.9 shows the current ripple due to synchronous SVM and SHE PWM at $M = 1.15$ for various pulse numbers N in PMSM’s rotor reference frame. The figure is obtained by calculating the steady state currents in PMSM for the same average torque. The corresponding d and q axis currents are plotted in rotor reference frame. The circular dotted line shows the current vector trajectory that can be synthesized. In the case presented, the d-axis current is 1.8A, while the q-axis current is 5.6 A. The current ripple in rotor reference frame is used for comparison between the two modulators for different pulse numbers. Following points can be inferred from the figures:

1. Both PWM methods can synthesize the steady state currents for low values of N.
2. The amplitude of current ripple increases as the value of N decreases. This mainly because the impedance offered by the motor phase windings is lower at reduced switching frequencies.
3. In all the four cases, SHE PWM offers lower current ripple than synchronous SVM.
4. For higher values of N, the benefit of applying SHE PWM reduces.

4.3.5. Programmed PWM with Synchronous Optimal Modulation

The selective harmonic elimination PWM eliminates certain harmonics in the current spectrum. The main drawback of the method is that the magnitude of harmonics that are not eliminated is considerably high. As a result, the overall harmonic distortion is high up to the modulation index of 1.1 considering N = 7. An alternative approach, known as synchronous optimal modulation was proposed in [4], where the voltage harmonics are minimized instead of being eliminated. This section deals with synchronous optimal modulation method for PMSM drives.

Figure 4.10shows the inverter phase voltage applied to the motor. The harmonics due to the PWM can be minimized by selecting the commutation angles $\alpha_1$and α_2. The derivation for the same shown below [4]:

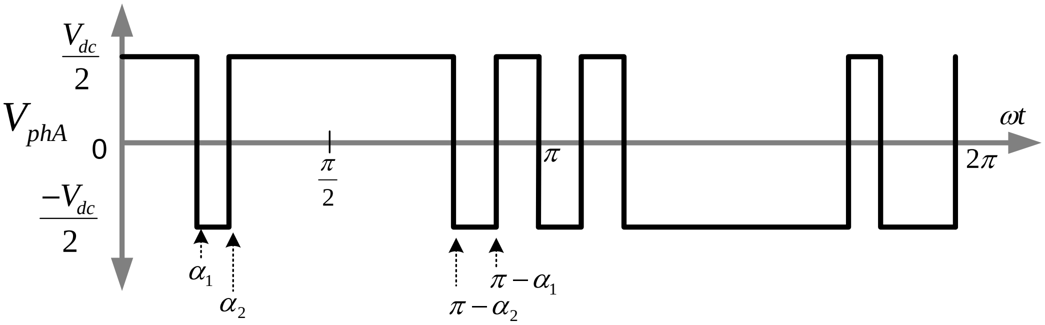

Figure 4.10. Synchronous optimal PWM scheme five pulses and switching frequency f_{sw}= 5*f_1

For the phase voltage waveform shown in Figure 4.10, the Fourier expression is given as,

$$V_{phA}\Big|_n = \frac{4}{\pi}\int_0^{\alpha_1} \frac{V_{dc}}{2} \sin(n\omega t)\, d(\omega t) - \frac{4}{\pi}\int_{\alpha_1}^{\alpha_2} \frac{V_{dc}}{2} \sin(n\omega t)\, d(\omega t) + \frac{4}{\pi}\int_{\alpha_{2?}}^{\frac{\pi}{2}} \frac{V_{dc}}{2} \sin(n\omega t)\, d(\omega t) \qquad (4.21)$$

where n is the harmonic number, $V_{dc}$is the DC link voltage and $V_{phA}\big|_n$is the voltage amplitude of the nth harmonic. Simplifying, the equation (4.21) becomes,

$$V_{phA}\Big|_n = \frac{4}{\pi}\frac{V_{dc}}{2}\left(\frac{1 - 2\cos(n\alpha_1) + 2\cos(n\alpha_2)}{n}\right) \qquad (4.22)$$

The above equation defines the phase voltage amplitude as a function of two commutation angles. Generalizing it for *k* commutation angles the harmonic voltage amplitudes are given as,

$$V_{phA}\Big|_n = (-1)^k \frac{4}{\pi}\frac{V_{dc}}{2n}\left(1 + 2\sum_{i=1}^{k}(-1)^i \cos(n\alpha_i)\right) \qquad (4.23)$$

and the fundamental voltage amplitude is given as,

$$V_{phA}\Big|_1 = (-1)^k \frac{4}{\pi}\frac{V_{dc}}{2}\left(1 + 2\sum_{i=1}^{k}(-1)^i \cos(\alpha_i)\right) \qquad (4.24)$$

Expressing the fundamental voltage in terms of modulation index *M* as,

$$V_{phA}\big|_1 = M\frac{V_{dc}}{2} \tag{4.25}$$

Then the equation(4.26) becomes,

$$M\frac{V_{dc}}{2} = (-1)^k \frac{4}{\pi}\frac{V_{dc}}{2}\left(1 + 2\sum_{i=1}^{k}(-1)^i \cos(\alpha_i)\right) \tag{4.27}$$

which is recast as,

$$f_1 = \left(1 - \frac{M}{(-1)^k}\frac{\pi}{4}\right) + 2\sum_{i=1}^{k}(-1)^i \cos(\alpha_i) \tag{4.28}$$

where f_1 is the function that must be optimized to achieve the fundamental output voltage given by (4.29). Similarly, the optimization functions for 5thand 7th harmonic voltages are given as,

$$f_5 = \frac{4}{5\pi}\frac{V_{dc}}{2}\left(1 + 2\sum_{i=1}^{k}(-1)^i \cos(5\alpha_i)\right) \tag{4.30}$$

and

$$f_7 = \frac{4}{7\pi}\frac{V_{dc}}{2}\left(1 + 2\sum_{i=1}^{k}(-1)^i \cos(7\alpha_i)\right) \tag{4.31}$$

Then the combined function that must be optimized to reduce the harmonic voltage amplitudes and achieve the desired output voltage is given as,

$$f_{opt} = {f_1}^2 + {f_5}^2 + {f_7}^2 + \cdots \tag{4.32}$$

Solving (4.33) numerically to minimize the resulting distortion factor given by,

$$\sigma = \sqrt{\frac{1}{2}\sum_{n=5,7\cdots}^{\infty}\left(\frac{V_n}{n}\right)^2} \tag{4.34}$$

and subject to the constraint of quarter wave symmetry of the commutation angles given as,

$$0 \le \alpha_1 \le \alpha_2 \ldots \le \alpha_i \le \frac{\pi}{2} \tag{4.35}$$

the values of the commutation angles are calculated as a function of modulation index.

When the function f_{opt} is minimized, the angles $\alpha_1 \ldots \alpha_i$ will result in optimized solution for $V_{phA}\big|_n$ such that σ is minimized. The above procedure is repeated for various values of N and as a function of modulation index M.

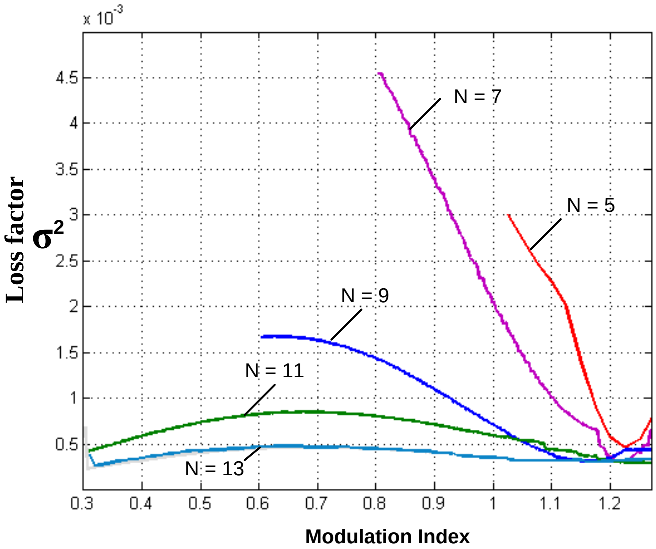

Figure 4.11. Loss factor vs. modulation index in case of synchronous optimal PWM for various pulse numbers

Figure 4.11 shows the loss factor as a function of modulation index considering synchronous optimal PWM for various values of N. It is seen that the amplitude of the distortion is high for lower values of *N*. When the modulation index is above 1.2, the loss factor for various pulse numbers is comparable. It implies that the switching frequency can be further reduced by changing to lower values of *N*. Such a changeover is commonly known as '*gearing*' and is applied to attain lowest switching frequency and loss factor simultaneously [12].

Figure 4.12(a) shows the relationship between the loss factor and modulation index for various pulse width modulators. The methods being compared are (a) synchronous optimal PWM with the number of switching pulses varied from N = 15up to $N = 5$, (b) discontinuous PWM with N = 7, (c) synchronous SVM with N = 9, (d) sine PWM with $N = 7$, and (e) SHE PWM with N = 7. From the figure, it is seen that synchronous optimal modulator with $N = 7$ and $N = 5$ yields lower loss factor than SHE PWM and DPWM with $N = 7$. To achieve a very low switching frequency considering synchronous optimal PWM, a gearing technique must be applied. Operation of optimal PWM considering induction motors has been reported in [12] but application of the same for PMSM has not been reported. The switching patterns for various pulse numbers N are computed offline and stored in lookup tables for real time implementation. The implementation of such a modulator for closed loop operation is discussed in Chapter 5.

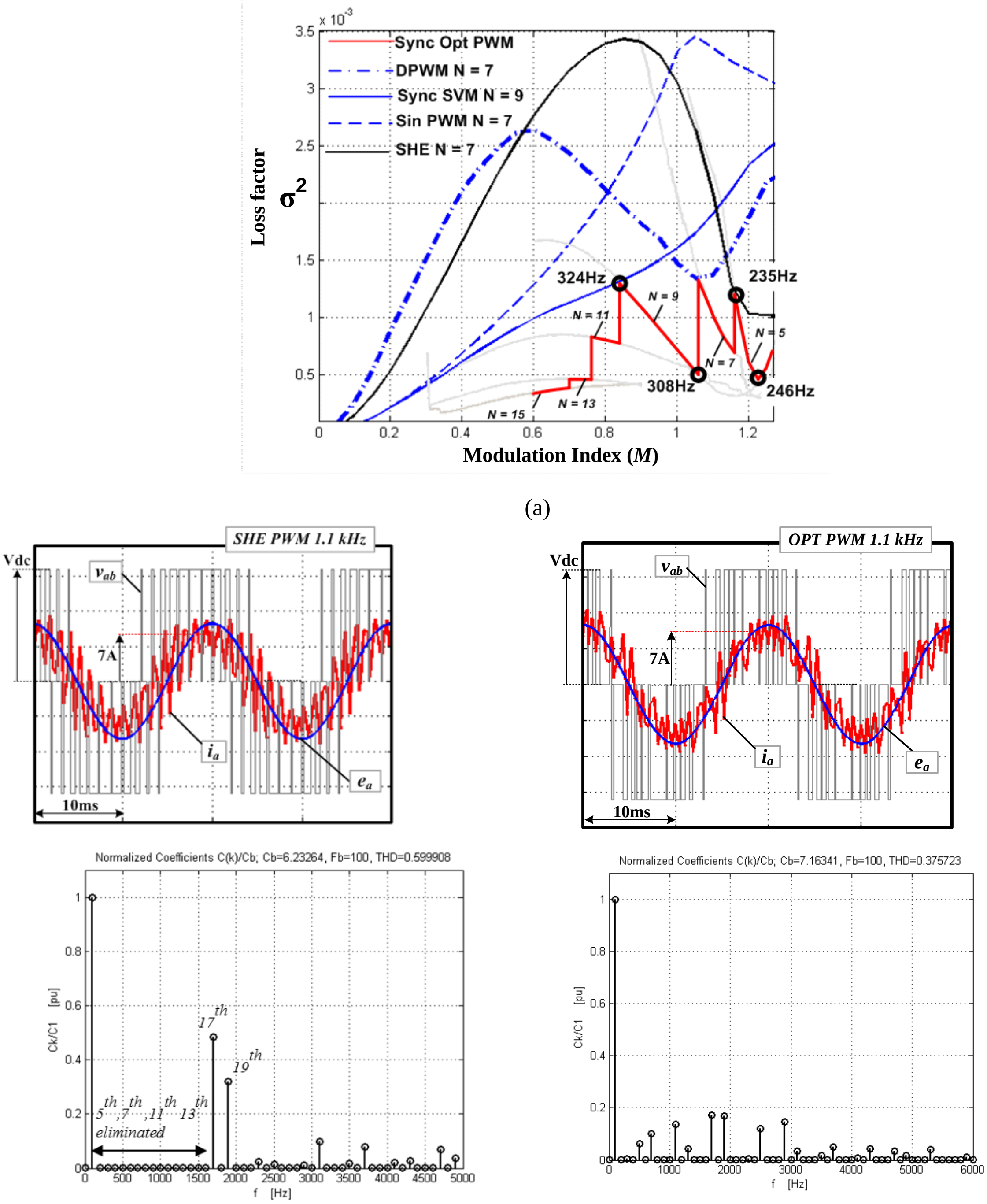

(a)

(b)

(c)

Figure 4.12.(a) Distortion versus modulation index for various PWM strategies. Simulation results: Comparison of operation of 2 kW PMSM with electrical frequency of 100 Hz and $M = 1.08$ considering (a) selective harmonic elimination PWM and (b) synchronous optimal PWM. The variables plotted are showing line-line voltage, motor phase back EMF voltage, current and its harmonic spectrum:

Figure 4.12 (b) and (c) shows the operation of a 2 kW PMSM considering SHE PWM and synchronous optimal PWM respectively. The Figure 4.12 (b) has been previously discussed in section 4.3.4 and is shown again for comparison. Figure 4.12 (c) shows that optimal PWM has lower current ripple than SHE PWM. The motor phase current spectrum shows that SHE PWM has considerably higher 17th and 19th harmonic amplitudes than optimal PWM. It is also noted that the total harmonic distortion of SHE PWM is 67 percent while that of optimal PWM is only 37 percent. The simulation results verify that optimal PWM has better performance considering the programmed modulation methods.

4.3.5.1. *Influence of motor inductance on rms value of the harmonic current*

Figure 4.13shows the relationship between inductance of the machine and the rms values of the harmonic current for various PWM methods. The pulse width modulators compared here are: (a) synchronous optimal PWM with N = 5, (b) SHE PWM with N = 7, (c) synchronous SVM with N = 15, and (d) six-step modulation at highest modulation index. From the figure, it is seen that for an impedance of 0.05 p.u, the synchronous optimal PWM with N = 5 has slightly higher amplitude than synchronous SVM with N = 15. Hence a three time reduction in switching frequency is achievable considering synchronous optimal PWM.

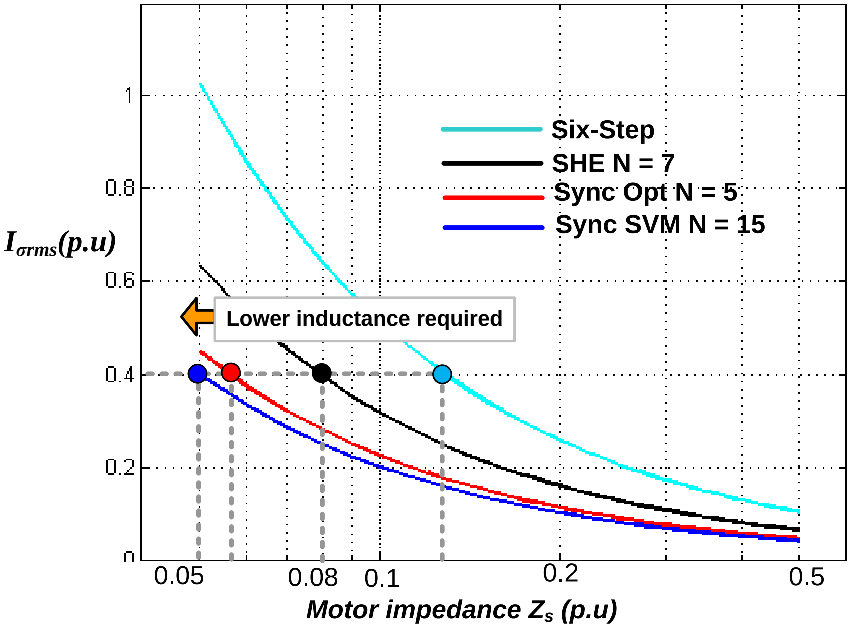

Figure 4.13. Comparison between SHE PWM at N=7, six-step and synchronized SVM at N=9, and Synchronous Optimal PWM N = 5 considering per unit inductance and harmonic current amplitude (p.u)

The analysis in [11] discusses about the synchronous inductance required for six-step and carrier based modulators to reduce the harmonic current amplitude. However it does not consider the influence of programmed PWM for further reduction of the current harmonic distortion. It should be noted that by applying programmed modulation techniques, the switching frequency can be significantly reduced in comparison to other carrier based modulators.

From the above results it is seen that the inductance of PMSM can be increased to suit low switching frequency operation. However such an approach is not preferred because the motor has to be redesigned. Therefore the focus of this research is centered on improving PMSM drive system efficiency by reducing the inverter switching frequency and applying PWM methods. Since PMSM motor harmonic loss analysis with synchronous optimal PWM has yet to appear, the following section will address it.

4.4. Analytical estimation of total losses in PMSM drive system

In the previous section, influence of various PWM methods on current harmonic distortion was discussed. In this section, the total losses in the PMSM motor and the inverter are analytically calculated considering reduced switching frequency operation. The PWM methods discussed previously are used for the comparative analysis.

In the following sections, predominant losses in the PMSM and the drive are estimated analytically. In case of PMSM, a comprehensive method for analyzing the stator resistive and core losses at reduced switching frequency is developed and validated using 2D finite element simulations. In case of inverter, the switching and conduction losses are calculated at reduced switching frequencies and accuracy of the method is validated using circuit simulations. Using the methodology for loss analysis, efficiencies of five PMSM drives of various power ratings are estimated. The results from analyses show that the efficiency of PMSM drives can be improved considerably by reducing the switching frequency of the inverter even at lower power levels.

4.4.1. Analytical estimation of losses in permanent magnet synchronous motors (PMSMs)

The total losses in the PMSM can be broken down into following components [8] as:

a. stator DC resistive losses,
b. stator AC resistive losses (skin and proximity effect),
c. stator core losses (eddy current and hysteresis),
d. rotor core losses (eddy current and hysteresis),
e. permanent magnet eddy current losses,
f. windage and frictional losses,

The contribution of the stator AC resistive losses, rotor core losses, permanent magnet eddy current losses, windage and frictional losses become significant mostly in high speed PMSMs operating at high fundamental frequencies (electrical frequency >400 Hz). Since the focus of this work is centered on low speed PMSMs, the analytical estimation of the losses associated with high speed machines will not be pursued further. Accordingly, the following sections will discuss the analytical estimation of the stator DC resistive losses and the core losses considering reduced switching frequency operation.

4.4.1.1. Stator resistive loss calculation

Any current carrying conductor will have losses associated with it. Since most of the electric machines use copper as a conductor, the resistive losses in them are generally referred as copper losses. However alternative conductors such as aluminum are also favored in some applications for their cost and hence the term stator resistive losses is used in this study [8]. Resistive losses are one of the PMSM motor's predominant losses. They are proportional to the magnitude of the square of the current and the resistance of the phase winding of the machine. The resistance of the phase winding is dependent on the temperature of the conductor and frequency of the current in the stator windings. When the fundamental frequency of the current is high, shrinking of the effective current carrying cross sectional area of the conductor due to skin and proximity effect occurs and the corresponding losses are known as AC resistive losses [8].

i. Certain assumptions are made in the estimation of stator resistive losses and they are: AC resistive losses are neglected in this analysis assuming that the skin and proximity effect in stator windings are small due to lower fundamental frequencies of the motors under consideration.

ii. Influence of temperature on increase of stator resistance has not been considered assuming that there is adequate coolant around the motor.

To estimate the stator resistive losses, it is essential to calculate the rms value of the stator current. The procedure is derived as follows:

For a PMSM motor operating at nominal torque and speed, its steady state model is given as [8]:

$$\begin{bmatrix} v_{ds}^r \\ v_{qs}^r \end{bmatrix} = \begin{bmatrix} r_s & \omega_r L_s \\ -\omega_r L_s & r_s \end{bmatrix} \begin{bmatrix} i_{ds}^r \\ i_{qs}^r \end{bmatrix} + \omega_r \lambda_m \begin{bmatrix} 0 \\ 1 \end{bmatrix} \tag{4.36}$$

where $i_{ds}^r$and $i_{qs}^r$are the d and q axis stator currents, $v_{ds}^r$and $v_{qs}^r$are the are the d and q axis stator voltages, ω_r is the electrical angular velocity of the rotor, r_s is the phase resistance of the winding, $L_s$is the synchronous inductance, and $\lambda_m$is the peak of flux linkage of the phase winding. The peak phase voltage that must be applied by the inverter to the PMSM motor is given as,

$$v_{spk}^r = \sqrt{{v_{ds}^r}^2 + {v_{qs}^r}^2} \tag{4.37}$$

while the phase angle φ between the stator current and voltage is given as,

$$\varphi = \tan^{-1}\frac{i_{dsr}^{r}}{i_{qsr}^{r}} - \tan^{-1}\frac{v_{dsr}^{r}}{v_{qsr}^{r}} \tag{4.38}$$

Then the motor instantaneous reference voltages are given as,

$$v_{as(t)} = v_{spk}^{r}\cos(\omega_r t + \varphi)$$

$$v_{bs(t)} = v_{spk}^{r}\cos\left(\omega_r t + \varphi - \frac{2\pi}{3}\right) \tag{4.39}$$

$$v_{cs(t)} = v_{spk}^{r}\cos(\omega_r t + \varphi + \frac{2\pi}{3})$$

Once the instantaneous voltages are calculated, the next step is to estimate the amplitude of the fundamental and harmonic currents. They are derived using the PMSM phasor model together with the inverter supply shown in Figure 4.14.

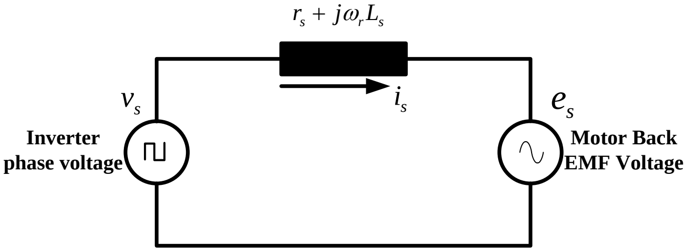

Figure 4.14. Equivalent circuit of a non-salient pole PMSM motor fed by a three phase inverter

The inverter phasor voltage and motor back EMF voltage are given as,

$$v_s = v_{spk}^{r}\cos(\varphi) + j\, v_{spk}^{r}\sin(\varphi) \text{ and}$$
$$e_s = \omega_r\lambda_m + j0 \tag{4.40}$$

respectively. The resulting stator current (i_s) is expressed as summation of the fundamental (I_{s1}) and harmonic current (I_{sh}) as,

$$i_s = I_{sf} + I_{sh} \tag{4.41}$$

The stator current is calculated as,

$$i_s = \frac{v_{spkn}^{r}(\cos(\varphi) + j\sin(\varphi)) - \omega_r\lambda_m}{r_s + jn\omega_r L_s} \tag{4.42}$$

The peak amplitude of the fundamental current is calculated from (4.39) as,

$$I_{s1} = \left\| \frac{v_{spk}^{r}(\cos(\varphi) + j\sin(\varphi)) - \omega_r \lambda_m}{r_s + j\omega_r L_s} \right\| \tag{4.43}$$

The harmonic current in the machine is expressed in terms of the stator harmonic voltage as,

$$I_{sh} = \frac{v_{spkn}^{r}}{r_s + jn\omega_r L_s} \tag{4.44}$$

where $v_{spkn}^{r}$is the peak amplitude of the nth harmonic of voltage v_s. The harmonic voltage amplitudes are calculated from Fourier analysis of the PWM voltage. The peak amplitudes of the harmonic currents are calculated as,

$$I_n = \left\| \frac{v_{spkn}^{r}}{r_s + jn\omega_r L_s} \right\| \tag{4.45}$$

Using equations (4.40) and (4.42), the rms motor current is given as,

$$I_{srms} = \sqrt{\frac{I_{s1}^2}{2} + \sum_{n=2,3,\cdots}^{\infty} \frac{I_n^2}{2}} \tag{4.46}$$

Illustration for analytical estimation of the rms current is given as follows: To estimate the rms current using the above procedure, a 230W, three-phase PMSM is considered with a phase resistance $r_s$of 0.35 ohm, inductance $L_s$of 0.6 mH, peak flux linkage λ_m of 0.056 V/rad/sec, operating at a speed of 2000 rpm and a load torque of 1.2 Nm. By using equations (4.31) through (4.42), the fundamental and harmonic currents are calculated for two operating conditions: (a) V_{dc} = 48V, and (b) V_{dc} = 42V. The corresponding modulation indices are calculated as M = 0.8 and M = 1.14 respectively. The harmonic amplitudes of phase voltages for the two modulation indices are calculated considering selective harmonic elimination PWM (*N = 11*) and listed in

Table 4-1.

In Table 4-1, V_n and I_n are the amplitude of the nth harmonic voltages and currents, respectively. Accordingly, the rms values of the motor phase currents are calculated using (4.43) as,

$$I_{srms}{}^{N=10}\Big|_{M=0.8} = \sqrt{\frac{7.345^2}{2} + \frac{4.76^2}{2} + \frac{0.547^2}{2}} = 6.201A$$

$$I_{srms}{}^{N=10}\Big|_{M=1.14} = \sqrt{\frac{7.303^2}{2} + \frac{1.019^2}{2} + \frac{1.5^2}{2}} = 5.32A$$

Table 4-1 Amplitude of voltage and current harmonics for M = 0.8 and M = 1.14 considering SHE PWM

M = 0.8	V_n	I_n
1st	25.54	7.345
17th	22.37	4.76
19th	2.877	0.547

M = 1.14	V_n	I_n
1st	25.11	7.303
17th	4.788	1.019
19th	1.429	1.5

To validate the accuracy of the method, the analytical values of rms currents as a function of modulation index are compared with the simulation results and shown in Figure 4.16. The results show a good correlation between the simulation and analytical results. It is also noted that although for the same fundamental current, the amplitude of the rms current reduces at higher modulation indices. This is because the voltage distortion due to SHE PWM reduces at higher modulation indices.

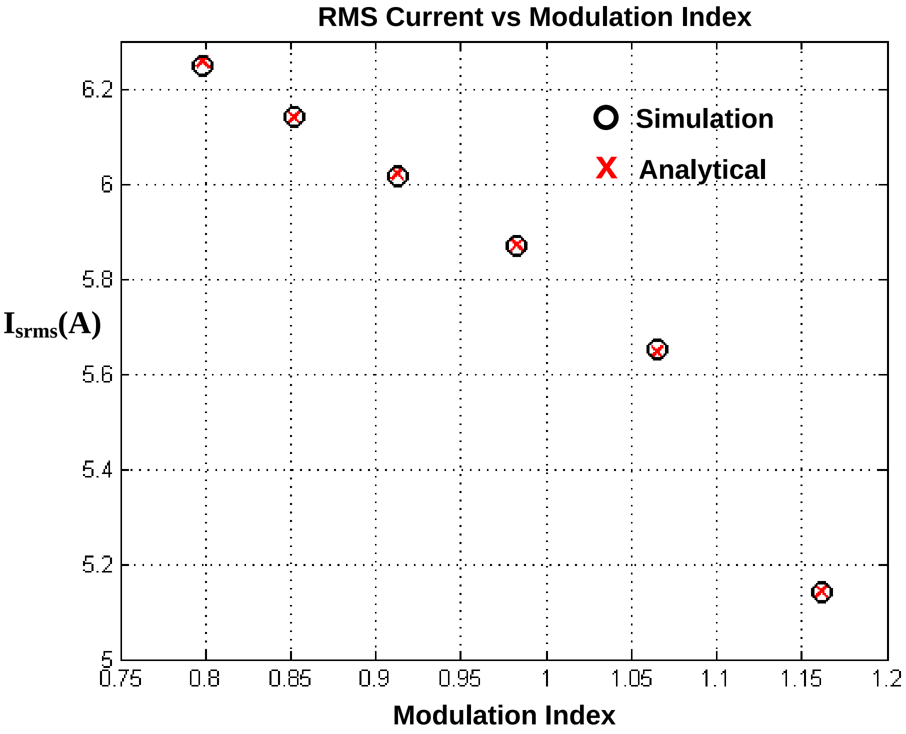

Figure 4.15. Comparison between analytical and simulation results of the rms motor current vs. modulation index.

Once the rms motor phase current is calculated, the stator resistive P_{cu} losses of a three phase PMSM are calculated as,

$$P_{cu} = 3r_s {I_{srms}}^2 \tag{4.47}$$

where, r_s is the phase coil resistance which is a function of operating temperature and frequency of the phase current. Another predominant loss in PMSM is the core loss and its estimation at reduced switching frequencies is discussed in the following section.

4.4.1.2. Analytical estimation of core losses

The procedure for estimating core losses in PMBDCM with non-sinusoidal currents has been described in chapter 3. The same procedure is used for calculating the core losses in PMSM operating at low switching frequency. The most important advantage of the analytical method is the reduced calculation time during loss optimization especially during selection of the lowest switching frequency. The method takes only a few seconds as compared to finite element simulations which can take several minutes if not hours. However, the two dimensional finite element simulations are used to validate the effectiveness of analytical core loss estimation procedure.

The core losses have two predominant components and they are eddy current and hysteresis losses [6]. Both of these components are a function of operating frequency and flux density in the core. Hence estimating the flux density is critical for accurate estimation of the core losses. In [6] and [8], analytical core loss estimation of the PMSM under no-load condition and using the trapezoidal flux density waveform approximation is provided. However, under loaded operation, effect of armature reaction on the stator and rotor flux densities has to be considered. Accordingly, in [20], a method for estimating core losses using superposition of a stator current induced flux linkage and rotor back electromotive force is developed. However, none of the methods mentioned above discuss in detail the estimation of flux density waveform in the stator tooth and yoke given the low switching frequency operation. Hence it is essential to understand and derive the expressions for the stator flux densities accurately. Following assumptions are critical for the analytical method.

(i) Only non-salient pole PMSMs with low-pole count are considered. Also the machine is assumed to be operating at low speed and in its linear region [6], [20].

(ii) Due to the absence of flux reversal in the rotor back core, the rotor core losses are not significant in comparison to stator. Hence only the core losses in the stator are considered henceforth. This assumption may not hold true in high speed machines (typically above electrical frequency of 600 Hz), where in the high fundamental frequency of the flux density, effect of slot harmonics, and the current harmonics can induce high eddy losses in the rotor magnets and the rotor back core. In such cases it is advantageous to resort to finite element methods to accurately estimate the rotor core losses [8].

(iii) The influence of stator time harmonics as a source of minor loops on magnet losses are not considered.

(iv) The influence of permanent magnet demagnetization under loaded condition is not considered. It is assumed that the permanent magnet operating point remains unchanged over the operating range of the motor. However, given the operational characteristics of the permanent magnet, this effect can be incorporated during the detailed design.

The following section describes the methodology used for estimating the flux density in stator tooth and yoke which can then be used for calculating the core losses.

Estimation of flux density in stator tooth and yoke

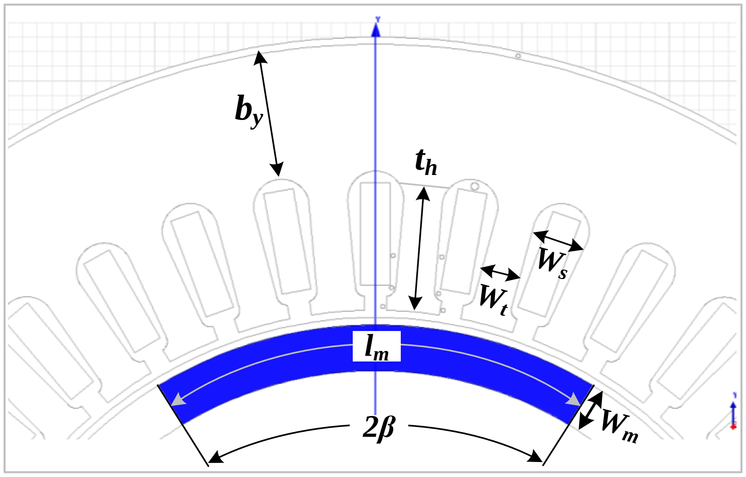

b_y yoke height
$t_h$tooth height
$W_t$tooth width
W_{s-} slot width
W_{s-}width of magnet
$l_m$length of magnet
2β pole arc

Figure 4.16 PMSM stator geometry required for estimation of flux density in stator tooth and yoke.

Figure 4.16 shows the PMSM stator geometry used for estimation of the flux densities. To estimate the core losses, generalized expressions for the no-load trapezoidal stator tooth and yoke flux densities as a function of rotor flux density are developed. Then the stator flux density in the absence of rotor induced EMF is calculated using the winding function and the motor current waveforms. The resultant air-gap flux density is then estimated using the superposition of flux densities due to the stator currents and no-load rotor induced EMF. The resultant stator tooth and yoke flux densities are calculated from using the PMSM stator geometry and the air-gap flux density. Finally, the total core losses are calculated using the resultant stator tooth and yoke flux densities at every harmonic frequency component. The following sections will describe them in detail.

a. Estimation of no-load flux densities

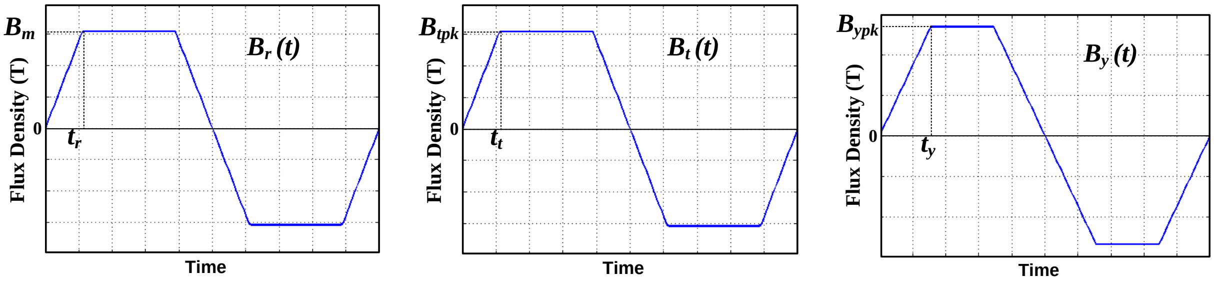

(a) (b) (c)

Figure 4.17 Flux density waveforms in (a) air-gap, (b) mid-point of stator tooth and (c) stator yoke

Generalized time series expressions for the no-load air-gap flux density shown in Figure 4.17 (a) is expressed [6], [8] as,

$$B_r(t) = \frac{4}{\pi} B_m \left\{ \begin{matrix} a_1 sin(\omega_r t) + a_3 sin(3\omega_r t) + a_5 sin(5\omega_r t) + a_7 sin(7\omega_r t) \\ + a_9 sin(9\omega_r t) + a_{11} sin(11\omega_r t) + a_{13} sin(13\omega_r t) + \ldots \end{matrix} \right\}$$

$$a_1 = \frac{sin(F)}{F} a_3 = \frac{sin(3F)}{3^2 F}, a_5 = \frac{sin(5F)}{5^2 F} \ldots \tag{4.48}$$

$$t_r = \epsilon \frac{T_s}{2} \frac{1}{3N_{s/P}}$$

$F = \omega_r t_r$ for no-load air-gap flux density

$$t_r = \epsilon \frac{T_s}{2} \frac{1}{3N_{s/P}} \tag{4.49}$$

where, $B_r(t)$ is the no-load air-gap flux density due to rotor magnets at a given spatial position, $t_t$is the time taken by the stator flux density to reach its peak value B_m, T_s in electrical time period, $N_{s/P}$is the number of slots per pole per phase, ω_r is the electrical angular velocity and, ϵ is the correction factor introduced to reduce the error in estimation of tooth flux density.

The flux density varies in amplitude at different spatial locations on the stator; as a result its estimation using the analytical method is approximate. To address this difference, correction factors are introduced in [6], [22]. They are calculated by matching the flux density results between the analytical and finite element methods for no-load operation of the machine. Once the correction factors are determined, they remain unchanged even under load condition. Such an approach is advantageous because it requires only one computation using FEA initially, which takes a few minutes, and then the analytical method can be applied which takes only a few seconds. Accordingly, the expressions for no-load air-gap flux density in (4.49) is modified using the correction factor ϵ to match the results from FEA [6], [22]. The tooth flux density as shown in Figure 4.17 (b) is given as,

$$B_t(t) = \frac{4}{\pi} B_{tpk} \begin{Bmatrix} a_1 sin(\omega_r t) + a_3 sin(3\omega_r t) + a_5 sin(5\omega_r t) + a_7 sin(7\omega_r t) \\ + a_9 sin(9\omega_r t) + a_{11} sin(11\omega_r t) + a_{13} sin(13\omega_r t) + \ldots \end{Bmatrix}$$

$$a_1 = \frac{sin(F)}{F} a_3 = \frac{sin(3F)}{3^2 F}, a_5 = \frac{sin(5F)}{5^2 F} \ldots \tag{4.50}$$

$$F = \omega_r t_t \text{ for stator tooth flux density}$$

$$t_t = \upsilon \frac{W_t}{r\omega_m}$$

where, $B_t(t)$ is the tooth flux density at given spatial position, $W_t$is the tooth width, t_t is the time taken by the tooth flux density to reach its peak value B_{tpk}, r is outer radius of stator, ω_m is mechanical angular velocity, υ is the correction factor introduced to reduce the error in estimation of yoke flux density based on finite element simulation results. The yoke flux density as shown in Figure 4.17 (c) is given as,

$$B_y(t) = \frac{4}{\pi} B_{ypk} \begin{Bmatrix} a_1 sin(\omega_r t) + a_3 sin(3\omega_r t) + a_5 sin(5\omega_r t) + a_7 sin(7\omega_r t) \\ + a_9 sin(9\omega_r t) + a_{11} sin(11\omega_r t) + a_{13} sin(13\omega_r t) + \ldots \end{Bmatrix}$$

$$a_1 = \frac{sin(F)}{F} a_3 = \frac{sin(3F)}{3^2 F}, a_5 = \frac{sin(5F)}{5^2 F} \ldots \tag{4.51}$$

$$F = \omega_r t_y \text{ for stator yoke flux density}$$

$$t_y = \upsilon \frac{W_m}{2r\omega_m}$$

where, $B_y(t)$ is the yoke flux density at given spatial position, $W_m$is width of magnet, t_y is the time taken by the yoke flux density to reach its peak value B_{ypk}, r is outer radius of stator, ω_m is mechanical angular velocity, the correction factor υ for tooth and yoke flux density is the same. As a next step, the stator flux densities in absence of rotor induced EMF is calculated in the following section.

b. Calculation of stator flux density with no magnets in the rotor

In order to estimate the stator flux density waveform due to stator excitation, the motor current waveforms must be defined first. In this analysis two current waveforms are considered for core loss comparison and they are sinusoidal currents due to inverter switching frequency of 10 kHz and sine-harmonic currents due to SHE PWM with *N* = *11*(switching frequency = 1.1 kHz).

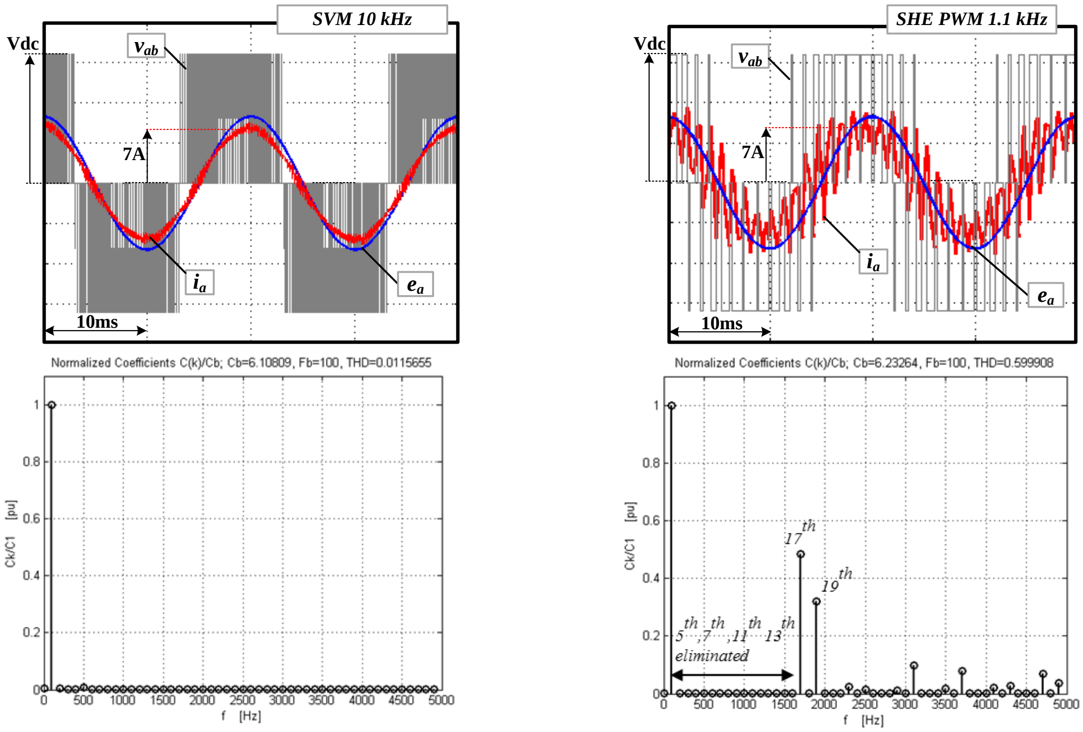

(a) (b)

Figure 4.18 Influence of switching frequency on motor illustrating line-line voltage v_{ab}, motor back EMF e_a and phase current i_a with: (a) Space vector PWM at 10 kHz switching frequency, and (b) SHE PWM with switching frequency of 1.1kHz.

Figure 4.18 (a) and (b) shows steady state voltage and current waveform of a 2 kW PMSM operating with SVM at 10 kHz and SHE PWM at1.1 kHz. The harmonic current spectrum is also shown in the same figure. It is seen that the current waveform is sinusoidal at 10 kHz however it has high current ripple at low switching frequency (1.1 kHz). Figure 4.18 (b) shows the harmonic spectrum of the current waveform with high amplitude of the 17th and 19th harmonic components. It is a characteristic of SHE PWM wherein the harmonics that are not eliminated have significantly higher amplitudes. Therefore it is essential to evaluate the influence of these harmonics on the PMSM's core losses and is considered henceforth. For analysis using sinusoidal currents, the amplitudes of these harmonic components are equated to zero. Considering the current spectrum as shown in Figure 4.18 (b) and ignoring the harmonic components above 20, the three-phase PMSM currents can be defined as,

$$\begin{aligned} I_{as}(t) &= I_m[b_1 sin(\omega_r t) + b_{17} sin(17\omega_r t) + b_{19} sin(19\omega_r t)] \\ I_{bs}(t) &= I_m\left[b_1 sin\left(\omega_r t - \frac{2\pi}{3}\right) + b_{17} sin\left(17\left(\omega_r t - \frac{2\pi}{3}\right)\right) + b_{19} sin\left(19\left(\omega_r t - \frac{2\pi}{3}\right)\right)\right] \\ I_{cs}(t) &= I_m\left[b_1 sin\left(\omega_r t + \frac{2\pi}{3}\right) + b_{17} sin\left(17\left(\omega_r t + \frac{2\pi}{3}\right)\right) + b_{19} sin\left(19\left(\omega_r t + \frac{2\pi}{3}\right)\right)\right] \end{aligned} \tag{4.52}$$

where,$I_{as}(t)$, $I_{bs}(t)$, $I_{cs}(t)$are the three phase instantaneous currents displaced by 120 degrees, I_m is the peak amplitude of the phase current, b_1, b_{17}, b_{19} are the amplitudes of the fundamental, 17th and 19th harmonic components of the phase current, and ω_r is the rotor velocity.

To estimate the air-gap flux density, it is essential to calculate the rotating magnetic field near the air gap. The rotating magnetic field is essentially the summation of the magneto-motive forces (MMFs) of the three phases per pole. The MMF per coil is a spatial function of the coil windings and the currents in them. The three-phase currents have been defined in (4.53), while the winding function is defined as follows.

With a balanced three phase winding sinusoidally distributed over space, and the same number of turns which are spatially displaced by 120 degrees, winding functions of the three phases $N_a(\theta)$, $N_b(\theta)$, $N_c(\theta)$ are given as,

$$\begin{aligned} N_a(\theta) &= N_{ph} sin(\theta) \\ N_b(\theta) &= N_{ph} sin\left(\theta - \frac{2\pi}{3}\right) \\ N_c(\theta) &= N_{ph} sin\left(\theta + \frac{2\pi}{3}\right) \end{aligned} \tag{4.54}$$

where, N_{ph} is the number of turns in the phase coil and θ is the spatial position. With the above definition, the individual magneto-motive force (MMF) per pole due to the three phase stator currents and the winding function are given as[8],

$$\begin{aligned} F_a(\theta,t) &= \frac{1}{P} I_{as}(t) N_a(\theta) \\ F_b(\theta,t) &= \frac{1}{P} I_{bs}(t) N_b(\theta) \\ F_c(\theta,t) &= \frac{1}{P} I_{cs}(t) N_c(\theta) \end{aligned} \tag{4.55}$$

where, $F_a(\theta,t)$, $F_b(\theta,t)$, $F_c(\theta,t)$ are the three-phase MMFs per pole P. Substituting (4.54) in (4.55) yields,

$$\begin{aligned} F_a(\theta,t) &= \frac{I_m N_{ph}}{P}[b_1 sin(\omega_r t) + b_{17} sin(17\omega_r t) + b_{19} sin(19\omega_r t)] sin(\theta) \\ F_b(\theta,t) &= \frac{I_m N_{ph}}{P}\left[b_1 sin\left(\omega_r t - \frac{2\pi}{3}\right) + b_{17} sin\left(17\left(\omega_r t - \frac{2\pi}{3}\right)\right) + b_{19} sin\left(19\left(\omega_r t - \frac{2\pi}{3}\right)\right)\right] sin\left(\theta - \frac{2\pi}{3}\right) \\ F_c(\theta,t) &= \frac{I_m N_{ph}}{P}\left[b_1 sin\left(\omega_r t + \frac{2\pi}{3}\right) + b_{17} sin\left(17\left(\omega_r t + \frac{2\pi}{3}\right)\right) + b_{19} sin\left(19\left(\omega_r t + \frac{2\pi}{3}\right)\right)\right] sin\left(\theta + \frac{2\pi}{3}\right) \end{aligned} \tag{4.56}$$

The resulting stator MMF also known as rotating magnetic field and is given as,

$$F_s(\theta,t) = F_a(\theta,t) + F_b(\theta,t) + F_c(\theta,t) \tag{4.57}$$

Substituting (4.56) in (4.57) yields,

$$F_s(\theta,t) = \frac{3I_m N_{ph}}{2P}\left[b_1 cos(\omega_r t - \theta) - b_{17} cos(17\omega_r t + \theta) + b_{19} cos(19\omega_r t - \theta)\right] \tag{4.58}$$

The rotating magnetic field expression shown above has three components. The terms with coefficients b_1 and b_{19} are the forward rotating components, while the term with coefficient b_{17} is the backward rotating components. From the rotating or revolving magnetic field, the stator flux density due to current excitation at any spatial location and without considering rotor induced EMF is given as,

$$B_s(\theta,t) = \frac{\mu_o}{g}\frac{3I_m N_{ph}}{2P}\left[b_1 cos(\omega_r t - \theta) - b_{17} cos(17\omega_r t + \theta) + b_{19} cos(19\omega_r t - \theta)\right] \tag{4.59}$$

where, $B_s(\theta,t)$ is the stator flux density without rotor induced EMF, $\mu_o$is the permeability of free space ($4\pi 10^{-7}$ N/A^2), and g is the air-gap length. In the above expression, only the fundamental component is useful for torque production while the remaining higher ordered harmonics result in losses in the machine. In (4.59), it is noted that the stator flux density amplitude can be controlled by the magnitude and frequency of the stator currents. It should be noted that when the phase of the rotating component is synchronous to the rotor spatial position θ, maximum stator flux density is produced. For loss analysis, a single spatial position $\theta = 0$ is considered. Thus the effective stator flux density near the air-gap due to time domain component is then given as,

$$B_s(t) = \frac{\mu_o F_s(t)}{g} \tag{4.60}$$

Graphical illustration of the stator flux density near the air-gap in absence of rotor induced EMF is shown in Figure 4.19 (a). The motor parameters used for the illustration are listed in appendix Table A.1. Figure 4.19 (b) shows the comparison between the analytical and two dimensional finite element (FEA) simulations of the absolute magnitude of stator flux density in absence of rotor magnets. This result validates the procedure for estimation of stator flux density in presence of various harmonics in the excitation current. The error between the analytical and FEA simulation is due (a) time-step size selection of the FEA simulation and (b) selection of the spatial location of the flux density waveform using the FEA simulation.

For core loss estimation in the stator tooth and yoke, the combined effect of stator flux density without rotor magnets and the no-load rotor flux density in presence of the magnets must be considered. The stator and rotor induced fluxes must be orthogonal to each other for torque production.

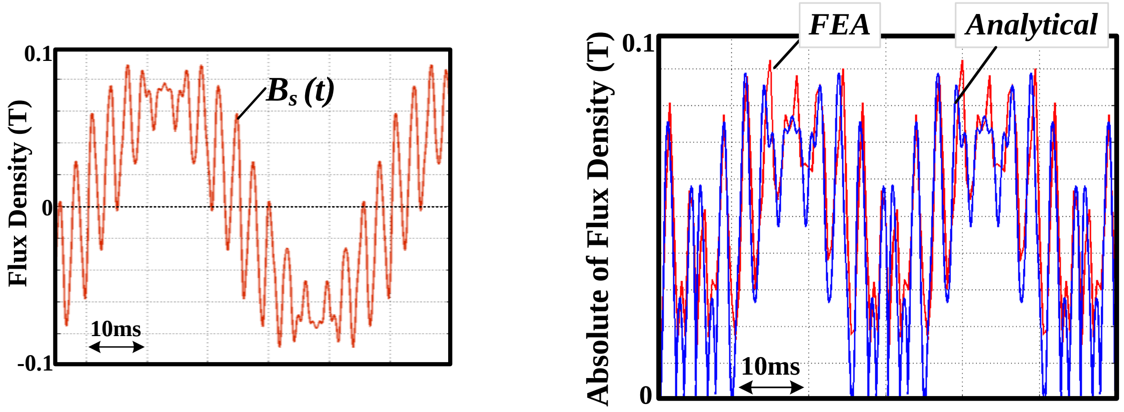

(a) (b)

Figure 4.19.(a) PMSM stator flux density near the air-gap in absence of rotor induced EMF (b) comparison between analytical and FEA simulation results of the absolute magnitude of the stator flux density near the air-gap.

c. *Superposition of stator and rotor flux densities.*

The resultant air-gap flux density at a given spatial position ($\theta = 0$) is calculated by using the superposition of the stator flux density due to stator excitation $B_s(t)$ and the no-load rotor induced flux density $B_r(t)$ due to magnets alone. It is given as,

$$B_g(t) = B_r(t) + B_s(t) \tag{4.61}$$

where, $B_g(t)$ is the resultant air-gap flux density.

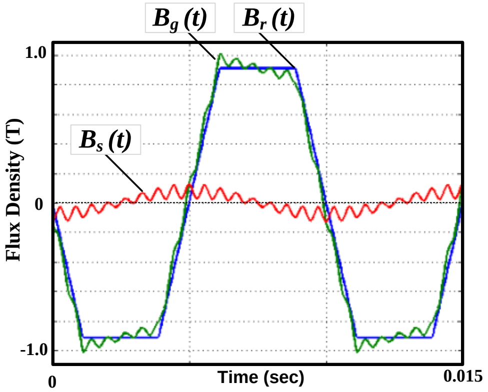

Figure 4.20 Resultant air gap flux density due to superposition of the stator and rotor flux densities.

For maximum torque production in PMSM machines, the angle between the no-load air-gap flux density and stator flux density should be 90 degrees. Illustration of the same is shown in Figure 4.20. For the case considered, the stator flux density is only 15 percent of the no-load air-gap flux density. In absence of stator flux density, the effective air gap flux density is trapezoidal. However in presence of the stator flux density, the effective air gap flux density waveform deviates from its trapezoidal waveform. This effect is known as armature reaction. This superposition also takes into account the high frequency harmonics due to the non-sinusoidal stator current excitation. Therefore, the resultant air gap flux density has the fundamental as well as the switching frequency harmonic components. The harmonic component increases the eddy and hysteresis losses in the stator tooth and yoke. Estimation of the flux density in the stator tooth and yoke based on the resultant air gap flux density is explained in the following section.

d. Estimation of tooth and yoke flux densities.

The resultant tooth and yoke flux densities$B_{ts}(t)$and $B_{ys}(t)$as a function of the resultant air gap flux density $B_g(t)$. The tooth flux density is given as [8],

$$B_{ts}(t) = \gamma \frac{W_t + W_s}{W_t} B_g(t) \tag{4.62}$$

where W_t, and W_s are tooth and slot widths respectively,γ is the correction factor introduced to reduce the error in estimation of the tooth flux density. The resultant yoke flux density is given as [8],

$$B_{ys}(t) = \varsigma \frac{W_m}{2b_y} B_g(t) \tag{4.63}$$

where ,W_m is magnet thickness and b_y is the yoke height.ς is the correction factor introduced to reduce the error in estimation of the stator yoke flux density.

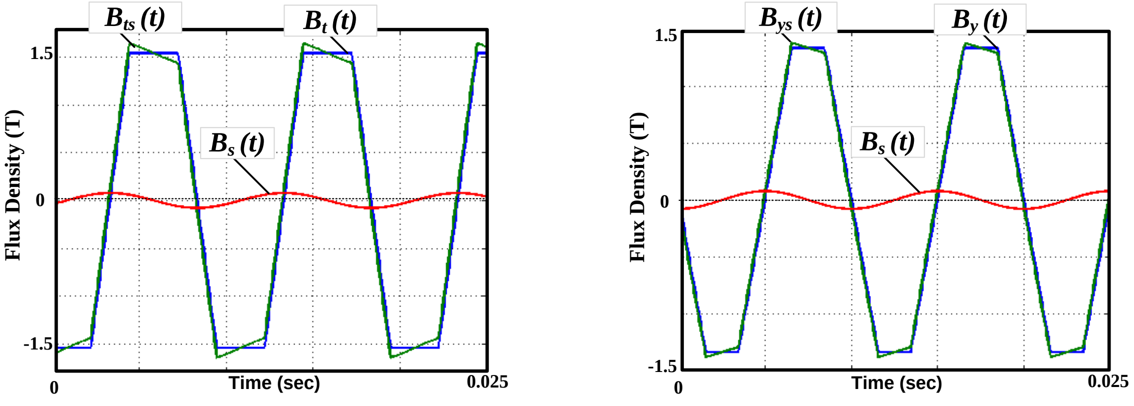

(a) (b)

Figure 4.21 Flux density in stator with and without load (a) tooth (b) yoke under sinusoidal excitation.

Figure 4.21 (a) and (b) shows the resultant tooth and yoke flux densities considering sinusoidal current excitation and using expressions in (4.64) and (4.65), respectively. The resultant stator tooth and yoke flux densities are distorted due to the influence of stator excitation. These resultant flux densities are used for estimation of the core losses. This completes the section on analytical method for estimation of the stator tooth and yoke flux densities under load condition.

e. Validation of analytical flux density estimation with 2 Dimensional Finite Element Analysis.

To validate the estimation of stator tooth and yoke flux densities, two dimensional finite element simulations are made on a 2 kW, 4-pole machine with parameters listed in Appendix A.2. As discussed in previous section, the various correction factors are required for the analytical method and are calculated based on FEA simulation result as$\epsilon = \frac{P}{2}$, $\upsilon = 1.1$, $\varsigma = 1.12.$, $\gamma = 0.71$.

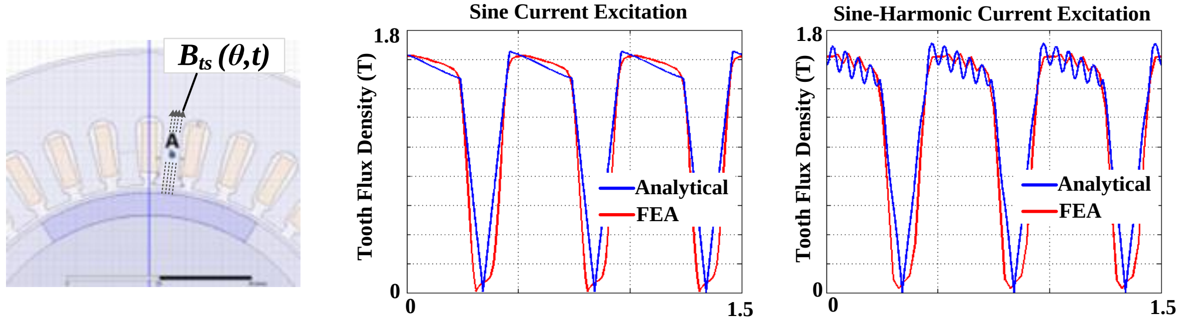

(a) (b) (c)

Figure 4.22(a) Analytical and FEA comparison of absolute magnitude of flux density in stator teeth at location A with (b) sinusoidal currents and (c) sine-harmonic excitation currents

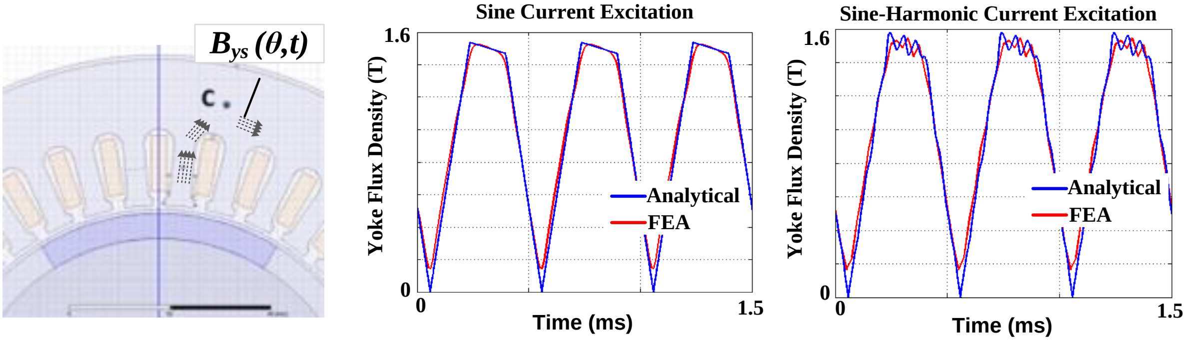

(a) (b) (c)

Figure 4.23 (a) Absolute magnitude of flux density in stator yoke at location C with: (b) sinusoidal currents, and (c) sine-harmonic excitation currents

Figure 4.22 (a) and Figure 4.23 (a) shows the spatial location of the stator tooth $B_{ts}(\theta, t)$and yoke flux density $B_{ys}(\theta, t)$ measured at points 'A' and 'C', respectively. The location of the points is chosen in order to get the average flux density in the stator tooth and yoke. The direction of the flux vectors is shown by the dotted lines.

Figure 4.22 (b) and (c) show the analytical and FEA simulation comparison of the absolute magnitude of the stator tooth flux density at location ‘A’ considering sinusoidal and sine-harmonic currents due to SHE PWM. The simulation results show that the analytical method provides good approximation of the flux density waveforms when compared with FEA simulations. The error between the two methods is mainly due to the trapezoidal approximation of the flux density waveform in case of analytical method.

Figure 4.23 (b) and (c) show the analytical and FEA simulation comparison of the absolute magnitude of the stator yoke flux density at location ‘C’ considering sinusoidal and sine-harmonic currents. The simulation results show that the analytical method provides good approximation of the flux density waveforms when compared with FEA simulations. Using the stator tooth and yoke flux densities, the total core losses can be estimated and is discussed in following section.

f. Total core_loss estimation using flux density harmonic decomposition

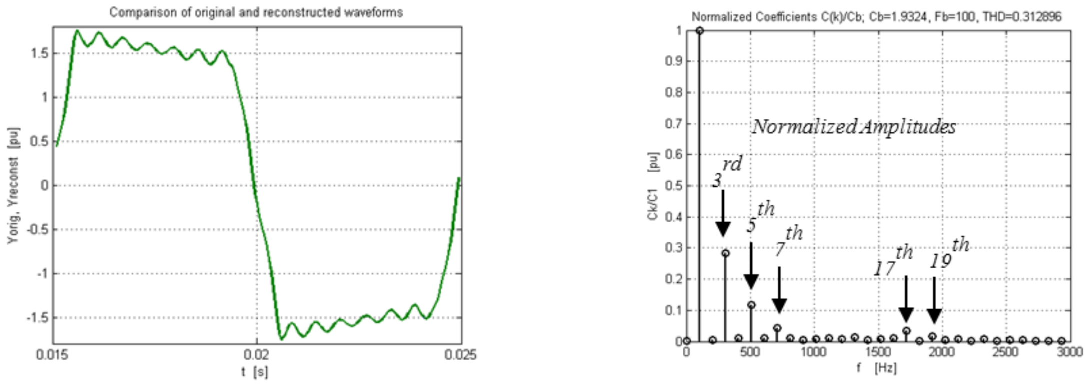

(a)

(b)

Figure 4.24(a) Resultant flux density in stator tooth using analytical method (b) FFT of the resultant flux density

The total core losses P_{fe} is the summation of the eddy current and hysteresis losses in the stator tooth and yoke at every harmonic frequency. It is given as,

$$P_{fe} = P_{et} + P_{ey} + P_{ht} + P_{hy} \tag{4.66}$$

where, P_{et} and P_{ey} are the total eddy current losses in the stator tooth and yoke respectively while P_{ht} and P_{hy} are the total hysteresis losses in the stator tooth and yoke respectively. The eddy current and hysteresis losses are given as [8],

$$P_{ey} = k_e \rho_i V_y \sum_{k=1}^{\infty} \left(k\omega_r B_{kym}\right)^2 \tag{4.67}$$

$$P_{et} = k_e \rho_i V_t \sum_{k=1}^{\infty} (k\omega_r B_{ktm})^2 \tag{4.68}$$

$$P_{ht} = k_h \rho_i V_t \sum_{k=1}^{\infty} k\omega_r (B_{ktm})^n \tag{4.69}$$

$$P_{hy} = k_h \rho_i V_y \sum_{k=1}^{\infty} k\omega_r \left(B_{kym}\right)^n \tag{4.70}$$

where, k_e and k_h are the eddy and hysteresis loss coefficients respectively of the lamination steel material, ρ_i is the mass density of the lamination steel in kg/m^3, V_t and V_y are the total stator tooth and yoke volumes respectively, B_{kym} and B_{ktm} are the peak yoke and tooth flux densities respectively for the k^{th} harmonic frequency and n is the Steinmetz coefficient whose value vary from 1.6 to 2 depending on the material properties. The above four equations capture the predominant core losses in the PMSM.

To calculate the losses at every harmonic frequency the resultant flux density must be decomposed. An illustration of the resultant stator tooth flux density waveform considering analytical method and its harmonic components are shown in Figure 4.24 (a) and (b), respectively. It should be noted that the amplitude of the flux densities at 17th and 19th harmonic frequencies is significantly lower than the 3rd, 5th and 7th harmonics. However the 17th and 19th harmonic components must not be ignored because the eddy current losses are proportional to the square of the harmonic frequency. By substituting the flux density harmonic components in equations (4.67)-(4.70), the total core losses can be calculated.

Accordingly, Table 4-2 shows the core loss comparison results using analytical and FEA simulation methods. The losses are calculated considering operation of PMSM with sine and sine-harmonic currents. From the results, it is seen that the losses estimated using analytical method are in agreement with the FEA simulations and the maximum error is below 6 percent.

Various lamination steel materials are used to compare and validate the effectiveness of the analytical method. In this case, both the lamination steels are assumed to have the same thickness. It is given that the M-19 steel has lower eddy and hysteresis losses than M-800 steel. Consequently, the total core losses due to M-800 steel are more than two times that due to M-19 steel. It is also noted that in case of M-800 steel, the total core losses due to sine-harmonic currents increased by 9.4 percent over sinusoidal excitation and in case of M-19 steel, the increase was only 4 percent. Hence for reduced switching frequency operation of PMSM, higher grade lamination steels are advantageous in order to improve total system efficiency.

Table 4-2 Comparison between analytical and FEA results at 100Hz for different steel materials

Steel type	***Analytical***	***FEA***	***% Error***
Sine			
M-19	73	69	5.7
M-800	175	170	3
Sine-Harmonic			
M-19	76	75	1.3
M-800	188	186	1

Relationship between the core losses versus motor fundamental frequency for no load and operation with sine and sine-harmonic excitation using M-800 lamination steel is shown in Figure 4.25.From the figure, it is seen that the core losses due to sinusoidal excitation is comparable with no load operation. However in case of sine-harmonic current excitation, the total core loss increase is noticeable after 60 Hz. The total increase is up to 9.4 percent at 100 Hz.

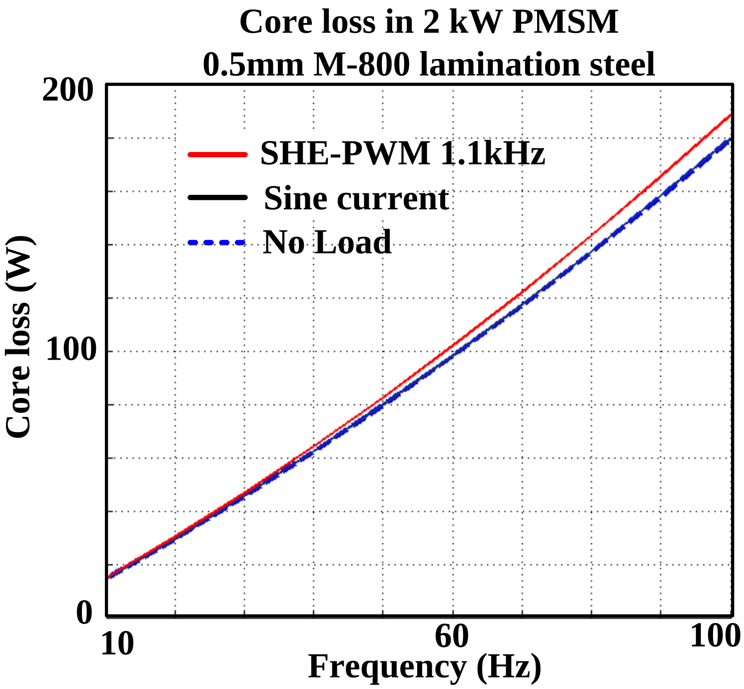

Figure 4.25Total core loss in machine as function of fundamental frequency with no-load, sinusoidal currents and sine-harmonic excitation currents

The above results show that the influence of flux density harmonic components due to low switching frequency on core losses is essentially dependent on the type of lamination steel. In case of low loss lamination steel, the switching frequency harmonics do not increase the core losses significantly. It implies that the inverter switching losses can be reduced without increasing the motor core losses considerably. The core loss estimation methodology considering switching frequency harmonics as explained in the above sections have not been discussed in [11], [12], and [13]. The analysis also provides a guideline for the choice of lamination material required depending on operating and switching frequency.

The next aspect of the research focuses on evaluating motor drive losses at reduced switching frequencies so that the total system loss assessment can be made. It is discussed in the following section.

4.5. Analytical estimation of drive losses at reduced switching frequencies

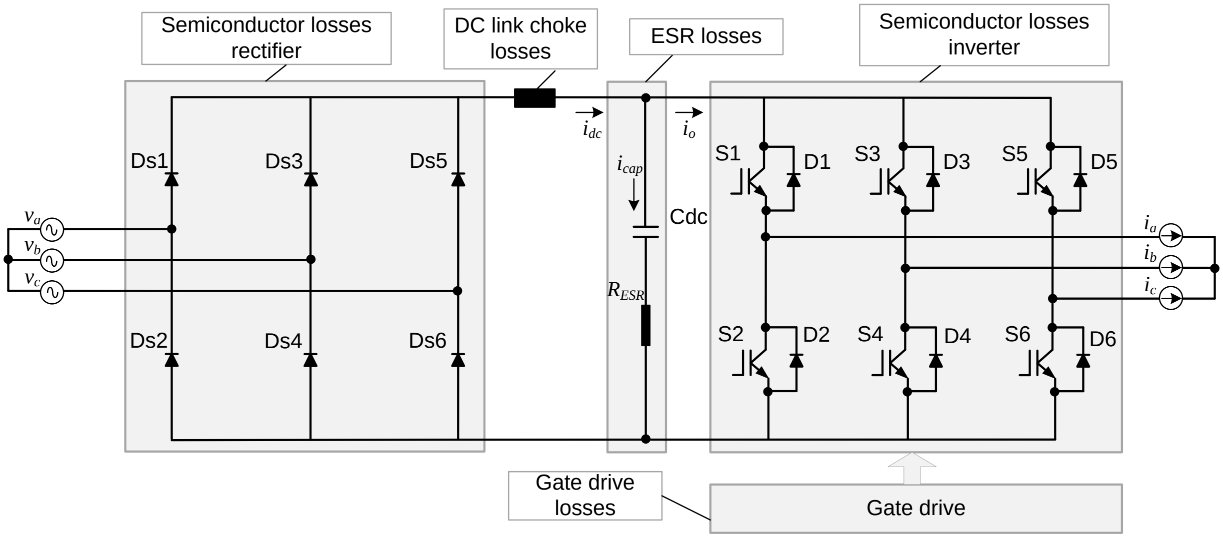

Figure 4.26 Three phase motor drive schematic showing constant voltage source and constant current load.

Figure 4.26 shows schematic of a typical three-phase motor drive and the loss distribution in it [23]. The motor drive has two sections: (i) input three-phase diode rectifier that is fed from a three-phase voltage source and (ii) the output inverter feeding a three-phase load. The switching of the inverter is controlled by a gate drive circuit. The two sections are connected by a passive LC (inductive and capacitive) filter. The total drive losses in the above circuit are broken down into five parts and they are:

a. semiconductor losses in the diode rectifier,
b. resistive and harmonic core losses in the DC link choke (inductor)
c. equivalent series resistive losses in the DC link capacitor
d. semiconductor device losses in the inverter and
e. losses in the gate drive circuit.

Since this research is centered on optimizing the inverter losses by reducing its switching frequency, it is critical to evaluate the losses in other drive components as well and is discussed in following sections. The input section and the DC link capacitor losses are qualitatively analyzed at reduced switching frequency by using simulation results and the parameters listed in Table 4-3.

Table 4-3.Drive parameters and variables

Parameter / Variables	***Value***
C_{dc}	4 mF
L_{dc}	200 uH
R_{esr}	0.02ohm
v_a	140 Vrms
i_a	20A peak
v_{dc}	350V
Power	4.9 kW

(i) *Semiconductor losses in the diode rectifier*

The losses in the three-phase diode rectifier are proportional to the square of the magnitude of commutated line current i_{as}. The line current is dependent on the DC link current i_{dc} which in turn is dependent on the inverter input current i_o. To evaluate the rectifier losses at various switching frequencies, a simulation of the topology shown in Figure 4.26is made with the parameters listed in Table 4-3. The two switching frequencies considered are 7.6 kHz and 660 Hz. The corresponding results are shown in Figure 4.27 (a) and (b). From the results, it is seen that reduction of switching frequency does not significantly affect the input line current waveform quality. This is because, the DC link capacitor absorbs most of the high frequency current ripple and the DC link choke offers further impedance to the switching frequency ripple component. Consequently, the losses in the input diode rectifier can be considered as constant for variation in switching frequencies henceforth in this analysis.

(ii) *Harmonic losses in DC link inductor*

The current in the DC link inductor is a function of the diode commutation events and the three phase line currents. The DC link inductor current i_{dc} also has low switching frequency ripple current component because most of the ripple is absorbed by the DC link filter capacitor. It is noticeable from Figure 4.27 (a) and (b). Hence the DC link choke losses can also be considered constant and independent of the switching frequency for this study.

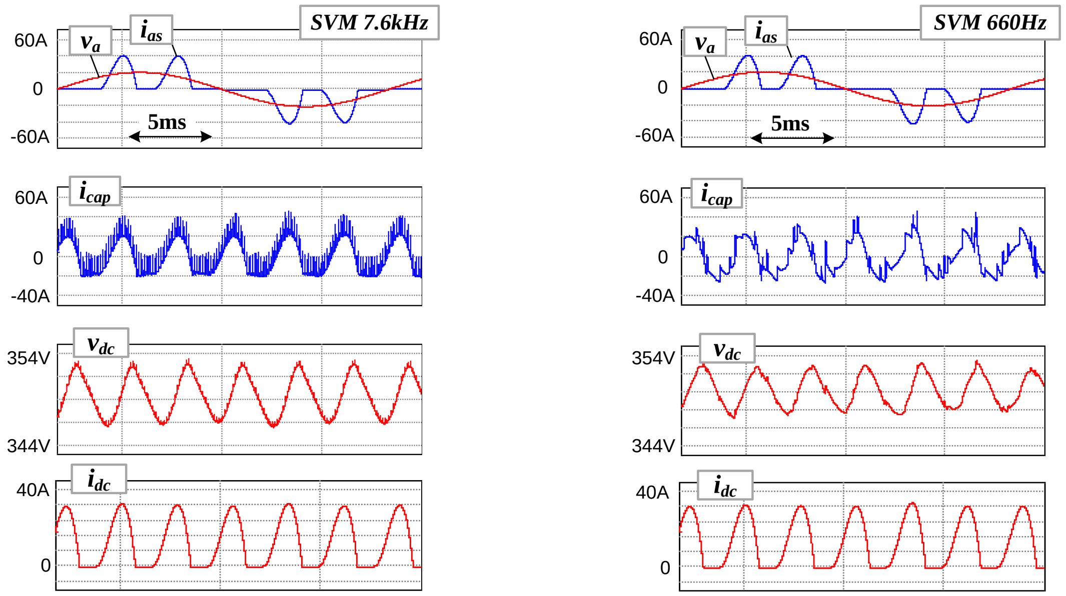

(a) (b)

Figure 4.27. Drive input side and DC link variable waveforms for switching frequency of: (a) 7.6 kHz, and (b) 660 Hz. The variables shown are defined as: v_a-source phase A voltage, i_{as}-input phase A line current, i_{cap}- capacitor current, v_{dc}- DC bus voltage, and i_{dc}- DC link choke current.

(iii) *Equivalent series resistive losses in DC link capacitor*

The losses in the equivalent series resistance (ESR) of the DC link capacitor are proportional to the square of the current through it [24]. The DC link capacitors are of electrolytic or film type and usually chosen to have low ESR value (<0.05 ohm) to handle the high current ripple caused by the commutation of input diode rectifier [25].

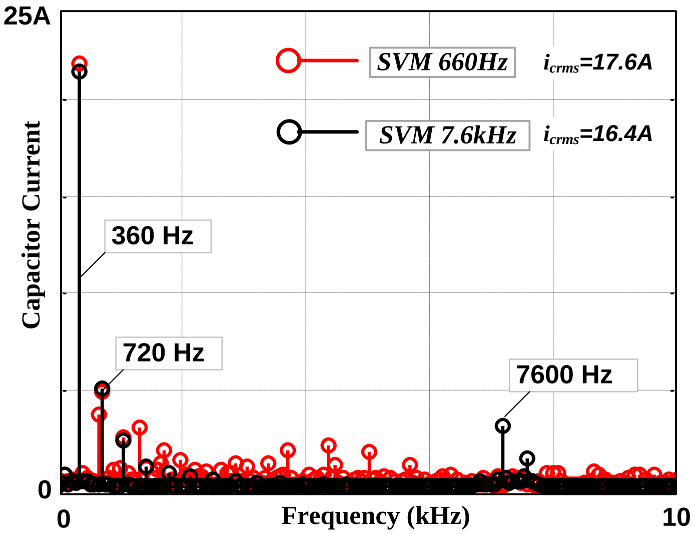

Figure 4.28 Fourier spectrum of the capacitor current at switching frequency of 7.6 kHz and 660 Hz

The DC link capacitor current spectrum is shown in Figure 4.28. It is seen that the capacitor current has predominant sixth harmonic current component (six times the input line frequency) due to the diode commutation. The switching frequency related harmonics have much smaller amplitudes than the sixth harmonic component. The ESR losses in the capacitor are given as,

$$P_{esr} = R_{esr}.i_{crms}{}^{2} \tag{4.71}$$

where R_{esr} is the equivalent series resistor of the capacitor and i_{crms} is the root mean square amplitude of the capacitor current. To evaluate the influence of switching harmonics on the root mean square amplitude of the capacitor current, the parameters and operating condition in Table 4.3 is evaluated. From the simulation results, it is seen that at switching frequency of 7.6 kHz, capacitor rms current is 16.35A, while that at 660 Hz is 17.58A. Thus for the given ESR of 0.02 ohms, the loss increase due to reduced switching frequency is only 0.8W. As a result, from PMSM drive system loss perspective, for the architecture shown in Figure 4.26, the ESR loss increase in the DC link capacitor is small and hence can be safely ignored for initial analysis. However for the power levels in hundreds of kilowatts, this assumption must be revisited and the capacitor harmonic losses must be reevaluated using detailed circuit simulations.

(iv) *Gate drive losses*

The gate drive power supply losses are very small in comparison to the total inverter losses and hence can be ignored for the initial analysis [26].

(v) *Semiconductor device losses in the inverter at low switching frequencies*

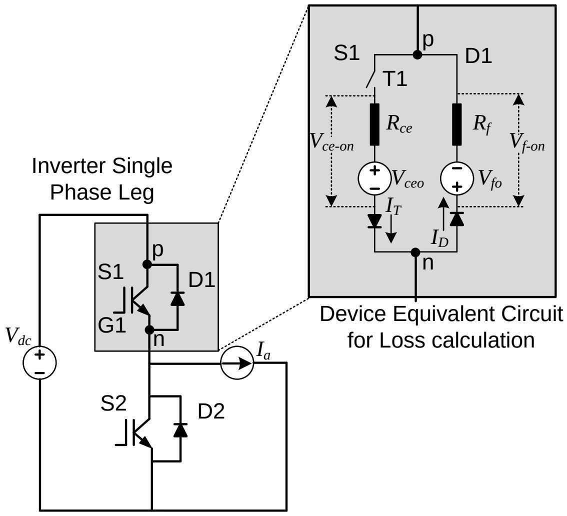

Figure 4.29 Semiconductor device loss estimation equivalent circuit

Figure 4.29 shows the semiconductor device loss equivalent circuit for a single device used in a phase leg of the inverter. Insulated Gate Bipolar Transistors (IGBTs) are considered for the loss analysis. Modeling the IGBT device for conduction and switching losses is discussed as follows.

As shown in Figure 4.29, the IGBT S1 is connected to an anti-parallel diode D1 between the junction p and n and the two devices do not conduct at the same time. The IGBT S1 is enabled by turning on the gate signal G1. It results in turning the switch T1 on and creating a threshold voltage drop of V_{ceo} across the junction. At this instant, the current i_T flows through an equivalent forward resistance R_{ce}. The total on state voltage drop across the junction is given denoted as $V_{ce\text{-}on}$. When the anti-parallel diode D1 conducts at a threshold voltage drop of V_{fo}, the current i_D flows through an equivalent forward resistance R_f. Then the total on state voltage drop across the junction is denoted as $V_{f\text{-}on}$. The operation repeats several times in a fundamental cycle resulting in conduction and switching losses in all the six devices. The conduction loss is proportional to the magnitude of the square of the current while the switching loss is a function of the current and switching frequency of the inverter. Analytical estimation of inverter losses have been widely reported in [27-32]. However, in these methods, the crucial assumption is that the semiconductor device current is sinusoidal and its amplitude remains constant during the switching period. Such an assumption cannot be used at very low switching frequencies as the current amplitude may vary significantly between the switching intervals. Operation of the three-phase inverter considering the equivalent circuit in Figure 4.29 and parameters given in Table 4-3 is simulated and presented in Figure 4.30.

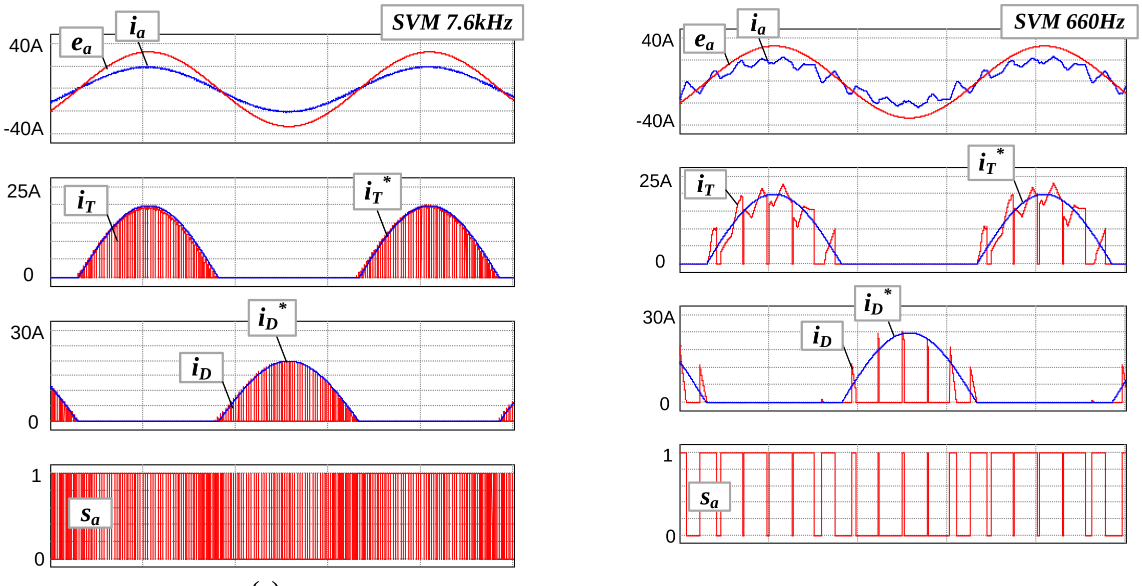

(a) (b)

Figure 4.30. Motor phase current and semiconductor device current waveforms for switching frequency of: (a) 7.6 kHz, and (b) 660 Hz. The variables shown are defined as: e_a-motor back EMF, i_a-motor phase current, i_T- active device switching current (IGBT), i_D-anti-parallel diode current, s_a- switching device reference signal.

Figure 4.30 (a) and (b) show the motor phase current and the semiconductor device current waveforms for switching frequency of 7.6 kHz and 660 Hz, respectively. It is noted that at low switching frequencies (Figure 4.30 (b)), the semiconductor device current i_T and the diode current i_D has significant variation of its amplitude during the switching interval than that at high switching frequencies (Figure 4.30 (a)). It implies that the assumptions used in [27-32] considering the peak switching current waveform to be constant during the switching interval may not be applicable at low switching frequencies. Also, as the device conduction losses are proportional to the square of the rms device current, accurate estimation of the latter is critical given the large current ripple. Therefore, a more accurate analytical method of estimating the semiconductor device losses at low switching frequency is desired and is derived as follows.

i. *Analytical conduction loss estimation considering low switching frequencies*

The conduction losses in the IGBT is given as [27],

$$P_{Tcon} = V_{ceo} I_{Tavg} + R_{ce} {I_{Trms}}^2, \tag{4.72}$$

Where I_{Tavg} and I_{Trms} are the average and rms currents, respectively, through the IGBT. The conduction loss through the diode is given as [27],

$$P_{Dcon} = V_{fo} I_{Davg} + R_f {I_{Drms}}^2 \tag{4.73}$$

where I_{Davg} and I_{Drms} are the average and root mean square currents, respectively, through the anti-parallel diode.

By assuming sinusoidal currents, and sine PWM with third harmonic injection, equations (4.73) and (4.74) can be solved to obtain the conduction losses in the IGBT (P_{Tcon}) and anti-parallel diode (P_{Dcon}) as [32],

$$P_{Tcon} = V_{ceo} \frac{I_{pk}}{2\pi}\left(1 + \frac{\pi}{4}\mathrm{M}_1\cos(\phi)\right) + R_{ce}\frac{{I_{pk}}^2}{2\pi}\left(\frac{\pi}{4} + \frac{2}{3}\mathrm{M}_1\cos(\phi) - \frac{2}{15}\mathrm{M}_3\cos(3\phi)\right) \tag{4.74}$$

and

$$P_{Dcon} = V_{fo} \frac{I_{pk}}{2\pi}\left(1 - \frac{\pi}{4}\mathrm{M}_1\cos(\phi)\right) + R_f\frac{{I_{pk}}^2}{2\pi}\left(\frac{\pi}{4} - \frac{2}{3}\mathrm{M}_1\cos(\phi) + \frac{2}{15}\mathrm{M}_3\cos(3\phi)\right) \tag{4.75}$$

where I_{pk} is the peak phase current into the load, φ is the power factor between the applied voltage and current, M_1 is the modulation index of the fundamental voltage and M_3 is the modulation index of the third harmonic voltage. For the loss analysis with space vector modulation the modulation, the value of M_3 is chosen as one-sixth of the fundamental [32] ($\mathrm{M}_3 = \mathrm{M}_1/6$).

The equations (4.75) and (4.76) are used when the currents are sinusoidal. However when the currents have high ripple due to low switching frequency, accurate estimation of their average and rms values are required. The amplitude of the average current I_{Tavg} and the root mean square current I_{Trms} in the IGBT device in presence of switching harmonics is given as,

$$I_{Tavg} = \frac{1}{\pi}\left[\left(\sum_{k=0}^{\infty}\frac{I_{Tp}}{p}\right) + \left(\sum_{k=0}^{\infty}\frac{I_{Tq}}{q}\right)\right],$$

$$I_{Trms} = \sqrt{\frac{1}{2}\left[\left(\sum_{k=0}^{\infty}{I_{Tp}}^2\right) + \left(\sum_{k=0}^{\infty}{I_{Tq}}^2\right)\right]} \tag{4.76}$$

$$p = 6k + 1, q = 6k - 1, \qquad k = 0,1,2 \ldots \infty, p > 0, q > 0$$

where, I_{Tp} and I_{Tq} are the peak amplitudes of the IGBT current harmonics, with the suffix p and q as its harmonic order. Neglecting the stator resistor, the fundamental amplitude of the device current I_{T1}in a permanent magnet motor drive operating with programmed PWM can be analytically calculated as,

$$I_{T1} = \frac{1}{\omega_r L_s}\left[V_{phA1} - \omega_r \lambda_m\right] \tag{4.77}$$

where, $V_{phA1}$is the fundamental average voltage amplitude across the switch, ω_r is the permanent magnet motor's rotor speed, L_s is the phase inductance, and λ_m is the peak flux linkage due to the permanent magnet. Substituting the voltage equation given by (4.24), the device current is given as,

$$I_{T1} = \frac{1}{\omega_r L_s}\left[(-1)^P \frac{4V_{dc}}{2\pi}\left(1 + 2\sum_{i=1}^{P}(-1)^i \cos(\alpha_i - \varphi)\right) - \omega_r \lambda_m\right] \tag{4.78}$$

$$0 \leq (\alpha_i - \varphi) \leq \pi$$

where, V_{dc} is the DC link voltage, P is the number of commutation angles α, and φ is the angle between the current and voltage vector. Since the current flows through the device for only half of the fundamental cycle, the constraint of $0 \leq (\alpha_i - \varphi) \leq \pi$ is applied. Similarly, the amplitudes of the other current harmonics in the device can be calculated as,

$$I_{Tn} = \frac{1}{n\omega_r L_s}\left[(-1)^P \frac{4V_{dc}}{2\pi}\left(1 + 2\sum_{i=1}^{P}(-1)^i \cos(n(\alpha_i - \varphi))\right)\right] \tag{4.79}$$

$$0 \leq (\alpha_i - \varphi) \leq \pi$$

where n is the current harmonic number.

The above method is applicable for estimating the diode currents as well. The amplitude of the average current $I_{Davg}$and the root mean square current I_{Drms} in the diode in presence of switching harmonics is given as,

$$I_{Davg} = \frac{1}{\pi}\left[\left(\sum_{k=0}^{\infty}\frac{I_{Dp}}{p}\right)+\left(\sum_{k=0}^{\infty}\frac{I_{Dq}}{q}\right)\right],$$

$$I_{Drms} = \sqrt{\frac{1}{2}\left[\left(\sum_{k=0}^{\infty}{I_{Dp}}^2\right)+\left(\sum_{k=0}^{\infty}{I_{Dq}}^2\right)\right]} \tag{4.80}$$

$$p = 6k+1, q = 6k-1, \qquad k = 0,1,2\dots, p > 0, q > 0$$

where I_{Dp} and I_{Dq} are the peak amplitudes of the IGBT current harmonics, with the suffix p and q as its harmonic numbers. Since the duty cycle of the anti-parallel diode is complementary to that of the IGBT, the instantaneous voltage across the diode has to be modified accordingly. Then the fundamental amplitude of the diode current I_{D1} in a permanent magnet motor drive operating with programmed PWM can be analytically calculated as,

$$I_{D1} = \frac{1}{\omega_r L_s}\left[\overline{V_{phA1}} - \omega_r\lambda_m\right] \tag{4.81}$$

where $\overline{V_{phA1}}$ is the complementary voltage across the anti-parallel diode. Substituting the Fourier expression of the phase A voltage in terms of the commutation angles α_i considering programmed PWM, the fundamental amplitude of the diode current is given as,

$$I_{D1} = \frac{1}{\omega_r L_s}\left[(-1)^P\frac{4V_{dc}}{2\pi}\left(1-2\sum_{i=1}^{P}(-1)^i\cos(\alpha_i-\varphi)\right)-\omega_r\lambda_m\right] \tag{4.82}$$
$$0 \le (\alpha_i - \varphi) \le \pi$$

Note that the negative sign in front of the summation implies complementary switching voltage across the diode. The amplitudes of the other odd *n* current harmonics in the device can be calculated as,

$$I_{Dn} = \frac{1}{n\omega_r L_s}\left[(-1)^P\frac{4V_{dc}}{n\pi}\left(1-2\sum_{i=1}^{P}(-1)^i\cos\left(n(\alpha_i-\varphi)\right)\right)\right] \tag{4.83}$$
$$0 \le (\alpha_i - \varphi) \le \pi$$

Using equations (4.73) through (4.82), the conduction losses in the IGBT and the anti-parallel diode can be estimated at reduced switching frequencies. The next step is to estimate the switching losses in them and is discussed in the following section.

ii. Analytical switching loss estimation considering low switching frequency operation

The analytical average switching losses in the IGBT P_T and the diode P_D are given by [32],

$$\begin{aligned} P_T &= \frac{f_{sw}\left(K_{on}+K_{off}\right)I_{pk}}{\pi}\frac{V_{dc}}{V_{ce}} \\ P_D &= \frac{f_{sw}K_{rr}I_{pk}}{\pi}\frac{V_{dc}}{V_{ce}} \end{aligned} \tag{4.84}$$

where K_{on}, $K_{off,}$ *and* K_{rr} are the slopes of the curves determining relationship between peak current I_{pk} and energy losses E_{on}, E_{off} and E_{rr} during the on, off and reverse recovery state respectively, V_{dc} is the DC link voltage, and V_{ce} is the collector to emitter test voltage in the manufacturers data sheet at which the losses are measured. The main assumption in the above equation is that the amplitude of the current ripple due to switching events in the device and the diode is very small. Figure 4.31 shows the operation of a three phase inverter with fundamental frequency of 60Hz and a switching frequency of 660 Hz. In this case, it is seen that the IGBT current i_T deviates from the sinusoidal waveform due to low switching frequency. The peak currents during the turn on and turn off events have large variations. Consequently, the approximation used in equation (4.85) will result in reduced accuracy of the switching losses.

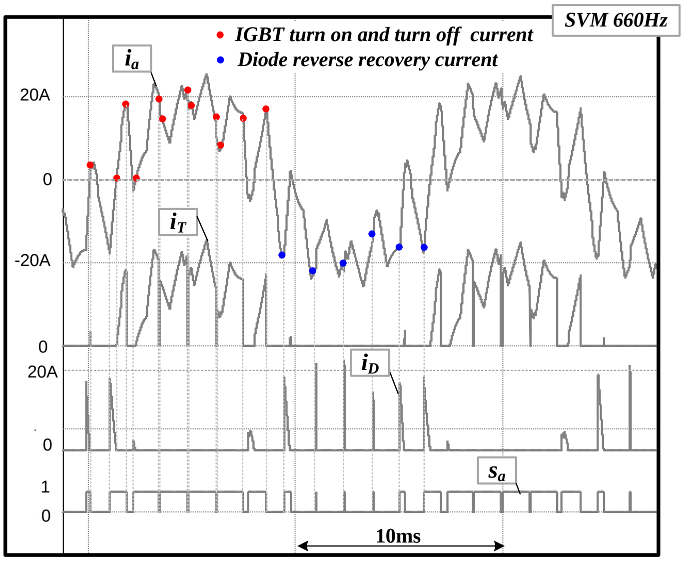

Figure 4.31 Instantaneous amplitude of the peak IGBT and diode currents during the turn on and turn off events at switching frequency of 660 Hz. The variables shown are defined as: i_a-motor phase current at 60 Hz, i_T- IGBT switching current, i_D-anti-parallel diode reverse recovery current, s_a- IGBT reference signal.

To improve the accuracy in estimation of losses, the instantaneous amplitudes of the device currents must be sampled during the turn on and turn off events. The IGBT and diode sampling instances are shown as ‘dots’ in Figure 4.31.In case of IGBT, the peak current during the turn on is defined as I_{pkon} while the same during turn off is defined as I_{pkoff}. Similarly, the peak diode current during its reverse recovery is defined as I_{drr}. The accurate magnitude of I_{pkon}, I_{pkoff} and I_{drr}during the switching events can be estimated using numerical solution of the motor dynamic equations or from circuit based simulation. Finally, using the new current definitions, equation (4.85) is modified as,

$$P_{Tsw} = \frac{f_{sw}\left(K_{Ton}I_{pkon} + K_{Toff}I_{pkoff}\right)}{\pi}\frac{V_{dc}}{V_{ce}}$$
$$P_{Dsw} = \frac{f_{sw}K_{rr}I_{drr}}{\pi}\frac{V_{dc}}{V_{ce}} \tag{4.85}$$

Table 4-4 Comparison between analytical and circuit based inverter loss comparison considering SVM PWM at various switching frequencies.

Switching Frequency	***Losses: Analytical***	***Losses: Circuit Based***	***% Error***
10 kHz	433	435.3	0.4
5 kHz	269.58	271	0.5
1 kHz	149	144	3.3
540 Hz-sine approximation	125	145	22
540 Hz sine harmonic approximation	152	145	4

To validate the aforementioned methodology, the total device losses are calculated considering a 350V DC, 8 kW PMSM drive operating at a fundamental frequency of 60 Hz. The comparison between analytical and circuit simulation based losses is shown in Table 4.4. The switching frequency is varied from 10 kHz to 540 Hz (N = 9). The comparison between the analytical and circuit based simulation shows that at 540 Hz, the sinusoidal current approximation results in 22 percent error in the estimated losses. This error is mainly because the harmonic content in the current is ignored. When the harmonic components are incorporated, the error in loss estimation is only 4 percent. Hence it is essential to obtain accurate estimation of the device current waveform for calculating the losses.

Based on the comparative results, it is seen that the analytical method discussed in this section provides an accurate approach for estimating the semiconductor losses even at low switching frequencies. This completes the analytical method for estimation of semiconductor device losses. The next step is to select the devices suitable for reduced switching frequency operation.

(c) ***Selection of switching devices***

Commercial semiconductor manufacturers offer devices that are optimized for conduction or switching losses. Devices optimized for lower conduction losses are slow and have higher switching losses. Conversely, devices optimized for switching losses have higher conduction losses.

Accordingly, Figure 4.32 shows the comparison between the fast (Skiip11AC12T4V1) and the slow (Skiip11AC126V1) Semikron 1200V, 10A IGBT devices. From the Figure 4.32(a) and (c), it is seen that the slow IGBT and diode has smaller conduction V_{ce} and forward voltage V_f drop than the faster devices. However, as shown in Figure 4.32(b), the slower devices have higher turn-on E_{on}, turn-off E_{off} and reverse recovery energy E_{rr} losses. The choice of the semiconductor device is based on the application under consideration. Faster switching devices, although expensive, are advantageous in applications requiring high dynamic performance and low acoustic noise. If the application does not require fast response, slower devices are preferred. This work will pursue operation with slower IGBT devices and focus on minimizing their conduction and switching losses considering fan type applications.

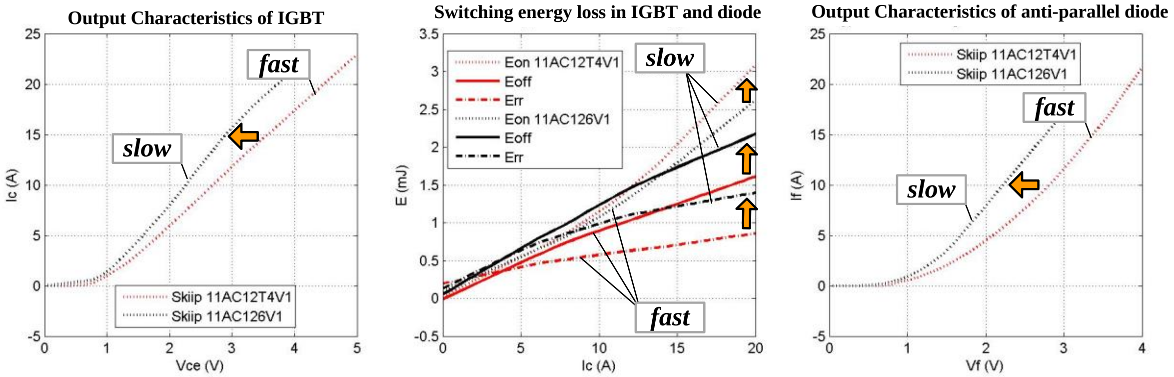

(a) (b) (c)

Figure 4.32Trade-off between turn-off losses and forward voltage drop of IGBT devices

4.6. Efficiency improvement evaluation in various PMSM drives considering reduced switching frequency operation.

In previous sections, analytical methods for estimating the inverter and motor losses including harmonics for reduced switching frequency operation are discussed. In this section, the analytical methods are applied to five PMSM drive systems of various power levels. The corresponding motor and drive parameters are listed in Table 4.5. The main objective is to estimate the total system efficiency improvement due to reduced switching frequency operation considering PMSMs of various power ratings.

Table 4-5.Various surface mount permanent magnet motors and their drives evaluated for efficiency improvement at reduced switching frequencies.

Cases	**1**	**2**	**3**	**4**	**5**
Machine Geometry (not to scale)	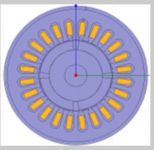	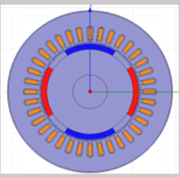	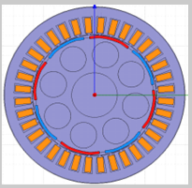	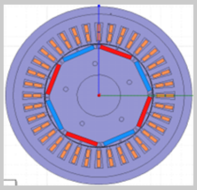	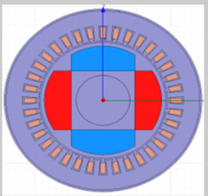
Power (kW)	**0.2**	**2.2 kW**	**8.5 kW**	**22 kW**	**125 kW**
Motor AC Voltage (V)	27	230	305	512	460
Speed (rpm)	2000	3000	3000	822	27000
Stator resistance (ohm)	0.25	0.35	0.22	0.25	0.023
Stator inductance (mH)	0.75	4.6	4.7	7.5	0.1
Max Electrical Frequency (Hz)	66.67	100	133.33	54.8	900
Torque (Nm)	1	18	42	250	48
Magnet Type	Ceramic 8D	NdFeB	NdFeB	NdFeB	NdFeB
Lamination Steel Type	M-800	M-800	M800	M-19	M-19
IGBT and Diode Rating	100V, 17A	600V, 20A	1200V, 30A	1200V, 55A	1200V, 450A
DC voltage (V)	48	310	640	800	750

For the cases studied, following assumptions are made with respect to operation of the motor and drive system:

(i) The load torque varies in proportion to square of the operating speed such that the rated torque is achieved at the rated speed. The motor speed is varied linearly from 50 percent to 100 percent of the rated value to cover the part and full load conditions. The load profile emulates the fan load application.

(ii) There is adequate coolant flow around the motor stator and rotor and hence the motor winding resistance does not increase significantly.

(iii) For the loss optimization, the switching frequency of the inverter is reduced until the overall system efficiency is optimized.

(iv) For the comparative analysis, the synchronous optimal PWM is used at lower switching frequencies while synchronized carrier based SVM is used for higher switching frequencies.

(v) Due to the voltage drop across the DC link inductor, the maximum modulation index of the inverter is extended up to 1.2. For PMSM drive systems that do not have a DC link inductor, the same modulation index of 1.2 is assumed to achieve maximum output power from the inverter.

(vi) The semiconductor conduction and switching losses are calculated considering the junction temperature of 150˚C as provided in the manufacturer’s datasheet.

(vii) The motor lamination steel and the semiconductor loss information are provided in the appendix.

Case I-

Figure 4.33 (a) shows parameter of a 4 pole 100 kW, 27000 rpm machine driven by an inverter with a 1200V, 450 A IGBT device. Figure 4.33 (b-f) show the variable speed performance of the PMSM drive system. The output power vs. speed profiles for space vector and optimal PWM are shown in Figure 4.33(b). For the case considered, the switching frequency is reduced from 20 kHz to 4.5 kHz to evaluate the influence of sinusoidal and sine-harmonic currents on total system efficiency. Using the analytical loss estimation method discussed in previous sections, the lowest switching frequency of 4.5kHz is chosen. The synchronous optimal PWM patterns are changed gradually from $N = 18$ to $N = 5$ as a function of operating speed.

Figure 4.33 (c) shows the total system efficiencies at various switching frequencies considering synchronized space vector (SVM) and synchronous optimal modulator (OPT PWM). It is seen that as the switching frequency is reduced from 20 kHz to 4.5 kHz, the efficiency of the system increases by one percent at the maximum load condition. It is also noted that, above 23000 rpm, the synchronous optimal PWM has higher efficiency than space vector modulators operating at higher switching frequencies. The increase in efficiency is due to decrease in the total drive system losses as shown in Figure 4.33 (d). The total drive system loss reduction is due to significant reduction of losses in the inverter while a very small increase in the motor harmonic losses. The inverter losses at various switching frequencies and as a function of operating speed are shown in Figure 4.33 (e) while the motor harmonic losses are shown in Figure 4.33 (f).

From Figure 4.33 (e), it is seen that at the maximum load condition, the inverter switching losses considering optimal PWM are 60 percent lower than those considering space vector modulation at 20kHz. The loss reduction is predominantly due to reduction of switching losses. It is also noted that, below 22000 rpm, space vector modulation operating at 9 kHz has similar losses in comparison to synchronous optimal PWM. Beyond this speed, synchronous optimal yields lower losses mainly due to the lower switching frequency. The variation in switching losses in synchronous optimal PWM above 23000 rpm is due to the PWM pattern change from $N = 18$ to $N = 5$.

Figure 4.33 (f) shows that the synchronous optimal PWM results in up to 5 percent higher motor harmonic losses than the space vector modulators at higher switching frequencies. The increase in motor harmonic losses will marginally increase the de-rating of the motor.

Therefore, from the analytical results it is shown that by the reducing switching frequency of the inverter, the total losses of the system are significantly reduced thereby increasing the total system efficiency. It is also shown that synchronous optimal PWM provides better performance at higher operating speeds corresponding to higher modulation indices.

Case-I

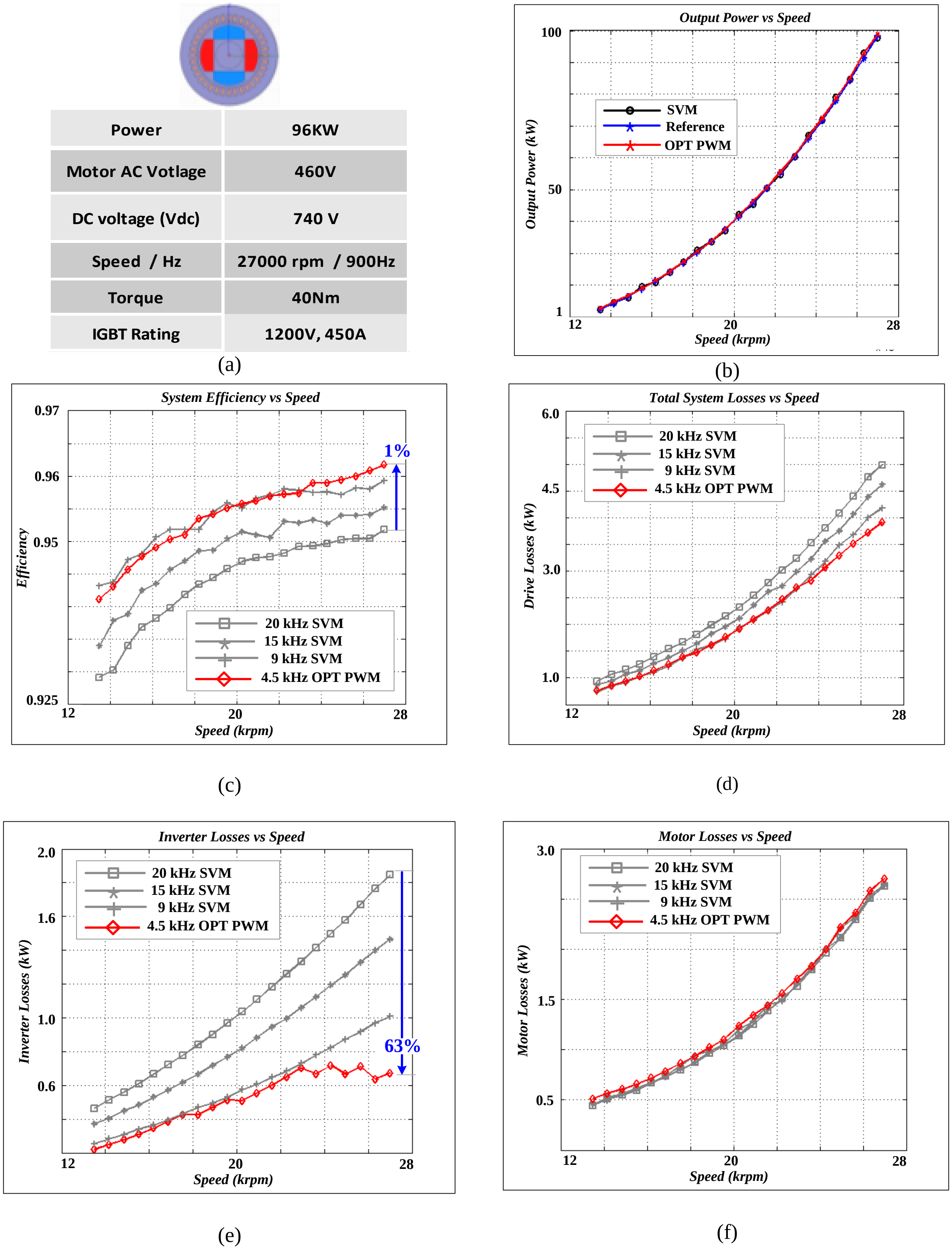

Power	96KW
Motor AC Votlage	460V
DC voltage (Vdc)	740 V
Speed / Hz	27000 rpm / 900Hz
Torque	40Nm
IGBT Rating	1200V, 450A

(a)

(b)

(c)

(d)

(e)

(f)

Figure 4.33Case-I 100 kW PMSM drive system

Case II-

Figure 4.34 (a) shows parameter of an 8 pole 22 kW, 822 rpm machine driven by an inverter with 1200V, 55 A IGBT devices. Figure 4.34(b-f) show the variable speed performance of the PMSM drive system. The output power vs. speed profiles for space vector and optimal PWM are shown in Figure 4.34 (b). For the case considered, the switching frequency is reduced from 10 kHz to 483 Hz to evaluate the influence of sinusoidal and sine-harmonic currents on total system efficiency. Using the analytical loss estimation method discussed in previous sections, the lowest switching frequency of 483 Hz was chosen. The synchronous optimal PWM patterns are changed gradually as a function of operating speed from $N = 15$ to $N = 9$.

Figure 4.34(c) shows the total system efficiencies at various switching frequencies considering synchronized space vector (SVM) and synchronous optimal modulator (OPT PWM). It is seen that as the switching frequency is reduced from 10 kHz to 483 Hz, the efficiency of the system increases by 1.2 percent at the maximum load condition. It is also noted that, above 750 rpm, synchronous optimal PWM has higher efficiency than space vector modulator for the same switching frequency. The increase in overall efficiency considering synchronous optimal PWM is due to decrease in the total drive system losses as shown in Figure 4.34(d). The total drive system loss reduction is due to significant reduction of losses in the inverter and a very small increase in the motor harmonic losses. The inverter losses at various switching frequencies and as a function of operating speed are shown in Figure 4.34(e) while the motor harmonic losses are shown in Figure 4.34(f).

From Figure 4.34(e), it is seen that at the maximum load condition, the inverter switching losses considering synchronous optimal PWM are 58 percent lower than those considering space vector modulation at 10 kHz. The loss reduction is predominantly due to reduction of switching losses. It is also noted that synchronous space vector modulation operating at 483 Hz has similar inverter losses in comparison to synchronous optimal PWM at the same switching frequency.

Figure 4.34(f) shows that the synchronous optimal PWM results in up to 5 percent increase in motor harmonic losses than the space vector modulators at higher switching frequencies. The increase in motor harmonic losses marginally increases the de-rating of the motor. It is also observed that above 700 rpm, synchronous optimal PWM at 483 Hz has lower motor harmonic losses than synchronous SVM operating at the same switching frequency. This is mainly due to the lower harmonic distortion offered by the synchronous optimal PWM.

From the case studied, it is seen that by reducing switching frequency of the inverter, the total losses of the system are significantly reduced thereby increasing the total system efficiency. It is also seen that synchronous optimal PWM provides better performance at higher operating speeds.

Case-II

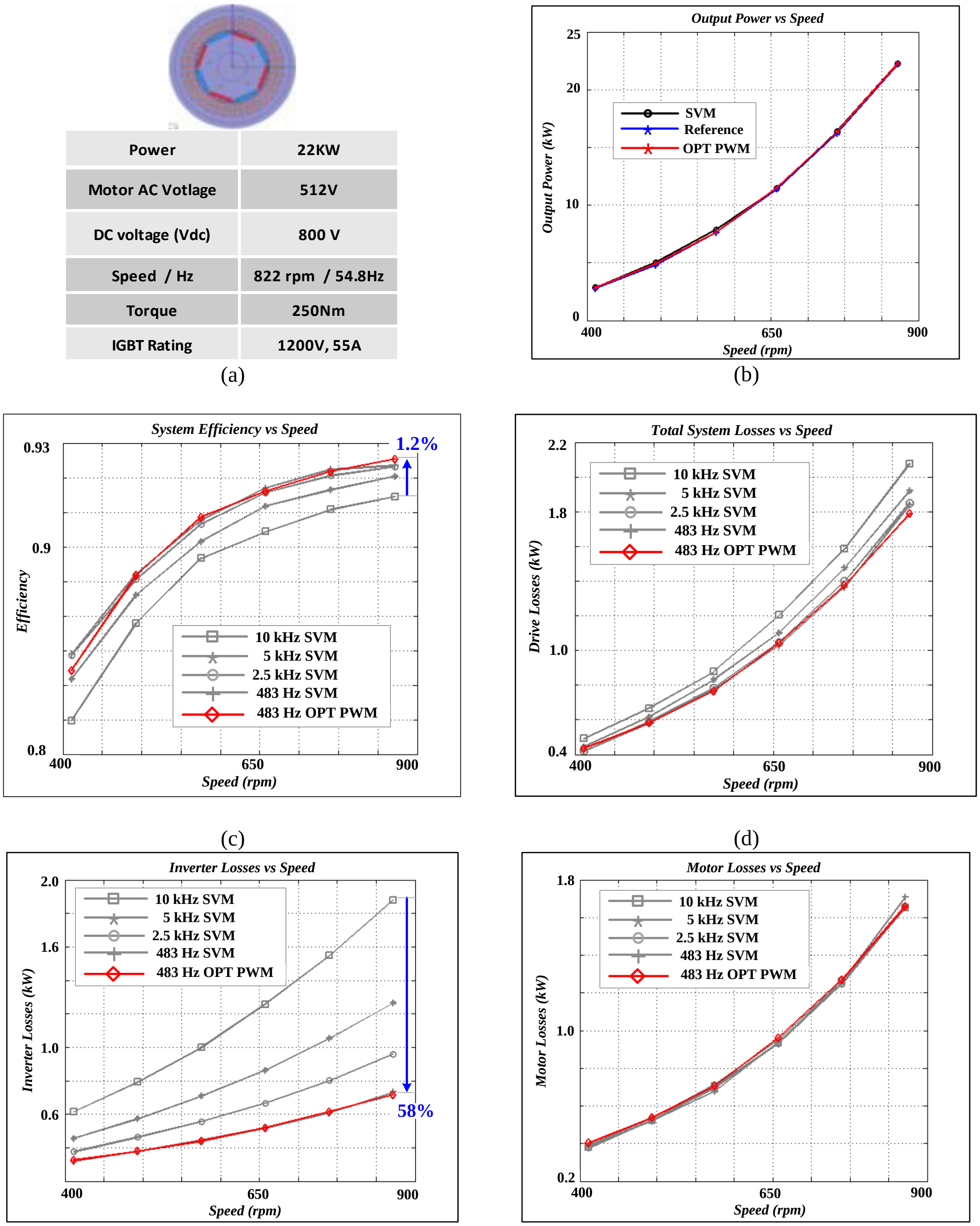

Power	22KW
Motor AC Votlage	512V
DC voltage (Vdc)	800 V
Speed / Hz	822 rpm / 54.8Hz
Torque	250Nm
IGBT Rating	1200V, 55A

(e) (f)

Figure 4.34Case-II 22 kW PMSM drive system

Case III-

Figure 4.35(a) shows parameters of an 8 pole 8.5 kW, 3000 rpm machine driven by an inverter with 1200V, 30 A IGBT device. Figure 4.35(b-f) show the variable speed performance of the PMSM drive system. The output power vs. speed profiles for space vector and optimal PWM are shown in Figure 4.35(b). For the case considered, the switching frequency is reduced from 10 kHz to 933 Hz to evaluate the influence of sinusoidal and sine-harmonic currents on total system efficiency. Using the analytical loss estimation method discussed in previous sections, the lowest switching frequency of 933 Hz was chosen. The synchronous optimal PWM patterns are changed gradually from $N = 15$ to $N = 7$ as a function of operating speed.

Figure 4.35(c) shows the total system efficiencies at various switching frequencies considering synchronized space vector (SVM) and synchronous optimal modulator (OPT PWM). It is seen that as the switching frequency is reduced from 10 kHz to 933 Hz, the efficiency of the system increases by 1.6 percent at the maximum load condition. It is also noted that, above 1900 rpm, the synchronous optimal PWM has higher efficiency than space vector modulator for the same switching frequency. The increase in overall efficiency considering synchronous optimal PWM is due to decrease in the total drive system losses as shown in Figure 4.35(d). The total drive system loss reduction is due to significant reduction of losses in the inverter while a very small increase in the motor harmonic losses. The inverter losses at various switching frequencies and as a function of operating speed are shown in Figure 4.35(e) while the motor harmonic losses are shown in Figure 4.35(f).

From Figure 4.35(e), it is seen that at the maximum load condition, the inverter switching losses considering synchronous optimal PWM are 58 percent lower than those considering space vector modulation at 10 kHz. The loss reduction is predominantly due to reduction of the switching losses. It is also noted that synchronous space vector modulation operating at 933 Hz has similar inverter losses in comparison to synchronous optimal PWM at the same switching frequency.

Figure 4.35(f) shows that the synchronous optimal PWM results in up to 3 percent higher motor harmonic losses than the space vector modulators at higher switching frequencies. The increase in motor harmonic losses will marginally increase the derating of the motor. It is also observed that above 1800 rpm, synchronous optimal PWM at 933 Hz has lower motor harmonic losses than synchronous SVM operating at the same switching frequency. The lower harmonic losses are due to lower current distortion offered by synchronous optimal PWM.

From the case studied, it is again validated that by the reducing switching frequency of the inverter, the total losses of the system are significantly reduced thereby increasing the total system efficiency. It is also shown that synchronous optimal PWM provides better performance at higher operating speeds (higher modulation indices).

Case-III

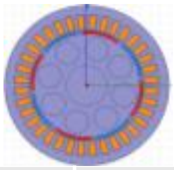

Power	8.5KW
Motor AC Votlage	305V
DC voltage (Vdc)	430 V
Speed / Hz	3000 rpm /133.33Hz
Torque	42Nm
IGBT Rating	1200V, 30A

(a)

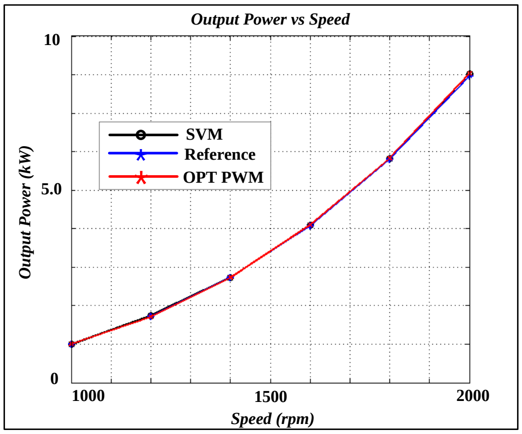

(b)

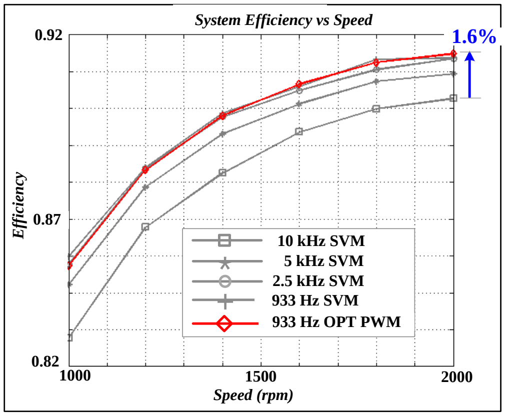

(c)

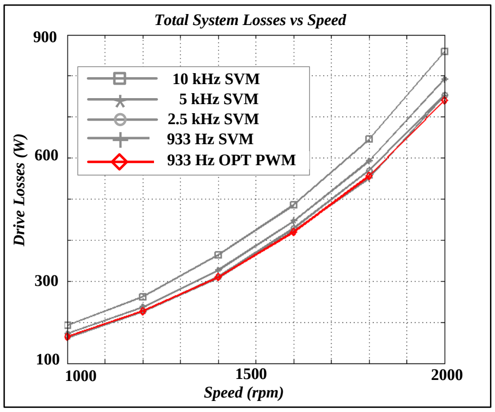

(d)

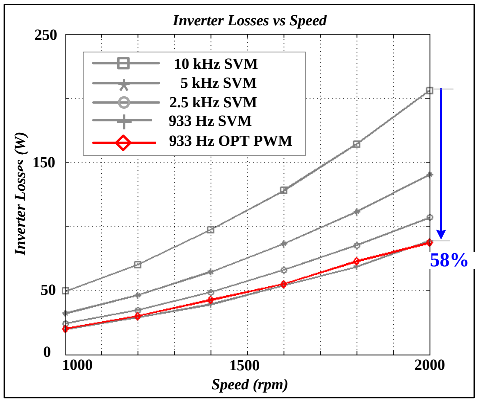

(e)

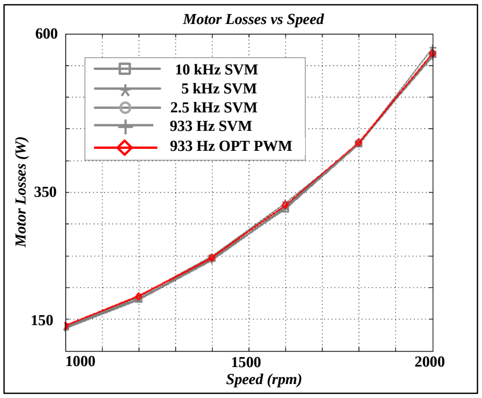

(f)

Figure 4.35Case-III 8.0 kW PMSM drive system

Case IV: Figure 4.36(a) shows parameters of a 4 pole 2.2 kW, 3000 rpm machine driven by an inverter with 600V, 20 A IGBT devices. Figure 4.36(b-f) show the variable speed performance of the PMSM drive system. The output power vs speed profiles for space vector and optimal PWM are shown in Figure 4.36(b). For the case considered, the switching frequency is reduced from 10 kHz to 700 Hz to evaluate the influence of sinusoidal and sine-harmonic currents on total system efficiency. Using the analytical loss estimation method discussed in previous sections, the lowest switching frequency of 700 Hz was chosen. The synchronous optimal PWM patterns are changed gradually as a function of operating speed from $N = 15$ to $N = 7$.

Figure 4.36(c) shows the total system efficiencies at various switching frequencies considering synchronized space vector (SVM) and synchronous optimal modulator (OPT PWM). It is seen that as the switching frequency is reduced from 10 kHz to 700 Hz, the efficiency of the system increases by 0.5 percent at the maximum load condition. It is also noted that, above 2800 rpm, the synchronous optimal PWM has higher efficiency than space vector modulator operating at 900 Hz. The increase in overall efficiency considering synchronous optimal PWM is due to decrease in the total drive system losses as shown in Figure 4.36(d). The total drive system loss reduction is due to significant reduction of losses in the inverter while a very small increase in the motor harmonic losses. The inverter losses at various switching frequencies and as a function of operating speed are shown in Figure 4.36(e) while the motor harmonic losses are shown in Figure 4.36(f).

From Figure 4.36(e), it is seen that at the maximum load condition, the inverter switching losses considering synchronous optimal PWM are 32 percent lower than the space vector modulation at 10 kHz. The reduction in inverter switching losses is lower in comparison to the previous cases because the lower voltage (600V) rating IGBT devices have lower switching losses than 1200V IGBT devices. Hence as the switching frequency is reduced, the percentage reduction in losses in devices of lower voltage rating is also lower. Consequently, the overall efficiency improvement achieved is lower than that seen in the previous cases.

Figure 4.36(f) shows that the synchronous optimal PWM results in higher motor harmonic losses, up to 2%, than the space vector modulators at higher switching frequencies. The increase in motor harmonic losses will marginally increase the de-rating of the motor. It is also observed that synchronous optimal PWM at 700 Hz has lower motor harmonic losses than synchronous SVM operating at 900 Hz. This is mainly due to the lower harmonic distortion offered by the synchronous optimal PWM.

From the case studied, it is seen that by the reducing switching frequency of the inverter, the total losses of the system are significantly reduced thereby increasing the total system efficiency. It is also shown that synchronous optimal PWM provides better performance at higher operating speeds.

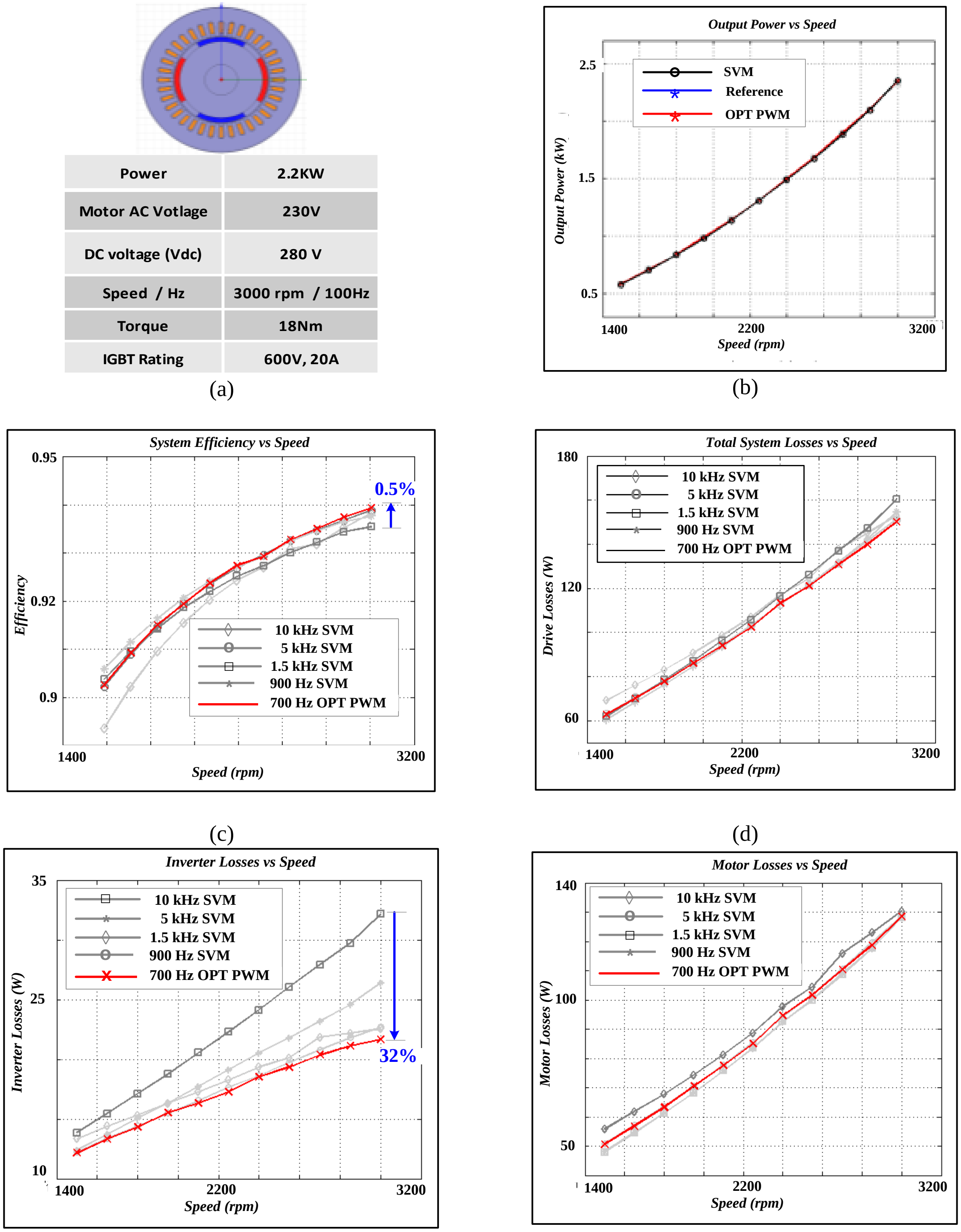

Power	2.2KW
Motor AC Votlage	230V
DC voltage (Vdc)	280 V
Speed / Hz	3000 rpm / 100Hz
Torque	18Nm
IGBT Rating	600V, 20A

(a) (b)

(c) (d)

(e) (f)

Figure 4.36. Case-IV 2.2 kW PMSM drive system

Case V: Figure 4.37(a) shows parameters of a 4 pole 300 W, 3000 rpm machine driven by an inverter with a 100V, 17 A IGBT device. Figure 4.37(b-f) show the variable speed performance of the PMSM drive system. The output power vs. speed profiles for space vector and optimal PWM are shown in Figure 4.37(b). For the case considered, the switching frequency is reduced from 10 kHz to 800 Hz to evaluate the influence of sinusoidal and sine-harmonic currents on total system efficiency. Using the analytical loss estimation method discussed in previous sections, the lowest switching frequency of 800 Hz was chosen. The synchronous optimal PWM patterns are changed gradually from $N = 15$ to $N = 7$ as a function of operating speed.

Figure 4.37(c) shows the total system efficiencies at various switching frequencies considering synchronized space vector (SVM) and synchronous optimal modulator (OPT PWM). It is seen that as the switching frequency is reduced from 16 kHz to 3 kHz, the efficiency of the system increases by 0.4% at the maximum load condition. It is also noted that the synchronous optimal PWM at low switching frequency does not offer higher efficiency as seen in the previous cases. It is mainly because: (a) the switching losses in low voltage semiconductor devices are low, and (b) the motor harmonic losses are considerably higher. The total drive system losses are shown in Figure 4.37(d). The inverter losses at various switching frequencies and as a function of operating speed are shown in Figure 4.37(e) while the motor harmonic losses are shown in Figure 4.37(f).

From Figure 4.37(e), it is seen that at the maximum load condition, the inverter switching losses considering 3 kHz switching frequency is 32 percent lower than those considering space vector modulation at 16 kHz. Since the 100V IGBT devices have lower switching losses than 600V IGBT devices, the percentage reduction in switching losses in low voltage devices is also lower. Hence the benefit of reducing the switching frequency is not as high as those in case of 1200V devices.

Figure 4.37(f) shows that the synchronous optimal PWM results in up to 8% higher motor harmonic losses than the space vector modulators at higher switching frequencies. The higher losses are mainly because the small phase inductance (0.75 mH) that allows higher harmonic content in the motor at reduced switching frequencies. The increase in motor harmonic losses will increase the derating of the motor. It is also observed that space vector PWM at 3 kHz has lower motor harmonic losses than synchronous optimal PWM operating at 800 Hz.

From the case studied, it is seen that by the reducing switching frequency of the inverter, the total losses of the system are marginally reduced and the total system efficiency is increased by only 0.4 percent. In this case, synchronous space vector modulation with switching frequency of 3 kHz offers better system efficiency than other modulators.

Case-V

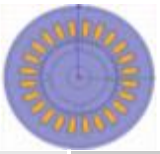

Power	**300W**
Motor AC Votlage	**27V**
DC voltage (Vdc)	**42 V**
Speed / Hz	**2000 rpm / 66.67Hz**
Torque	**1.5Nm**
IGBT Rating	**100V, 17A**

(a)

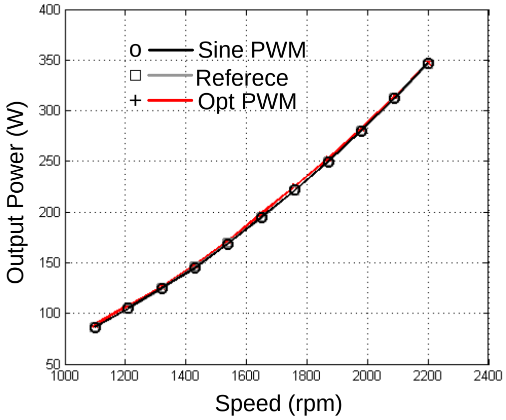

(b)

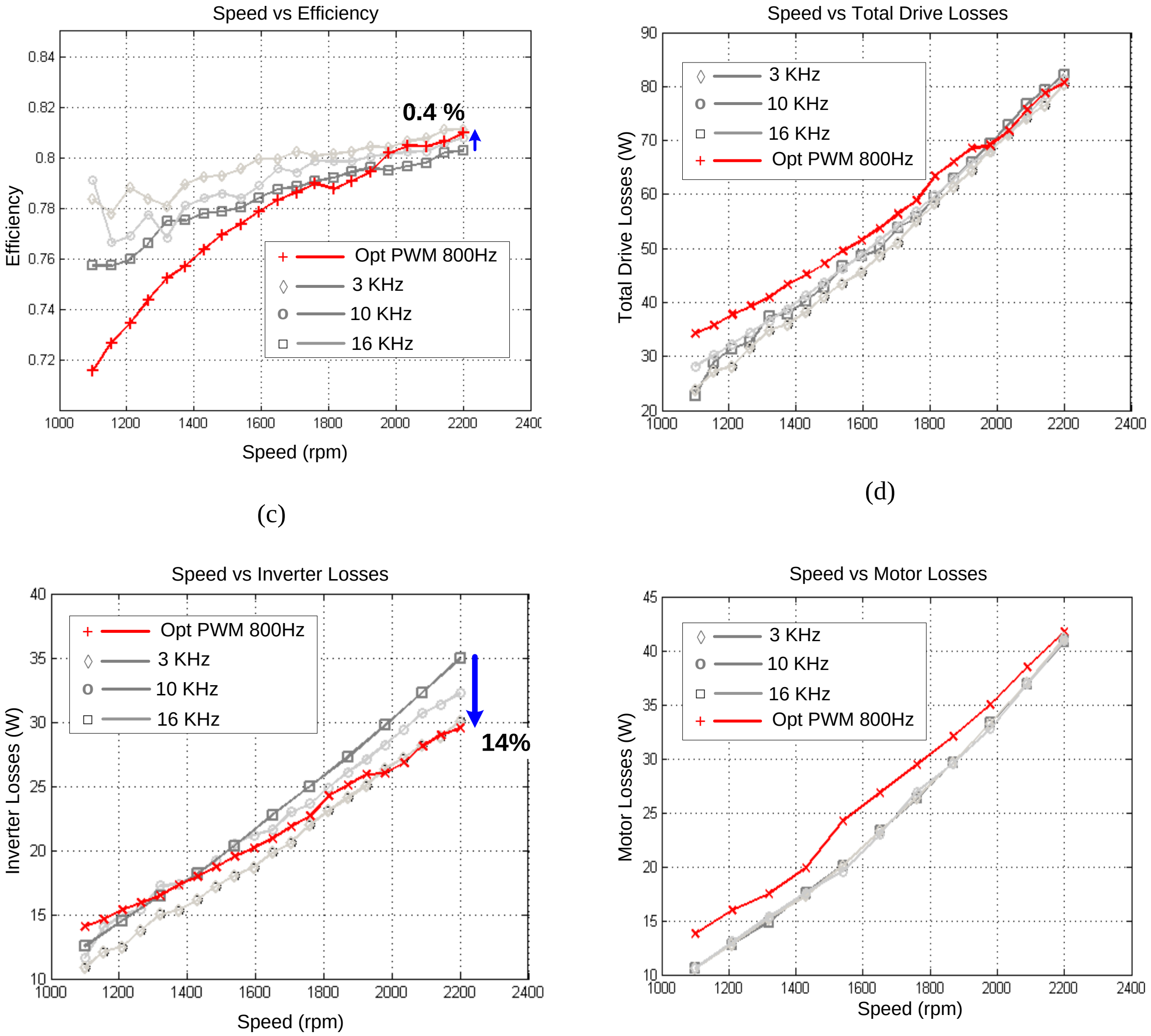

(c)

(d)

(e)

(f)

Figure 4.37. Case-V 300W PMSM drive system.

Following conclusions can be drawn from the case studies***:***

1. The five case studies show that the total system efficiency can be improved by reducing the switching frequency of the inverter. The percentage improvement in efficiency is predominantly dependent on the semiconductor device voltage rating.
2. In case of PMSM drive operating with 1200V IGBT devices, the switching frequency of the inverter could be reduced such that the inverter losses decrease by more than half while the motor harmonic losses increased by only 5 percent. The total system efficiency improvement at peak load considering higher voltage semiconductor devices (1200V) is above 1% while the same considering low voltage devices (<600V) is less than 0.5% .
3. The motor resistive and core losses increase due to reduced switching frequency operation. In the above cases, the maximum increase in total motor harmonic losses is less than 8%.
4. Considering reduced switching frequency operation and at higher modulation indices, synchronous optimal PWM yields higher system efficiency and lower inverter loss than carrier based space vector modulators. A combination of synchronized SVM and synchronous optimal PWM must be considered as a hybrid approach to achieve higher system efficiency for the entire operating range.

This completes the efficiency improvement analysis of various PMSM drive systems operating at reduced switching frequencies. The aforementioned conclusions validate the proposed methodology of operating PMSM drive systems at very low switching frequencies. Such an analysis has not been discussed in [11-13] and hence underscores the contribution of this work. To highlight the advantages of PMSM operating at reduced switching frequency over induction machines qualitatively, a comparative analysis is made in the following section.

4.6.1. Qualitative comparison between induction and PMSM drives operating at low switching frequency.

Induction motors have windings in the rotor that contribute to additional harmonic losses when compared to PMSMs. Thus reducing the switching frequency of inverter in induction motor will result in higher harmonic losses in the stator as well as in the rotor. To evaluate the same, an 8 kW, 4 pole 3000 rpm induction motor as shown in Figure 4.38 is considered. The motor has stator resistance of 0.304 ohms, rotor resistance (referred to stator) of 0.195 ohms, stator reactance of 1.293 ohms, rotor reactance of 4.98 ohms and a magnetizing impedance of 37.6 ohms. The rotor slip at rated condition is 2% of the nominal speed. The two switching frequencies considered for the motor harmonic loss evaluation are 10 kHz and 1.1 kHz, respectively. The performance of the induction motor is compared with an 8 kW PMSM from Case-III. The induction motor harmonic losses are calculated based on the procedure described in [20, pp 361]. The stator resistive and core losses of the two motors operating at various switching frequencies are listed in Table 4-6.

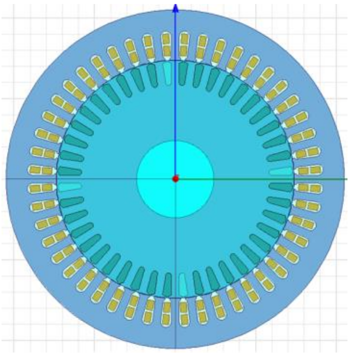

Figure 4.388 kW 4 pole induction motor

Table 4-6. Harmonic loss comparison between induction and permanent magnet motors operating at high and low switching frequencies.

Induction Motor 8 kW-3000 rpm, 4 poles (M = 1.2)

Switching Frequency	***10 kHz***	***1.1kHz (OPT-PWM)***	***% Increase***
Resistive losses	468	482	3
Core Losses	261	342	31
Total Losses	**729**	**824**	**13**

PMSM – 8 kW 2000 rpm, 8 poles (M = 1.2)

Switching Frequency	***10 kHz***	***665 Hz(OPT-PWM)***	***% Increase***
Resistive losses	254	257	1.2
Core Losses	312	320	2.5
Total Losses	**566**	**577**	**2**

The fundamental operating frequency of the induction motor is 100 Hz, while that of the PMSM is 133 Hz. Both the machines are operated using space vector PWM for high switching frequencies and synchronous optimal PWM at reduced switching frequencies. The modulation index in both cases is 1.2. Following observations are made from the table:

1. The reduction in switching frequency results in higher resistive losses in induction motor than in PMSM. The higher losses in induction motor are due to higher losses in the motor's stator and rotor. Since PMSM does not have rotor windings, the increase in resistive losses is small.
2. The increase in the core losses of the induction motor is higher than in PMSM. This is primarily because of the higher harmonic content in both the stator and rotor of the induction motor. Since the core losses are proportional to the square of the amplitude of the harmonics included flux density as well as square of the harmonic frequency, the corresponding core losses in both the stator and rotor are higher.
3. At reduced switching frequencies, the total harmonic loss increase in case of induction motor is 13% while that of PMSM is only 2% .

The above results show that PMSMs are more suitable for reduced switching frequency operation than induction machines. It also implies that the switching frequency in case of PMSM can be further reduced in comparison to induction motor. This advantage of PMSM over induction machine is yet to be reported.

4.7. Conclusions

This chapter focused on evaluating the PMSM drive system efficiency improvement considering reduced switching frequency operation. It was shown that given an optimally designed permanent magnet machine and its control algorithm, the system efficiency can be improved by reducing the inverter switching losses by minimizing its switching frequency. Following are the significant contributions and conclusions of this work:

1. Various pulse width modulators operating at reduced switching frequencies are compared considering their loss factors. Synchronous optimal pulse width modulators with multiple pulse patterns are preferred over both carrier based and selective harmonic elimination based modulators due to their lower loss factor. It was also shown that synchronous optimal PWM requires smaller value of motor inductance than other modulation methods.
2. A comprehensive procedure for estimating PMSM's predominant losses in the form of stator resistive and core losses was derived analytically. The accuracy of the method for estimating core losses was validated using finite element simulations. It was shown that for

high grade lamination steel material, and programmed PWM, the influence of reduced switching frequencies on core loss increase is small.

3. An analytical method for estimating the semiconductor losses at reduced switching frequencies and considering programmed PWM was developed. The method takes into account the actual current waveform including harmonics due to programmed PWM instead of sinusoidal approximation. The accuracy of the method was validated using detailed simulation circuit models.
4. Using the analytical loss models of the motor and inverter, total system losses of five PMSM drive systems rated from 250W up to 100 kW were analyzed. It was shown that for systems utilizing 1200V semiconductor devices, the efficiency improvement is more than 1 percent. For systems utilizing 600V and lower voltage semiconductor devices, the efficiency improvement is less than 0.5 percent. The case studies validate the proposed approach of improving the total system efficiency by reducing the inverter switching frequency. This improvement in efficiency translates to significant cost reduction for applications requiring long hours of operation.

APPENDIX

Table A.1. Machine with geometry and coefficients

Name	Value	Name	Value
Inner radius of stator (mm)	58.5	Stator length (mm)	76.3
Outer radius of stator (mm)	95	Tooth width (mm)	5.303
Thickness of magnets (mm)	4.8	Yoke depth (mm)	19.3
Tooth flux density (T)	1.6	Tooth height (mm)	17.2
Yoke Flux density (T)	1.2	Magnet Coverage (mm)	56.9
Tooth Volume (m^3)	2.94e-4	Slot width (mm)	7.6
Yoke Volume (m^3)	7.86e-4	Air gap length (mm)	2
Number of turns	24	Magnet Arc 2β (deg)	120
Number of Slots	36	Permeability coefficient	4πe-7
Mass Density of Steel (Kg/m^3)	7650	Steinmetz coefficient	2

References

[1] P.H. Nayak, and R.G. Hoft, "Optimizing the PWM Waveform of a Thyristor Inverter." *IEEE Trans. Ind. Appl.*, no. 5 (October 1975), pp. 526–530.

[2] P.N. Enjeti, P.D. Ziogas, and J.F. Lindsay, "Programmed PWM Techniques to Eliminate Harmonics - A Critical Evaluation." *IEEE Industry Applications Society Annu. Mtg., 1988, Conference Record of the 1988*, vol.1, pp. 418 – 430, 1988.

[3] B.D. Bedford, R.G. Hoft, *Principles of Inverter Circuits*, J Wiley, New York , 1964.

[4] G.S. Buja, and G.B. Indri, "Optimal Pulsewidth Modulation for Feeding AC Motors." *IEEE Trans. Ind. Appl.*, vol. IA-13, no. 1 (January 1977): 38 –44.

[5] J. Holtz, and B. Beyer,"OptimalPulsewidth Modulation for AC Servos and Low-cost Industrial Drives." *IEEE Trans. Ind. Appl.*, vol. 30, no. 4 (August 1994): 1039 –1047.

[6] G.R. Slemon and X. Liu, "Core losses in permanent magnet motors," *IEEE Trans. Magnetics*, vol. 26, no. 5, pp. 1653-1655, Sept.1990.

[7] T.M. Jahns, "Torque production in permanent-magnet synchronous motor drives with rectangular current excitation," *IEEE Trans. Ind. Appl*., vol. 20, no. 4, pp. 803-813, July/Aug. 1984.

[8] R. Krishnan, *Permanent Magnet Synchronous and Brushless DC Motor Drives*, CRC Press, 2010.

[9] E. Dlala and A. Arkkio, "A General Model for Investigating the Effects of the Frequency Converter on the Magnetic Iron Losses of a Squirrel-Cage Induction Motor," *Magnetics, IEEE Transactions on*, vol. 45, no. 9, pp. 3303 –3315, Sep. 2009.

[10] T. Jahns, G. Kliman, and T. Neumann, "Interior PM Synchronous Motors for Adjustable Speed Drives", IEEE Trans. on Ind. Appl., vol. IA-22, July/Aug 1986, pp. 738-747.

[11] J. Itoh, T. Ogura, "Evaluation of Total Loss for an Inverter and Motor by Applying Modulation Strategies", *EPE-PEMC* 2010, S12-21 – S12-28

[12] J. Holtz, "Pulsewidth Modulation for Electronic Power Conversion." *Proc. IEEE 82,* no. 8 (August 1994): 1194 – 1214.

[13] D. Sato, J. Itoh "Total Loss Comparison of Inverter Circuit Topologies with Interior Permanent Magnet Synchronous Motor Drive System", *ECCE* 2013, pp 57-543.

[14] D. Holmes, "The Significance of Zero Space Vector Placement for Carrier-Based PWM Schemes," *IEEE Trans. Ind. Appl.*, vol. 32, no. 5, pp. 1122-1129, Sep./Oct. 1996.

[15] V. Blasko, "Analysis of a Hybrid PWM Based on Modified Space-Vector and Triangle-Comparison Methods," *IEEE Trans. Ind. Appl.*, vol. 33, no. 3, pp. 756-764, May/June 1997.

[16] A. Hava, R. Kerkman, and T. Lipo, "A High-Performance Generalized Discontinuous PWM Algorithm," *IEEE Trans. Ind. Appl.*, vol. 34, no. 5, pp. 1059-1071, Sep./Oct. 1998.

[17] S.R. Bowes, and D. Holliday, "Optimal regular-sampled PWM inverter control techniques," *IEEE Trans. Ind. Electron.*, vol. 54, no. 3, pp. 1547–1559, 2007.

[18] J. Ojo, "The generalized discontinuous PWM scheme for three-phase voltage source inverters", *Ind Electron IEEE Trans on*. Vol. 51. No. 6, Dec 2004, pp-1280-1289

[19] D. Chung, and S. Sul, "Minimum-Loss Strategy for Three-Phase PWM Rectifier," *IEEE Trans. Ind. Electron.*, vol. 46, no. 3, pp. 517-526, June 1999.

[20] R. Krishnan, *Electric Motor and Drives- Modeling Analysis and Control*, Prentice Hall Inc., 2001.

[21] R. Rabinovici, T.J.E. Miller, "Eddy-current losses of surface-mounted permanent magnet motors", *IEE Proc.Electr. Power Appl.*, Vol 144, No 1, Jan 1997, pp. 61-64.

[22] C. Mi, G.R. Slemon, and R. Bonert, "Modeling of iron losses of permanent-magnet synchronous motors," *Industry Applications, IEEE Transactions on*, vol. 39, no. 3, pp. 734–742, Jun. 2003.

[23] M. Swamy, T. Kume, "Present state and a futuristic vision of motor drive technology", *Optimization of Electrical and Electronic Equipment Conf*, May 2008, pp- XLV – LVI.

[24] J. Kolar, S. Round, "Analytical calculation of the RMS current stress on the DC-link capacitor of voltage-PWM converter systems", IEE Proceedings, Electric Power Applications, Volume:153 , Issue: 4, Jul 2006, pp 535 – 543.

[25] J. Bond, "Advances in capacitors and ultra –capacitors for power electronics", *Applied Power Electron Conf.*, Ind Session 1.3, Mar 2013

[26] A. Calmels, "Advanced IGBT Driver APPLICATION MANUAL", App Note 1903, Microsemi, July 2006.

[27] P. Dahono, Y. Sato, T. Kataoka, “Analysis of Conduction Losses in Inverters,” IEE Proc. Elec. Pow. Appl., vol. 142, no. 4, pp. 225-232, July 1995.

[28] L. Mestha, and P. Evans, “Analysis of On-State Losses in PWM Converters,” IEE Proceed. Part B, vol. 136, no. 4, pp. 189-195, 1989.

[29] F. Casanellas, “Losses in PWM Inverters Using IGBTs,” IEE Proc. Elec. Pow. Appl., vol. 141, no. 5, pp. 235-239, Sep. 1994.

[30] L. Mestha, and P. Evans, “Optimization of Losses on PWM Converters,” Conf. Proc. PE-VSD., pp. 394-397, 1988.

[31] F. Blaabjerg, U. Jaeger, S. Munk-Nielsen, and J. Pedersen, “Power Losses in PWM-VSI Inverter using NPT or PT IGBT Devices,” IEEE Trans. Power Electron., vol. 10, no. 3, pp. 358-367, May 1995.

[32] J. Kolar, H. Ertl, and F. Zach, “Influence of the Modulation Method on the Conduction and Switching Losses of a PWM Converter System,” IEEE Trans. Ind. Appl., vol. 27, no. 6, pp. 1063-1075, Nov./Dec. 1991.

Chapter 5 Implementation and Experimental Validation of Efficiency Improvement in PMSM Drives through Switching Frequency Reduction

5.1. Abstract

. Efficiency improvement analysis of permanent magnet synchronous motor drive system through reduced switching frequency operation has been made in the previous chapter. It was shown that the efficiency in PMSM drive system can be improved by reducing the switching frequency of the inverter. This chapter will focus on vital implementation aspects connected with the switching frequency reduction and its application to improving the system efficiency of the PMSM drive.

For low switching frequency operation, programmed pulse width modulators (PWM) are advantageous as they yield low harmonic distortion of the current waveform. The programmed PWM pulses are generated using commutation angles which are calculated offline as a function of the modulation index. These angles are stored in the form of loop-up tables and called back during real time synthesis of the switching pulses. However it is difficult to implement programmed PWM on state of art digital signal processor dedicated for motor drives because of its limitation on maximum allowable counter periods and the clock frequency. Given the limitations, a novel approach of carrier based programmed PWM generation is proposed and its implementation is discussed in detail.

For high efficiency operation of PMSM drive, it is essential to control the magnitude and phase of current phasor with respect to the motor back electromotive force (EMF) voltage phasor. Current control of permanent magnet synchronous motors at reduced switching frequencies becomes difficult due to low resolution of the inverter output voltage and the feedback sampling rate. To address the same, three current controller designs are analyzed using space phasor modeling approach and they are: (a) proportional integral (PI) current controller, (b) complex variable current controller and (c) PI current controller with feedback oversampling. The three current controllers are compared in detail using simulation while, operation of PI current controller with feedback oversampling is verified experimentally due to its simple implementation and stable performance.

PMSM drive system efficiency is experimentally evaluated using three modulation methods and they are; (a) space vector modulation (SVM), (b) discontinuous PWM (DPWM) and (c) programmed PWM. For the comparison, SVM is used for higher switching frequency operation while DPWM and programmed PWM are considered for lower switching frequency operation. The experimental measurements show that the total system losses are lower when the switching frequency of the inverter is reduced there by validating the improvement in the total system efficiency.

5.2. Introduction

Most of the previous work on low switching operation of motor drives has been focused on induction machines. Application of the same for PMSM must be carefully evaluated as the two machines have different operational and control characteristics. The following sections highlight the differences between the relevant prior work and topics that have not been addressed on implementation and experimental validation of efficiency improvement in PMSM drives through switching frequency reduction.

A. Implementation of PWM algorithms at low switching frequencies

When the switching frequency of the inverter is reduced, its switching losses are reduced in proportion resulting in higher output power rating of the inverter [1]. At low switching frequencies, the inverter is controlled using programmed PWM because it offers lower current harmonic distortion than carrier based PWM [2]. However carrier based PWM is easier to implement on digital hardware than programmed PWM [3-7]. To implement carrier based PWM, a sinusoidal reference signal is compared with a high frequency triangle (or carrier) signal. The high frequency carrier signal is generated using an up-down counter which is readily available in microcontrollers for motor control. The programmed PWM, on the other hand, is implemented by storing offline calculated commutation angles in lookup tables and then recalled for PWM generation using dedicated digital logic circuit [8-10]. Therefore the microcontrollers that have digital hardware catered for carrier based PWM and cannot be easily modified for programmed PWM generation [6]. Due to the complexity of implementation and hardware requirements, programmed PWM is less favored in low voltage drives [6], [9].

To simplify the implementation, a regular-sampled method for generating programmed PWM was proposed in [7]. The implementation is made using two sinusoidal phase shifted signals to generate rising and falling edge pulses. Such an approach requires four counters to synthesize the switching waveform. If a single counter approach is used then the computation time of the PWM algorithm increases [7]. Since the state of art microcontrollers do not have so many timers dedicated for PWM generation, the approach becomes tedious. In [11], an alternative method to generate the programmed PWM using principles of carrier based PWM was proposed. The approach focused on comparing a sine wave voltage reference with a modified triangle to generate the programmed PWM pulses using an analog comparator circuit. The digital implementation of the same was not discussed. Although the feasibility of the method was shown, it is difficult to implement the same on state of art digital signal processor because of limitation on maximum allowable counter period and the processor clock frequency.

Based on the above review it is seen that implementation of programmed PWM on commercially available microcontrollers is complex and difficult. A simple implementation similar to that of a carrier based PWM on a state of art digital signal processor has yet to appear, and highly desired.

B. Stable operation of PMSM under limited switching pulses or low inverter bandwidth

Dynamic response of permanent magnet motors is superior to induction machines due to its lighter rotor and its higher capacity for peak torques. This is true only if the exact rotor position is available and the inverter control can achieve accurate alignment of stator currents with the motor back-EMFs [12]. In case of sensorless position control, accurate estimation of rotor position during transient operation can be challenging. In such cases, stability of the system can be determined through open-loop operation of the machine. It is known that induction machine inherently has stable open loop response while PMSM [13-15] can be operated on open loop only for a short duration of time with oscillatory speeds and chaotic torque generation. Hence it can be inferred that during low switching frequency operation, when the inverter control bandwidth is low, induction machines can have more stable operation while the capacity for the stable operation of PMSM is extremely limited both in its torque and speed responses as well as shrunken torque capabilities. The current literature only covers low switching frequency operation of induction motors, while the challenges for applying the same or similar techniques for PMSM are yet to appear. Two important aspects that must be considered in the low switching frequency control of PMSM drives are: (a) current regulation and (b) rotor position control. Both of these aspects are critical to avoid pull-out of PMSM under transient load conditions at low switching frequency operation. Current regulation at low switching frequency has been demonstrated on induction machines using complex variable current regulators [16]. Complex variable current regulation of PMSM with low carrier to fundamental ratio (lower switching pulses) has been shown in [17] only for high speed traction application. Current regulation method for programmed PWM has not been discussed in any of the published literature so far.

C. Experimental PMSM drives system efficiency evaluation at low switching frequency:

Previous work on low switching operation of motor drives has been focused on induction machines [1], [2], [18] and [19]. In [18], total system efficiency optimization of induction motor drive using programmed PWM was shown. Strategy for computation of commutation angles based on total system losses was evaluated. It was shown that commutation angles calculated using simple inductive loads gave near optimal performance in minimizing total system losses.

In [20], the improvement in inverter efficiency of medium voltage induction motor drive was demonstrated by applying synchronous optimal programmed PWM. It was experimentally shown that the motor phase current harmonic distortion with optimal PWM at switching frequency of 250 Hz was similar to that of a space vector PWM at 1 kHz. The reduction in switching frequency doubled the power rating of the inverter. The research mainly focused on reducing switching losses of the inverter while harmonic losses analysis of the motor was not discussed.

In [21], total system losses incurred in the inverter as well induction motor due to reduced switching frequency was experimentally evaluated. Programmed PWM was implemented to reduce the current harmonic distortion at low switching frequency. For efficiency evaluation, the motor losses were measured using a calorimeter. Based on single measurement point, it was concluded that programmed PWM at low switching frequency (650 Hz) resulted in lower system losses than space vector modulation at high switching frequency (20 kHz). It was also shown that programmed PWM had lower harmonic losses in the motor than six step square wave modulation. Although a total system efficiency improvement was claimed, it is to be noted that the benefits diminished when the operation at low switching frequency (650Hz) was compared to the one at 10 kHz. This is because the reduction of losses of the inverter was offset by the increase in the motor harmonic losses. Since induction motor has higher harmonic losses in stator as well as rotor, the benefits of reducing switching frequency is lower comparison to PMSM [22].

In [23], system loss analysis of a 3kW interior permanent magnet synchronous motor (IPMSM) drive operating at various switching frequencies was made. For lower current distortion operation, a three level inverter was considered. Operation of a carrier based PWM with switching frequency of 5 kHz was compared with a six-step mode of operation. Based on experimental measurements, it was shown that at higher operating speeds, six-step operation was more efficient than carrier based PWM at 5 kHz. It should be noted that three-level inverter requires twice the number of switching devices and capacitors in comparison to two-level converter. While the conclusions favored operation at low switching frequency using three-level six-step commutation, the research did not explore the advantages of programmed PWM in a two-level inverter when the switching frequency is reduced below 5 kHz.

Based on the above discussions, it is seen that given a two-level inverter, experimental evaluation of PMSM drive system efficiency at low switching frequency has not been studied in depth. Also application of programmed PWM for improving PMSM drive system efficiency has not been reported. Experimental validation of benefits of reduced switching frequency incorporating various PWM methods for permanent magnet motors driven by two-level inverters and its experimental validation has yet to appear.

Accordingly, the proposed research work and resulting contributions on the topics discussed above are:

1. ***Carrier based programmed PWM and its implementation:***

   Implementation of carrier based PWM techniques along with experimental results will be summarized in section 5.3as a benchmark. Then a simple carrier based implementation method for programmed PWM is proposed and explained in section 5.4. The proposed implementation method is validated experimentally using state of art digital signal processor.

2. ***Closed loop current regulation at low switching frequency:***

   As the switching frequency is reduced, the corresponding sampling rate is also reduced which results in larger sampling delay of the feedback signals with the attendant compromised current regulator performance. In section 5.5, current controller design using feedback oversampling methods for programmed PWM methods will be explained using space phasor modeling approach to endow a very good current regulator performance.

3. ***Experimental PMSM drive system efficiency evaluation at low switching frequency:***

   In section 5.6, experimental steady state measurements of the PMSM drive system using various modulation methods are obtained to evaluate combined motor and drive system efficiency. The results show that in the given experimental setup, programmed and discontinuous PWM techniques operating at low switching frequencies offer higher system efficiency in comparison to space vector modulation (SVM) technique and operating at higher switching frequency. The results validate the motor and drive system analysis discussed in chapter 4.

5.3. Implementation of carrier based SVM and DPWM method

Carrier based SVM and DPWM techniques are well known and extensively reported in existing literature [24-25]. This section briefly summarizes their implementations.

Block diagram of carrier based SVM and DPWM method is shown in Fig 5.1. The implementation is based on zero sequence injection method explained in chapter 4 as given by the equations (4.1)-(4.7). With reference to Fig 5.1 the command voltages, v_{dqsr}^{*},are the outputs of the current regulators. These voltages are transformed to three-phase voltages v_{abc}, in *abc* reference frame using a d-q to abc inverse transformation in rotor reference frame.

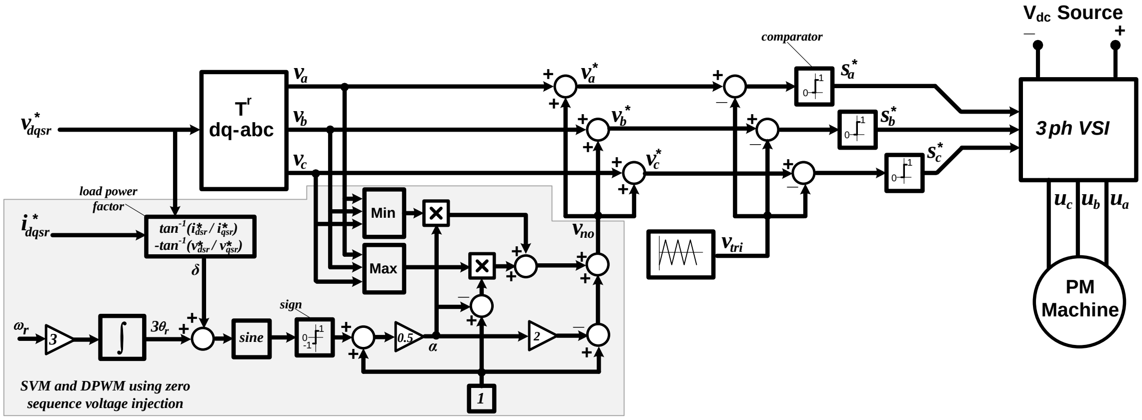

Figure 5.1 Carrier based SVM and DPWM implementation block diagram.

A zero sequence voltage v_{no} based on the generalized equation provided in (4.7) is then added to the three-phase voltages v_{abc} to generate carrier based SVM or DPWM reference voltages v_{abc}^*. The block diagram of zero sequence voltage generation is shaded in gray. The reference voltages are then compared with carrier signal v_{tri} to synthesize the switching patterns S_{abc}^* which are applied to the inverter. In the above block diagram, when $\alpha=0.5$, a space vector modulation waveform is synthesized while discontinuous PWM waveforms are synthesized when $\alpha = 1 - 0.5 \cdot (1 + sgn[sin(3\omega_r t + \delta)])$. Corresponding experimental results of SVM and DPWM waveforms for various values of power factor angles δ are shown in Fig. 5.2 (a-d).

(a)
α(t)=0.5

(b)
δ=0

(c)
δ=60

(d)
δ=75

Figure 5.2. Experimental results: carrier based modulators with zero sequence added (a) SVM, (b-d) DPWM with $\alpha = 1 - 0.5 \cdot (1 + sgn[sin(3\omega_r t + \delta)])$.for various values of δ

Fig 5.2(a) shows the SVM voltages v_a^* and v_b^* for phases A and B, respectively, for a modulation index of 0.9. For a three-phase inverter with floating neutral, these reference voltages are bound by +/-

$v_{dc}/2$. Fig 5.2(b-c) shows various discontinuous waveforms of the reference voltages. It is seen that the voltages are clamped to +/-$v_{dc}/2$ at various angles in a fundamental cycle. The clamping is determined by the load power factor angle δ. Clamping the voltage to the DC link for one third of fundamental cycle allows thirty percent reduction in switching frequency of the inverter. The method shown in Fig 5.1 is simple and easy to implement and will be used for efficiency comparison.

5.4. Implementation of programmed PWM using high frequency carrier signal

This section will discuss on the implementation methods of programmed PWM at low switching frequencies. A novel implementation method of programmed PWM using carrier signal is proposed and verified experimentally.

In comparison to carrier based modulators, programmed PWM does not require sine and triangle comparison. The pre-calculated commutation angles are compared directly with the reference rotor position to synthesize the switching events. Typical digital hardware required for such an implementation comprises of timers, counters, comparators and memory with lookup tables [6]. Such an approach is commonly used for open loop Volts per Hertz applications. State of art digital signal processors are customized for carrier based modulators and modifying them for programmed PWM is difficult. In the following subsections, a simple approach for generating programmed PWM on state of the art digital signal processors is proposed. The implementation consists of the following steps:

(i) Expression of commutation angles in a polynomial form for various number of commutation pulses. This step is performed offline.

(ii) Comparison of commutation angles with rotor position to generate programmed PWM pulse patterns. This step is performed online during every update cycle.

(iii) Selection of carrier signal frequency for output PWM generation. This step is done offline and is essential to ensure good output voltage resolution

(iv) Comparison of programmed PWM pulse patterns with carrier signal to generate output switching waveform. This step is performed online during every update cycle.

The above four steps will generate the programmed PWM pattern. The following subsections will describe each step in more details.

5.4.1. Polynomial curve fitting of commutation angles

In section 4.2.3, calculation of commutation angles for lower current harmonic distortion is explained. These angles are stored in look-up tables as a function of modulation index. To calculate the commutation angles, the modulation index is varied from 0 to 1.15 with the maximum angle being limited to $\pi/2$. As an example, seven commutation angles and their relation to modulation index are shown in Fig 5.3. The angles usually have small variations from its mean value due to the tolerance settings of the numerical solvers. This can be resolved by using polynomial curve fitting functions within the modulation range of interest. The commutation angles can be expressed as a function of modulation index in polynomial form as

$$\alpha_k = \sum_{j=0}^{n} w_j M^{j+1} \tag{5.1}$$

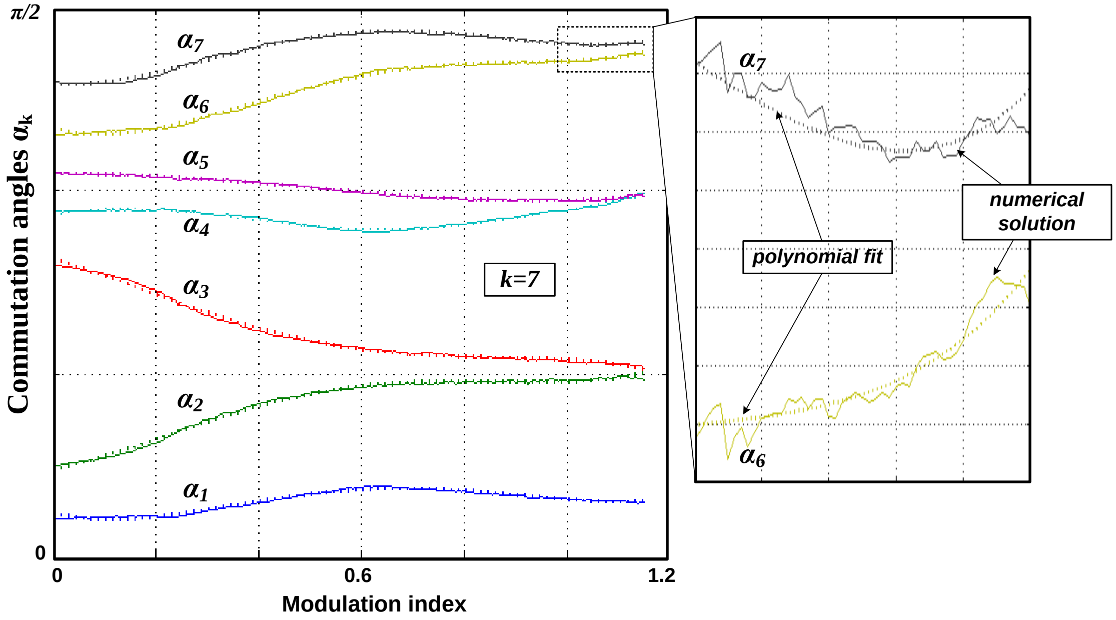

Figure 5.3. Computed commutation angles (k =7) and corresponding 4th ordered polynomial fit function

where, α_k are the k commutation angles, n is the order of polynomial with coefficients w, and M is the modulation index. A fourth-order polynomial approximation is sufficient in most of the cases. The polynomial coefficients for the seven commutation angles as function of modulation index are listed in Table 5.1. Comparison between the numerical solution and polynomial fitting function is shown in the zoomed region of Fig 5.3. The simulation results validate the approach used.

Table 5-1 Optimal PWM switching angles k = 7 and polynomial coefficients

Angles/coefficients	w_4	w_3	w_2	w_1	w_0
α_1	0.963	-2.437	1.839	-0.328	0.121
α_2	0.901	-1.958	1.018	0.279	0.239
α_3	-0.732	1.541	-0.691	-0.392	0.813
α_4	-0.712	1.969	-1.567	0.327	0.931
α_5	0.008	0.187	-0.290	0.024	1.045
α_6	1.187	-3.072	2.457	-0.389	1.171
α_7	1.223	-2.878	1.895	-0.133	1.292

Fig 5.4(a) shows commutation angles with polynomial curve fitting for k =*4*, *5*, *6* and *7*. In case of variable speed operation, the number of commutation angles k is determined by the overall system efficiency. In Fig 5.4(b), consider the selection of number of commutation angles k as a function of modulation index, M. In the case shown, the fundamental frequency f_{ref} is proportional to the modulation index M while the switching frequency is increased by $(2k + 1).f_{ref}$. When the switching frequency f_{sw} exceeds the desired limit (1 kHz), the value of k is decreased. Detailed analysis on selection of $k$for total system efficiency improvement for various machine power levels has been discussed in sections 4.2.5 to 4.3.4.

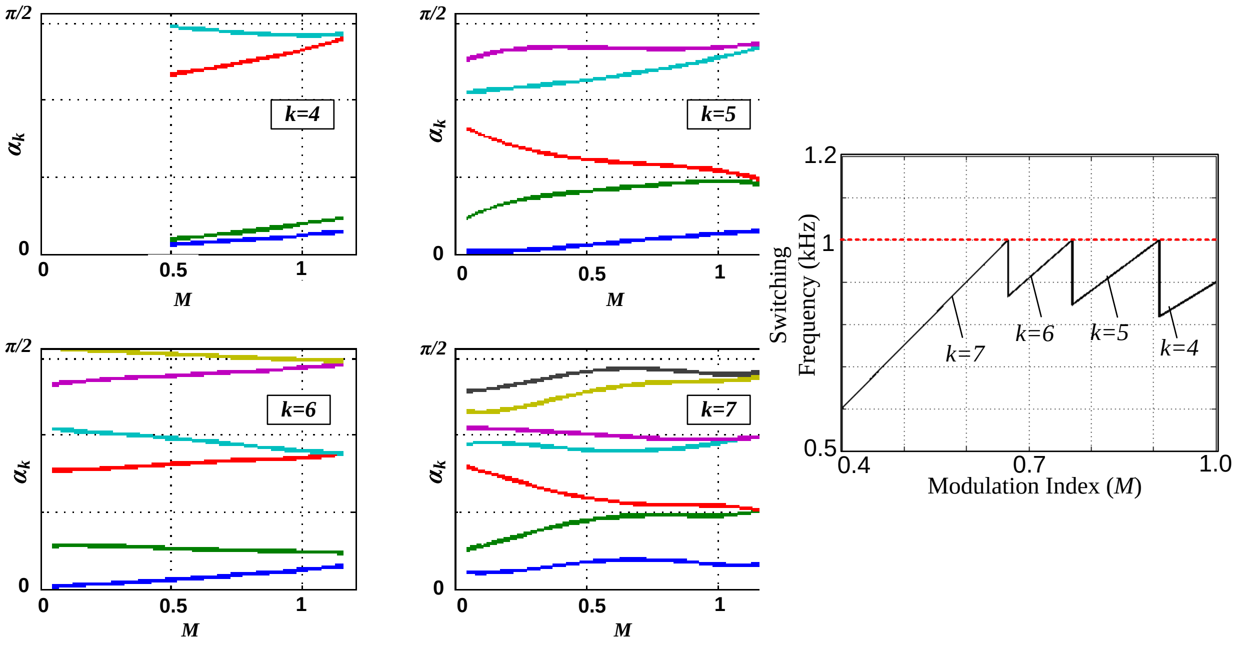

(a) (b)

Figure 5.4. (a) Computed commutation angles for k =4, 5, 6 and 7 (b) selection of $k$as function of modulation index to keep switching frequency below desired value(1kHz)

5.4.2. Programmed pulse pattern generation using commutation angles

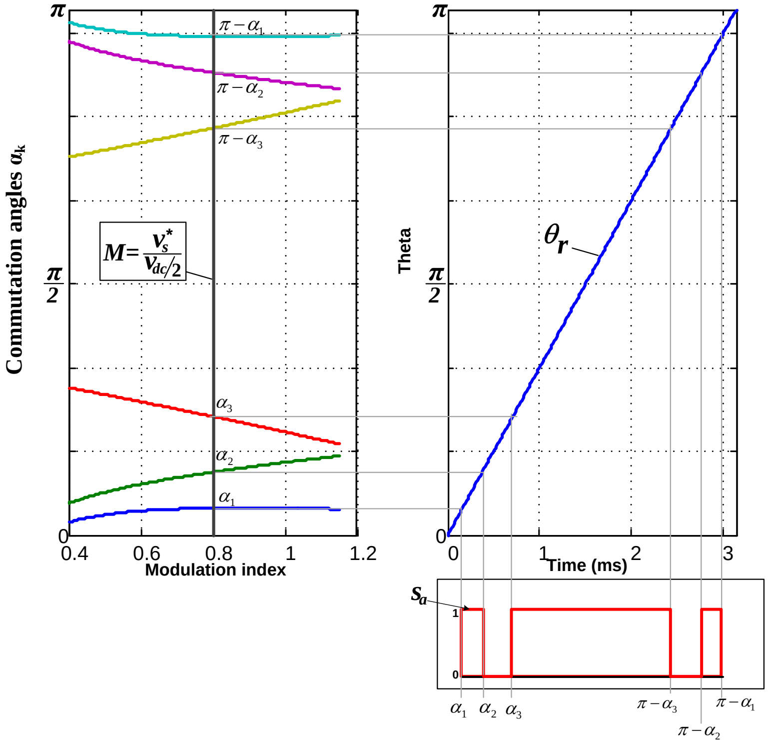

Figure 5.5. Generation of PWM pulses based on programmed commutation angles and carrier signal.

Fig 5.5 shows step-by-step sequence of programmed PWM generation using three commutation angles for half of the fundamental cycle. For a modulation index of *0.8*, using the polynomial fit functions described by (5.1), the commutation angles are calculated as $\alpha_1, \alpha_2$and α_3. As the PWM waveform exhibit quarter wave symmetry, the angles above$\pi/2$ are given as $\pi-\alpha_1, \pi-\alpha_2$and $\pi-\alpha_3$. The six commutation angles are then compared with the rotor position θ_r to generate the switching patternS_a.The above figure provides an insight into programmed pulse width pattern generation in a simple way. From this figure, it can be seen that when the modulation index increases , the width of the pulses S_a. increases and vice versa. It is noted that when $\theta_r < \pi/2$, the commutation angles with odd indices generate rising pulse edges e those with even indices generate falling pulse edges whereas when $\theta_r > \pi/2$, the commutation angles with odd integers generate falling pulse edges while those with even integers generate rising pulse edges.

While the aforementioned logic is fairly straightforward to implement using discrete digital logic or FPGA hardware, implementing the same on digital signal processor dedicated for motion control poses some challenges. The following section addresses it.

5.4.3. Switching pattern generation using high frequency carrier signal

A *Motivation*

State of the art motion control DSP's has internal PWM generation units. They are primarily designed for higher switching frequency operation (above 2 kHz) and carrier based modulators. The relationship between the switching and DSP clock frequency for a given counter value is given by

$$f_{sw} = \frac{f_{clk}}{2 \cdot T_{BCTR}} \tag{5.2}$$

where f_{sw} is the switching frequency, f_{clk} is the clock frequency and T_{BCTR} is the counter value used in the PWM generation units.For lower switching frequencies, either the clock frequency must be reduced or the number of bits in the counter must be increased. The maximum counter value of for 16-bit microprocessor is 65536. Then the lowest switching frequency is determined by the clock frequency. The relationship between the counter period value and switching frequency is provided in Table 5.2. From the table, it is seen that in order to achieve switching frequency of 381Hz, the clock frequency must be 50 MHz which is three times slower than the maximum clock frequency of 150 MHz. Then reducing the clock frequency increases execution time of the control algorithm and delays in the control loop. Consequently, reducing the clock frequency dynamically is not preferred.

Table 5-2 Clock frequency and minimum switching frequency with largest counter value of 2^{16}

Clock Frequency (MHz)	**Minimum Switching Frequency (Hz)**
150	1144
100	763
86	656
75	572
50	381
25	191

Table 5-3 Counter bit value and minimum switching frequency with clock frequency of 150MHz

Number of Bits 2^N	**Maximum Counter Value**	**Minimum Switching Frequency (Hz)**
16	65536	1144
17	131072	572
18	262144	286
19	524288	143
20	1048576	72
21	2097152	36

In case of programmed PWM the switching frequency varies between each switching period. To synthesize the programmed PWM, look-up tables with commutation angles should account for the variation in clock frequency as well as counter period values during every switching cycle. Also synchronizing the PWM for three-phases requires synchronization between the three PWM timer units using the rotor position. The PWM generation unit of motion control digital signal processor is not equipped to perform such function.

An alternative option to the above challenge is to increase the number of counter bits, if possible. Accordingly, table 5.3 shows the values for minimum switching frequency achievable with fixed clock frequency of 150 MHz and higher bit counters. The larger counter values can be achieved by staggering two 16 bit timers. Since such a provision in not available in the PWM generation unit of the existing 16-bit DSPs, alternative methods are desired.

B Alternative low switching frequency PWM implementation method

The aforementioned limitations are resolved by considering the low switching frequency PWM as a discontinuous train of pulses that can clamp the DC link to +/-$v_{dc}/2$. As shown in Fig 5.6, the reference pulses are compared with high frequency carrier signal to generate the desired output switching patterns. In this approach, the clock frequency is kept to the highest value (150 MHz) and the carrier frequency to a desired maximum value (15 kHz). The sampling frequency is kept similar as the carrier frequency. Using this method, neither the clock nor the number of counter bits has to be dynamically updated. Since the frequency of the carrier signal is independent of the switching frequency, the delay in control algorithm execution time is significantly reduced. A feature of the proposed implementation is the ability to transition from carrier based modulators to programmed PWM enabling a hybrid approach.

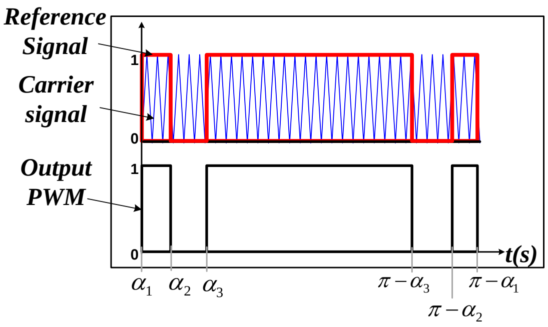

Figure 5.6. Comparison of low frequency programmed PWM pulses with high frequency carrier signal

C Selection of carrier frequency

The above approach can be considered as asynchronous sampling of the reference signal by the carrier signal, the phase error φ between the reference and output PWM is determined by the carrier frequency. Assuming first order time delay approximation, the relationship between the maximum switching frequency f_{sw} and carrier frequency f_{tri} is given by [26]

$$f_{tri} = \frac{f_{sw}}{tan(\varphi)} \tag{5.3}$$

From (5.3), it is seen that the carrier frequency is inversely proportional to $tan(\varphi)$. Hence for very small phase error, the denominator approaches to zero resulting in very high carrier frequency or nearly continuous sampling. From (5.3), assuming$\varphi = 0.05$ rad, and maximum PWM frequency of 1 kHz, the carrier frequency is calculated as20 kHz. The relationship between carrier frequency and switching frequency for various phase errors is shown in Fig 5.7.Although highest carrier frequency is desirable, the lowest carrier frequency is determined by the influence of phase error on output current waveform distortion. If the phase error is too large, then the asynchronous sampling of the reference voltage will result in output voltage of smaller magnitude and large phase delays. That may result in unstable closed loop system operation.

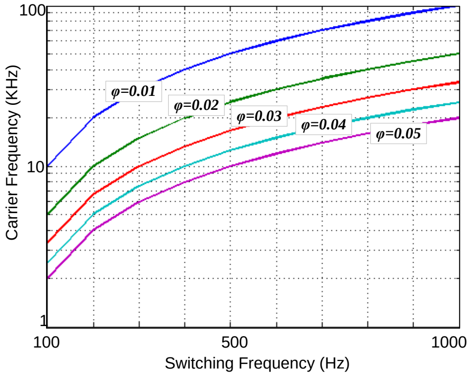

Figure 5.7. Relationship between carrier frequency and switching frequency for various phase angles φ (rad)

Fig 5.8 (a) and (b) show the motor current trajectory and time domain response using the proposed carrier based PWM implementation. The switching frequency is 1 kHz while the carrier frequency is 20 kHz and 50 kHz for the cases illustrated in Fig 5.8 (a) and (b) respectively. As seen in Fig 5.8 (a), when the phase error φ is large (0.05 rad), the three-phase currents are unbalanced. The stator current trajectory has offset from the origin. The current amplitude is also smaller due to lower voltage applied to the motor. When the phase error is reduced to 0.02 rad by increasing the carrier frequency to 50 kHz, the current unbalance is removed- and shown in Fig 5.8(b). Note that the stator current trajectory also becomes symmetric around the origin.

From the above illustration, choice of carrier frequency is critical in the proposed implementation. Fig 5.7 provides a guideline for selection of this frequency.

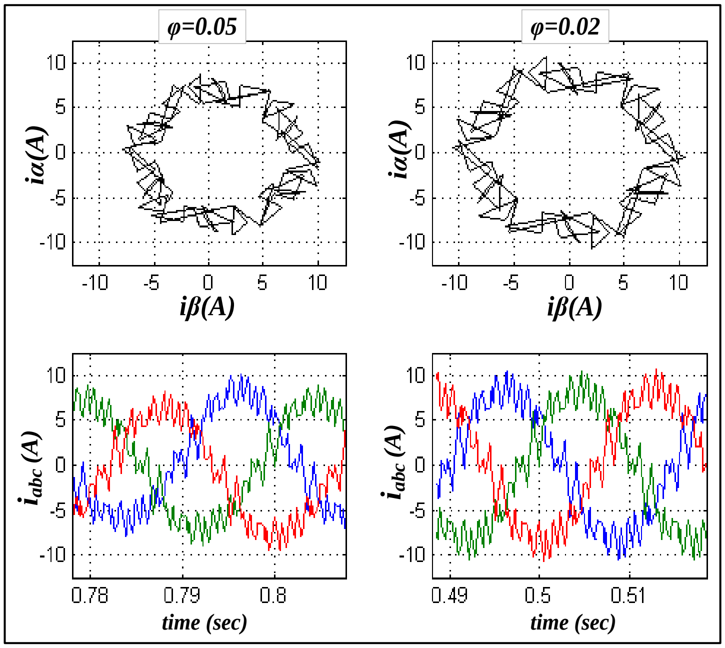

(a) (b)

Figure 5.8. (a) Motor current trajectory and time domain response for phase errors at 1 kHz switching frequency applying programmed modulation technique (a) $\varphi = 0.05\ rad$ and (b)$\varphi = 0.02\ rad$

5.4.4. Block diagram of Programmed PWM implementation

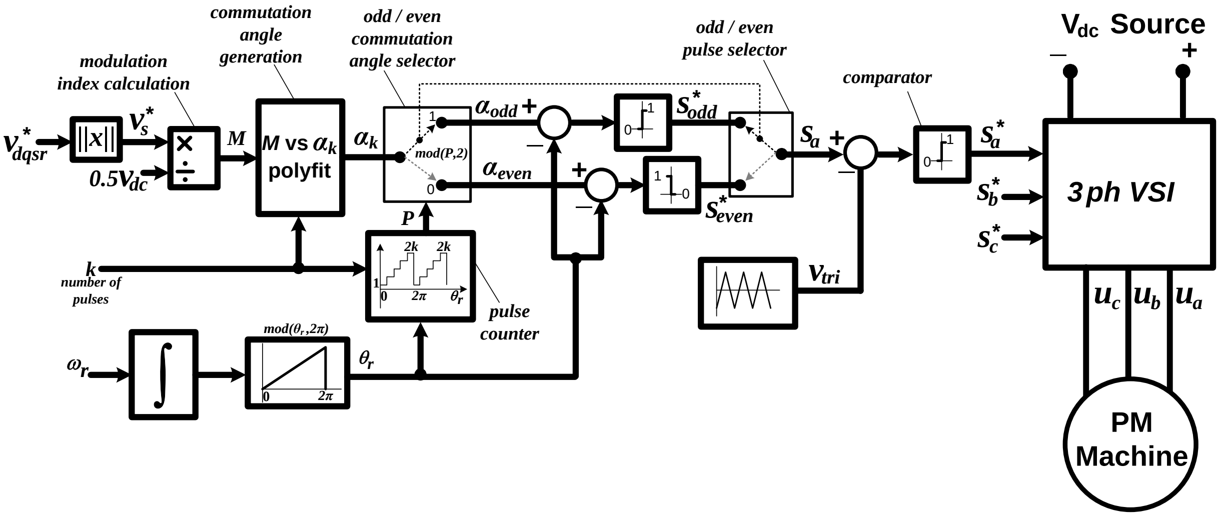

Figure 5.9. Programmed PWM implementation block diagram.

Based on the explanation in previous sections, detailed block diagram of the proposed programmed PWM implementation is shown in Fig 5.9. The inputs to the PWM generator are the reference voltages $v_{dqsr}{}^{*}$in rotor reference frame, number of switching pulses k, and rotor positionθ_r. From the reference voltages $v_{dqsr}{}^{*}$, the scalar magnitude of the voltage vector $v_s{}^{*}$is calculated as $v_s{}^{*}$ = sqrt($(v_{qsr}{}^{2}+v_{dsr}{}^{2})$. The modulation index is calculated based on the DC link voltage as $M = v_s{}^{*}/(v_{dc}/2)$. The k commutation angles $\alpha_k$corresponding to the reference modulation index are calculated by using

(5.1) and Table 5.1.These angles are then compared with the rotor angle to synthesize the odd switching pulses S_{odd}^* and even switching pulses S_{even}^* These pulses are selected and combined to produce the desired switching pattern S_a. The modulating waveform $S_a$is compared with high frequency carrier signal resulting in PWM signals S_a^*. The switching signals for phase B and C are generated similarly by offsetting the rotor position by $-2\pi/3$ *rad* and $2\pi/3$ *rad* respectively.

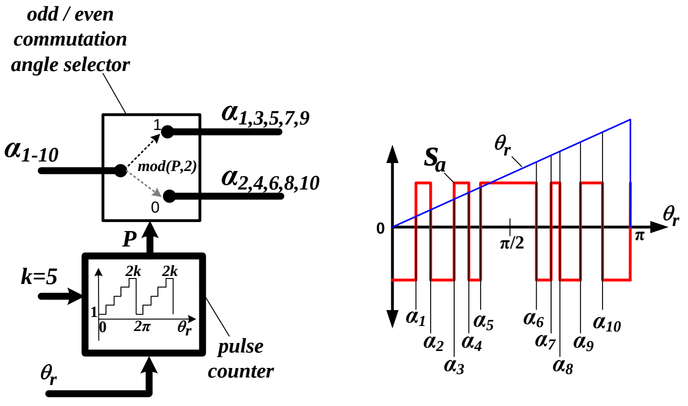

(a) (b)

Figure 5.10. Commutation angle selection logic.

To illustrate the commutation angles selection logic, a case with k=5 is considered. Logic for odd and even angle selection for phase A is shown in Fig 5.10(a).At first, given k and modulation index M, the angles $\alpha_{1\text{-}5}$ are calculated from Table 5.1. Due to quarter wave symmetry, these angles are unfolded above$\pi/2$ as $\alpha_6=\pi-\alpha_5$, $\alpha_7=\pi-\alpha_4$, $\alpha_8=\pi-\alpha_3$,$\alpha_9=\pi-\alpha_2$,and$\alpha_{10}=\pi-\alpha_1$. The ten commutation angles and their relationship between rotor position and switching waveform are shown in Fig 5.10(b).From the switching waveform S_a, all the commutation angles corresponding to rising edge (α_1, α_3, α_5,α_7, α_9) are odd while those for falling edge (α_2, α_4, α_6,α_8, α_{10}) are even. Therefore in Fig 5.10(a), the selection of angles with odd and even indices is made by the function *mod(P,2)*.After every commutation event, the pulse-counter in incremented by one until the counter value P= 2k has been reached. It is then reset to one for next half cycle. The cycle is repeated from π-2π; however, the switching waveforms are the negative of S_a and are calculated as (1-S_a.).

Based on the implementation scheme in Fig 5.9, experimental results for programmed PWM generation of phase A voltage and corresponding line-line voltage v_{ab} for k = *3*,*5*,*6* and *7* are shown in Fig 5.11 (a-d). The symmetric PWM patterns around the fundamental voltage $v_s(t)^*$due to optimized commutation angles can be seen. Also for k commutation angles, there are 2k+1 switching pulses of the phase voltage u_a^*in one cycle. The results validate the proposed implementation method.

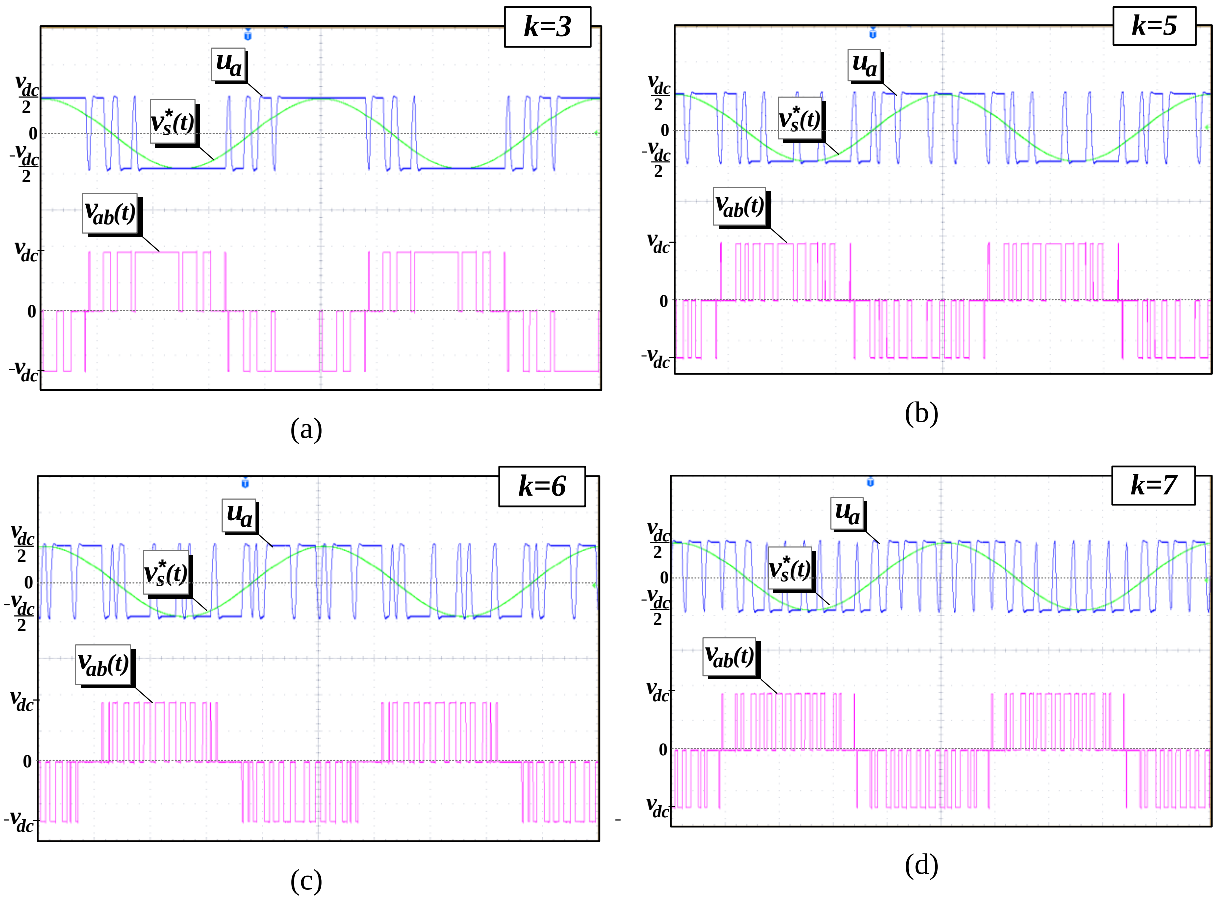

(a) (b)

(c) (d)

Figure 5.11. Experimental results: programmed PWM with modulation index M=0.9 showing phase A voltage u_a^*, reference fundamental voltage $v_s(t)^*$ and line-line votage $v_{ab}(t)$ for various commutation angles (a) $k = 3$, (b) k=5, (c) k=6 and (d) $k = 7$. (Note that number of pulse $N = 2k+1$)

This concludes the section on pulse width modulator implementation at low switching frequency. In the previous sections, continuous, discontinuous and programmed pulse width modulators and their implementation strategy was discussed.

Before testing PMSM system efficiency with various modulators, it is essential to understand the challenges of current control of the motor at low switching frequency and is discussed in following sections.

5.5. Current control methods of PMSM drive at reduced switching frequency

In this section current controller at low switching frequency is considered. In order to understand and evaluate their performance, the section is organized as follows:

- In section 5.5.1, using a space phasor model, various current control methods will be analyzed. The limitations of classical proportional and integral (PI) current controller for PMSM drive operating at low switching frequency will be highlighted in section 5.5.2 A.

- Complex variable current controller and will be explained and analyzed in sections 5.5.2 B while current controller with feedback oversampling for low switching frequency application is discussed in 5.5.2 C. In section 5.5.2.C, it will be shown through analysis and experimental verification that current regulation with feedback oversampling can achieve acceptable stable performance.
- Influence of current ripple due to low switching frequency on the modulation error will be discussed and guideline for controller structure and gain selection will be provided in section 5.5.2 C.

5.5.1. Space phasor modeling of PMSM and inverter

.Classical *dq* modeling approach requires analysis of PMSM with two stator time constants and the cross coupling between the d and q axes due to rotor speed. Using the space phasor modeling approach, it is easy to visualize PMSM as a DC machine [12]. In separately excited DC machines, keeping the field current constant and varying the armature current, the electromagnetic torque can be controlled directly. Similarly, in case of PMSM, for a constant permanent magnet field, the torque is directly proportional to stator current phasor. Consequently, the stator can be modeled as single time constant instead of two when compared with the classical *dq* modeling approach. The space phasor approach reduces the model size and allows more intuitive insight into the relationships between the motor state variable (*current or flux*) and the cross coupling between the orthogonal windings [27]. The following sections will review the space phasor modeling of permanent magnet machine and inverter.

A. PMSM space phasor model

For a non-salient PMSM, the machine model in rotor reference frame is given as [12],

$$\begin{bmatrix} v_{ds}^r \\ v_{qs}^r \end{bmatrix} = \begin{bmatrix} r_s & -\omega_r L_s \\ \omega_r L_s & r_s \end{bmatrix} \begin{bmatrix} i_{ds}^r \\ i_{qs}^r \end{bmatrix} + \begin{bmatrix} L_s & 0 \\ 0 & L_s \end{bmatrix} \frac{d}{dt} \begin{bmatrix} i_{ds}^r \\ i_{qs}^r \end{bmatrix} + \begin{bmatrix} 0 \\ \omega_r \lambda_m \end{bmatrix} \tag{5.4}$$

wherei_{dqs}^r is the d and q axis stator currents, v_{dqs}^r is the per phase applied stator phase voltage, ω_r is the electrical angular velocity of the rotor, r_s is the per phase stator resistance, $L_s$is the per phase stator self-inductance, and $\lambda_m$is the peak of flux linkage of a phase. The two voltage and current vectors in rotor reference frame can be combined into one voltage and current phasor in complex plane as $v_s^r = v_{qs}^r + jv_{ds}^r$ and $i_s^r = i_{qs}^r + ji_{ds}^r$ respectively. Hence (5.4) can be expressed as

$$v_s^r = (r_s + pL_s + j\omega_r L_s) i_s^r + \omega_r \lambda_m \tag{5.5}$$

where $p = d/dt$. Block diagram representation of the same is shown in Fig 5.12.

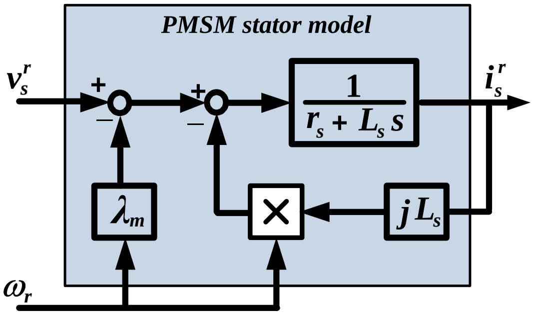

Figure 5.12. Space phasor model of PMSM machine in rotor reference frame

The advantage of modeling in complex domain is the representation of the machine in compact form. Multiple input multiple output system represented by (5.4) is simplified to single input single output system given by (5.5). The model has only one time constant instead of two. The two cross coupling terms are reduced to one complex term. From the above model of PMSM, it is seen that for fixed permanent magnet field λ_m, by varying the stator voltage, the stator current can be controlled. Torque is the product of three variables: (i) stator current phasor, (ii) rotor flux linkages or known as rotor field, and (iii) sine of the angle between the current phasor and the rotor field and this angle is known as torque angle. Hence torque can be controlled by controlling the stator current phasor and the torque angle when the rotor field is constant. The complex variable form of representation leads to simpler analytical solution of dynamical transients of the machine as there is only one differential equation to solve [12]. Similar space phasor modeling approach is applicable to modeling of the inverter and is discussed in the following section.

B. Inverter space phasor model

Block diagram of three-phase inverter driving a PMSM is shown in Fig 5.13(a). The voltage applied to the motor is controlled by the inverter switching events. The switching devices of the inverter are controlled by gating pulses generated by the microprocessor. The gating pulses are updated after every duty cycle computation. The duty cycle values are updated based on the sampled feedback current and the current controller. Fig 5.13(b) shows the inverter operation in one PWM cycle. The carrier signal is denoted by v_{carr}, and the corresponding period is denoted as T_{carr}. The phase current i_a and the corresponding sampling instants indicates that the instantaneous current is sampled twice per carrier period. The three-phase switching events for phases A, B and C are shown as S_a, S_b, *and* S_c respectively. It is seen that the sampling events are aligned when all the three switches are either ON or OFF and exactly in the middle of these instances.

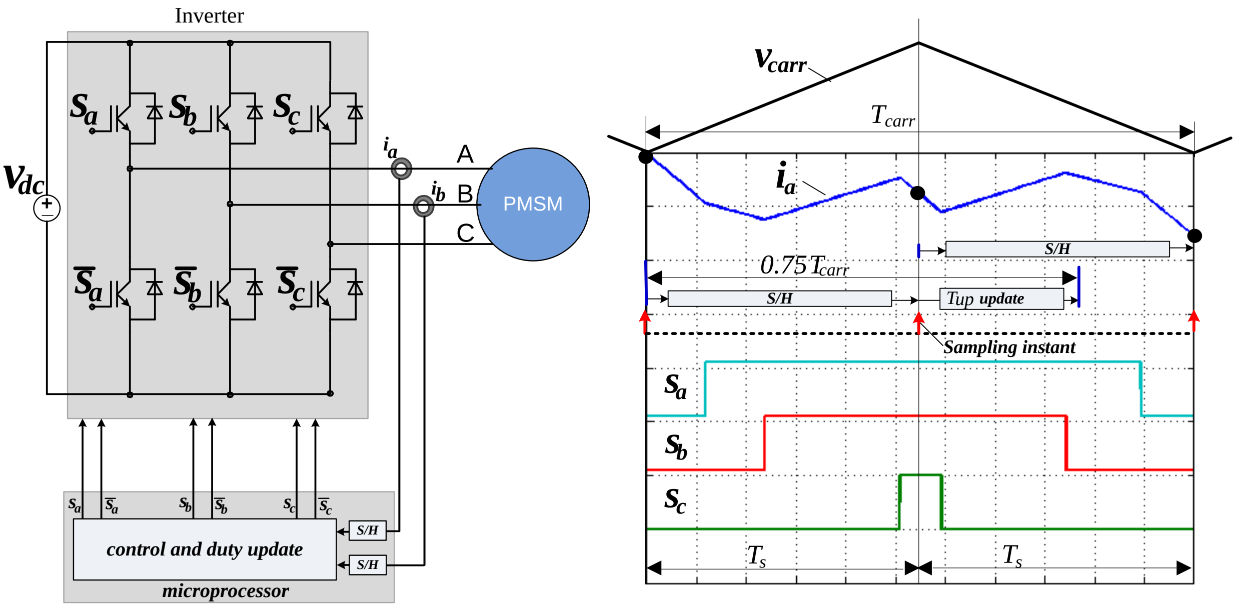

(a)

(b)

Figure 5.13. (a) Three-phase inverter and microprocessor block diagram. (b) Inverter current sampling and timing diagram for one PWM cycle.

Such an approach results in sampling the average value of the phase current without using feedback filters and hence the sampled current is almost ripple-free [36]. With that approach, the inverter sampling delay is half the carrier period (T_s = 0.5 T_{carr}). With the update rate same as the carrier period [18], the microprocessor computation and update time is approximately T_{up} = T_{carr}. Hence the total time delay τ_d is given by sum of the sampling and computation delay ($\tau_d = T_{up} + T_s$ = 1.5 T_{carr}). Since the update rate is fixed with the switching frequency, the delays that can be varied are the feedback signal sampling delay and the algorithm computation delay. The sampling delay is the larger contributor of the two. In [18], it is shown that for synchronous sampling and asynchronous PWM method, the smallest feedback delay is $0.75\ T_{carr} = 1.5\ T_s$.

Based on the timing diagram in Fig 5.13 (b), the inverter is modeled as a gain with first-order time delay approximation. When the inverter time delay is much smaller than the stator time constant τ_r, the cross coupling between the d and q axis inverter voltages can be ignored. However, when the switching frequency is reduced, the inverter time delay τ_d approaches the stator time constant and the cross coupling due to rotor frequency should not be ignored. The inverter model is developed as follows [16]. In stationary reference frame, the relationship between the inverter reference voltage as output of the current regulator v_s^{s*} and the motor terminal output voltage v_s^s is given by,

$$v_s^s = v_s^{s*} / \left(\tau_d \frac{d}{dt} + 1 \right) \tag{5.6}$$

where $\tau_d = 1.5/(2f_{sw})$ and f_{sw} is the inverter switching frequency. Equation (5.6) can be rearranged as,

$$\tau_d \frac{d}{dt} v_s^s + v_s^s = v_s^{s*} \tag{5.7}$$

Since the PMSM model is derived in rotor reference frame, applying co-ordinate transformation $T(\theta_r)$ in rotor reference frame, the equation (5.7) becomes,

$$\tau_d \left(\frac{d}{dt}[T(\theta_r)]v_s^s\right) + [T(\theta_r)]v_s^s = [T(\theta_r)]v_s^{s*} \tag{5.8}$$

which is expanded and given as,

$$\tau_d \left(\frac{d}{dt}[T(\theta_r)]\right) v_s^s + \tau_d \frac{d}{dt}([T(\theta_r)]v_s^s) + [T(\theta_r)]v_s^s = [T(\theta_r)]v_s^{s*} \tag{5.9}$$

substituting $[T(\theta_r)]v_s^s = v_s^r$, the equation (5.9) becomes,

$$j\omega_r \tau_d v_s^r + \tau_d \frac{d}{dt} v_s^r + v_s^r = v_s^{r*} \tag{5.10}$$

which is rearranged as,

$$v_s^r \left(1 + \tau_d \frac{d}{dt} + j\omega_r \tau_d\right) = v_s^{r*} \tag{5.11}$$

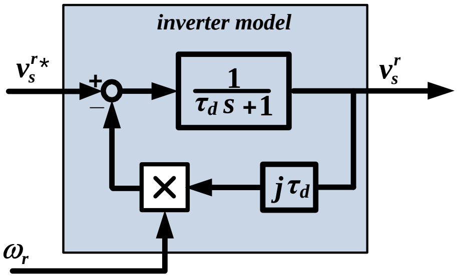

Figure 5.14. Space phasor model of inverter with time delay approximation

Equation (5.11) represents the space phasor model of the inverter. Block diagram representation of the same is shown in Fig 5.14. The model shows time delay between the input and output voltage signals along with the influence of rotor frequency on the output voltage phasor. When the ratio between switching and fundamental frequency, denoted as *N*, is very high (>*40*), the complex term ($j\omega_r\tau_d$) can be ignored. However, when *N* is small, the cross coupling effect must be included in the model [16]. Space phasor model for small values of *N* has been reported in high speed and high power drives. Since this work focuses on applying smaller values of *N* for high efficiency PMSM drives, the aforementioned inverter space phasor model will be used henceforth for current controller design.

5.5.2. Current control at low switching frequency

Various current controller methods have been reported in the literature [19-26]. The most commonly used current controllers are

(i) Hysteresis control [28],
(ii) Proportional Integral (PI) current control [29],
(iii) PI current control with feedback oversampling [30]
(iv) Complex variable current control [16], [17], [31]
(v) Dead-beat current control [32], [33] and
(vi) Model predictive current control [34,35]

While all of the aforementioned methods show good performance at higher switching frequencies, only a few have acceptable performance at low switching frequencies.

Hysteresis current controller is not suitable at low switching frequency operation because the resulting output switching pulses are asynchronous with the rotor angle and not optimized for lower current harmonic distortion. (with regard to what; state that clearly)

The PI current controller is more widely used for PMSM and has acceptable performance for systems with low dynamic requirements. For systems requiring fast dynamic response at low switching frequency, feedback oversampling, complex variable current, dead-beat and model predictive current controllers are advantageous [32-35].

Dead-beat and model predictive current controllers can be sensitive to parameter variations and un-modeled time delays in the system. At low switching frequencies, the cross coupling between the inverter d and q axes due to sampling delay becomes significant and must be compensated [16]. The inverter delay compensation is achieved through complex variable current regulators resulting in improved dynamic performance even at low switching frequencies [16].

Current control affects in general not the system efficiency but only the damping and possible instability. Accordingly, for stable motor performance, simple current controller implementation is essential. The existing literature [25], [26] focuses on complex variable current and model predictive control of induction motor drives operating low switching frequency. An alternative simple approach of controlling current with feedback oversampling in combination with optimized PWM for PMSM drives has not been discussed in literature and is attempted in the following sections.

For a comparative evaluation, three current controller designs are considered in this section, they are: (a) PI current controller, (b) complex variable current controller and (c) current regulator with feedback oversampling. Performance of these controllers is analyzed using simulations while operation of current controller with feedback oversampling will be verified experimentally.

A. Proportional Integral (PI) current controller

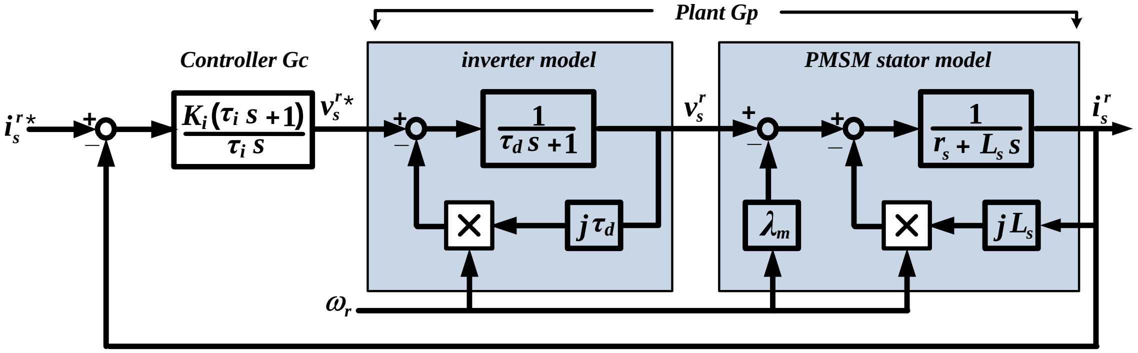

Figure 5.15. Current regulator block diagram of PMSM drive system using PI current controller

Block diagram of proportional integral (PI) current control of PMSM drive system is shown in Fig 5.15. The current controller $G_c$and the plant model $G_p$incorporatinginverter time delays and cross coupling effect between the windings are given as,

$$G_c = \frac{K_i(1+s\tau_i)}{s\tau_i}, G_p = \frac{K_p}{(1+s\tau_r+j\omega_r\tau_r)(1+s\tau_d+j\omega_r\tau_d)} \tag{5.12}$$

.The plant gain $K_p = 1/r_s$, the PMSM stator time constant is $\tau_r = L_s/r_s$, τ_d is sampling and microprocessor delay, τ_i is current controller time constant and K_i is the PI controller gain. The open loop plant transfer function is

$$G_cG_p = \frac{K_pK_i(1+s\tau_i)}{s\tau_i(1+s\tau_r+j\omega_r\tau_r)(1+s\tau_d+j\omega_r\tau_d)} \tag{5.13}$$

Applying pole zero cancellation by setting $\tau_i = \tau_r$, and comparing the characteristic equation with a second order system having a damping ratio of 0.707, the PI regulator parameters are:

$$K_i = \frac{\tau_r}{2K_p\tau_d}\ , \tau_i = \tau_r \tag{5.14}$$

theclosed current loop transfer function becomes,

$$\frac{G_cG_p}{1+G_cG_p} = \frac{\frac{\tau_r}{2\tau_d}(1+s\tau_r)}{s\tau_r(1+s\tau_r+j\omega_r\tau_r)(1+s\tau_d+j\omega_r\tau_d)+\frac{\tau_r}{2\tau_d}(1+s\tau_r)} \tag{5.15}$$

Classical current regulator design methods ignore the influence of cross coupling termswith the assumption that the sampling time delay $\tau_d \ll \tau_r$. The corresponding closed loop transfer function can be derived using (5.15) and substituting $\omega_r = 0$ as

$$\frac{G_cG_p}{1+G_cG_p} = \frac{1}{2\tau_d{}^2s^2+2\tau_ds+1} \tag{5.16}$$

From equation (5.16), it is seen that the stator time constant is eliminated and the closed loop system is not dependent on rotor speed. The approximation provides satisfactory results as long as $\tau_d \ll \tau_r$. This is mostly true for higher switching frequencies (above 2 kHz, *N*> 40). Since the sampling frequency is twice the switching frequency, the corresponding delays are small and therefore even in presence of cross coupling between the d and q axis the current controller is able to force the stator current to track the reference value.

When $\omega_r \neq 0$ and value of$\tau_d$is close to τ_r, the cross coupling effect between the d and q axis must be accounted. The characteristic equation (5.15) then becomes,

$$C(s) = 1 + G_c G_p = s^3 + as^2 + b + c$$

where

$$a = \frac{\tau_d + \tau_r + j2\omega_r\tau_d\tau_r}{\tau_d\tau_r}, b = \frac{K_i + 1 - \tau_d\tau_r{\omega_r}^2 + j\omega_r(\tau_d + \tau_r)}{\tau_d\tau_r}, c = \frac{1}{{\tau_d}^2\tau_r} \tag{5.17}$$

Equation (5.17) is of third order and has three roots denoted as p_1, p_2 and p_3. The roots p_1 and $p_2$are single complex poles whenever $\omega_r \neq 0$, whereas for $\omega_r = 0$, they form a complex conjugate pair. The intercept on real axis of the poles p_1 and $p_2$is mainly determined by the inverter time delay. The root $p_3$is closer to the imaginary axis and its trajectory must be carefully evaluated when the rotor speed is varying. The root p_3 is derived from (5.17) as

$$p_3 = \frac{1}{\Delta}\left(\frac{b}{3} - \frac{a^2}{9}\right) - \frac{a}{3} - \Delta$$

$$\text{where } \Delta = \left[\frac{c}{2} - \frac{ab}{6} + \sqrt{\left(\frac{b}{3} - \frac{a^2}{9}\right)^3 + \left(\frac{a^3}{27} - \frac{ab}{6} + \frac{c}{2}\right)^2} + \frac{a^3}{27}\right]^{1/3} \tag{5.18}$$

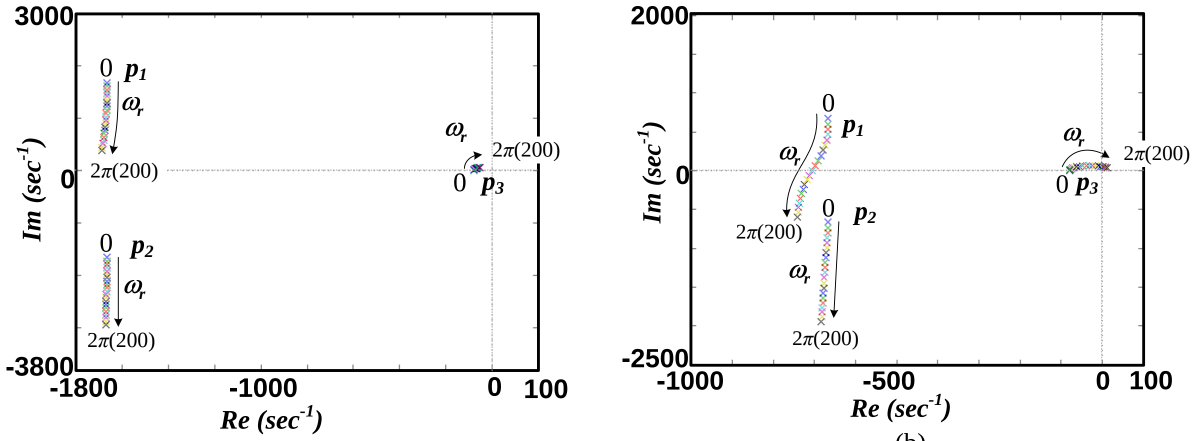

(a) (b)

Figure 5.16. Roots of the closed loop transfer function of current controller with fundamental frequency varied from 0 to 200Hz at a sampling frequency of (a) 5 kHz (b) 2kHz.

Root locus of the characteristic equation (5.18) with sampling frequency of 5 kHz and 2 KHz is shown in Fig 5.16(a) and Fig 5.16(b) respectively. In this illustration, the motor operating frequency is varied from zero to 200 Hz. In both cases, all the poles move from their initial location when the rotor speed is varied. Following observations are in order:

(a) when the sampling rate is high (5 kHz) as shown in Fig 5.16(a), the corresponding inverter delay is small and all the roots are on left half of the complex plane even when the rotor speed is varied from zero to its rated value.

(b) when the sampling rate is smaller (2 kHz)as shown in Fig 5.16(b), the root p_3 approaches the imaginary axis when the rotor speed approaches 200 Hz. Consequently, the system will tend to exhibit poor dynamic performance and even unstable operation.

(c) In Fig 5.16(b), the complex pole $p_3$is compensated by the classical current regulator at zero speed because the pole has only real part at this operating point. However, at higher speeds due to presence of imaginary part, the pole remains uncompensated. Consequently, the influence of cross coupling between the d and q axis is seen when the pole moves towards imaginary axis due to rotor speed variation.

(d) In general at low switching frequency and lower sampling rate, it is essential to design the current controller and sampling rate such that all the three roots are on the left half of the complex plane.

An alternate method is to design the controller that can compensate the cross coupling terms as well as the time delays. Such controller is known as complex variable current regulators and is discussed in next section.

B. Complex variable current regulators

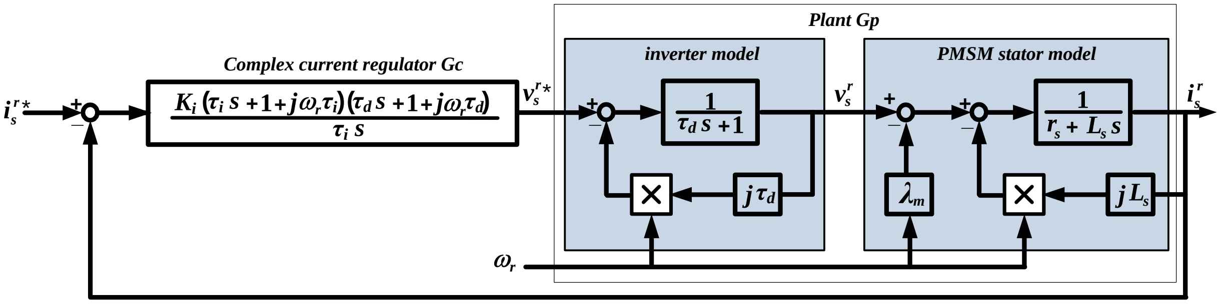

Figure 5.17. Space phasor based block diagram of PMSM drive with complex variable current regulator

From the previous section, it is seen that using classical PI current control design and ignoring the cross coupling terms may lead to unstable system operation especially at low sampling rates. This limitation can be addressed by applying complex current controller [13], [14], [22].Use of complex current regulator for low switching frequency for induction motor was shown in [13]. Design of complex current regulator for PMSM operating at low switching frequency is discussed as follows.

Block diagram of such a scheme is shown in Fig 5.17. The complex current regulator is given by

$$G_c = \frac{K_i(1 + s\tau_i + j\omega_r\tau_i)(1 + s\tau_d + j\omega_r\tau_d)}{s\tau_i} \tag{5.19}$$

The objective of the complex current regulator is to perform the pole zero compensation including the complex pole due to the cross coupling terms. Hence the current regulator is designed with two zeros, first for compensating the stator time constant and second for the inverter delay. The open loop transfer function based on the plant in (5.12) becomes

$$G_cG_p = \frac{K_pK_i(1 + s\tau_i + j\omega_r\tau_i)(1 + s\tau_1 + j\omega_r\tau_1)}{s\tau_i(1 + s\tau_r + j\omega_r\tau_r)(1 + s\tau_d + j\omega_r\tau_d)} \tag{5.20}$$

Applying pole zero cancellation by setting $\tau_i = \tau_r$, and $\tau_1 = \tau_d$, and with damping ratio of 0.707, the gain of the current regulator is given as

$$K_i = \frac{\tau_r}{K_p(2\tau_d)} \tag{5.21}$$

The open loop transfer function becomes,

$$G_cG_p = \frac{1}{s(2\tau_d)} \tag{5.22}$$

and accordingly, the closed loop transfer function is given as

$$\frac{G_cG_p}{1 + G_cG_p} = \frac{1}{(2\tau_d)s + 1} \tag{5.23}$$

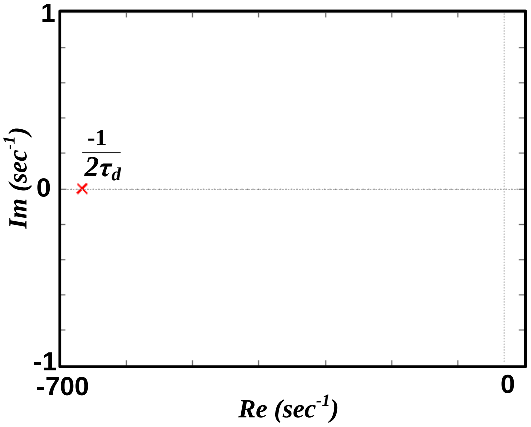

Figure 5.18. Roots of the closed loop transfer function of current controller with fundamental frequency varied from 0 to 200Hz and sampling frequency = 2kHz.

The root locus of closed loop plant transfer function for rotor speed variation from 0-200 Hz is shown in Fig 5.18. It is seen that the closed loop transfer function has only one real pole on the left half of the complex plane. Based on the selection of complex zeroes, the effect of cross coupling is completely eliminated. The dynamics of the system is determined by the inverter delay and not the stator time constant. The closed loop system is damped and represents first order behavior. It can be concluded that the complex current regulator can achieve good dynamic response even at lower switching frequency and lower sampling rate. It is noted that the complex variable current controller is based on plant model and its gains are dependent on two parameters (stator time constant and inverter delay) and one variable (rotor speed). Error in estimation of inverter delay in case of programmed PWM or rotor speed in sensorless mode of operation will result in deteriorated or unstable performance of the system. Therefore it is desirable to develop a current controller where the gains that are not dependent on the rotor speed and inverter delay. Such an approach is developed in the following section.

C. Current regulators with feedback oversampling

Another approach of designing the current regulators with stable operation at low switching frequency without resorting to complex variable current regulator is by increasing the sampling rate of the feedback currents to reduce the sampling delays. Also if the new reference voltages are computed after every sampling instant and the most updated value is applied at the next switching cycle, the controller bandwidth can be significantly improved. An illustration of inverter sampling at 8 times during the carrier period and update rate four times the switching period is shown in Fig 5.19. Based on the illustration, if the switching frequency is 1 kHz, the sampling rate is 8 kHz, and the update rate is 4 kHz. With this approach, the sampling delay is reduced four times and computation delay by half. The system with new inverter delay τ_{d2} is shown in Fig 5.20.

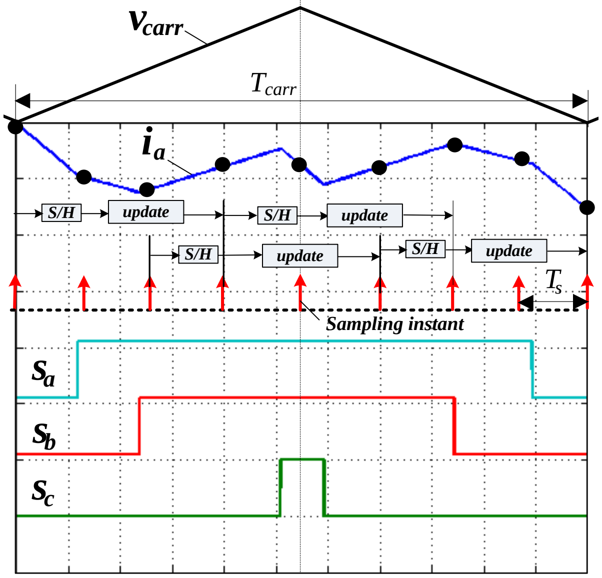

Figure 5.19. From top to bottom-carrier signal (v_{carr}), instantaneous phase current i_a, and sampling instants with over sampling at 8 times per carrier period and duty cycle update 4 times per carrier period, three-phase switch voltages S_{abc}

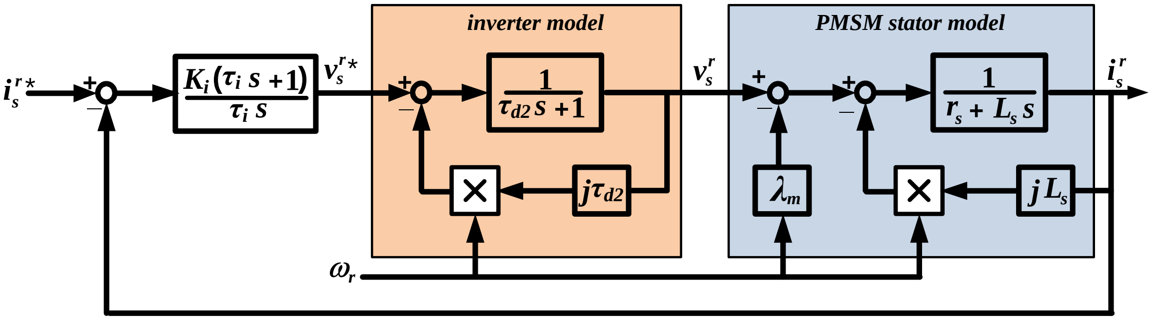

Figure 5.20.Current regulator block diagram of PMSM drive system using feedback oversampling

Fig 5.21 shows the root locus of the characteristic equation $1 + G_c G_p$at various sampling frequencies with fundamental frequency of 200 Hz. It is seen that when the sampling frequency is increased from 2.5 kHz to 10 kHz, the pole p_3 moves toward left half of complex plane while the complex poles, $p_1$andp_2 move further left. Using this approach, the assumption $\tau_d \ll \tau_r$ holds and the current controller can be designed using the method described in part A of this section.

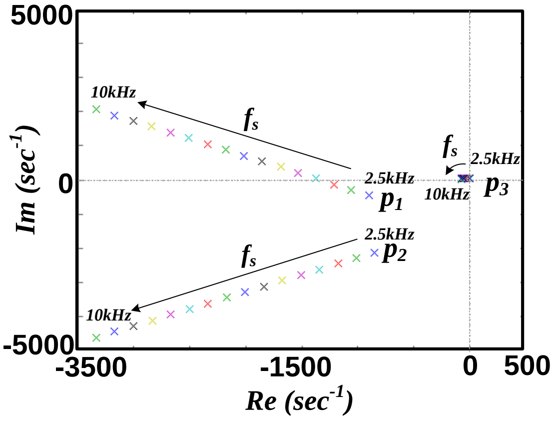

Figure 5.21.Root locus of closed loop transfer function using current feedback oversampling. Fundamental frequency 200Hz and sampling frequency varied from 2.5 kHz to 10 kHz.

Fig 5.22 (a) shows the root locus of the closed loop system using current feedback oversampling. The rotor frequency is varied from 0-200Hz. In the illustration, the sampling frequency is 4 kHz. Due to smaller time delay, the asymmetric complex poles p_1 and p_2 move almost along a straight line and parallel to the imaginary axis. In comparison to the results in Fig 5.16(b), the pole p_3 is barely displaced even with variation of rotor speed. The root locus validates the stable operation of the current controller; however, the dynamic response is limited due to the location of pole p_3. Corresponding time domain step response of the closed loop transfer function at various rotor frequencies is shown in Fig 5.22(b).

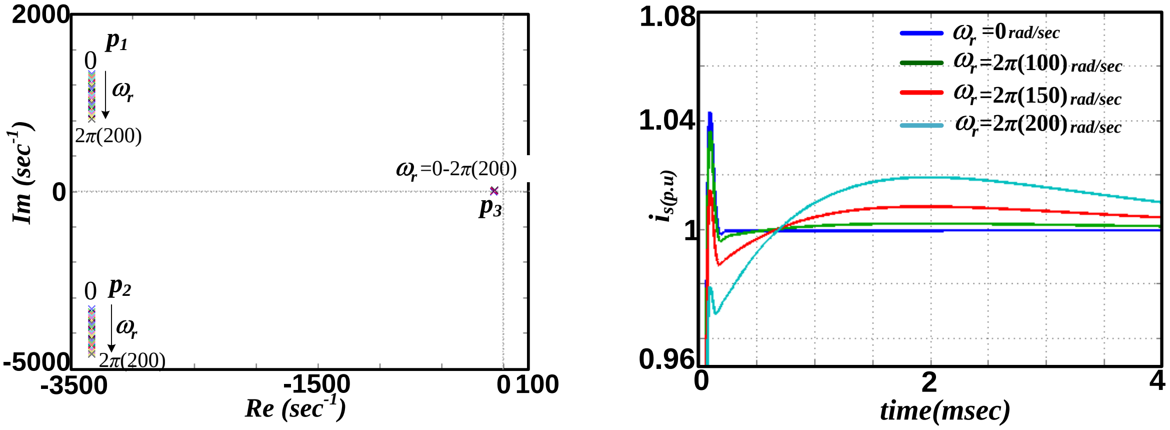

(a)

(b)

Figure 5.22. Performance of current regulator using oversampling method at various rotor frequencies (0-200 Hz). (a) Root locus of closed loop transfer function. (b) Step response of the closed loop transfer function.

The results show stable response at all the operating speeds. It is seen that the dynamic response becomes slower at higher rotor frequencies. The response is mainly determined by the location of the complex pole p_3. Depending on the application, the complex pole $p_3$can be left uncompensated. However, for faster dynamic response the complex pole p_3 must be compensated by a complex zero in which case the regulator takes the form of complex current controller as discussed in the previous section.

It should be noted that in the above analysis, only fundamental component of the current is considered. The influence of harmonics associated with modulation error at low switching frequency has not been included. Modulation error occurs when the current ripple in the motor, due to low switching frequency, is too high. Since the difference between the reference and feedback current is high, the amplitude and slope of current error is also high. Consequently, for stable operation the gain of the current controller should be reduced. This can be achieved by replacing the sampling delay by switching delay. Thus the gains of the current controller are given by

$$K_i = \frac{\tau_r}{2\tau_{dn}}, \tau_{dn} = \frac{2}{f_{sw}}, f_{sw} = Nf_1, \tau_i = \tau_r \tag{5.24}$$

where τ_{dn} is the inverter PWM delay which is inversely proportional to the switching frequency f_{sw}. The switching frequency for programmed PWM is given by the number of pulses times the fundamental frequency f_1. The integral time constant of the controller is set to be the same as the stator time constant for pole zero cancellation.

The current controller bandwidth can be increased by increasing the proportional gain K_i. As discussed earlier, the distortion in current (or current ripple)is worse with larger controller gain. This is because the switching patterns of programmed PWM are computed under ideal steady state operating conditions. The modulation ripple causes deviation from the programmed switching instant after every update cycle resulting in even higher current distortion. The error in output voltage due to presence of ripple on the reference voltage is known as modulation error [13]. This error can be reduced by using a low pass filter at the output of current controller. The filter time constant is chosen as $\tau_f = 1/(2f_{sw})$.

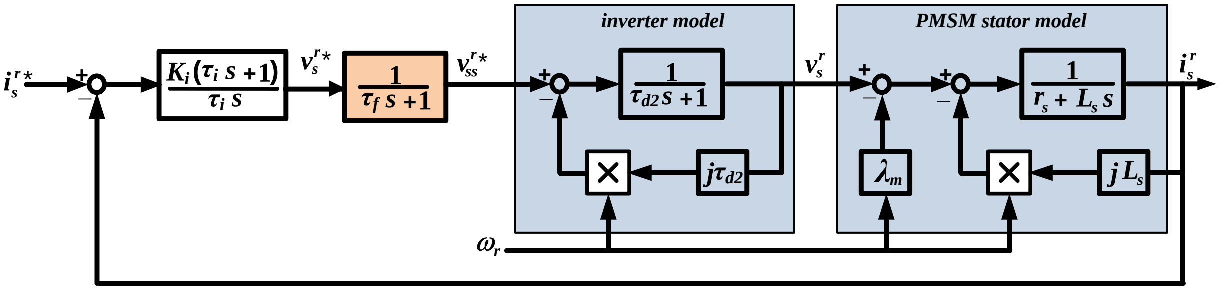

Figure 5.23. Block diagram implementation of practical current regulator at low switching frequency and feedback oversampling.

A practical implementation of current controller at low switching frequency for programmed PWM is shown in Fig 5.23.Based on the implementation in Fig 5.23, Fig 5.24 shows the influence of various filter time constants τ_f on the current controller performance.

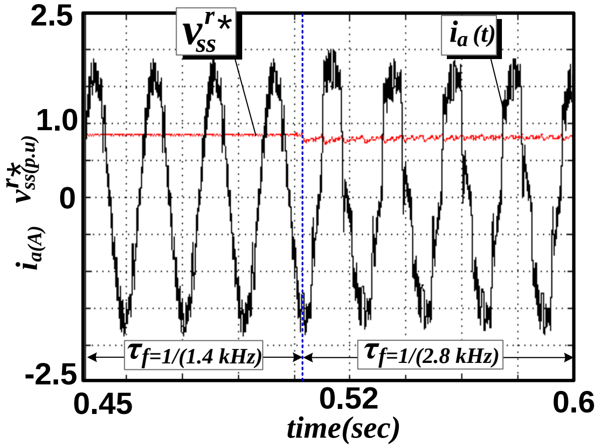

Figure 5.24. Influence of filter time constant τ_{f2}on output current waveform distortion.

In this example, the operating frequency is 46 Hz, switching frequency is 700 Hz and the sampling frequency is 14 kHz. It is seen that for smaller filter time constant, the current distortion is larger. The corresponding reference voltage $v_{ss}{}^{r*}$ also has higher ripple content due to higher modulation error. The higher (?) filter time constant can improve the controller bandwidth at the expense of higher harmonic distortion. Thus in the above case, for high efficiency operation, there exists a tradeoff between the current controller bandwidth requirement and its harmonic distortion.

Most of the variable speed drive applications for climate control systems, in general, do not require fast dynamic response. In such applications, the speed loop bandwidth requirement is low, and therefore the current controller bandwidth is also low.

Figs 5.25 (a) and (b) show experimental results of the current controller with feedback oversampling for programmed PWM and switching frequency of 319Hz. In this implementation, the current controller bandwidth was kept below 10 Hz to reduce harmonic current distortion. In Fig 5.25(a) transient response of current controller to a step reference change is shown. It is seen that the feedback current i_{qs} tracks the reference current $i_{qs}{}^{*}$ within 40 msec†. The motor stator time constant τ_r is 12.5 msec. As discussed earlier, the current control bandwidth is kept low to reduce current harmonic distortion.

Figs 5.25(b) shows steady state operation of the current controller in a PMSM drive with sensorless vector control and torque mode operation. The motor fundamental frequency is 21.3 Hz while the switching frequency is 319 Hz. As shown in the figure, the line-line voltages are synthesized using carrier based programmed PWM. Steady state torque with average value of 9.2Nm is generated with peak phase current amplitude of 8.8A (torque constant of the motor is 1.044 N/A). The inverter input dc current has average value of 4.9 A. The steady state operation validates the effectiveness of the current control implemented in this section.

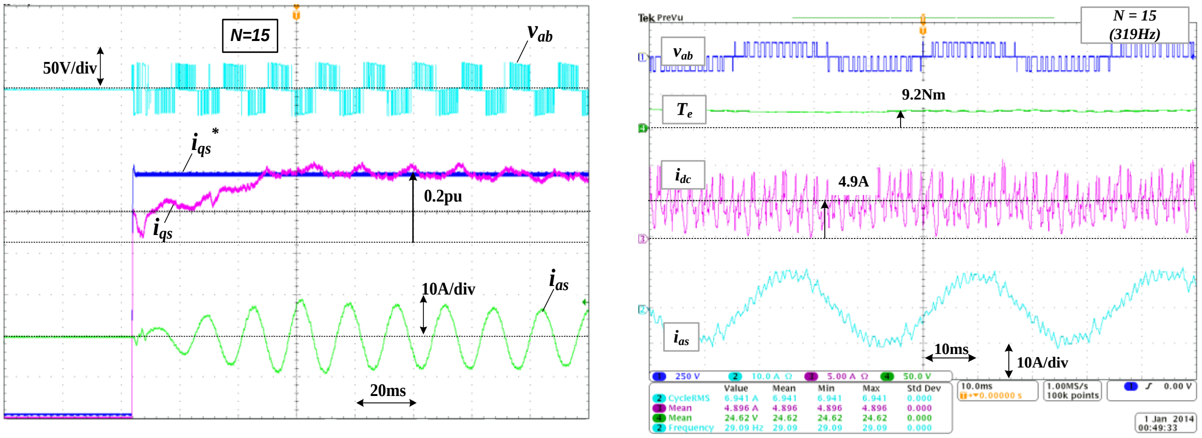

(a)

(b)

Figure 5.25. Programmed PWM (N = 15) based current controller performance (a) transient response (b) steady state. Switching frequency = 319 Hz.

5.6. Efficiency evaluation of PMSM drive system - experimental results

This section focuses on experimental efficiency evaluation of PMSM drive system operating at low switching frequency. Key aspects of the section are summarized as follows:

1 In section 5.6.1, PMSM drive system efficiency is evaluated using three modulation methods (a) Space Vector Modulation (SVM) at high switching frequency, (b)Discontinuous PWM (DPWM) and (c) Programmed PWM.

2 In section 5.6.3, it is shown that it is possible to reduce the total system losses and thus increase drive system efficiency by reducing the switching frequency.

3 Since the switching losses in the semiconductor devices increases linearly with its power level, opportunity for PMSM drive system loss reduction is proportional. Scaling analysis of system efficiency improvement using the proposed approach is shown in section 5.6.4.

5.6.1. Experimental setup

Fig 5.26(a) shows block diagram of the experimental setup used for efficiency evaluation. The system comprises of a three-phase PMSM drive supplied with 150 V_{dc} power supply. The drive is connected to a Siemens PMSM test motor. The parameters of the test motor are listed in Table 5.4. A three-phase induction motor serves as the load. The operating point on the load motor is adjusted using the load inverter. A speed and torque transducer on the coupling between the load and test motor is used for monitoring the shaft power. For test motor input power measurements, three-phase currents and voltages are monitored. For the inverter input power measurement, DC link voltage and current are monitored. Two oscilloscopes (Tektronix 3104 and Yokogawa DL750) are used for monitoring steady state operation and data acquisition. The corresponding hardware pictures are shown in Fig 5.26 (b) and (c). The power and efficiency analyses are performed offline.

A commercial off the shelf Semikron SKAI automotive inverter with maximum DC link voltage rating of 750 Vdc and phase current rating of 400A is used for driving the PMSM. The maximum switching frequency of the inverter is 20 kHz. The system under study is analogous to the case III evaluated in chapter 4.

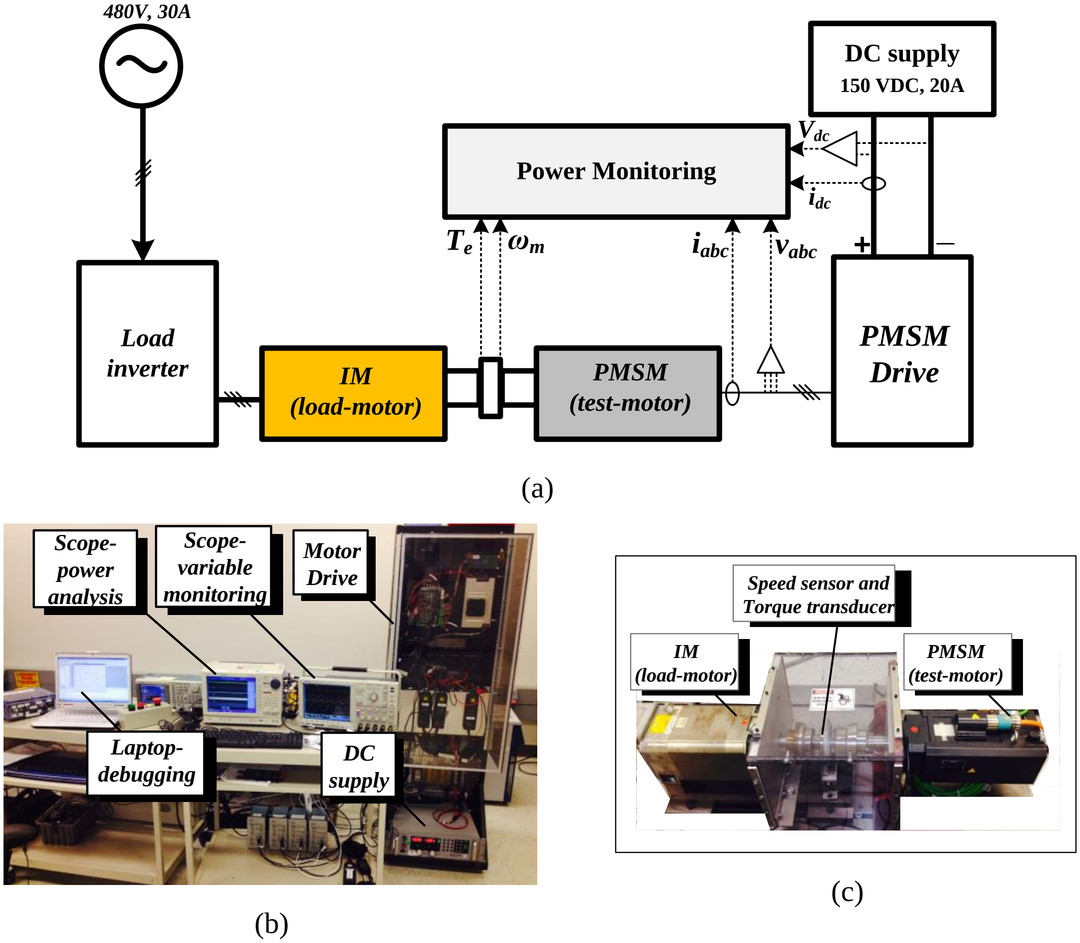

(a)

(b)

(c)

Figure 5.26. Experimental setup of the PMSM drive system for efficiency evaluation at low switching frequency. (a) Block diagram of the setup (b) PMSM drive and monitoring (c) Test and load motor setup.

Table 5-4. Machine parameters

Symbol	***PMSMparameters***
r_s	0.37 ohm
L_s	4.7 mH
λ_m	0.2 Vp/rad/s
Poles	8
Speed	2000 rpm
Torque	40 Nm
Power	7.5 kW

5.6.2. PMSM drive efficiency evaluation test procedure

To test the efficiency of the drive system, the load motor is set in speed mode while the test motor is set in constant torque mode of operation. Note that the constant torque load is common in some compressor applications. The power level is increased by increasing the speed.

In the given setup, for efficiency measurement, the speed of load motor is increased to desired value. Then the position estimator of the controller is enabled to align the estimated rotor position with the test motor back EMF. Once the rotor position is obtained, the drive inverter is turned on with current closed loop operation. The q-axis reference current is set to generate the desired load torque while the d-axis reference current is set to zero. The operating power of the test motor is varied by varying the rotor speed while the torque is kept constant. The corresponding input and output power measurements are recorded for post processing analysis.

The output power of the test inverter and motor is limited by the DC link voltage. For proof of concept, the DC link voltage is chosen as 150Vdc. The PMSM voltage limit is approximately given as $\omega_r\lambda_m < v_{dc}/\sqrt{3}$ where ω_r(rad/sec) is the rotor velocity and $\lambda_m$is the peak magnet flux linkage (v/rad/sec). Accordingly, at 150 V_{dc} and electrical frequency of 45 Hz, the modulation index *M* of the controller is 0.9. In the given setup, the modulation index is varied from 0.5 to 0.9 by changing the operating frequency from 25 Hz to 45 Hz. For each operating point, the input and output power measurements are recorded.

The aforementioned test procedure is performed on the three modulators and the results are compared.Based on the analysis provided in section 4.2.5 in chapter 4, for drive system efficiency evaluation,the three modulation methods as given in the following have beenimplemented:

(a) Space Vector Modulation (SVM) at high switching frequency (10 kHz),

(b) Discontinuous PWM (DPWM) at 1.67 kHz and

(c) Programmed PWM with N = 15 and maximum switching frequency of 675 Hz.

Fig 5.27 shows the steady state PMSM stator current trajectory $i_s$and its fundamental component $i_{s1}$for the three modulators. The results are presented in stationary reference frame. The DC bus voltage is 150V and the modulation index is 0.9.The results validate the implementation of PWM modulators and the current control methods discussed in previous section. It can be observed that the distortion on the current trajectory (also referred as current ripple) increases as the switching frequency is reduced. Thus the SVM at 10 kHz has the lowest amplitude of current ripple while the programmed PWM has the highest current ripple amplitude.

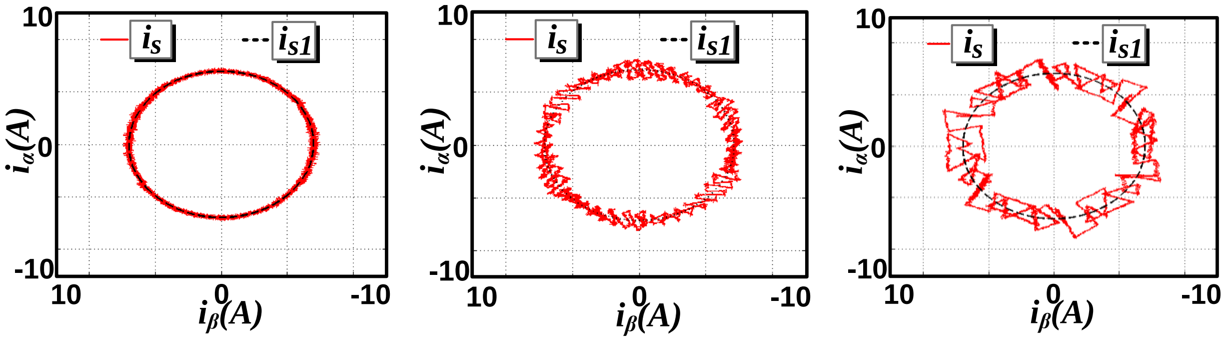

(a) (b) (c)

Figure 5.27. PMSM stator current trajectory waveform comparison based on various modulators (a) SVM at 10 kHz (b) Discontinuous PWM at 1.67 kHz and (c) programmed PWM at 675 Hz. Fundamental frequency = 45 Hz, Modulation index M = 0.9 and reference current i_{qs}^* = 7A.

5.6.3. PMSM drive efficiency evaluation: Results and discussion

Time domain oscillograms for the operating point discussed in Fig 5.27 are shown in Fig 5.28 (a-c). The waveforms in top to bottom order are: line-line voltage with maximum DC link voltage of 150V, motor load torque, inverter input dc current and the motor phase A current. Based on the results, following observations are made:

The three modulation methods can generate the desired load torque at the given operating speed. The torque ripple due to programmed PWM is marginally higher than SVM and DPWM.

(ii) As seen from the line-line voltages, programmed PWM at 675 Hz has lower switching pulses in comparison to SVM at 10 kHz and DPWM at 1.67 kHz. Accordingly, the distortion in motor output current and also the DC link current is higher.

(iii) For the given operating point, the average input DC current in case of programmed PWM and DPWM is lower than SVM at 10 kHz. The results imply that, for given case, at reduced switching frequency and appropriate modulation method selection, the total power consumption of the motor and drive system can be reduced.

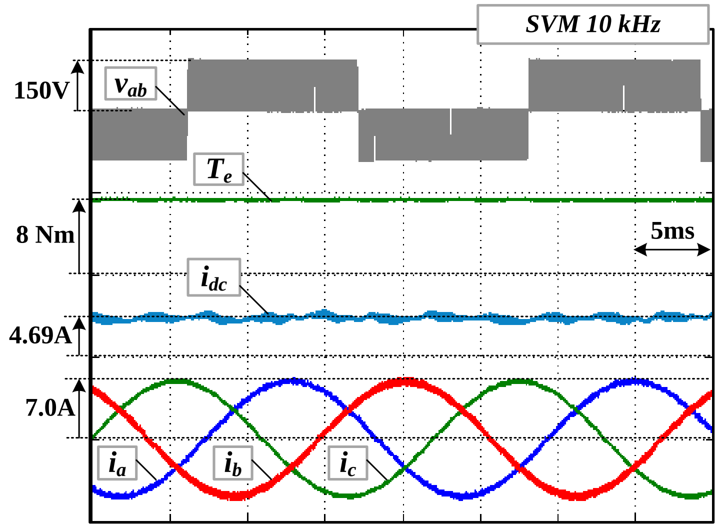

(a) Space Vector Modulation: switching frequency = 10 kHz.

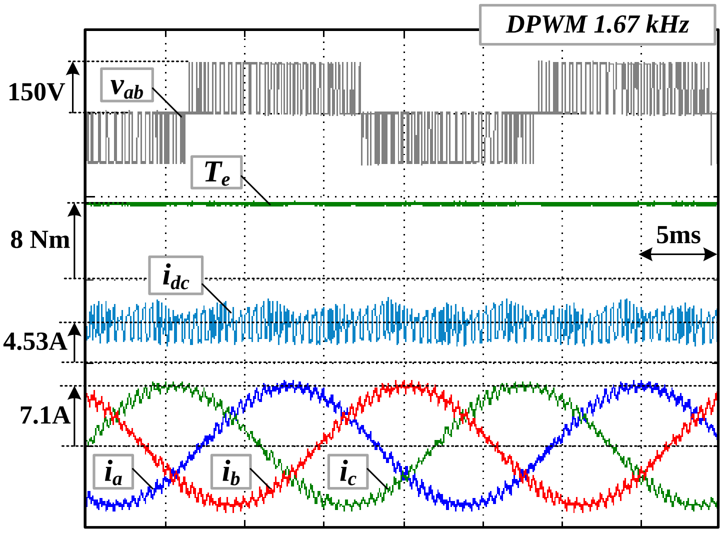

(b) Discontinuous Modulation: switching frequency = 2kHz, effective switching frequency = 1.67 kHz.

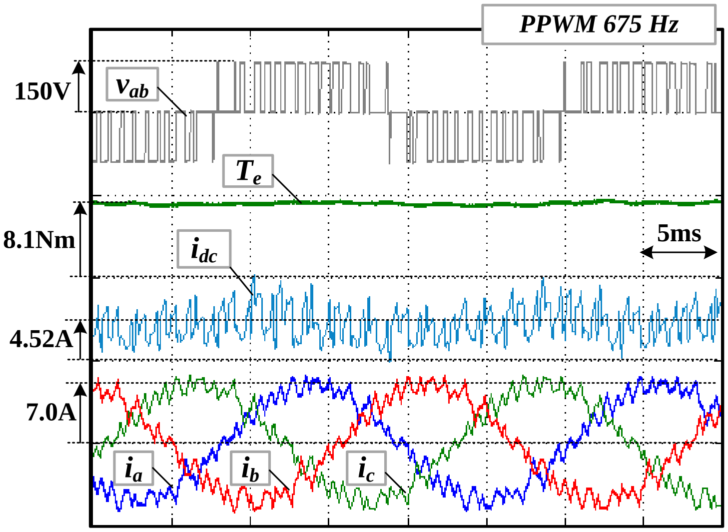

(c) Programmed Modulation: switching frequency = 675 Hz, N = 15.

Figure 5.28. PMSM drive efficiency evaluation based on various modulators Fundamental frequency = 45 Hz, modulation index M = 0.9 and reference current i_{qs}* = 7A.

The above test is repeated at different operating points to validate efficiency improvement. As shown in Fig 5.29(a), the load torque is kept constant at around 8.1 Nm and the rotor frequency is varied from 25 Hz to 45 Hz proportionally varying shaft output power from 320 W up to 570W. The corresponding modulation index varies from 0.5 to 0.9.

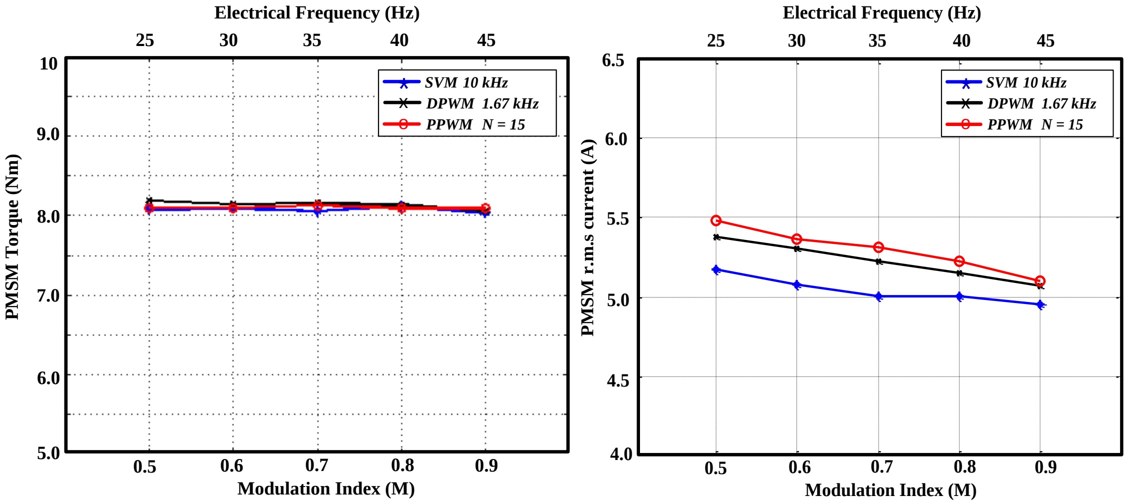

(a) (b)

Figure 5.29. (a) PMSM output torque at various rotor speeds for the three modulation schemes (b) Resulting motor root mean square amplitude of the phase current at various rotor speeds for the three modulation schemes.

Fig 5.29(b) shows that the motor root mean square amplitude of the current for three modulation methods (a) SVM at 10 kHz, (b) DPWM at 1.67 kHz and (c) programmed PWM with N = 15 with maximum switching frequency of 675 Hz. It is seen that in all cases, the root mean square amplitude of the current reduces as the modulation index increases. This is mainly because the inverter output voltage distortion amplitude and hence the resulting harmonic current amplitude decreases as the modulation index becomes higher. It is noted in Fig 5.29 (b) that the programmed PWM has highest root mean square amplitude of the current amongst the three modulators, while SVM at 10 kHz has the lowest. Large root mean square value of the current implies higher resistive losses in the motor and conduction losses in the inverter.

For the given output power, the total input power consumed by the drive system at different switching frequencies and modulation methods is listed in Table 5.5. Since the load torque was kept constant; the output power is proportional to the speed or electrical frequency of the motor.

Based on the input and output power measurements, percentage losses in the drive and motor can be analyzed for various operating points. If the drive input power is measured as P_d, motor input power as P_m and the shaft output power as P_o then the normalized motor and inverter losses are given as:

Table 5-5.Measurement results: Input and output power of the drive system

Freq (Hz	***Input Power (Watts)***			***Output Power (Watts)***		
	SVM-10kHz	DPWM-1.67 kHz	PPWM-325-675 Hz	SVM-10kHz	DPWM-1.67 kHz	PPWM-325-675 Hz
25	446.77	431.51	436.13	318.14	322.42	318.74
30	510.16	493.40	486.61	382.38	384.75	382.61
35	569.64	556.17	556.91	443.44	449.11	447.16
40	641.30	620.68	624.78	511.49	512.16	509.54
45	705.85	681.04	679.25	570.98	572.08	572.93

$$P_{loss\_motor(p.u)} = \frac{P_m - P_o}{P_d}, \qquad P_{loss\_inv(p.u)} = \frac{P_d - P_m}{P_d} \tag{5.25}$$

where P_{loss_motor} and P_{loss_inv} are the normalized motor and inverter losses. The normalization is done with respect to the total system losses at each operating point.

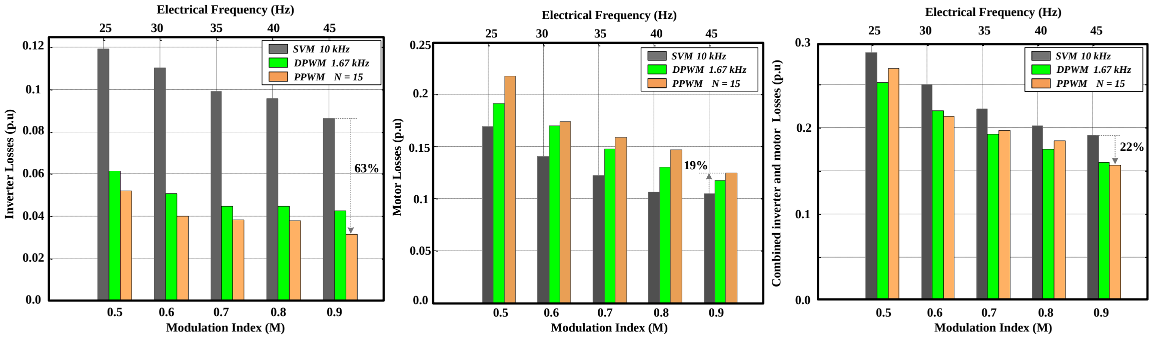

(a) (b) (c)

Figure 5.30. Losses at various rotor speeds and switching frequencies (a) inverter losses (b) motor losses. Losses normalized to total system input power for each operating point.

Normalized losses of inverter and motor are shown in Fig 5.30(a) and (b) respectively. Following observations are made from Fig 5.30(a):

(a) The losses in all three modulation schemes decrease as the modulation index increases.. This trend is due to the reduction of the root mean square amplitude of the current at higher operating frequencies as shown in Fig 5.29(b). Since the conduction loss of the inverter is proportional to the square of the motor phase root mean square amplitude of the current, the normalized losses of the inverter demonstrate similar trend.

(b) Considering the operating point at 45 Hz and modulation index of 0.9, it is seen that both DPWM and programmed PWM methods operating at reduced switching frequencies result in more than fifty percent (39 W) inverter loss reduction in comparison to SVM operating at 10 kHz. In the given setup and operating condition, programmed PWM with N=15 has lowest inverter losses amongst the three modulation methods.

Following observations are made from Fig 5.30(b):

(a) The normalized losses of motor are higher than that of inverter. Hence the motor has lower efficiency than the inverter.

(b) Motor harmonic losses in all three modulation schemes decreases as the modulation index is increased. This trend is due to the reduction of the root mean square amplitude of the current at higher operating frequencies as shown in Fig 5.29(b).

(c) Since the motor losses are directly proportional to the harmonic current distortion, programmed PWM and DPWM schemes show higher losses than SVM at 10 kHz. Considering the operating point at 45 Hz and modulation index of 0.9, it is seen that programmed PMW method results in twelve percent (or 10 W) higher motor losses when compared to SVM at 10 kHz. Thus the net loss reduction in the motor and drive system at the given operating point is 29 W.

5.30(a) and (b) shows that, with DPWM and programmed PWM, the motor harmonic losses increased by 25 percent while the inverter losses were reduced by 58 percent resulting in net loss reduction of 23 percent at modulation index of 0.9. This loss reduction was achieved at no additional cost of control hardware or machine re-design.

Fig 5.30(c) shows the total system losses for the three modulation schemes under consideration. It is seen that both DPWM and PPWM has lower system losses than SVM. The result shows that the total system losses of PMSM drive can be improved by reducing the switching frequency. It is noted that at 45 Hz, and modulation index of 0.9, the total system loss reduction of PPWM is 20 percent lower than SVM.

Based on the above result it can be deduced that, by reducing the switching frequency, the percentage reduction in inverter losses are much higher than the percentage increase in motor losses. Hence from a system perspective, the total power consumption is reduced leading to efficiency improvement.

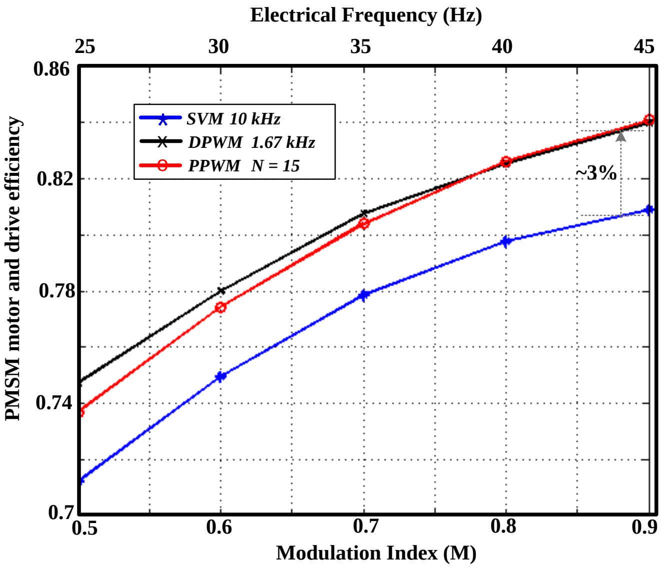

Figure 5.31. System efficiency comparison of PMSM and inverter using SVM, DPWM and PPWM

The total system efficiency comparison of the three modulation schemes is provided in Fig 5.31. From the figure it is seen that, in the given setup and test conditions, PMSM drive system utilizing DPWM and PPWM schemes will have up to 3 percent higher efficiency than SVM at 10 kHz. This result validates the proposed methodology of improving total system efficiency of PMSM drives by reducing the switching frequency of the inverter. It should be noted that DPWM, at modulation index below 0.8, has higher efficiency than PPWM, while PPWM has marginally higher efficiency than DPWM above $M = 0.8$. The low efficiency of PPWM at lower modulation indices is due to the higher harmonic content in the stator currents. The difference in efficiencies between PPWM and DPWM becomes noticeable as the power level and loss in the semiconductor devices increases.

To compare the difference between DPWM and PPWM methods for higher efficiency operation, it is essential to understand their loss factorσ^2. Although the comparative analysis was made and discussed in Chapter 4, the topic is revisited to highlight the significance of PPWM over DPWM. Fig 5.32 shows comparison of various modulation methods and their current distortion as a function of modulation index. It is seen that programmed PWM (Sync Opt PWM, N = 7) has more than 50 percent lower distortion than DPWM (N = 7) method at modulation index of 1.15. Hence for higher power levels when the ratio of switching frequency to fundamental frequency becomes small (N<10), the programmed PWM becomes advantageous. Efficiency improvement with low switching frequency and its scaling for higher power level PMSM drive system is discussed in the following section.

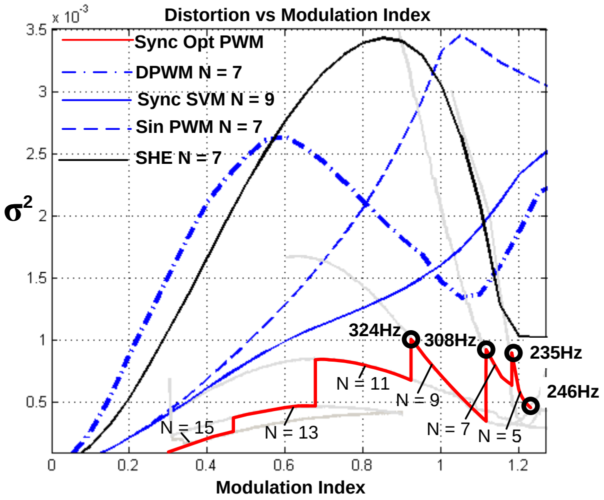

Figure 5.32.Current harmonic distortion comparison between various PWM strategies.

5.6.4. PMSM drive efficiency results - Scaling for higher power rating

To understand the system loss reduction, three motors of various power ratings are considered. The losses are estimated using analysis developed in Chapter 4. To be consistent with experimental results, constant load torque application is considered. The output power is varied by varying the motor speed. The corresponding system losses for 8 kW, 20 kW and 90 kW motor drives are shown in Fig 5.33 (a-c). It is seen that at higher power levels, the percentage loss reduction is higher. This is attributed to inherent higher switching losses in higher power devices. It is assumed here that the increase in motor losses is acceptable. Thus an appreciable loss reduction at system level is seen.

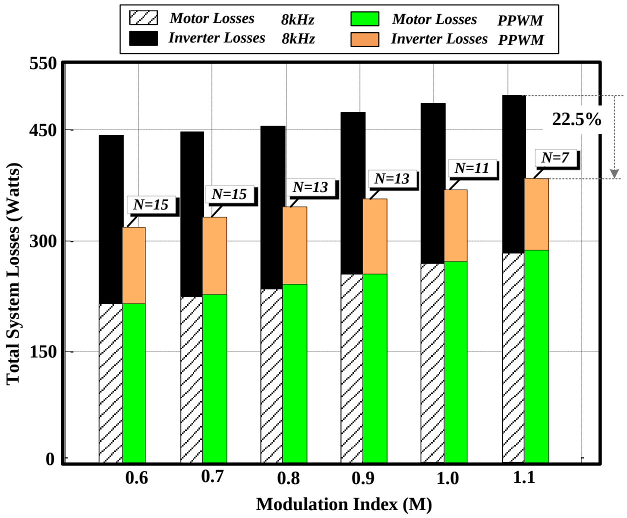

(a) 8kW motor-drive loss comparison between SVM at 8 kHz and programmed PWM with maximum switching frequency of 1kHz.Motor maximum electrical fundamental frequency = 133 Hz. Te = 38 Nm.

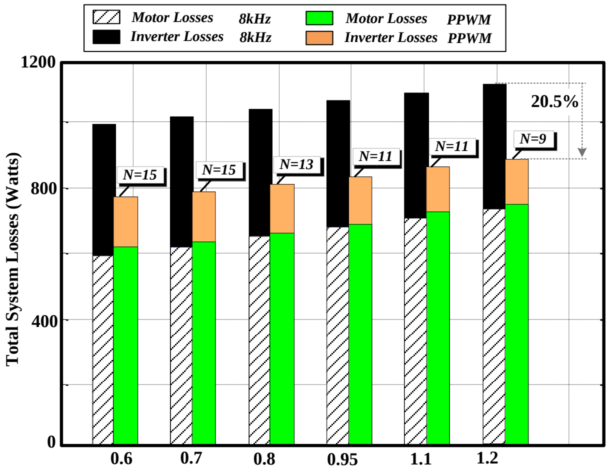

(b) 20kW motor-drive loss coparison between SVM at 8 kHz and programmed PWM with maximum switching frequency of 600 Hz.Motor maximum electrical fundamental frequency = 67 Hz. Te = 258 Nm.

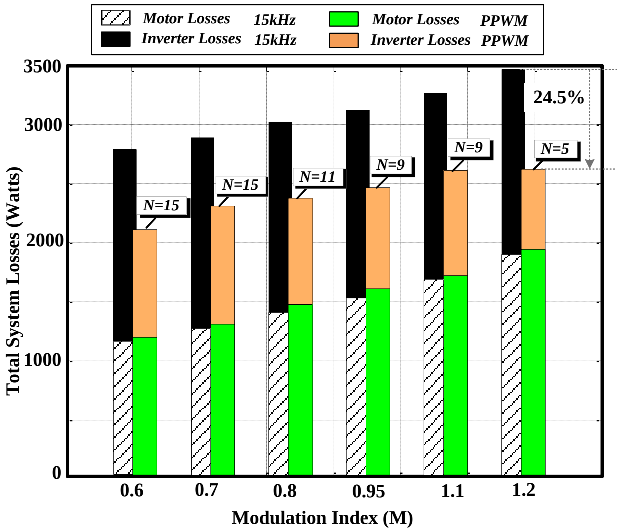

(c) 90kW motor-drive loss comparison between SVM at 15 kHz and programmed PWM with maximum switching frequency of 5kHz.Motor electrical fundamental frequency = 833 Hz. Te = 34.8 Nm.

Figure 5.33. Total system loss comparison in PMSM and inverter using SVM at high switching frequency and PPWM for various pulse numbers

5.6.5. Summary and conclusions

The main focus of this chapter was on experimental validation of efficiency improvement in PMSM drive system operating at low switching frequency. Following contributions led to the validation through experimental results

1. For low switching frequency operation programmed PWM (PPWM) is advantageous. Implementation of PPWM on a present state of art digital signal processor has limitations as they are customized for carrier based modulators. Therefore a novel method of implementing programmed PWM using carrier signal is proposed and is experimentally demonstrated on state of art digital signal processor. The use of carrier signal in the proposed method allows ease of transition between programmed, continuous and discontinuous modulators enabling a hybrid approach.
2. Current control of PMSM is essential for stable operation. At low switching frequencies, the sampling rate and PWM update rate are low. This results in unstable operation of the motor. An alternative current controller approach with feedback signal oversampling is applied in conjunction with programmed PWM. The analysis and experimental results show that the method can achieve stable operation with acceptable dynamic performance at low switching frequencies. The method is simple and provides an alternative approach to the complex variable current controllers.
3. PMSM drive system efficiency is experimentally evaluated using three modulation methods (a) Space Vector Modulation (SVM) at high switching frequency (10kHz), (b)Discontinuous PWM (DPWM) at 1.67kHz and (c) Programmed PWM at 675 Hz. The experimental results show that the total system losses can be reduced by reducing the switching frequency. Since motor harmonic losses do not increase significantly at reduced switching frequency, the total system efficiency is improved. Programmed PWM method is advantageous at higher modulation indices due to its lower harmonic distortion content. The scaling analysis at various power levels using the proposed approach shows that the percentage efficiency improvement increases at higher power and voltage levels.

APPENDIX-C

Table C. 1 Optimal PWM switching angles *k = 6* and polynomial weights generation

Angles/Weights	w_4	w_3	w_2	w_1	w_0
α_1	0.963	-2.437	1.839	-0.328	0.121
α_2	0.901	-1.958	1.018	0.279	0.239
α_3	-0.732	1.541	-0.691	-0.392	0.813
α_4	-0.712	1.969	-1.567	0.327	0.931
α_5	0.008	0.187	-0.290	0.024	1.045
α_6	1.187	-3.072	2.457	-0.389	1.171

Table C. 2 Optimal PWM switching angles *k = 5* and polynomial weights generation

Angles/Weights	w_4	w_3	w_2	w_1	w_0
α_1	0.963	-2.437	1.839	-0.328	0.121
α_2	0.901	-1.958	1.018	0.279	0.239
α_3	-0.732	1.541	-0.691	-0.392	0.813
α_4	-0.712	1.969	-1.567	0.327	0.931
α_5	0.008	0.187	-0.290	0.024	1.045

Table C. 3 Optimal PWM switching angles *k =4* and polynomial weights generation

Angles/Weights	w_4	w_3	w_2	w_1	w_0
α_1	0.963	-2.437	1.839	-0.328	0.121
α_2	0.901	-1.958	1.018	0.279	0.239
α_3	-0.732	1.541	-0.691	-0.392	0.813
α_4	-0.712	1.969	-1.567	0.327	0.931

References

[1] J. Holtz and X. Qi, “Optimal Control of Medium-Voltage Drives—An overview,” *IEEE Trans. Ind. Electron.*, vol. 60, no. 22, pp. 5472–5481, Dec 2013.

[2] G.S. Buja, and G.B. Indri, “Optimal Pulsewidth Modulation for Feeding AC Motors.” *IEEE Trans. Ind. Appl.*, vol. IA-13, no. 1 (January 1977): 38 –44.

[3] J. Sun, and H. Grotstollen, “Optimized Space Vector Modulation and Regular Sampled PWM: A Reexamination,” Conf. Proc. IEEE IAS’96, vol. 2, pp. 956-963, 1996.

[4] S. Bowes, and Y. Lai, “The Relationship Between Space-Vector Modulation and Regular-Sampled PWM,” IEEE Trans. on Ind. Elec., vol. 44, no. 5, pp. 670-679, Oct. 1997.

[5] S.R. Bowes, and A. Midoun, “New PWM switching strategy for microprocessor controlled inverter drives,” IEE Proceedings Electric Power Applications, B, vol. 133, no. 4, pp. 237–254, 2008.

[6] S.R. Bowes, and D. Holliday, “Optimal regular-sampled PWM inverter control techniques,” IEEE Trans. Ind. Electron., vol. 54, no. 3, pp. 1547–1559, 2007.

[7] S.R. Bowes, and A. Midoun, “Microprocessor implementation of new optimal PWM switching strategies,” IEE Proceedings Electric Power Applications, B, vol. 135, no. 5, pp. 269–280, 2002.

[8] P.H.Nayak, and R.G. Hoft, “Optimizing the PWM Waveform of a Thyristor Inverter.” *IEEE Trans. Ind. Appl.*, no. 5 (October 1975), pp. 526–530.

[9] P.N.Enjeti, P.D. Ziogas, and J.F. Lindsay, “Programmed PWM Techniques to Eliminate Harmonics - A Critical Evaluation.” *IEEE Industry Applications Society Annu. Mtg., 1988, Conference Record of the 1988*, vol.1, pp. 418 – 430, 1988.

[10] J. Holtz, and B. Beyer,“OptimalPulsewidth Modulation for AC Servos and Low-cost Industrial Drives.” *IEEE Trans. Ind. Appl.*, vol. 30, no. 4 (August 1994): 1039 –1047.

[11] J.R. Wells, B.M. Nee, P.L. Chapman, and P.T. Krein, “Selective Harmonic Control: A General Problem Formulation and Selected Solutions.” *IEEE Trans. Power Electron.*, vol. 20, no. 6 (2005), pp. 1337–1345.

[12] R. Krishnan, *Permanent Magnet Synchronous and Brushless DC Motor Drives*, CRC Press, 2010.

[13] T. Sebastian, G. R. Slemon, “Operating Limits of Inverter-Driven PermanentMagnet Motor Drives”, *IEEE Trans. Ind. Appl.*, Vol. Ia-23, No. 2, March/April 1987.

[14] R. Krishnan, *Electric Motor and Drives- Modeling Analysis and Control*, Prentice Hall Inc., 2001.

[15] R. S. Colby and D. W. Novotny, “Efficient operation of surface mounted PM synchronous motors,” IEEE Trans. Ind. Appt., vol. IA-23, no. 6, pp. 1048-1054, Nov./Dec. 1987.

[16] J. Holtz, J. Quan, G. Schmittt, J. Pontt, J. Rodriguez, P. Newman, and H. Miranda, “Design of Fast and Robust Current Regulators for High Power Drives Based on Complex State Variables.” *Industry Applications Conference, 2003. Conf. Rec 38th IAS Annu. Mtg*., vol.3, pp. 1997 – 2004, 2003

[17] J-S Yim,S K Sul, B H Bae, N R. Patel, S Hiti, “Modified Current Control Schemes for High-Performance Permanent-Magnet AC Drives With Low Sampling to Operating Frequency Ratio”, *IEEE Trans. Ind. Appl.*, vol. 45, no. 2 pp.763 –771, Apr 2009.

[18] F.C. Zach, and H. Ertl, “Efficiency Optimal Control for AC Drives with PWM Inverters.” *IEEE Trans. Ind. Appl.*, IA-21, no. 4 (July 1985), pp. 987 –1000.

[19] D. Murphy and F.G. Turnbull, *Power Electronic Control of AC Motors*, Pergamon Press, Oxford, 1988

[20] N. Oikonomou, J. Holtz, “Closed-Loop Control of Medium-Voltage Drives Operated With Synchronous Optimal Pulsewidth Modulation,” *IEEE Trans. Ind. Appl.*, vol. 44, no. 1, pp. 115–123, Jan-Feb 2008.

[21] C.Y.Leong, N-A. Parker-Allotey, R.A. McMahon, “Loss Comparison between an SPWM and Harmonic Elimination Excited Small, (<1kW) Induction Motor Drive using Pspice Simulation and Calorimetry” *IEEE IAS Conf, 2008*, pp 1-6.

[22] E. Dlala and A. Arkkio, “A General Model for Investigating the Effects of the Frequency Converter on the Magnetic Iron Losses of a Squirrel-Cage Induction Motor,” *Magnetics, IEEE Transactions on*, vol. 45, no. 9, pp. 3303 –3315, Sep. 2009.

[23] D. Sato, J. Itoh “Total Loss Comparison of Inverter Circuit Topologies with Interior Permanent Magnet Synchronous Motor Drive System”, *ECCE* 2013, pp 57-543.

[24] J. Holtz, “Pulsewidth Modulation for Electronic Power Conversion.” *Proc. IEEE 82*, no. 8 (August 1994): 1194 – 1214.

[25] V. Blasko, “Analysis of a Hybrid PWM Based on Modified Space-Vector and Triangle-Comparison Methods,” *IEEE Trans. Ind. Appl.*, vol. 33, no. 3, pp. 756-764, May/June 1997.

[26] A. Hambley , “Electrical Engineering: Principles And Applications”, 4th Edition, Pearson Education, Inc, 2008

[27] J. Holtz, “The Representation of AC Machine Dynamicsby Complex Signal Flow Graphs”, *IEEE Trans onInd Electron*. Vol. 42. No. 3, June 1995

[28] M. P. Kazmierkowski and L. Malesani, Current Control Techniques for Three-Phase Voltage-Source PWM Converters: A Survey“, *IEEE Transactions on Industrial Electronics*, Vol. 45,No. 5, Oct. 1998, pp. 691-703.

[29] T. Ohmae, T. Matsuda, K. Kamiyama, and M. Tachikawa, “A Microprocessor-Controlled High-Accuracy Wide-Range Speed Regulator for Motor Drives,” *IEEE Trans. Ind. Electron.*, vol. IE-29, no. 3, pp. 207 –211, Aug. 1982.

[30] Bocker, J, Buchholz, O. “Can oversampling improve the dynamics of PWM controls?”, (ICIT), IEEE International Conference on Industrial Technology, pp 1818 – 1824, Feb. 2013,

[31] F. Briz, M.W. Degner, and R.D. Lorenz, “Analysis and Design of Current Regulators Using Complex Vectors,” *IEEE Trans. Ind. Appl.*, vol. 36, no. 3 (June 2000), pp. 817 –825.

[32] L.Springob, and J. Holtz. “High-bandwidth Current Control for Torque-ripple Compensation in PM Synchronous Machines.” *IEEE Trans. Ind. Electron.*, vol. 45, no. 5 (October 1998): 713–721.

[33] J. Holtz and N. Oikonomou, “Fast dynamic control of medium voltage drives operating at very low switching frequency—An overview,” *IEEE Trans. Ind. Electron.*, vol. 55, no. 3, pp. 1005–1013, 2008.

[34] J. Holtz and S. Stadtfeld, ‘‘A predictive controller for the stator current vector of AC machines fed from a switched voltage source,’’ in Proc. Int. Power Electronics Conf. (IPEC), Tokyo, 1983, pp. 1665–1675.

[35] T. Geyer and G. Papafotiou, ‘‘Model predictive control in power electronics: A hybrid systems approach,’’ in Proc. 4th IEEE Conf. Decision and Control and European Control Conf., Seville, Spain, 2005, pp. 5606–5611.

[36] V. Blasko, V. Kaura, W. Niewiadomski, “Sampling of Discontinuous Voltage and Current Signals in Electrical Drives:A System Approach,” *IEEE Trans. Ind. Appl.*, Vol 34, no. 5,1998, pp. 1123 –1130.

[37] P. Kshirsagar, R.P Burgos, J. Jang, A.Lidozzi, , F. Wang, D. Boroyevich, S. K. Sul, “Implementation and Sensorless Vector-Control Design and Tuning Strategy for SMPM Machines in Fan-Type Applications”, *IEEE TransonInd Appln Joint Special Issue - Nov/Dec 2012*.

Chapter 6 Sensorless Position Control of PMSM Operating at Low Switching Frequency for Climate Control Systems

6.1. Abstract

This chapter focuses on sensorless vector control of permanent magnet synchronous motor (PMSM) drives operating at low switching frequencies for climate control systems. Such systems require variable speed motor drives for space cooling and air-conditioning applications. Due to their widespread use, higher system efficiency along with lower cost of component is desired. Based on previous chapter, improving efficiency of PMSM motor-drive system by reducing switching frequency of the inverter has been taken for study. To reduce cost of the system, operation of the PMSM drive without position sensor is essential. Sensorless control strategies for PMSM drives at low switching frequency along with programmed PWM methods have not been reported and hence taken up for research study. A suitable position sensorless for the considered drive is developed, analyzed and its laboratory implementation is presented in this chapter. Simulation and experimental results validate both the design methodology and the expected performance attained by the proposed control strategy.

6.2. Introduction

Electric motor driven systems are amongst the largest consumers of electricity in US and account for approximately 60% of the total energy consumption. Residential and commercial buildings require high volume of electric motors for climate control systems (CCS). These systems comprise of vapor compressors, chillers, fans, pumps and blowers which are mainly driven by variable speed motor drives. These systems are cost and energy efficiency sensitive. PMSM drives require position information for their operation and most of the high performance drives use expensive resolvers and position encoders resulting in high cost [1].The position sensors are also an additional source of reliability concern,–applications operating under harsh environmental conditions, thus making them unsuitable in practice from this point of view as well. Cost sensitivity and other described features and functions require position sensorless operation while high efficiency operation requires low inverter and machine losses positioning it for a low switching frequency operation. Unlike high performance motor drives, these applications do not need high dynamic response or low speed operation or lower torque ripple [2]. Therefore, sensorless control techniques capable of operation with low switching frequency of the inverter are sufficient for considered applications in this research.

References [3-5] have shown operation of induction machine at very low switching frequency using trajectory tracking control. This operation requires velocity feedback from the induction motor for synchronizing the inverter switching pulses with respect to the motor back EMF. Programmed PWM and speed encoder-less operation has been demonstrated only in open loop voltz per hertz control of induction machines [6-9].

In case of sensorless position control, accurate estimation of rotor position during transient operation becomes difficult due to inaccurate information of the motor and inverter models used for online calculations. The inaccuracy is due to the following reasons (a) the parameter variation in the models used to calculate the rotor position (b) inverter nonlinearities (dead-time) and uncompensated sampling delays, (c) delays and dc offsets during measurements of feedback currents (d) errors in motor terminal voltage estimation. For vector control, if the information of rotor position is not accurate, then the phase of the currents injected by the inverter is not aligned with the phase of the motor back EMF. The amplitude and phase error of the currents increases in proportion to the position error. When the angular error between the current and back EMF exceeds 90° (in case of PMSM), the machine rotor field loses synchronism with the stator field. In such case, the operation of the system in sensorless mode can also be considered as an open loop system because the exact information of the rotor position is not available. Thus the stability of the system can be determined through open-loop operation of the machine. It is known that induction machine has more stable open loop response than PMSM [10,11]. Hence it can be inferred that during low switching frequency operation, when the inverter control bandwidth is low, control of induction motor will have more stable operation than PMSM. Since the existing literature only covers low switching frequency operation of induction motors, control challenges for applying the same techniques for PMSM are yet to appear.

In [12], a six-step mode of operation was shown to be more efficient than PWM with 5 kHz switching frequency for a certain inductance value of the machine. The PMSM drive was controlled using open loop volts per hertz and current feedback stabilization method. In [13], it was shown that field oriented control of PMSM has better performance over open loop Volts per Hertz control especially during low operating speed.

In [14], a back EMF based position sensorless control of PMSM has been demonstrated using high switching frequency. The same algorithm cannot be used for reduced switching frequency operation due to following reasons:

1. When the sampling frequency is significantly reduced due to smaller switching frequencies, the current controller designed in [14] becomes unstable. Hence alternative current control strategy is desired as discussed in chapter 5.

2. A suitable sampling technique is also critical for the state observer and tracking controller for their stable operation at reduced switching frequencies. At low switching frequencies, the switching ripple on the current is high. Consequently, the variables of the state observer and rotor position estimator will have higher harmonic content in them. This in turn introduces more distortion in the feedback d and q-axis currents due to the three-phase to two-phase co-ordinate transformation. The observer and the tracking controller must be designed to filter the switching harmonics along with enough stability margins.
3. The algorithm in [14] works only with asynchronous space vector modulation which is typically used at higher switching frequencies. However at reduced switching frequencies, it is essential to switch to synchronous carrier based or programmed PWM methods. The transition must be controlled with reference to the estimated rotor position. Such a sensorless algorithm has yet to appear.

Given the above limitations, design of a sensorless rotor position control that will avoid loss of synchronism and resulting pull out of PMSM under transient load conditions at low switching frequency operation is reported in this study for the first time.

Accordingly, this chapter will focus on back EMF based position sensorless operation of PMSM at low switching frequency and the integration of programmed PWM in overall control scheme. Following are the significant contributions of this work:

1. A novel sensorless position control scheme incorporating asynchronous and programmed PWM for high efficiency operation of the PMSM drive system.
2. Development of a starting sequence for the sensorless control scheme from stand still to steady state along with the switching frequency reduction for high efficiency operation.
3. Analysis and design of back EMF state observer and rotor position tracking controller for low switching frequency operation.
4. Experimental correlation of the proposed sensorless scheme with the simulation results is made.

6.3. Rotor Position Sensorless Control Scheme for Low Switching Frequency

6.3.1. Introduction

For sensorless operation of PMSM at low switching frequencies, three aspects must be considered in developing the controller:

4. A PWM unit for generating asynchronous and programmed pulse width modulation,
5. Closed loop vector controller unit with d and q-axis current regulators in estimated rotor reference frame and,
6. Sensorless rotor position and speed estimators for coordinate transformation and speed regulation respectively.

The asynchronous and programmed pulse width modulation methods and their implementation have been discussed in chapters 4 and 5, respectively. The transition between the asynchronous and programmed PWM is determined by the modulation index and the desired switching frequency. The asynchronous PWM is used at lower modulation indices (typically below 0.6) while programmed PWM is used at higher modulation indices (typically above 0.6). The reference switching frequency is calculated offline for higher drive system efficiency operating points. The estimated rotor position is used for generating the commutation pulses in case of programmed PWM.

The closed loop current regulators, using feedback oversampling method for vector control at low switching frequencies have been described in chapter 5.The estimated rotor position is necessary for sensorless vector control operation.

For sensorless rotor position and speed estimation, a back EMF observer and tracking controller from [14] is adopted and modified for low switching frequency operation in [15]. The state observer estimates the d-q axes back EMF voltages using the motor model, feedback currents and reference voltages in rotor reference frames. The tracking controller synchronizes the estimated $d-q$ frame with the actual rotor reference frame by forcing the estimated d-axis back EMF voltage to zero. The output of the tracking controller is the estimated rotor speed and position. The estimated speed is used to close the speed loop while the estimated rotor position is used in all transformations between the *abc* and $d-q$ rotor reference frames and generating the commutation angles in case of programmed PWM.

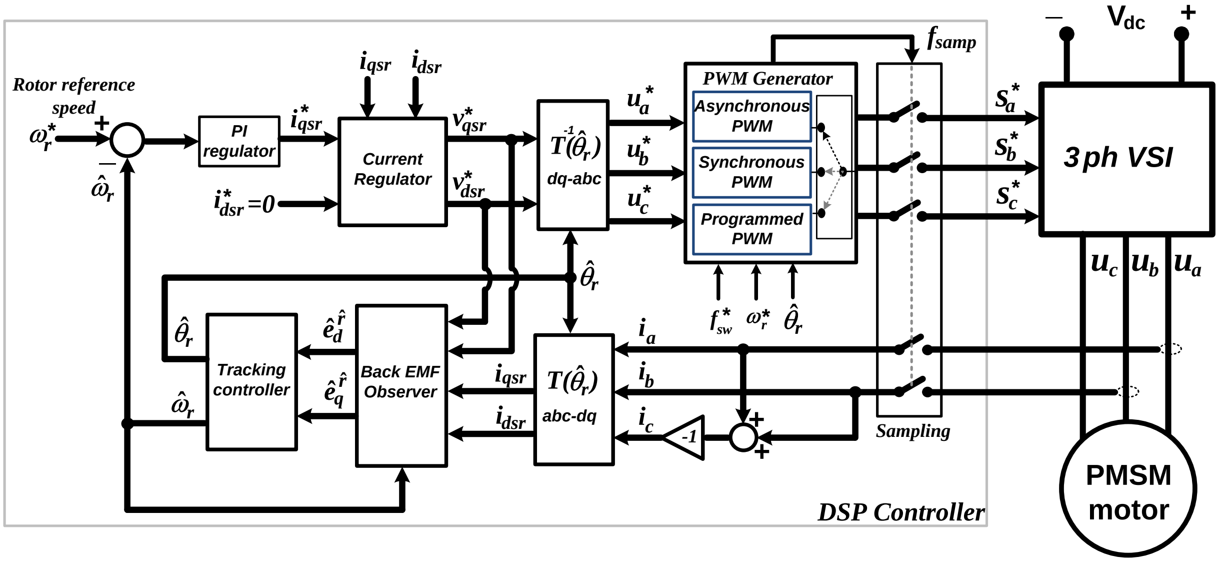

Figure 6.1. Rotor position sensorless control scheme for low switching frequency operation

Based on the description above, Figure 6.1shows the proposed rotor position control scheme of PMSM operating at low switching frequency [15]. It consists of a closed loop speed and current regulator, back EMF observer and tracking controller in rotor reference frames, and PWM generation and sampling units. For sensorless vector control, the estimated rotor position from the tracking controller is used for co-ordinate transformation.

For variable speed application, asynchronous and synchronous carrier based PWM modulators are favored at low modulation indices due to better current controllability during starting. The programmed PWM is applied at higher modulation indices for improving system efficiency. Due to low switching frequency operation, feedback oversampling is used for closed loop current control. Irrespective of the switching frequency, the sampling frequency (f_{samp}) of the PWM generator, current controller, observer and tracking controller is kept the same (10 kHz). The oversampling allows better tracking of the motor back EMF and hence the rotor position leading to good dynamic response in the chosen application even with a very low number of switching pulses. Influence of sampling frequency on PWM generation and current controller performance has been discussed in chapter 5.

6.3.2. Motor Starting Algorithm

Figure 6.2(a) shows the operating regions for starting the motor in sensorless mode and the corresponding PWM pattern selection strategy based on the ratio of switching frequency to fundamental frequency N. Initially, the switching frequency of the motor drive is set at 2 kHz and carrier based space vector asynchronous modulation described in chapter 4 is used.

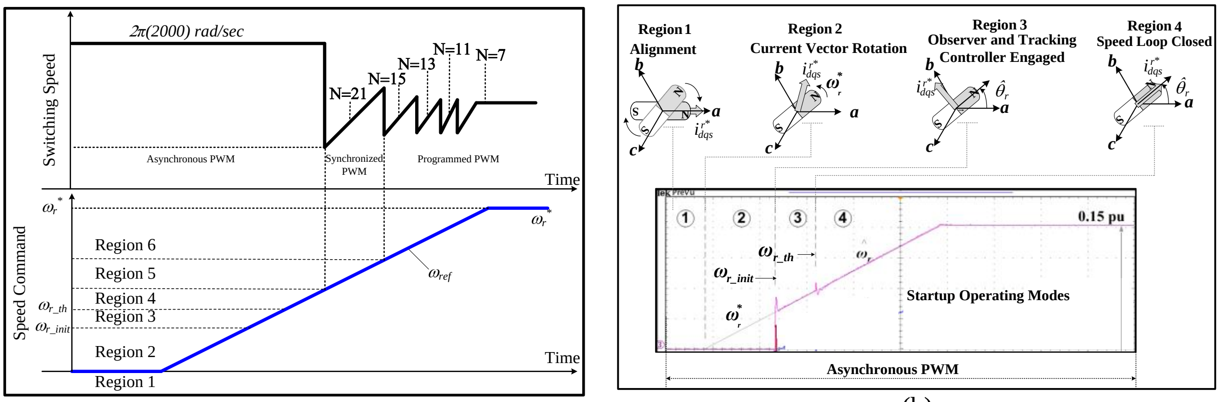

(a) (b)

Figure 6.2. (a) Operating regions and PWM pattern selection strategy (b) Experimental results and illustration of motor startup operation in the first four regions.

The speed command spanning from standstill to nominal speed has been divided into six operating regions: *Region 1* is used to align the rotor of machine with a given phase. This is achieved by injecting 0.1 p.u of DC current in phase A of the motor winding. The stator field produced by this current attracts the rotor with permanent magnets towards the stator phase A. *Region 2* accelerates the machine with open speed loop and with the closed current loop. The current loop is closed using the reference rotor position obtained in region 1 operation. In *Region 3* the state observer and tracking controller are engaged after passing a predefined rotor velocity value ω_{r_init}, and in *Region 4* the speed-loop is closed around the threshold velocity ω_{r_th} after the estimated speed and rotor position values have converged. These modes have been elaborated in [15]. In *Region 4,* a phase locked loop (PLL) of the rotor position with the motor back EMF is achieved by the tracking controller in Figure 6.2. Experimental operation of the first four regions is shown in Figure 6.2 (b) [15]. A robust PLL is essential to synthesize the synchronous PWM voltage and reduce the transients in the output currents. Subsequently, in *Region 5*,a carrier based synchronous PWM operation is enabled when the modulation index is greater than 0.6. The carrier frequency is odd integral multiple of the reference velocity, $N = 21$. *Region 6* is attained when the modulation index is above 0.8due to the increase in motor velocity. In chapter 4 it was shown that synchronized PWM has higher current distortion than programmed PWM, and hence the latter is enabled for modulation index above 0.8. Initially, the phase voltage has 15 switching pulses ($N = 15$) for one fundamental cycle. The number of pulses is slowly dropped with the increase in modulation index to reduce the total system losses. Finally, with a steady state fundamental frequency of 66 Hz and $N = 7$, the lowest switching frequency achieved is 462 Hz.

Sensorless control strategies for PMSM drives at low switching frequency along with programmed PWM method is yet to appear. However there are two control methods for induction motor drives employing programmed PWM which can be considered as a comparative benchmark for the topic under study:

a. open loop Volts per Hertz [7-10] and
b. closed loop synchronous optimal PWM with trajectory tracking control [4-6].

The open loop volt per hertz is the most commonly used sensorless scheme with programmed PWM for induction motors [7-9] because of its simplicity and stable open loop performance. The PWM patterns are calculated offline and synthesized using open loop frequency and voltage reference to the motor. Since the method is of open loop type, the speed regulation is not adequate.

In [5], a closed loop synchronous optimal PWM control with high dynamic performance for induction motors was proposed; however the algorithm requires measurement of the rotor speed. This speed information is used to synchronize the estimated machine model and obtain the fundamental and harmonic components of the variables used in the control. The control algorithm shows good dynamic performance. The behavior of the closed loop controller in absence of rotor speed information has not been discussed.

When compared with induction machines, similar methods incorporating programmed PWM and rotor position sensorless control for permanent magnet motor drives have yet to appear. The proposed sensorless vector control algorithm and its development are therefore novel and unique. The main challenge is to maintain stable closed loop operation in presence of current harmonics due to low switching frequency. The back EMF observer and the tracking controller act like a low pass filter on the current harmonics and create a phase locked loop on the rotor position. Hence the algorithm does not require estimation of the fundamental components as discussed in [5]. Also the current regulator has a low pass filter on its output to reduce the modulation error as discussed in chapter 5. Although, the dynamic performance is a trade-off, such an approach makes the control algorithm more stable even in presence of current transients. The feedback oversampling allows higher bandwidth of the current controller, back EMF observer and the tracking controller. Hence the algorithm discussed above provides a novel approach to high efficiency sensorless control PMSM without resorting to model based methods discussed in [4-6].

6.4. Sensorless Vector Control

In non-salient PMSMs, for producing maximum torque at given operating point in constant torque region, the stator current vector is aligned with the motor back EMF vector using the measured rotor position. In sensorless mode of operation, due to lack of information of the rotor position, deviation from the above result occurs. The current and speed controllers operate in the estimated reference frame. The relative angular error between the rotor position in the actual and estimated rotor reference frames is taken as

$$\tilde{\theta}_r = \theta_r - \hat{\theta}_r \tag{6.1}$$

where $\theta_r$thetar is the position in actual rotor reference frame, and $\hat{\theta}_r$ is the position in estimated rotor reference frame. Figure 6.3shows the d and q axes for the both the actual and estimated rotor reference frames with respective induced EMFs. Equations relating the estimated back-EMF ($\hat{e}_d$and $\hat{e}_q$) and the actual rotor speed ω_r can be established as follows [14].

$$\hat{e}_d = \omega_r \lambda_m \sin\tilde{\theta}_r \text{ , } \hat{e}_q = \omega_r \lambda_m \cos\tilde{\theta}_r \tag{6.2}$$

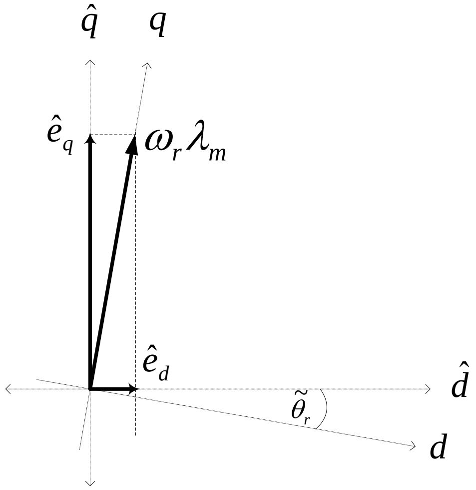

Figure 6.3. Relationship between the actual and the estimated synchronous reference frames, depicting angular misalignment [14].

These relations show that when the error between reference frames is zero, the machine back-EMF on the q-axis will equal $\omega_r \lambda_m$ as can been easily observed in Figure 6.3. Accordingly, the tracking controller, also referred as speed estimator, must be designed to minimize the position error. To achieve such a control, two-fold estimation procedure is applied for estimation of speed and position [14].

Referring to Figure 6.1, in the first step, the state observer estimates the q and d axis back EMF based on plant model, measured currents and reference voltages to the motor. Then, a PLL based tracking controller forces the back EMF on d-axis to zero by minimizing the error on rotor position estimation. The resulting output of controller is the estimated speed. Estimated position is obtained by integration of the estimated speed. These variables are used for co-ordinate transformation in order to achieve vector control. Operation of the state observer and tracking controller for low switching frequency operation is explained in in the following sub-sections.

6.4.1. State Observer

For a non-salient PMSM, the machine model is given as [15],

$$\begin{bmatrix} v_{ds}^r \\ v_{qs}^r \end{bmatrix} = \begin{bmatrix} R_s & -\omega_r L_s \\ \omega_r L_s & R_s \end{bmatrix} \begin{bmatrix} i_{ds}^r \\ i_{qs}^r \end{bmatrix} + \begin{bmatrix} L_s & 0 \\ 0 & L_s \end{bmatrix} \frac{d}{dt} \begin{bmatrix} i_{ds}^r \\ i_{qs}^r \end{bmatrix} + \begin{bmatrix} -\hat{e}_d \\ \hat{e}_q \end{bmatrix} \tag{6.3}$$

where i_{ds}^r and $i_{qs}^r$are the d and q axis stator currents,$v_{ds}^r$and $v_{qs}^r$are the per phase applied stator phase voltages, ω_r is the electrical angular velocity of the rotor, $R_s$is the per phase stator resistance, $L_s$is the per phase stator self-inductance, and $\lambda_m$is the peak of flux linkage of a phase.

Given the PMSM model, the back-EMF terms ($\hat{e}_d$ and $\hat{e}_q$) can be represented as the state variables assuming that the rotor speed and position remain constant during a control cycle (switching period). Such an assumption is true since the sampling period is significantly smaller as compared to the mechanical time constants. Hence (6.2) becomes,

$$\dot{\hat{e}}_d = 0, \text{ and } \dot{\hat{e}}_q = 0\ . \tag{6.4}$$

With6and6, the state-space observer model is constructed as

$$\dot{\hat{\mathbf{x}}} = \mathbf{A}\hat{\mathbf{x}} + \mathbf{B}\mathbf{u} + \mathbf{L}\left(\mathbf{y} - \mathbf{C}\hat{\mathbf{x}}\right)$$

$$\mathbf{x} = \begin{bmatrix} i_{ds}^{\hat{r}} & i_{qs}^{\hat{r}} & e_d^{\hat{r}} & e_q^{\hat{r}} \end{bmatrix}^T, \ \mathbf{u} = \begin{bmatrix} v_{ds}^{\hat{r}} & v_{qs}^{\hat{r}} \end{bmatrix}^T \ , \ \mathbf{y} = \begin{bmatrix} i_{ds}^{\hat{r}} & i_{qs}^{\hat{r}} \end{bmatrix}^T$$

$$\mathbf{A} = \begin{bmatrix} -\frac{R_s}{L_s} & \hat{\omega}_r & \frac{1}{L_s} & 0 \\ -\hat{\omega}_r & -\frac{R_s}{L_s} & 0 & -\frac{1}{L_s} \\ 0 & 0 & 0 & 0 \\ 0 & 0 & 0 & 0 \end{bmatrix}, \ \mathbf{B} = \begin{bmatrix} \frac{1}{L_s} & 0 \\ 0 & \frac{1}{L_s} \\ 0 & 0 \\ 0 & 0 \end{bmatrix}, \ \mathbf{C} = \begin{bmatrix} 1 & 0 & 0 & 0 \\ 0 & 1 & 0 & 0 \end{bmatrix} \tag{6.5}$$

where **L**, defined as

$$\mathbf{L} = \begin{bmatrix} l_{11} & l_{21} & l_{31} & l_{41} \\ l_{12} & l_{22} & l_{32} & l_{42} \end{bmatrix}^T \tag{6.6}$$

and it is the feedback gain matrix that determines the exponential state error dynamics. The resulting characteristic equation of the error dynamic matrix, **c(s) = det(sI-(A-LC)),**is given as:

$$c(s) = s^4 + 2K_1 s^3 + \left(K_1^{\ 2} - \frac{l_{31} - l_{42}}{L_s} - K_2 K_3 \right) s^2 + \frac{K_1}{L_s}\left(l_{31} - l_{42}\right)s - \frac{l_{31} l_{42}}{L_s^{\ 2}} \tag{6.7}$$

where,

$$l_{11} = l_{22} = -\frac{R_s}{L_s} + K_1 \ , \qquad l_{12} = \hat{\omega}_r + K_2\ , \qquad l_{21} = -\hat{\omega}_r + K_3\ , \tag{6.8}$$

Comparing (6.7) with the desired second ordered characteristic equation given as,

$$c_{des}(s) = \left(s^2 + 2\zeta\omega_o s + \omega_o{}^2\right)^2 \tag{6.9}$$

where ω_o is the closed loop observer bandwidth, ζ is the damping factor at the corner frequency ω_o. Comparing (6.7) with (6.9), the gains of the observer are given as:

$$\boldsymbol{L} = \begin{bmatrix} -\frac{R_s}{L_s} + 2\zeta\omega_o & l_{12} \\ l_{21} & -\frac{R_s}{L_s} + 2\zeta\omega_o \\ \omega_o^2 L_s & 0 \\ 0 & -\omega_o^2 L_s \end{bmatrix} \tag{6.10}$$

The choice of the observer bandwidth ω_o, damping factor ζ and the gains l_{12}, l_{21} considering reduced switching frequency operation is evaluated in the following section.

6.4.1.1. Influence of reduced switching frequency on observer bandwidth $\omega_o$and closed loop Eigen values

In [14], the tuning of the closed loop observer is described based on high switching frequency and fixed sampling rate. When the switching frequency is reduced, the sampling rate is also reduced and the observer closed loop bandwidth must be reduced in proportion. As a result, the influence of rotor speed due to sampling delay on the observer performance can be significant resulting in unstable operation. Hence the approach in [14] cannot be used directly for estimation of rotor speed at reduced switching frequencies.

The closed loop observer bandwidth ω_o is mainly dependent on the sampling frequency. For asynchronous pulse width modulation methods, the sampling frequency is twice the switching frequency in order to sample the instantaneous average value of the feedback current [16]. Given the sampling rate, the maximum observer bandwidth that can be chosen is one tenth of the switching frequency [17] while the lowest bandwidth should be at least five times the tracking controller bandwidth [14]. Given these constraints, it is essential to understand the stability of the observer given the smaller sampling rates and limited observer bandwidth. If the characteristic equation of the state observer shows unstable performance, then feedback oversampling method as described in chapter 5 must be considered for estimation of the state variables. This section will discuss the same with illustrations and provide a guideline for design of the observer considering oversampling approach.

Consider a case where the switching frequency of the inverter varies from 8 kHz to 100 Hz and the sampling frequency is twice the switching frequency. Then the observer bandwidth can vary from 800 Hz to 10Hz based on the above discussion. To analyze the Eigen values and stability of the observe, two cases of observer bandwidth variation are considered and they are (i) 800 Hz to 200 Hz and (ii) 200Hz to 10 Hz.

6.4.1.2. Observer bandwidth varied from 800 Hz to 200 Hz.

Figure 6.4 (a-c) shows the influence of observer bandwidth variation from 800 Hz to 200 Hz on three different methods of gain selection in (6.10). The objective is to evaluate the stability of the observer for different gains. The Eigen values are plotted by calculating the roots of the characteristic equation (6.7).

In Figure 6.4 (a), the observer bandwidth ω_o is varied with the gains $l_{12}=l_{21} = 0$. In this case, it is seen that the observer poles vary along with the rotor speed. At lower observer bandwidth (200Hz), the poles move closer to imaginary axis as the influence of electrical frequency of the motor on the cross coupling terms in the observer is larger. However at higher observer bandwidths, this influence is small leading to more stable operation. Hence considering low switching frequency operation, the cross coupling gains $l_{12} = l_{21} = 0$ cannot be used.. Alternatively, the gains must be chosen with same value as the electrical velocity ω_r to cancel the influence of rotor speed. With this choice of gains, the cross coupling terms are decoupled thereby reducing or eliminating the influence of rotor speed.

The damping factor ζ can be selected according to the pole locations of the plant. From the system matrix in (6.3), the poles of the plant can be given as $s_{1,2}= R_s/L_s \pm j\ \omega_r$ Therefore, if the damping ratio is selected as $\zeta = R_s/\sqrt{}\ (R_s^2+ \omega_r^2 L_s^2)$, the poles of plant and observer have the same phase angle. Drawback of this approach is that when the rotor speed is increased, the poles move closer to the imaginary axis as seen in Figure 6.4(b). The effect is observed in case of all the observer bandwidths considered.

Considering $l_{12} = l_{21} = \omega_r$, and $\zeta = 0.707$, the roots are fixed for a given observer bandwidth. The corresponding Eigen values are invariant to the rotor speed as seen in Figure 6.4 (c). These gains assure a stable operation of the state observer.

Case II: Observer bandwidth varied from 200 Hz to 10 Hz.

The case study is same as discussed previously, except that the influence of lower observer bandwidths on the root locus is highlighted in Figure 6.5 (a-c). It is seen that as the observer bandwidth is reduced, the poles move closer to the imaginary axis predicting an unstable operation of the state observer. Even for the case where the observer gains are $l_{12} = l_{21} = \omega_r$, and $\zeta = 0.707$, the Eigen values are close to the imaginary axis limiting the choice this tuning approach.

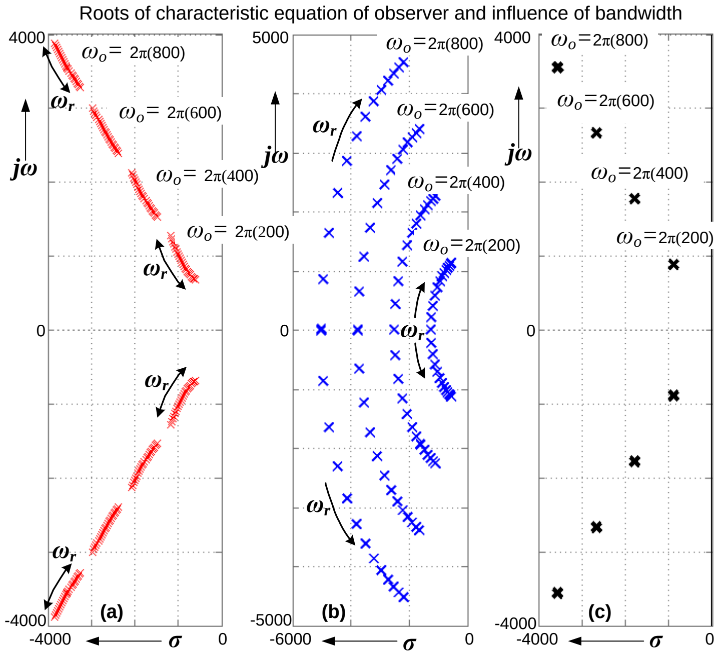

Figure 6.4. Influence of observer bandwidth and rotor speed on roots of characteristic equation for the following conditions:(a) $l_{12}=l_{21}=0$, (b) $l_{12}=l_{21}=\omega_r, \zeta = R_s/\sqrt{(R_s^2+\omega_r^2 L_s^2)}$ and (c) $l_{12}=l_{21}=\omega_r$, $\zeta = 0.707$. Observer bandwidth varied from 800Hz to 200Hz

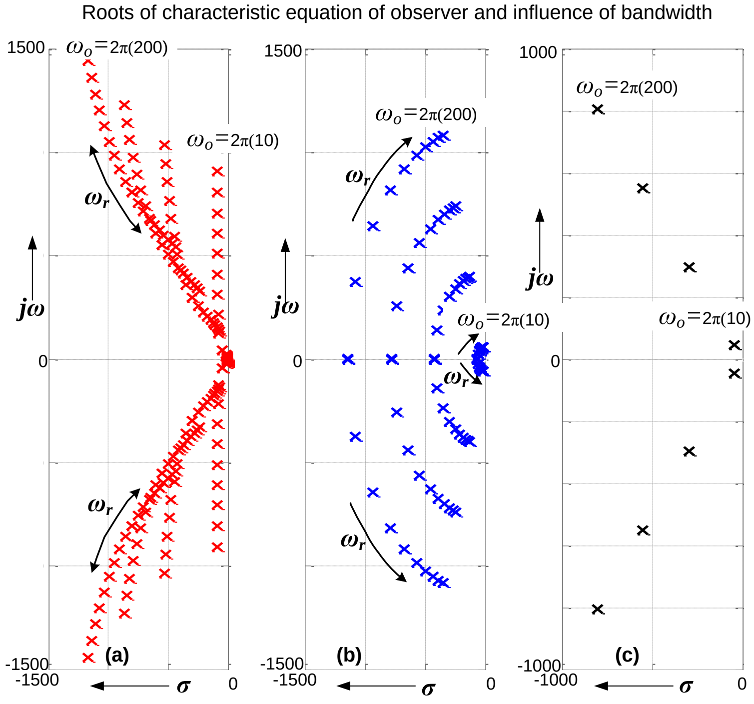

Figure 6.5. Influence of observer bandwidth and rotor speed on roots of characteristic equation for the following conditions:(a) $l_{12}=l_{21}=0$, (b) $l_{12}=l_{21}=\omega_r, \zeta = R_s/\sqrt{(R_s^2+\omega_r^2 L_s^2)}$ and (c) $l_{12}=l_{21}=\omega_r$, $\zeta = 0.707$. Observer bandwidth varied from from 200Hz to 10Hz

Based on the analysis, it is essential to design observer with larger bandwidth even at lower switching frequencies. To achieve this, higher sampling frequency or oversampling is essential. The oversampling reduces the influence of the rotor speed based cross coupling terms on the stability of the observer. Hence for an observer bandwidth of 200 Hz, the sampling frequency must be at least 4 kHz. Accordingly, the observer bandwidth is selected to be 20 times smaller than the sampling frequency and at least five times larger than the tracking controller bandwidth. Thus the limits for selection of ω_0 are:

$$\omega_o < 0.05\omega_{samp} \text{ and } \omega_o > 5\omega_t \tag{6.11}$$

where, ω_{samp} is the sampling frequency, ω_t is the tracking controller bandwidth, ω_{sw} is the switching speed is the switching speed in rad/sec. The observer as such represents the fastest dynamic in the sensorless control strategy. Hence irrespective of the pulse width modulation method, the sampling frequency can be kept fixed as high as possible (typically above10 kHz). In this case, the oversampling rate of the observer and the current controller is kept similar. Finally, the gains of the observer based on the above analysis are given as:

$$\mathbf{L} = \begin{bmatrix} -\frac{R_s}{L_s} + 2\zeta\omega_o & \hat{\omega}_r \\ -\hat{\omega}_r & -\frac{R_s}{L_s} + 2\zeta\omega_o \\ \omega_o^2 L_s & 0 \\ 0 & -\omega_o^2 L_s \end{bmatrix} \tag{6.12}$$

The selection of observer gains and the sampling methods for low switching frequencies have not been considered in [15]. Hence the analysis presented above is unique with respect to the influence of reduced switching frequency operation on observer Eigen values.

6.4.2. Tracking Controller

A tracking controller is implemented using a PLL to synchronize the estimated rotating *d*-*q* frames to the actual rotating *d*-*q* frames as shown in Figure 6.6. This is achieved simply by regulating the *d*-axis back-EMF component $\hat{e}_d^{\hat{r}}$ to zero. The closed-loop transfer function for the PLL is accordingly given by [14],

$$\frac{e_{d\_ref}^{\hat{r}}(s)}{e_d^{\hat{r}}(s)} = \frac{(k_{pt}s + k_{it})\omega_r\lambda_m}{s^2 + \omega_r\lambda_m k_{pt}s + \omega_r\lambda_m k_{it}} \tag{6.13}$$

with the closed-loop poles dependent on the rotor speed located at,

$$poles_{1,2} = -\frac{\omega_r \lambda_m k_{pt}}{2}\left(1 \pm \sqrt{1 - \frac{4k_{it}}{\omega_r \lambda_m k_{pt}^2}}\right) \tag{6.14}$$

Figure 6.6 shows the use of state feedback linearization by means of gain G_{lin} which ensures a constant linear dynamic response of the tracking controller regardless of the PMSM rotor speed. The dependency of rotor speed is established in (6.2). The corresponding linearization gain is defined by

$$G_{lin} = \frac{-1}{\sqrt{\hat{e}_d^2 + \hat{e}_q^2}} \tag{6.15}$$

The gains of the tracking controller which is a proportional plus integral controller are k_{pt} and k_{it} and they are determined by setting the desired closed-loop response according to the following second order polynomial,

$$s^2 + 2\zeta\omega_t s + \omega_t^2 \tag{6.16}$$

which, in turn, yields the following proportional and integral gains as,

$$k_{pt} = 2\zeta\omega_t\,,\ k_{it} = \omega_t^2 \tag{6.17}$$

Applying the analogy from (6.11), the tracking controller is set 6 times faster than speed loop.

Figure 6.7 shows the poles of the characteristic equation (6.12) and influence of rotor speed, with and without linearization. It is seen that, at low rotor speeds, the poles move close to imaginary axis Figure 6.7 (a). By applying feedback linearization, the poles are independent of rotor speed and are away from imaginary axis Figure 6.7 (b). Thus for a speed-loop bandwidth of 0.75 Hz, the remaining controller bandwidths are computed and summarized in Table 6-1.

Table 6-1Sensorless vector control bandwidths vs sampling and PWM frequency

Control Loop	Symbol	Value [Hz.]
Speed Controller	ω_s	0.75
Current Controller	ω_c	100
Tracking controller	ω_t	2.5
State observer	ω_o	200

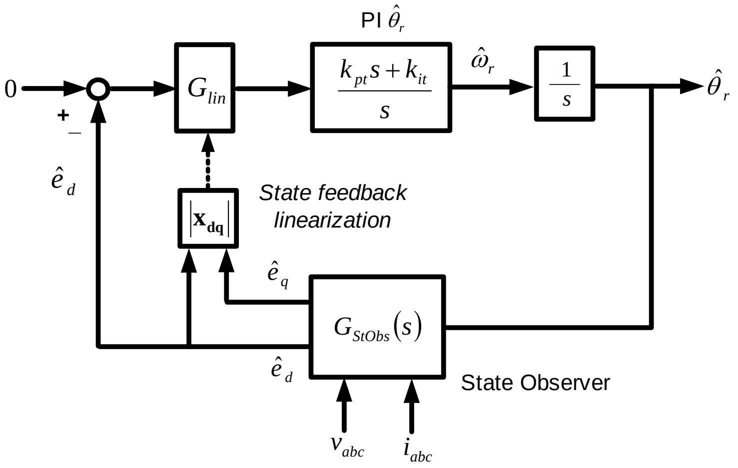

Figure 6.6. PLL-based rotor speed and position estimation scheme using a PI controller to regulate the *d*-axis back-EMF $\hat{e}_d^{\hat{r}}$ to zero [14].

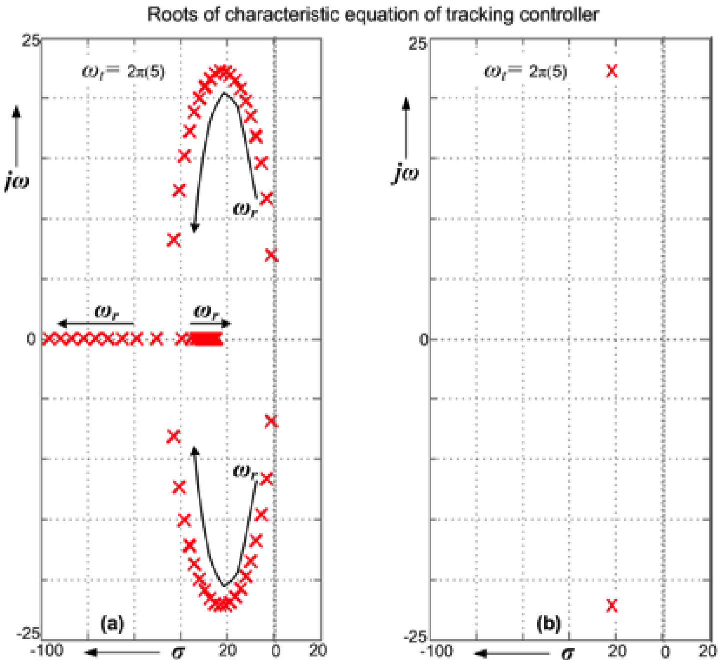

Figure 6.7. Influence of observer bandwidth and rotor speed on roots of characteristic equation (a) without linearization (b) with linearization

6.5. Simulation and Experimental Results

The simulation results will first consider startup operation of PMSM machine using the proposed sensorless control strategy. The parameters for simulation are listed in Table 6.2. As explained in section 6.2, various regions of operation are required to achieve the desired operating point. The load torque is increased linearly in proportion to the rotor velocity. Initially, the switching frequency is set at 2 KHz. In Figure 6.8 (a), the machine is ramped up using open speed loop and closed current loop control. The current loop is closed using reference position and 1 p.u amplitude of reference current as shown in Figure 6.8 (b). The points 3 through 6 are onset of the *Regions* defined in section 6.2. Due to lack of information of actual position, the open loop operation results in oscillation in speed during startup. Then at onset of *Region 3*, the state observer and tracking controller are engaged. It can be seen in Figure 6.8 (a) that the estimated speed tracks the actual speed, with some dynamics. Then at beginning of *Region 4* the speed loop is closed and the estimated and actual speed follows the reference speed. The tracking and speed controller together determines the transient response. When the speed loop is closed, amplitude of the reference current drops as shown in Figure 6.8 (b). In this region, machine continues to accelerate. The PWM is changed from asynchronous carrier based to synchronous space vector PWM at the beginning of *Region 5*. It can be seen that current ripple of the feedback current increases significantly. This is due to the effect of a decrease in the switching frequency. The switching frequency at this point is 320 Hz. The machine is then accelerated with synchronous PWM up to the onset of *Region 6* where the PWM is changed to synchronous optimal programmed PWM. At steady state the switching frequency is 660Hz which is 3 times lower than startup frequency and 12 times smaller than default switching frequency of a commercial drive.

The various transition modes in *Regions 5* and *6* highlight the stable operation of the proposed strategy. The zoomed view of the phase currents and the corresponding back EMF are shown in Figure 6.9. The error in synchronization between the rotor position and voltage pulse during every pulse drop causes current overshoot. If this error is not minimized, it may result in triggering the overcurrent protection in the drive. As seen in the figure, the current overshoot during every PWM transition is below 1.5 times the rated current, thus demonstrating a stable operation. The distortion in the currents during speed ramping is mainly because the back EMF is increasing in its amplitude while the inverter output voltage with programmed PWM is optimized for steady state operation.

Table 6.2.Machine parameters

Symbol	Values
r_s	0.35 ohm
L_s	1.2mH
λ_m	0.0495 Vp/rad/s
Poles	4
Speed	2200 rpm
Torque	1 Nm
Power	200W
Vdc	48V

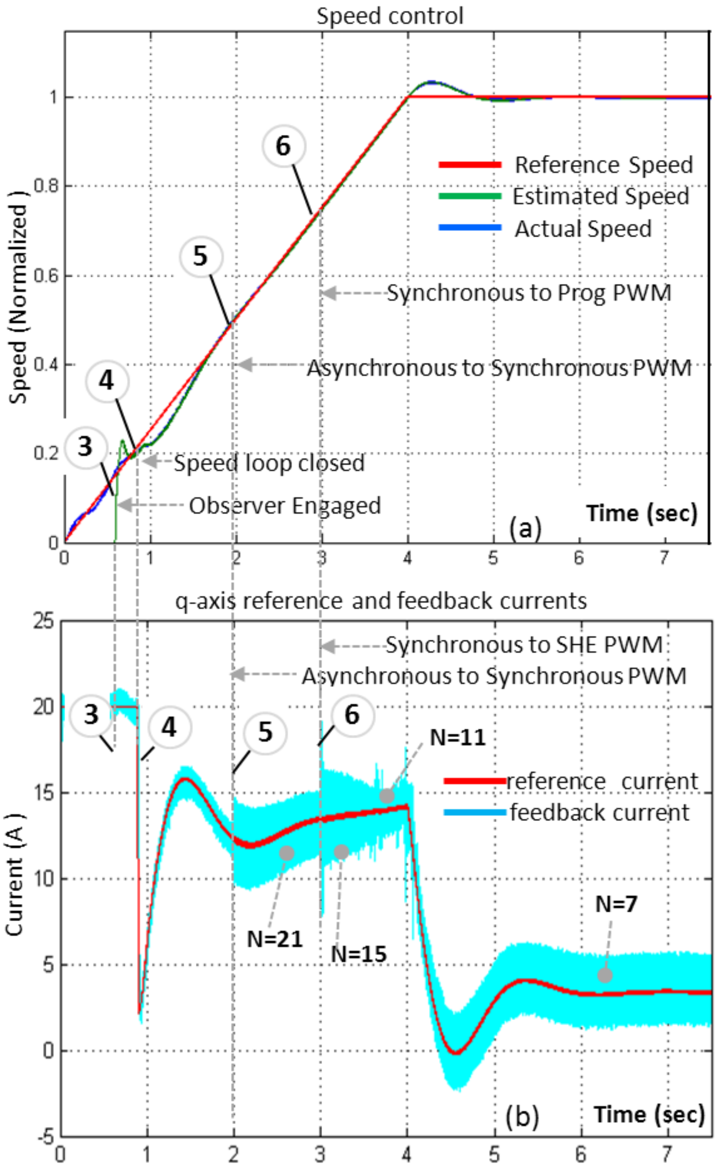

Figure 6.8. Simulation results: Starting operation of PMSM machine with various operating regions and PWM transition modes (a) speed profile (b) reference and feedback currents

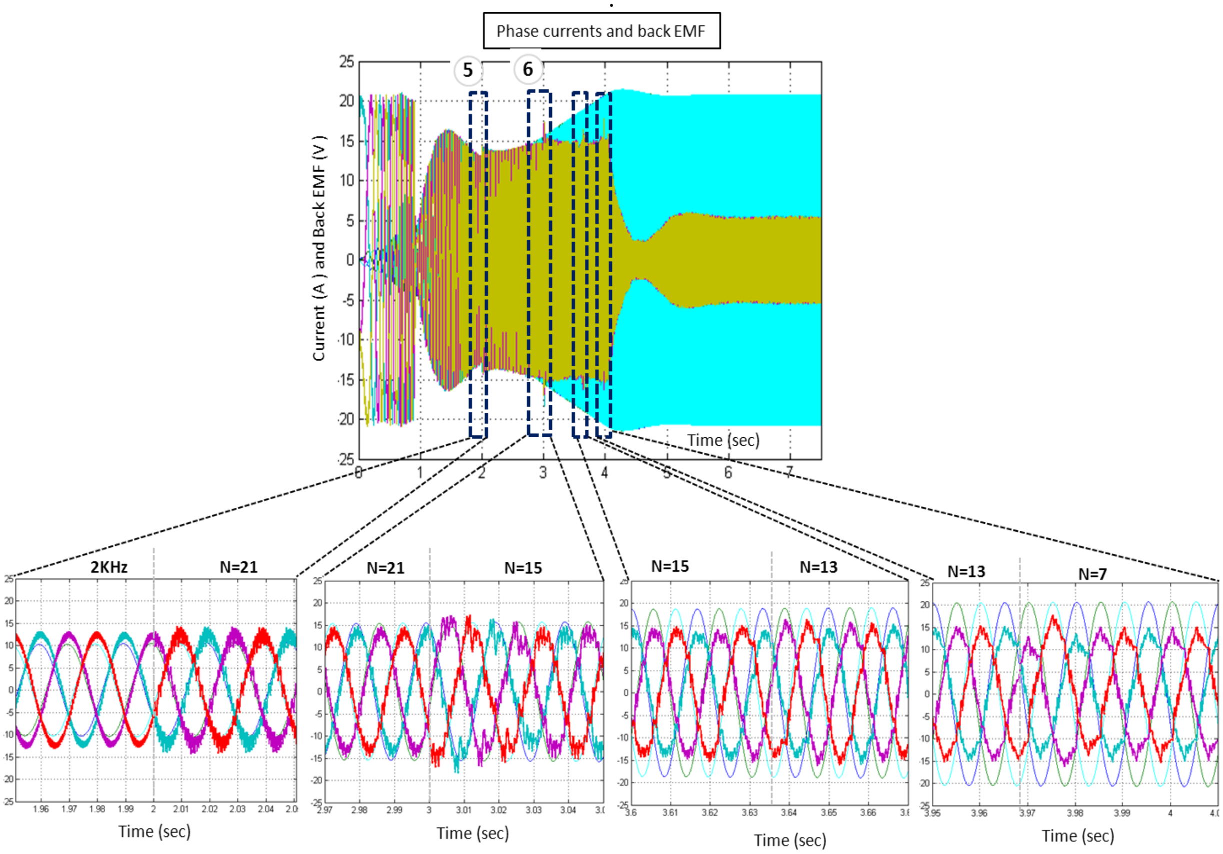

Figure 6.9. Simulation results: Three phase currents and corresponding back EMF of the machine

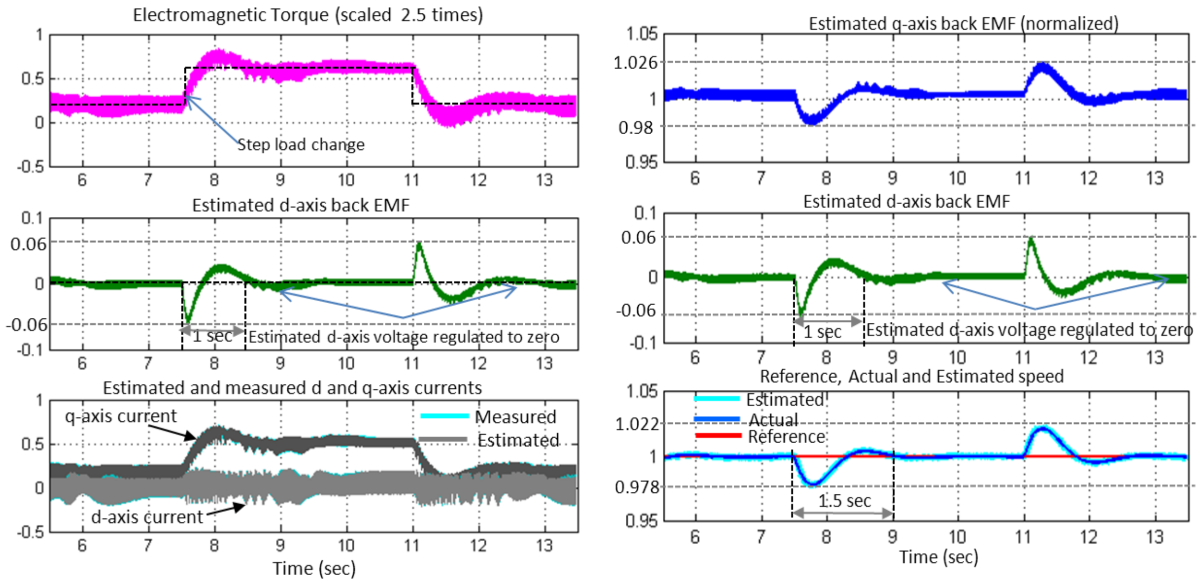

Figure 6.10. Simulation results Performance of sensorless controller for a 40 % load step (a) Observer performance (b) tracking and speed controller performance

To validate the stable closed loop dynamic performance of the scheme, a 40% step load change was applied to the motor at the time 7.5 sec. Figure 6.10 (a) shows the response of electromagnetic torque to the step load change. During this transient, the tracking controller regulates the estimated d-axis back EMF to zero within 1 sec. The estimated d and q axis current tracks the measured currents validating the tuning procedure. Figure 6.10 (b) shows the estimated q-axis back EMF voltage and the speed controller response for the same transient. It is seen that following the transient load change, the speed is regulated to its reference value within 1.5 sec. The slow response of the controllers is mainly due to lower control bandwidth available at low switching frequency. As described in section 6.2, climate control systems applications do not need fast dynamic performance hence the prescribed control strategy is suitable.

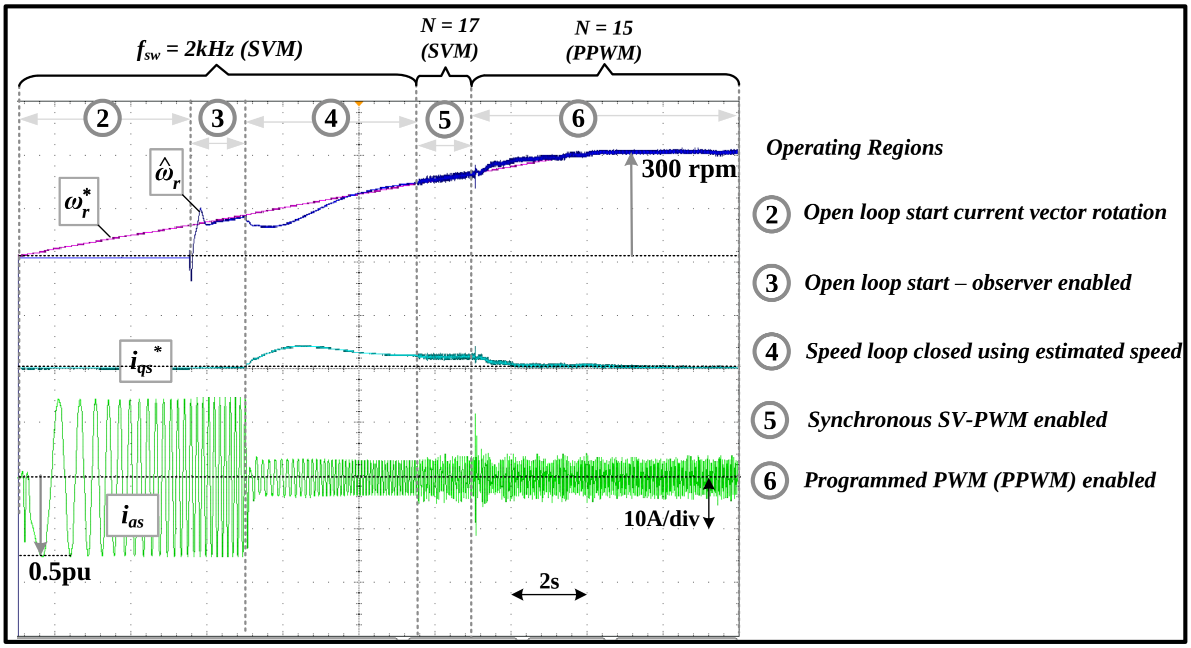

Figure 6.11. Experimental results: starting of PMSM with various operating regions and transitioning to programmed PWM modulation.

Figure 6.11 shows the experimental results of startup operation of the PMSM machine using the proposed sensorless control strategy. As explained previously, various regions of operation are defined to guide the motor speed to the desired operating point. The objective of the experimental result is to validate the PMSM rotor position sensorless operation at low switching frequency considering programmed PWM method. The operation from startup to steady state in Figure 6.11 is explained as follows:

Region 2–In this mode the machine is ramped up with speed open loop and closed current loop. This mode is also referred as current vector rotation. The current loop is closed using the reference rotor position. The amplitude of the d- axis reference current is limited to 0.5A p.u and that of the q-axis reference current is set to zero. As the reference speed is increases, the rotating current vector generates a rotating stator field that links with the rotor field in the air-gap causing the motor to spin in synchronism. During the open loop operation, there is usually an angular error between the stator field and rotor field causing torque oscillations at the excitation frequency. This error is minimized after closing the speed loop.

Region 3 –In this mode, the motor is still operating in open speed loop using current vector rotation. When the reference speed reaches 0.03 p.u. the state observer and tracking controllers are enabled. It is seen that the estimated speed $\hat{\omega}_r$tracks the reference speed ω_r^*after an initial transient.

Region 4 –When the reference speed reaches 0.05 p.u. the speed loop is closed. It is seen that the amplitude of the estimated speed reduces and then eventually tracks the reference speed. This transient response is predominantly determined by the tracking and speed controller. To reduce the error between the estimated and reference speed, the speed controller increases the amplitude of the q-axis reference current proportionally until steady state has been reached.

During the transition between *Regions 3* and *4*, the amplitude of the phase A current drops from 0.5 A p.u to 0.1A p.u due to the change in the reference amplitude of the d-axis current. The d-axis current amplitude is maintained at 0.1 A p.u to maintain the modulation index above certain threshold value (0.5) during the mode transitions.

Region 5 –When the reference speed reaches 0.07 p.u. the switching frequency is reduced from 2 kHz to 238 Hz. The pulse width modulation is changed from asynchronous carrier based space vector modulation (SVM) to synchronous SVM with $N = 17$ pulses. The reduction in switching frequency increases the current ripple of the phase current and is noted in the figure. Given the reduced switching frequency operation, it is seen that the closed loop observer and tracking controller can estimate the speed very well while the speed controller maintains the speed regulation. Thus the efficacy of the controller tuning method described in previous section is noted.

Region 6 –.When the reference speed reaches 0.08p.u., the pulse width modulation is changed from synchronous SVM to synchronous optimal programmed PWM with $N = 15$. During the transition between *Regions 5* and *6*, considering closed current loop operation, the error between the voltage pulse width of the synchronous SVM and that of the programmed PWM causes a current overshoot which is proportional to the width of the modulation, DC link voltage and the back EMF voltage. If this error is not minimized, it may result in triggering the overcurrent protection in the drive. As seen in the figure, the current overshoot during every PWM transition is below the open loop current of 0.5 A p.u, thus demonstrating a stable operation. Finally at steady state, the switching frequency of the inverter is only 300Hz while the electrical frequency of the motor is 20 Hz.

Figure 6.12. shows the zoomed view of the steady state operation of the PMSM with programmed PWM. The results show the tracking of the reference speed by the estimated speed. The estimated speed has some switching ripple (the amplitude of the switching ripple is less than 5 percent). Since there is no load applied on the system, the amplitude of the q-axis current is small. The d-axis current amplitude is maintained at 0.1 A p.u to maintain the modulation index above certain threshold value (0.5) during the mode transitions. Hence the steady state phase A current is regulated at 3 A peak.

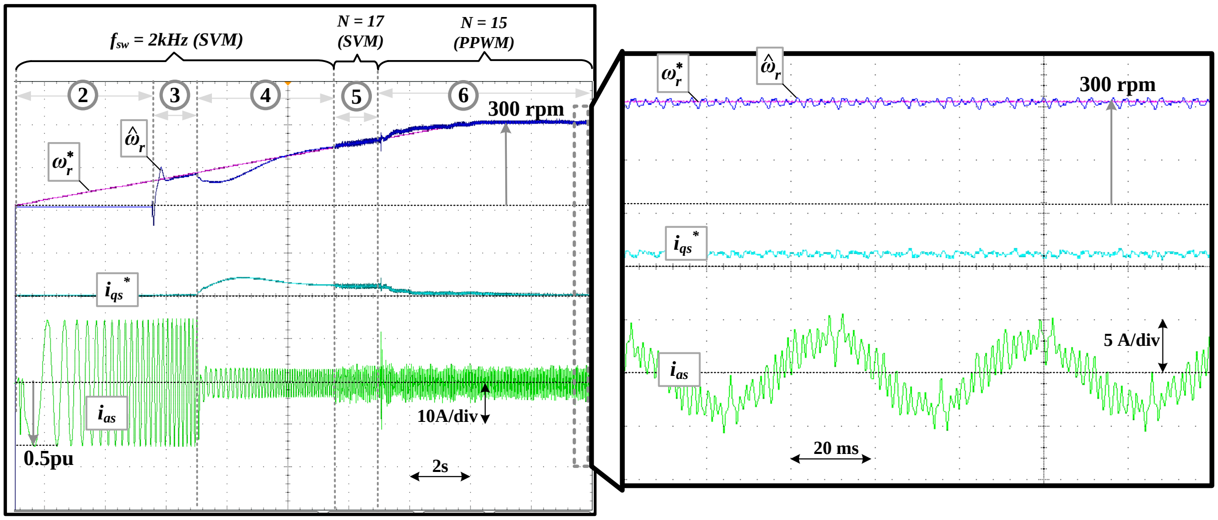

Figure 6.12. Experimental results: Starting operation of PMSM with various operating regions and transitioning to programmed PWM modulation and zoomed view.

The sensorless operation of PMSM considering the proposed strategy has not been reported and hence considered as a novel implementation. The important features to achieve the stable operation in this implementation are (i) the current controller with feedback oversampling discussed in chapter 5 and (ii) back EMF observer and tracking controller tuned for reduced switching frequency operation.

The above results considered speed mode of operation. Figure 6.13 (a) and (b) show the steady state experimental results considering torque mode operation of the PMSM incorporating programmed PWM. The drive is operating at switching frequency of 435 Hz and the fundamental electrical frequency of the motor is 29 Hz. The result is generated as follows: (a) Once the load motor steady state speed has been reached, the sensorless rotor position estimator is engaged. (b) Within two cycles, the current loop is closed using the estimated rotor position. (c) The output torque generated by the test motor which is proportional to the reference current on the q-axis. The reference current on the d-axis is zero. Figure 6.13 (a) shows the steady state estimated rotor position along with the measured phase current, modulation index and the q-axis feedback current. For the same case, Figure 6.13 (b) shows the line-line PWM voltage waveform with 150 Vdc, measured load torque of 9.2 Nm, DC link current with average value of 4.9A and phase A current with 8.5 A peak.

The results validate the torque mode sensorless closed loop operation of PMSM drive at low switching frequency.

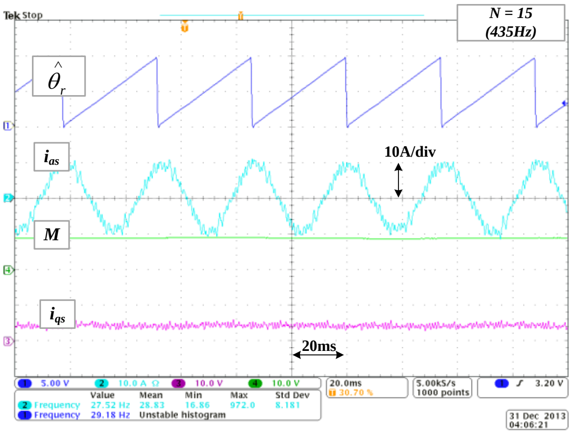

(a)

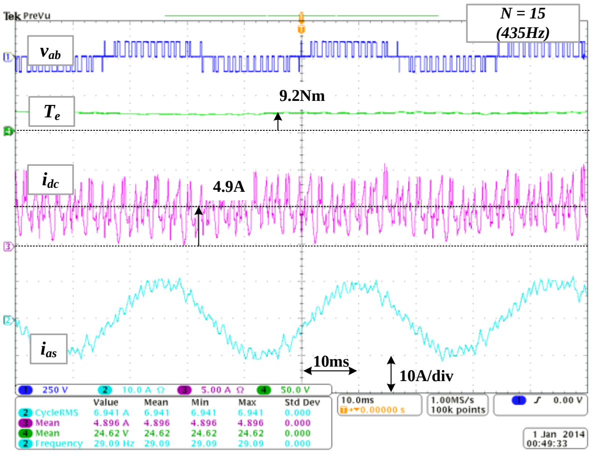

(b)

Figure 6.13 Experimental results: sensorless operation of PMSM at 29 Hz switching frequency of 435Hzand signal traces from top to bottom (a) estimated rotor position, phase current, modulation amplitude and q-axis reference current (b) line to line motor voltage, measured load torque, DC link current into the inverter and phase current.

6.6. Summary and Conclusions

This chapter focused on a sensorless vector control of permanent magnet synchronous motor (PMSM) drives operating at low switching frequencies for low cost, high efficiency climate control system application. A novel combination of position sensorless algorithm with programmed PWM for PMSM is developed and its laboratory implementation is shown. Stability analysis of back EMF observer and tracking controller for low switching frequency operation was shown and a guideline for selection of the controller gains was provided. The simulation and experimental results validate both the design methodology and the expected performance attained by the proposed control strategy.

The proposed algorithm demonstrates that both high system efficiency and low cost sensorless operation of PMSM drive is feasible.

References

[1] R. Krishnan, Permanent Magnet Synchronous and Brushless DC Motor Drives, CRC Press, 2010.

[2] D. Murphy and FG. Turnbull, *Power Electronic Control of AC Motors*, Pergamon Press, Oxford, 1988

[3] J. Holtz, and E. Bube. "Field-oriented Asynchronous Pulse-width Modulation for High-performance AC Machine Drives Operating at Low Switching Frequency." *IEEE Trans. Ind. Appl.*, vol. 27, no. 3 (June 1991): 574 –581.

[4] J. Holtz and N. Oikonomou, "Fast dynamic control of medium voltage drives operating at very low switching frequency—An overview," *IEEE Trans. Ind. Electron.*, vol. 55, no. 3, pp. 1005–1013, 2008.

[5] J. Holtz, "Pulsewidth Modulation for Electronic Power Conversion." *Proc. IEEE 82*, no. 8 (August 1994): 1194 –1214.

[6] P.H. Nayak, and R.G. Hoft, "Optimizing the PWM Waveform of a Thyristor Inverter." *IEEE Trans. Ind. Appl.*, no. 5 (October 1975), pp. 526–530.

[7] P.N. Enjeti, P.D. Ziogas, and J.F. Lindsay, "Programmed PWM Techniques to Eliminate Harmonics - A Critical Evaluation." *IEEE Industry Applications Society Annu. Mtg., 1988, Conference Record of the 1988*, vol.1, pp. 418 –430, 1988.

[8] G.S. Buja, and G.B. Indri, "Optimal Pulsewidth Modulation for Feeding AC Motors." *IEEE Trans. Ind. Appl.*, vol. IA-13, no. 1 (January 1977): 38 –44.

[9] S.B. Dewan, and J.B. Forsythe, "Harmonic Analysis of a Synchronized Pulse-Width-Modulated Three-Phase Inverter." *IEEE Trans. Ind. Appl.*, vol. IA-10, no. 1 (January 1974): 117 –122.

[10] T. Sebastian, G. R. Slemon, "Operating Limits of Inverter-Driven Permanent Magnet Motor Drives", *IEEE Trans. Ind. Appl.*, Vol. Ia-23, No. 2, March/April 1987.

[11] R. S. Colby and D. W. Novotny, "Efficient operation of surface mounted PM synchronous motors," IEEE Trans. Ind. Appt., vol. IA-23, no. 6, pp. 1048-1054, Nov./Dec. 1987.

[12] J.I. Itoh and T. Ogura, "Evaluation of Total Loss for an Inverter and Motor by Applying Modulation Strategies", IEEE EPE'10, CD-ROM, 2010

[13] Itoh. I. J, Nomura. N, Ohsawa. H, "A Comparison between V/f Control and Position-Sensorless Vector Control for the Permanent Magnet Synchronous Motor", Proc of Power Conversion Conference, vol.3, pp 1310 – 1315, 2002

[14] P. Kshirsagar, R.P Burgos, J. Jang, A.Lidozzi, , F. Wang, D. Boroyevich, S. K. Sul, "Implementation and Sensorless Vector-Control Design and Tuning Strategy for SMPM Machines in Fan-Type Applications", *IEEE TransonIndAppln Joint Special Issue - Nov/Dec 2012*.

[15] P. Kshirsagar and R. Krishnan, "Sensorless Control of Permanent Magnet Motors Operating at Low Switching Frequency for Climate Control Systems," *IEEE Sensorless Electric Drives Conference, Sept 2012*

[16] T. Ohmae, T. Matsuda, K. Kamiyama, and M. Tachikawa, "A microprocessor controlled high-accuracy wide-range speed regulated for motor drives," IEEE Trans. Ind. Electron., vol. IE-29, pp. 207-21 I , 1982.

[17] V. Blasko, V. Kaura, W. Niewiadomski, "Sampling of Discontinuous Voltage and Current Signals in Electrical Drives:A System Approach," *IEEE Trans. Ind. Appl.*, Vol 34, no. 5,1998, pp. 1123 –1130.

Chapter 7 Conclusions

7.1. Introduction

Energy efficiency improvement in variable speed motor drives is of widespread interest because of the rising cost of energy. Permanent magnet motor drives are especially favored in long running variable speed applications due to their high efficiency of operation. Given the PMBDCM and PMSM drives, two novel current control options for improving the efficiency of the motor drive system are proposed, analyzed and experimentally validated in this research.

The conclusions and contributions for first part of this research focused on injecting sinusoidal and non-sinusoidal currents in PMBDC machines based on their back EMF waveforms for higher system efficiency are discussed in section 7.2.

Section 7.3 covers the conclusions and contributions for second part of this research which is centered on system efficiency improvement of PMSM drives by reducing the switching frequency of inverter. Finally, the next steps to pursue this research further are discussed in section 7.4.

7.2. Efficiency improvement strategies in PMBDCMs with sine and non-sinusoidal current excitation waveforms

PMBDC machines have back-EMF voltage waveforms that can vary anywhere from trapezoidal to sinusoidal. To cover wide range in practice, a generalized analysis that can show the influence of higher harmonics in back-EMF and stator current excitation waveform on the torque ripple and motor harmonic losses is essential. Also, the present literature does not discuss the influence of non-sinusoidal currents on core losses of PMBDCM. Although injection of harmonics in the stator flux minimizes the torque ripple and stator resistive losses, they increase the stator core losses. Low cost and low horsepower machines can have core losses as high as stator resistive losses. These losses are higher at higher speeds of operation and increases in proportion to square of the harmonic frequency. Hence current control strategy that reduces the stator resistive as well as core losses in PMBDCM is desired. Accordingly following are the salient contributions for the first part of this research:

1. The generalized expressions as a function of back EMF characteristics are derived to evaluate the motor performance. Using these expressions, the torque ripple, stator resistive losses, iron losses, and power conversion ratio of the square, sinusoidal and non-sinusoidal currents are evaluated and presented for motors having different back EMF waveforms.

2. An analytical approach to estimate qualitative and quantitative core losses in the motor under loaded condition for various stator excitation schemes show that sinusoidal current injection yields lowest core losses.
3. Efficiency and loss comparisons of sine, square and NSHI current control made on two PMBDCMs at various speeds validates the trade-off highlighted using analytical loss estimation methods. In this aspect, it is advantageous to use NSHI scheme in the speed range until the sum of drive conduction and stator resistive losses exceeds core losses of the machine. When core losses become dominant, the algorithm is modified to sinusoidal current control thus maintaining higher efficiency operation.
4. The proposed hybrid approach enables higher efficiency operation in entire speed range for variable speed drives applications.
5. Closed form solution for non-sinusoidal currents and corresponding controller implementation yields better tracking performance over conventional approaches.

7.3. Efficiency improvement strategies in PMSM drive through switching frequency reduction.

This part of the research focused on evaluating the PMSM drive system efficiency improvement considering reduced switching frequency operation. While reduction of switching frequency reduces the losses in the inverter, it increases the stator resistive and core losses proportionally. Hence a comprehensive analysis of the total losses in the machine and inverter is required to quantify the total efficiency improvement considering suitable pulse width modulation strategy. Accordingly, following are the significant contributions of this part of the work:

1. Carrier based and programmed modulators operating at reduced switching frequencies are compared considering their loss factors. Given a PMSM drive system, synchronous optimal pulse width modulators with multiple pulse patterns are preferred over both carrier based and selective harmonic elimination based modulators due to their lower loss factor. It is also shown that synchronous optimal PWM requires smaller value of PMSM inductance than other modulation methods.
2. Given reduced switching frequency operation, a comprehensive procedure for estimating PMSM's predominant losses in the form of stator resistive and core losses are derived analytically. The accuracy of the method for estimating core losses is validated using finite element simulations. An analytical method for estimating the semiconductor losses at reduced switching frequencies and considering programmed PWM is developed. The method takes into account the actual current waveform including harmonics due to programmed PWM instead of

sinusoidal approximation. The accuracy of the method is validated using detailed simulation circuit models.

3. Using the analytical loss models of the motor and inverter, total system losses of five PMSM drive systems rated from 250W up to 100 kW are analyzed. It is shown that for systems utilizing 1200V semiconductor devices, the efficiency improvement is more than 1 percent. The case studies validate the proposed approach of improving the total system efficiency by reducing the inverter switching frequency. This improvement in efficiency translates to significant energy savings and cost reduction for applications requiring long hours of operation.
4. The proposed PMSM drive system efficiency is experimentally evaluated using three modulation methods (a) Space Vector Modulation (SVM), (b)Discontinuous PWM (DPWM) and (c) Programmed PWM. The experimental results show that the total system losses can be reduced by reducing the switching frequency. Since motor harmonic losses do not increase significantly at reduced switching frequency, the total system efficiency is improved. Programmed PWM method is advantageous at higher modulation indices due to its lower harmonic distortion content. The scaling analysis at various power levels using the proposed approach shows that the percentage efficiency improvement increases at higher power and voltage levels.

The implementation aspects connected with the switching frequency reduction and its application to improving the system efficiency of the PMSM drive are essential. Accordingly, following are the significant contribution of this work related to the same:

1. Implementation of programmed PWM on a present state of art digital signal processor has limitations as they are customized for carrier based modulators. Therefore a novel method of implementing programmed PWM using carrier signal is proposed and is experimentally demonstrated. The use of carrier signal in the proposed method allows ease of transition between programmed, continuous and discontinuous modulators enabling a hybrid approach.
2. Current control of PMSM is essential for stable operation. At low switching frequencies, the feedback sampling rate and the PWM update rate are slow. The resulting delays cause unstable operation of the motor. An alternative current controller approach with feedback signal oversampling is applied in conjunction with programmed PWM. The analysis and experimental results show that the method can achieve stable operation with acceptable dynamic performance at low switching frequencies. The method is simple and provides an alternative approach to the model based complex variable current controllers.
3. For reduced cost and improved reliability, rotor position sensorless vector control of permanent magnet synchronous motor (PMSM) drives is desired. Such an operation at low switching

frequencies becomes challenging. Accordingly, a novel combination of position sensorless algorithm with programmed PWM for PMSM is developed and its laboratory implementation is shown. Stability analysis of back EMF observer and tracking controller for low switching frequency operation is shown and a guideline for selection of the controller gains is provided. The simulation and experimental results validate both the design methodology and the expected performance attained by the proposed control strategy.

7.4. Recommendations for future work

This research focused on efficiency improvement strategies through control of permanent magnet machines. Analyses as well as practical aspects of the proposed current control strategies are provided for ease of adoption into industrial applications. Although system efficiency improvement in PMBDCM and PMSM drives is demonstrated through control, the research can be extended especially for advanced motor designs considering wide range of applications. Following are the topics that can be taken for further study:

1. **PMBDCM design for non-sinusoidal currents**: Redesign of trapezoidal PMBDCMs to achieve higher amplitude of non-triplen harmonics in back EMF waveform. Then the corresponding NSHI current waveform can be applied for higher torque with low ripple and lower stator resistive losses. To reduce the core losses in PMBDCMs, coreless motors with smaller air-gap can be considered. To improve the power density, Hall back permanent magnet arrays can be used to increase the air-gap flux density. For improved reliability and higher power density, NSHI methods can be extended to multi-phase PMBDCMs.
2. **PMSM design for reduced switching frequency operation:** Redesign of PMSMs considering reduced switching frequency operation of the inverter. Such an approach will allow selection of optimized motor inductance for given average torque and reduced motor harmonic losses. The selection of the low loss lamination steel to reduce the motor harmonic core losses.
3. **Online real-time efficiency improvement through loss estimation:** The proposed current control options improve efficiency through pre calculated operating envelope and offline loss estimation based on an operating point. However given the loss estimation methods developed in this research, online estimation of the losses can be calculated real time to search for high efficiency operating point.
4. **Improved transient performance at reduced switching frequencies:** In this research, the applications under consideration did not require high dynamic performance hence control methods at reduced switching frequencies for improved dynamic can be further studied. In this aspect, model based methods have been reported in the present literature. One approach is to increase the switching frequency dynamically to improve the transient performance. This may be possible as the transient operation lasts for short duration only. Hence the higher losses due to high switching frequency can

be sustained during transient operation. Then the operation can be reverted to reduced switching frequency during steady state.

5. **Further evaluation of motor harmonic losses:** Estimation of other motor harmonic losses in the form of skin, proximity effect and magnet eddy current losses considering programmed pulse width modulation methods. Also system performance considering vibration and acoustic noise generated needs further study.
6. **Reduced switching frequency operation of multi-level converters:** A three-level has almost 50% lower current harmonic distortion than a two level inverter. Hence the switching frequency reduction in multi-level inverters is higher. Hence performance and system efficiency evaluation of the proposed reduced switching frequency operation of PMSM drives considering multi-level inverters can be beneficial.